Microscopy of 2D Fermi Gases

Exploring excitations and thermodynamics

Dissertation
zur Erlangung des Doktorgrades
des Department Physik
der Universität Hamburg

vorgelegt von
Kai Henning Morgener
aus Goslar

Hamburg
2014

Abstract

This thesis presents experiments on 3D and 2D ultracold fermionic ^{6}Li gases providing local access to microscopic quantum many-body physics. A broad magnetic Feshbach resonance is used to tune the inter-particle interaction strength freely to address the entire Bose-Einstein condensate (BEC)-Bardeen-Cooper-Schrieffer (BCS) crossover.

We map out the critical velocity in the crossover from BEC to BCS superfluidity by moving a small attractive potential through the 3D cloud. We compare the results with theoretical predictions and achieve quantitative understanding in the BEC regime by performing numerical simulations, validating our approach. Of particular interest is the regime of strong correlations, where no theoretical predictions exist. In the BEC regime, the critical velocity should be closely related to the speed of sound, according to the Landau criterion and Bogoliubov theory. We measure the sound velocity by exciting a density wave and tracking its propagation along the cloud. The results are compared to the measured critical velocity.

The focus of this thesis is on our first experiments on general properties of quasi-2D Fermi gases. We realize strong vertical confinement by generating a 1D optical lattice by intersecting two blue-detuned laser beams under a steep angle. Due to the large resulting lattice spacing, we prepare a single planar quantum gas deeply in the 2D regime. The first measurements of the speed of sound in quasi-2D gases in the BEC-BCS crossover are presented. In addition, we present preliminary results on the pressure equation of state, which is extracted from in-situ density profiles. Since the sound velocity is directly connected to the equation of state, the results provide a crosscheck of the speed of sound. Moreover, we benchmark the derived sound from available equation of state predictions. We find very good agreement with recent numerical calculations and disprove a sophisticated mean field approach.

These studies are carried out with a novel apparatus which has been set up in the scope of this work. An all-optical cooling scheme and optical transport is employed to provide us with ultracold atomic clouds inside a separate small vacuum cell with optimal optical access. Above and below this cell, two high numerical aperture microscope objectives are placed to image and probe the Fermi gases in-situ on length scales comparable to the intrinsic length scales of the gases.

Zusammenfassung

In dieser Arbeit werden Experimente mit drei- und zweidimensionalen fermionischen ^{6}Li Gasen vorgestellt, die einen lokalen Zugang auf die quantenmechanische Vielteilchenphysik erlauben. Eine breite magnetische Feshbach-Resonanz erlaubt es uns, die Wechselwirkungsstärke frei einzustellen, um den gesamten BEC-BCS Übergangsbereich zu adressieren.

Wir messen die kritische Geschwindigkeit im Übergang von BEC- zu BCS-Suprafluidität, indem wir ein kleines attraktives Potential durch eine dreidimensionale Atomwolke bewegen. Die Ergebnisse werden verglichen mit theoretischen Vorhersagen. Dank numerischer Simulationen erlangen wir ein quantitatives Verständnis für die Messergebnisse im BEC-Bereich und können die Validität unserer Vorgehensweise untermauern. Von besonderem Interesse ist der Bereich starker Korrelationen, für den keine theoretischen Vorhersagen existieren. Dem Landau-Kriterium und der Bogoliubov-Theorie zu Folge, sollte die kritische Geschwindigkeit im BEC-Bereich eng verknüpft sein mit der Schallgeschwindigkeit. Diese messen wir, indem wir eine Dichtewelle anregen und ihre Propagation durch die Wolke verfolgen. Die Ergebnisse werden verglichen mit den gemessenen kritischen Geschwindigkeiten.

Der Fokus dieser Arbeit liegt auf unseren ersten Studien allgemeiner Eigenschaften von quasi zweidimensionalen Fermi Gasen. Den starken Einschluss der Gase realisieren wir mit einem eindimensionalen optischen Gitter. Dieses wird durch die Überlagerung zweier blau verstimmter Laserstrahlen unter steilem Winkel erzeugt. Durch den großen resultierenden Gitterabstand sind wir in der Lage, ein einzelnes, isoliertes Quantengas tief im zwei-dimensionalen Regime herzustellen. Wir präsentieren die ersten Messungen der Schallgeschwindigkeit in einem quasi zweidimensionalem Gas im BEC-BCS Übergang. Außerdem zeigen wir vorläufige Ergebnisse der thermodynamischen Druck-Zustandsgleichung, welche wir aus in-situ Dichteprofilen extrahieren. Da die Schallgeschwindigkeit direkt mit der Zustandsgleichung verknüpft ist, bieten diese Messungen einen Vergleich mit den direkten Schallmessungen. Darüber hinaus leiten wir die Schallgeschwindigkeit aus den verfügbaren theoretischen Zustandsgleichungen ab und finden eine sehr gute Übereinstimmung mit kürzlich veröffentlichten numerischen Simulationen. Die Vorhersage einer erweiterten Molekularfeld-Theorie können wir widerlegen.

All diese Untersuchungen wurden mit einem neuem Experiment durchgeführt, dessen Aufbau Teil dieser Arbeit war. Mit einem rein optischen Kühlungs- und Transportschema erzeugen wir ultrakalte Gase, mit denen die eigentlichen Experimente schließlich in einer kleinen, separaten Vakuumkammer mit optimalem optischen Zugang durchgeführt werden. Über und unter dieser kleinen, separaten Vakuumkammer befinden sich zwei Mikroskop-Objektive mit hoher numerischer Apertur. Diese werden genutzt, um die präparierten Fermi gase in-situ abzubilden und auf Längenskalen zu untersuchen, die den intrinsischen Längenskalen der Gase entsprechen.

Contents

1. Introduction

The first degenerate atomic Fermi gas was created just before the turn of the century [1], followed by the realization of a molecular BEC of bosonic dimers formed from fermionic atoms [2–4]. This seminal achievement signalled the advent of research on strongly interacting fermionic model systems, bringing new perspectives on phenomena which have occupied physicists for decades. These phenomena were often accessible only in limiting cases like BCS superconductivity of weakly interacting Cooper pairs. Today, ultracold atoms enable us to address the entire crossover from the BCS regime to the BEC regime with the turn of a knob [5–9].

Both BEC and BCS theory have been tremendously successful in providing the theoretical foundation for one of the most striking macroscopic phenomena originating from microscopic quantum effects: frictionless flow of particles [10–13]. Its appearance is remarkably widespread, ranging from superconductivity in solids to superfluidity in liquids and dilute gases of either bosonic or fermionic atoms. These phenomena are most robust in the strongly correlated regime [14–16]. Here, two-dimensional (2D) systems are of particular interest due to the connection to high-temperature superconducting materials [17–19] and the dominant role of fluctuations in lower dimensions [20, 21]. Fluctuations make 2D systems difficult to describe and open questions remain, which are not only of fundamental significance but also of technological importance.

To address these questions on a microscopic level, the ability to perform local measurements on the length scale of the interparticle separation is highly desirable. While this is very challenging in solids and liquids, ultracold atoms have emerged as an excellent platform to study strongly correlated low-dimensional superfluids. In recent years, there has been a remarkable development of techniques, providing high resolution imaging and an unprecedented degree of control [22–25]. However, so far only one experiment combined high spatial resolution with low-dimensional Fermi gases, enabling fascinating studies of transport phenomena [26–28]. Here, we present a novel apparatus which is tailored for the research on local properties of three- and two-dimensional fermionic ^{6}Li quantum gases. Our experimental setup incorporates a high performance optical system for probing and in-situ imaging with a resolution of $\sim 700\,\mathrm{nm}$.

We investigate one of the defining properties of superfluids, namely the critical velocity. We demonstrate the breakdown of superfluid flow in the BEC-BCS crossover by moving a point-like obstacle through the atomic cloud [29].

We observe heating only above the critical velocity and compare the results with corresponding measurements of the speed of sound. Due to our high spatial resolution and large interparticle spacing, the experiment is in close analogy with Landau's Gedankenexperiment for the first time. Our results in combination with numerical simulations by *V. Singh* and *L. Mathey* provide the opportunity to isolate relevant effects in very a pure and controllable environment.

Moreover, we are capable of creating isolated single layer quantum degenerate 2D Fermi gases. Reducing the spatial dimension of a many-body system influences the underlying physics fundamentally and gives rise to surprising effects. Consequently, one of the great challenges of contemporary research is the understanding of complex low-dimensional phases. Well-known examples in one-dimensional (1D) geometry are the strongly correlated Tonks-Girardeau gas [30, 31] and the Luttinger liquid [32, 33]. The 2D geometry is special in the sense that it is known to exhibit distinct effects not encountered in three-dimensional (3D) and 1D counterparts. For instance, fluctuations destroy true long-range order and prevent the emergence of a BEC in uniform 2D systems at any finite temperature [34–36]. Instead, a qualitatively different type of phase transition occurs. Below a critical temperature, the system becomes superfluid but the phase is only quasi-coherent, causing an algebraic decay of the first order correlation function. This is the Berezinskii-Kosterlitz-Thouless (BKT) phase transition, which is associated with the pairing of vortices [37, 38]. Another peculiar feature of 2D gases with respect to 3D is the fundamentally altered scattering physics. The scattering amplitude is energy dependent with a logarithmic divergence [39] and a bound state always exists, even for positive scattering length. The ability to probe 2D gases locally enables us to gain new insights into 2D fermionic quantum gases.

We present the first 2D speed of sound measurements to map out the BEC-BCS crossover. With a small attractive potential in the cloud centre, a density wave is created and its propagation tracked. The sound velocity is directly connected to the 2D equation of state, whose theoretical predictions are inconsistent and its complete behaviour is still unknown. To benchmark the theoretical equations of state, we calculate the corresponding sound velocities and compare them to the measurement. We find very good agreement between experiment and the results we obtain from numerical calculations [40], which are expected to be the most reliable prediction so far. We are furthermore able to invalidate a sophisticated mean field approach [41]. From in-situ density profiles, we extract the experimental 2D pressure equation of state and derive the speed of sound, which is in excellent agreement with results from the direct measurement.

Beyond these investigations, our experiments pave the way for a deeper understanding of 2D systems. In the near future, we hope to observe the BKT phase transition locally and to explore exotic phases like Fulde-Ferrell-Larkin-Ovchinnikov (FFLO) superfluids in imbalanced mixtures [42, 43].

This thesis is organized as follows:

- In Chapter 2 we summarize the basic theory of 3D and 2D Fermi gases. The given overview is enclosed by an outline of our experimental capabilities to motivate the content of the succeeding chapters. We conclude with a short summary of the distinct features of 2D Fermi gases.
- Chapter 3 and 4 present the design and build process of our experimental apparatus. We give an overview of the different parts and steps which are required to produce degenerate single layer 2D clouds of fermionic ^{6}Li. Furthermore, the development and realization of our magnetic field setup is presented, which was one my main responsibilities in the early stages of the experiment.
- In Chapter 5, we present measurements of the critical velocity, demonstrating the breakdown of superfluidity in 3D Fermi gases in the BEC-BCS crossover. We compare the results to the speed of sound and theory predictions.
- Chapter 6 turns the attention to the physics in quasi-2D Fermi gases, discussing the 2D scattering problem and the phase diagram with the focus on the BKT phase transition. On classical grounds, we show that no BEC emerges in 2D and demonstrate the important role of phase fluctuations in reduced dimensionality. We compare the available 2D equation of state predictions and develop a benchmark against our experiment.
- In Chapter 7 we present the speed of sound measurements in quasi-2D Fermi gases in the BEC-BCS crossover. We furthermore determine the pressure equation of state from in-situ density profiles. We extract the speed of sound from the measured and theory equations of state and compare it to the results of the direct measurement. These efforts on 2D thermodynamics are fortified by temperature measurements of strongly interacting 2D Fermi gases.

Publications in the context of this thesis

- **The critical velocity in the BEC-BCS crossover**
  W. Weimer, K. M., V. P. Singh, J. Siegl, K. Hueck, N. Luick, L. Mathey, and H. Moritz
  arXiv:cond-mat/1408.5239v1, accepted in Phys. Rev. L.

2. Fermionic Quantum Gases in Three and Two Dimensions

Quantum-degenerate Fermi gases offer the unique possibility to access magnetic Feshbach resonances to tune the sign and strength of the inter-particle interaction to change the nature of quantum statistics freely from fermionic to bosonic behaviour. The crossover between the two regimes has been the subject of considerable interest for many years.

This chapter provides the basic theoretical background for the remainder of this work. We first give a compact overview of the parameters relevant to describe Fermi gases in three and two dimensions. Both cases are treated in parallel to emphasize the difference of the underlying physics. Then, a description of the 3D scattering properties forms the basis for the subsequent introduction into Feshbach resonances. The corresponding sections are kept short since there already exists a variety of literature on theses topics.

Since the focus of this work is on experiments in 2D gases, we begin by outlining our experimental aims in respect to the 2D quantum systems. We will end this chapter by briefly outlining the distinct features arising in 2D, whereas an extensive discussion of the 2D physics is given in Ch. 6.

2.1. Experimental System

Our apparatus is tailored for the production of ultracold 2D Fermi gases with tunable interactions to explore the entire crossover between gases consisting of composite bosonic pairs and gases consisting of fermionic Cooper pairs. Reducing the dimensionality of many-body systems is achieved by subjecting the gas to a tight harmonic confinement such that only the quantum mechanical ground state in that direction is occupied. This has important consequences for the microscopic properties of 2D quantum gases and gives rise to new physical effects not encountered in their 3D counterparts. For instance, the scattering behaviour is fundamentally changed and a two-body bound state is present even on the fermionic side of the magnetic Feshbach resonance, where no 3D bound state exists. A comprehensive understanding of the distinct features of 2D gases is still missing and some theoretical predictions seem to be consistent with experimental observations [44, 45].

Against this background, our experiment is the first to connect two particular capabilities to push the frontiers of research. We combine the realization

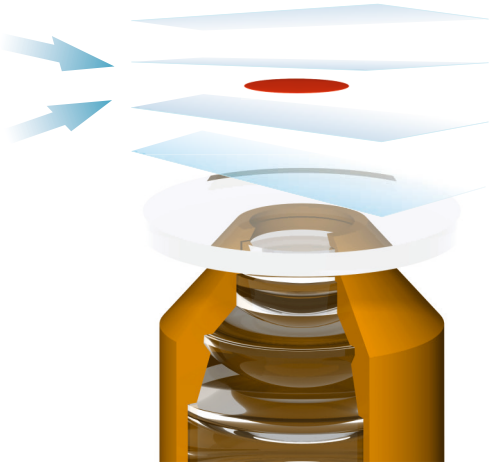

Figure 2.1.: Single layer 2D Fermi gases are created in an anti-node of the blue-detuned optical lattice. The steep angle of intersection between both lattice beams leads to a large lattice spacing of 2.9 µm. The lower of the two microscope objectives is used to image the clod with a high spatial resolution of ~ 700 nm. Drawing not to scale.

of a single 2D cloud with the ability to manipulate and probe the samples locally with very high resolution. Using fermionic ^{6}Li is particularly favourable due to the large background scattering rate, the broad magnetic Feshbach resonance, and the low particle mass in respect to the study of, e. g. dynamics in bulk-, lattice- and mesoscopic systems.

To create 2D quantum gases in our experiment, an ultracold cold has to be sufficiently strongly compressed in one direction to freeze out all corresponding excitations. This is due to the fact that the tight confinement causes all relevant energy scales to be much smaller than the energy level spacing to the first excited state in the strongly confined direction.

Our planar Fermi gases are produced in a single anti-node of a blue-detuned 1D lattice. The lattice is generated by two blue-detuned laser beams which intersect under an angle of 10.4° to form an interference pattern with a spacing of 2.9 µm, as shown in Fig. 2.1. The realized trap frequency in the transverse direction of 25 kHz generates very high trap aspect ratios of $\omega_r/\omega_z \approx 1000$ and therefore quantum gases deep in the 2D regime. The blue detuning and hence the absence of radial optical confinement enables us to realize such high ratios and, in principle, to perform efficient evaporative inside the optical lattice. This is due to the fact that no optical confinement restricts the hot atoms from leaving radially. As a consequence, very low temperatures are accessible which is a benchmark for most research interests, such as anti-ferromagnetic ordering or the BKT superfluid phase transition. At present, a weak harmonic confinement is still provided by the curvature of the magnetic field applied.

The typical starting point for experiments is a degenerate 2D Fermi gas

with up to 20 000 atoms in each of the two lowest, equally populated, hyperfine spin states. The particle density in the centre of the cloud is on the order of $1\,\mu m^{-2}$. The cloud diameter is typically about 100 µm.

Below and above the 2D Fermi gases, two microscope objectives form a high performance optical system with a diffraction limited resolution of ~ 700 nm. Through the upper microscope, arbitrarily shaped potentials, optical lattices, or dipole traps can be imprinted on the atoms. Therefore, the 2D gases can be probed on the relevant intrinsic length-scales, i. e. the healing length, the inter-particle distance, or in future experiments, the lattice spacing in 2D Fermi Hubbard systems. Absorption imaging is carried out with the lower microscope in combination with a telephoto lens in front of an electron-multiplying charged-couple device (EMCCD) camera to resolve, e. g. local density fluctuations and potentially single atoms in individual lattice sites. With only one layer of atoms, there is no integration along the line of sight, which makes a single 2D cloud is particularly advantageous for the imaging of smallest features.

2.2. Ideal Fermi Gases

The case of an ideal homogeneous Fermi gas is a good starting point for a more detailed description as it already gives access to important properties of trapped Fermi gases.

At very low temperature T, the de Broglie wavelength $\lambda_{dB} = \sqrt{2\pi\hbar^2/(m k_B T)}$ of particles is comparable to the inter-particle distance and degeneracy sets in. Particles with an integer total spin, i. e. bosons, condense and become superfluid. Fermions with a half-integer spin obey a fundamentally different microscopic mechanism, as presented in the following.

2.2.1. Homogeneous Case

The energy states in an ideal Fermi gas at zero temperature are exactly filled up to the Fermi energy E_F and then the occupation drops to zero, see Fig. 2.2. Since identical fermions repel each other due to the Pauli exclusion, each energy state is filled with exactly one particle. For a mixture of two different hyperfine spin states, one of each kind can share the same energy.

The chemical potential μ is the energy which is required to add a particle to the system. Thus, the chemical potential at zero temperature is identical to the Fermi energy $\mu = E_F$. For $T \neq 0$, the energy states close to the Fermi edge become thermally populated. The sharp edge at E_F becomes washed out and the occupation is described by the Fermi-Dirac distribution

$$f_{FD}(E,T) = \frac{1}{e^{(E-\mu)/k_B T} + 1}. \tag{2.1}$$

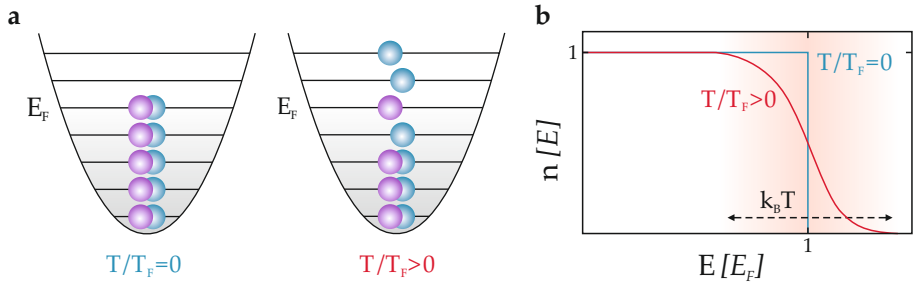

Figure 2.2.: a) Fermi statistics for zero and finite temperature. Exactly one fermion per spin can occupy each energy state. For zero temperature $T/T_F = 0$, fermions fill the available states in the Fermi sea up to the Fermi energy E_F. For finite temperature $T/T_F > 0$, states with energies higher than E_F become thermally accessible in a blurred region around the Fermi surface. b) The Fermi distribution as a function of energy for two different temperatures. At zero temperature, all available states are filled up to the Fermi edge. For finite temperature, the sharp edge is blurred over a region with a width of the energy $k_B T$.

Integration yields the particle number

$$N = \int_0^{E_F} \rho^d_{DOS}(E) f_{FD}(E,T) dE. \tag{2.2}$$

Here, $\rho^d_{DOS} \propto E^{d/2-1}$ is the density of states in d dimensions. In a homogeneous 3D gas, the density of states is proportional to the square root of the energy $\rho^{3D}_{DOS} \propto \sqrt{E}$, whereas the 2D density of states ρ^{2D}_{DOS} is energy independent, see Table 2.1. The smallest length scale in the system is given by the Fermi wave vector k^d_F, which depicts the radius of the Fermi surface in momentum space.

Non-interacting Fermi gases are experimentally feasible, but they always require a confinement to restrict the particle movement to a defined volume. This is typically an optical trap, in the simplest case realized by a Gaussian beam. For small distances from the centre, the generated trapping potential can be assumed as harmonically. This case is discussed in the following.

2.2.2. Harmonically Trapped Case

The harmonic trapping potential V_{trap} imposes an inhomogeneity on the gas. As a consequence, the global chemical potential μ becomes ill-defined and is replaced by the local quantity

$$\mu_{LDA} = \mu - V_{trap}. \tag{2.3}$$

Homogeneous gas	2D	3D
Fermi energy E_F	$\frac{2\pi n\hbar^2}{m}$	$\frac{(6\pi^2 n)^{2/3}\hbar^2}{2m}$
Fermi vector k_F	$(4\pi n)^{1/2}$	$(6\pi^2 n)^{1/3}$
Density of states ρ_{DOS}	$\frac{mV}{2\pi\hbar^2}$	$\frac{m^{3/2}V}{\sqrt{2}\pi^2\hbar^3}\sqrt{E}$
Energy per particle $\frac{E}{N}$ $(T > T_F)$	$k_B T$	$\frac{3}{2}k_B T$

Table 2.1.: Characteristic quantities of homogeneous Fermi gases in two and three dimensions in absence of interaction. At zero temperature all fermions fill the Fermi sea which has the radius k_F^d in the d-dimensional momentum space. Further implications and the corresponding dimension-depending formulas are given in the text.

The total chemical potential μ_{LDA} resembles the sum of the chemical potential μ of a homogeneous gas and the trapping potential V_{trap}, where μ is fixed by particle number conservation.

On a local scale, the trapped gas has the same properties as a homogeneous gas at finite temperature with a chemical potential μ_{LDA} and the local, spatially dependent Fermi wave vector $k_F(\mathbf{r})$. This is the local density approximation (LDA), which is valid if the trapping potential varies only slowly over a length scale given by $1/k_F(\mathbf{r})$ and the de Broglie wavelength λ_{dB} so that the energy difference of two neighbouring states is small compared to the temperature T.

The Fermi-Dirac distribution $f_{FD}(E)$ in the framework of the LDA is given by

$$f_{LDA}(\mathbf{r},\mathbf{p}) = \frac{1}{e^{\mathbf{p}^2/2m+(V_{trap}(\mathbf{r})-\mu)/k_B T}+1}. \tag{2.4}$$

Integration either over the spatial vector $\mathbf{r}$ or the momenta $\mathbf{p}$ gives the atomic density or momentum distribution in the trap. In a semiclassical approximation, the density distribution of the thermal non-interacting gas reads

$$n(\mathbf{r}) = \int \frac{d\mathbf{p}^d}{(2\pi\hbar)^d} f_{LDA}(\mathbf{r},\mathbf{p}) \tag{2.5}$$

$$= -\frac{1}{\lambda_{dB}^d}\mathrm{Li}_{d/2}(-\zeta e^{-V_{trap}(\mathbf{r})/k_B T}), \tag{2.6}$$

where $\mathrm{Li}_{d/2}$ is the $d/2$th polylogarithmic function $\mathrm{Li}_n(z) \equiv \Sigma_{k=1}^{\infty} z^k/k^n$ and the fugacity is $\zeta \equiv \exp(\mu/k_B T)$. At zero temperature, f_{LDA} can be replaced by a step function which greatly simplifies the integral.

For finite temperature, integration of Eq. 2.6 over all $\mathbf{r}$ yields the particle

Harmonically trapped gas	2D	3D
Fermi energy E_F	$(2N)^{1/2}\hbar\bar{\omega}$	$(6N)^{1/3}\hbar\bar{\omega}$
Fermi vector k_F	$(4\pi n_0)^{1/2}$	$(6\pi^2 n_0)^{1/3}$
Density of states ρ_{DOS}	$E/(\hbar^2\bar{\omega}^2)$	$E^2/(2\hbar^3\bar{\omega}^3)$
Chemical potential $\mu(T)/E_F$	$1-\frac{\pi^2}{6}\left(\frac{k_B T}{E_F}\right)^2$	$1-\frac{\pi^2}{3}\left(\frac{k_B T}{E_F}\right)^2$
Degeneracy T/T_F	$(-2\mathrm{Li}_2(-\zeta))^{-1/2}$	$(-6\mathrm{Li}_3(-\zeta))^{-1/3}$

Table 2.2.: Comparison between trapped Fermi gases in two and three dimensions. The particle density at the centre of the trap is given by n_0. The d-dimensional mean trapping frequency is given by $\bar{\omega}_d = \Pi_d(\omega_d)^{1/d}$ and the polylogarithmic function $\mathrm{Li}_{d/2}$ is defined in the text.

number

$$N = -\left(\frac{k_B T}{\hbar\bar{\omega}_d}\right)^d \mathrm{Li}_d(-\zeta), \tag{2.7}$$

where $\bar{\omega}_d = \Pi_d(\omega_d)^{1/d}$ is the mean frequency of the harmonic trapping potential $V(\mathbf{r})$ in d dimensions. With Eq. 2.7, the Fermi energy in the zero-temperature limit becomes

$$E_F^d = ((d-1)!\,d\cdot N)^{1/d}\,\hbar\bar{\omega}_d. \tag{2.8}$$

A measure for the degeneracy of ultracold Fermi gases is given by degeneracy parameter

$$\frac{T}{T_F^d} = (-1\cdot(d-1)!\,d\cdot\mathrm{Li}_d(-\zeta))^{-1/d}, \tag{2.9}$$

which is given in terms of the fugacity ζ.

The evaluation of the above stated expressions for the 3D and 2D case yields the quantities presented in Table 2.2.

In the experiment, the cloud properties are typically retrieved via absorption images. In case of a 3D cloud, the imaging light projects the 3D density distribution onto a 2D optical density (OD) map[1]. In the case of a 2D cloud, we have direct access to the density distribution, which is advantageous in many cases.

[1] The image analysis is straightforward, even in the case of a given expansion time. Since both, potential and kinetic energy in the corresponding single particle Hamiltonian are quadratic in respectively $\mathbf{r}$ and $\mathbf{p}$, the time of flight (TOF) leads to no significant change of the cloud shape and the density distribution is directly related to the in-situ distribution by simple rescaling.

2.3. Fermi Gases with Tunable Interactions

So far, we have neglected inter-particle interactions. The density distribution of non-interacting gases simply represents Fermi statistics, which is interesting to a limited extent. We now consider two-component Fermi gases which give rise to the ability to precisely tune the interaction between particles in different hyperfine states via magnetic Feshbach resonances. The possibility to control the collisional behaviour allows us to efficiently reach quantum-degeneracy via evaporative cooling and moreover, to realize intriguing systems with non-trivial correlations and interesting many-body states.

This section gives an introduction to the elastic scattering behaviour of ultracold atoms in 3D and briefly explains the phenomenon of Feshbach resonances. Afterwards, the crossover of 3D Fermi gases between the BCS and the BEC regime is presented. We emphasize that the treatment here is kept deliberately short whereas an extensive discussion of the 2D scattering problem is given in Ch. 6.

2.3.1. Elastic Scattering

The scattering behaviour of ultracold fermionic alkali atoms is typically dominated by two-body collisions [46]. The corresponding length-scale is the van der Waals length which is about two orders of magnitude smaller than the typical inter-particle spacing $n^{-1/3} \simeq 500\,\mathrm{nm}$ in our experiment.

Solving the 3D radial wave equation for a given angular momentum l and spin quantum number s yields the scattering properties between two colliding particles. In general, the two-body wave-function must be symmetrized so that the spatial wave function is anti-symmetric in case of a collision between two identical fermions. Then, s-wave scattering is forbidden at low temperatures, which is why spin-polarized mixtures are non-interacting and spin mixtures are typically used in the experiment.

When considering two different fermions, the solution $\phi_{\mathbf{k}}$ of the radial wave equation, written in the partial wave expansion in l, is given by an incoming plane wave which is superimposed with an outgoing spherical wave

$$\psi_{\mathbf{k}} = e^{i\mathbf{k}\mathbf{r}} + \frac{e^{ikr}}{r} f_l(\mathbf{k}, \mathbf{k}'). \tag{2.10}$$

Here, $\mathbf{k}'$ is the wave vector of the outgoing wave and f_l the scattering amplitude of the partial wave with angular momentum l.

The total cross section is then

$$\sigma = \int d\Omega |f(\mathbf{k}, \mathbf{k}')|^2. \tag{2.11}$$

The isotropic s-wave contribution is dominant in the low energy limit $k \to 0$, which is due to the emergence of a centrifugal barrier for higher angular

momenta. As a consequence, all other partial waves are suppressed if the spherical symmetric scattering potential $V(r)$ vanishes fast enough for large distances r. The effective potential is then given by

$$V_{\text{eff}}(r) = V(r) + \frac{\hbar^2 l(l+1)}{2mr^2}, \tag{2.12}$$

where $V(r)$ is of the form r^{-6}, and m is particle mass.

For $k \to 0$, the influence of the scattering potential on the outgoing wave function is expressed by a phase shift δ_0 depending on the 3D s-wave scattering length

$$a_{3D} = -\lim_{k\to 0} \frac{\tan \delta_0(k)}{k}. \tag{2.13}$$

The scattering amplitude can be written as $f(k) = 1/k \cot \delta_0 - ik$, where the case $\delta_0 \to \pi/2$ depicts a resonant contribution to the phase shift and thus a diverging scattering length a_{3D}. This is referred to as the 3D scattering resonance.

We now advance to the description of s-wave scattering in presence of a Feshbach resonance where resonant coupling to a two-body bound state can change the scattering length dramatically.

2.3.2. Feshbach Resonances

A Feshbach resonance occurs whenever a bound state is resonantly coupled to the collision of two particles. If these two particles feature different molecular bound states, each state gives rise to a separate Feshbach resonance [5]. For alkali atoms, the hyperfine interaction between the electron spins and the nuclear spins leads to coupling between different spin states, i. e. singlet and triplet states, see Fig. 2.3 a. The energetically available channel is called entrance or open channel, which in the case of ^{6}Li, describes the s-wave scattering of the triplet state. The scattering potential of the called closed channel has a higher asymptotic energy and is not accessible due to energy conservation.

The different magnetic moments $\Delta\mu$ of the states in the different channels enable us to tune the energy difference between their asymptotes. This allows us to tune the bound state in the closed channel in or out of resonance with the two colliding atoms in the open channel and hence to adjust the scattering length by an external magnetic offset field [47]

$$a_{3D}(B) = a_{bg}\left(1 - \frac{\Delta B}{B - B_0}\right)(1 + \alpha(B - B_0)). \tag{2.14}$$

Here, a_{bg} is the off-resonant background scattering length, ΔB the width and B_0 the position of the Feshbach resonance in terms of the magnetic field strength, as shown in Fig. 2.3 b. The correction factor α results in a 99 % agreement of the analytical expression in Eq. 2.14 with the empirical values in the range 600 G to 1200 G [48].

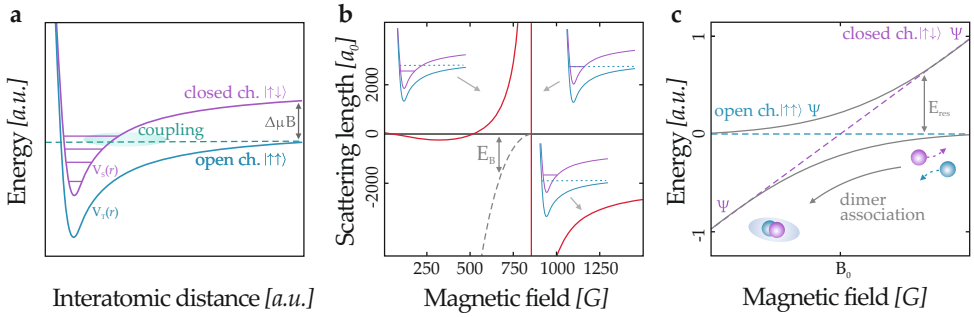

Figure 2.3.: Scattering in presence of a magnetic Feshbach resonance. a) Two-channel model of the Feshbach scattering resonance. Shown are the Lennard-Jones potentials of a pair of fermions in the closed channel and open channel. The relative offset between the closed and the open channel is tuned with an external magnetic field acting on the different magnetic moments μ_B. A bound state in the closed channel can be resonantly coupled to the asymptotic energy of the open channel. b) Scattering length a_{3D} between the $|1\rangle|2\rangle$ mixture in ^{6}Li as a function of the external magnetic field. The insets sketch how the open channel is tuned through the resonance. For scattering lengths $a_{3D} < 0$, the energy of the bound state is higher than energy of an incoming particle. Crossing the resonance to the regime of positive scattering lengths $a_{3D} > 0$, the scatterers can form composite dimers with an binding energy E_B. c) The two-level model description of the resonance dynamics between the scattering constituents. The level of the scattering state of the open channel and the level of the bound state of the closed channel feature an anti-crossing at the position of the resonance. Ramping the magnetic field from field strength higher than the resonance into the BEC regime leads to dimer formation.

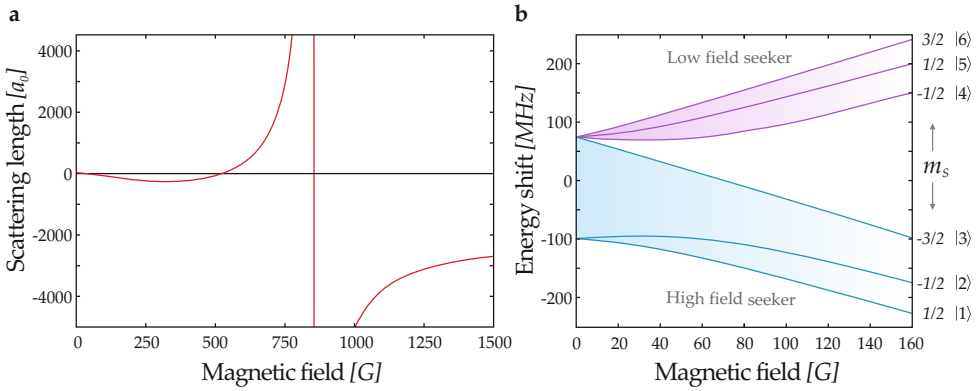

Figure 2.4.: a) Scattering length between the hyperfine states $|1\rangle$ and $|2\rangle$ of ^{6}Li as a function of the external magnetic field. The scattering length is given in units Bohr's radius a_0. The Feshbach resonance is located at a magnetic field strength of 834.15 G. b) Energy of the hyperfine states $|1\rangle$ to $|6\rangle$ as a function the magnetic field. The energy is given in units of the magnetic-dipole hyperfine constant for the ground state $2^2S_{1/2}$ without hyperfine interaction. m_s denotes the z-component of the angular momentum of the corresponding hyperfine state [49].

We can therefore change from repulsive interaction ($a_{3D} > 0$), where the bound energy asymptote is lower than the energy of the closed channel, to attractive interaction ($a_{3D} < 0$), where the energy of the bound state is higher, see Fig. 2.3 b.

The probability density of the two-particle wave function $|\psi|^2$ in the closed channel is only large near resonant coupling between two fermions in the open channel to the bound state in the closed channel. Then the Feshbach resonance is reached and the scattering length diverges. The energy of the singlet and triplet wave function are correlated and feature an anti-crossing along the scattering resonances which is depicted in Fig. 2.3 c. The magnetic field dependence of the energy for the different hyperfine states of ^{6}Li is shown in Fig. 2.4 b. The states are numbered in ascending order, corresponding to higher energies in an external magnetic field. Typical experiments are carried out at magnetic field strengths between 600 G to 1000 G. Above 500 G, the electronic spin of the hyperfine states $|1\rangle$, $|2\rangle$, and $|3\rangle$ are fully polarized and aligned parallel to each other. Therefore, two ^{6}Li atoms in any two different of the lower three hyperfine states scatter as a triplet.

We use a mixture of the two lowest states $|1\rangle$ and $|2\rangle$. Mixtures of higher hyperfine states feature channels for losses via inelastic collisions, which are however, relatively small in case of the three lowest states.

The exact positions of the magnetic Feshbach resonances of ^{6}Li are listed in Table 2.3. The $|1\rangle|2\rangle$ mixture features an extremely narrow resonance at 543.28 G. The strong contribution of the closed channel at narrow resonances

Mixture	B_0	ΔB	a_{bg}
$\|1\rangle\|2\rangle$	834.15 G	300.0 G	$-1405\,a_0$
$\|1\rangle\|2\rangle$	543.28 G	0.4 G	$-1405\,a_0$
$\|1\rangle\|3\rangle$	690.43 G	122.3 G	$1727\,a_0$
$\|2\rangle\|3\rangle$	811.22 G	222.3 G	$1490\,a_0$

Table 2.3.: Position B_0 and width ΔB of the magnetic Feshbach resonances between different hyperfine states in ^{6}Li [50, 51]. The background scattering length a_{bg} is given in units of the Bohr radius a_0. We work with the $|1\rangle|2\rangle$ mixture which features a very broad resonance at a magnetic field strength of 834.15 G.

leads to a fast decay of dimers and thus enhanced losses. A second resonance is located at 834.15 G, which is approximately 300 G wide, as shown in Fig. 2.4 a. In terms of energy, this width is much larger than the typical Fermi energy and makes this resonance ideally suited for almost all our experiments. At a magnetic field strength of 527.5 G, the scattering length features a zero-crossing and the $|1\rangle|2\rangle$ mixture is non-interacting.

A particularly interesting property of ultracold fermions is the possibility to explore the attractive and the repulsive side of the resonance. Along the crossover, weakly bound dimers are formed in the BEC regime, and Cooper pairs exist in the BCS regime. In between both limits, exactly on resonance, the Fermi gas is in the unitary limit and exhibits universal thermodynamic properties.

2.3.3. BEC-BCS Crossover

In 3D, the crossover between BEC- and BCS-regime is described by the dimensionless parameter $1/(k_F^{3D}\,a_{3D})$. Values of $1/(k_F^{3D}\,a_{3D}) > 0$ depict the BEC side of the resonance, whereas the BCS side corresponds to $1/(k_F^{3D}\,a_{3D}) < 0$. Values between -1 and 1 denote the crossover regime and strong interactions, not accurately described by either weakly interacting Bose- or Fermi-gas models. The schematic phase diagram of 3D Fermi gases is in shown in Fig. 2.5. Here, we briefly present the physics of the three different regimes and already point out that the BEC-BCS crossover in 2D Fermi gases is strikingly different to the 3D case. We come back to this statement at the end this section.

BEC Regime On the repulsive side of the Feshbach resonance, two different fermions can form weakly bound molecules with a net spin of zero. Performing evaporative cooling in this regime leads to the formation of a BEC of bosonic dimers. The composite bosons populate the highest vibrational

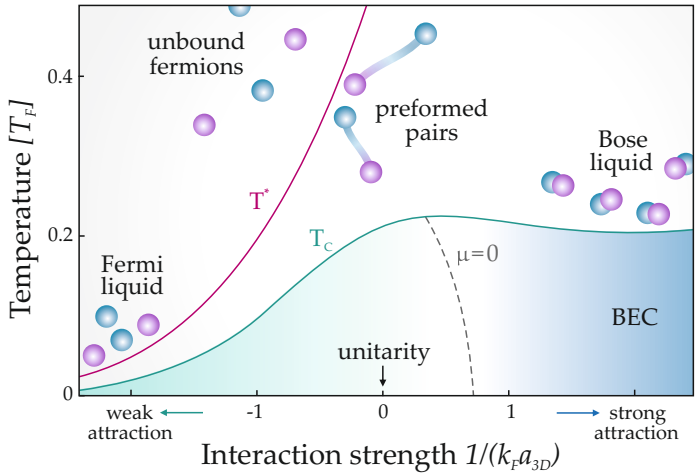

Figure 2.5.: Qualitative phase diagram for ultracold 3D Fermi gases. Two different temperature scales T_C and T^* describe the system. T_C is the critical temperature for the emergence of phase coherence and condensation. T^* describes the onset of pairing, below which pairs can be formed without the existence of a superfluid phase. For low temperature $T < T_C$ and positive interaction strength $1/(k_F^{3D} a_{3D}) > 0$, fermions form a superfluid consisting of tightly bound composite dimers. In case of weak attraction, where $1/(k_F^{3D} a_{3D}) < 0$, weakly bound Cooper pairs are formed. Between both regimes the chemical potential features a zero crossing. For $1/(k_F^{3D} a_{3D}) \to 0$, the gas is said to be in the unitary limit. The regime where the interaction strength is between -1 and 1 is called crossover. For higher temperature $T > T_C, T^*$, the gas is in the normal state, i. e. in the limits of weak and strong attraction the gas is a Fermi liquid or a Bose liquid, respectively. The Figure is adapted from Ref. [52].

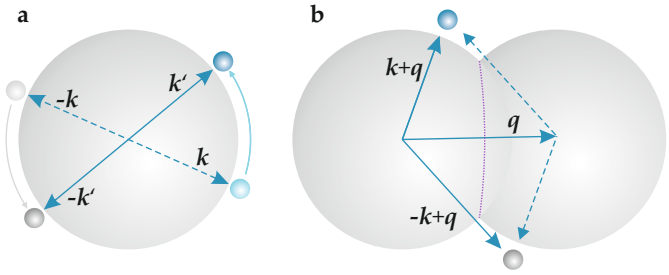

Figure 2.6.: Cooper pairing of two particles scattering on the Fermi surface where the only energetically accessible states are located. a) In case of two particles with equal momenta and opposite sign k and $-k$, the whole surface of the Fermi sea is accessible. Momentum conservation is always fulfilled. b) For a finite total momentum q, particles can only scatter in a narrow region defined by a circle on the Fermi surface (velvet dashed line). As a consequence, the formation of Cooper pairs with zero momentum is energetically favourable.

bound state. Their binding energy E_B^{3D} depends on the s-wave scattering length a_{3D} and can be written as $E_{B,BEC}^{3D} = \hbar^2/(2m_M a_{3D}^2)$, with the dimer mass $m_M = 2m$.

Compared to the inter-particle separation, the size of the molecules is large and approximately $\sim a_{3D}$. The fermions still experience Pauli exclusion so that collisions and three-particle recombinations are suppressed, which stabilizes the molecules. Far in the BEC regime the binding energy increases and as the molecules get smaller in size, the lifetime becomes shorter due to fast decay into lower molecular states.

In the BEC limit where $1/(k_F^{3D} a_{3D}) \to \infty$, the critical temperature for condensation of dimers is $T_c^{3D} \approx 0.55\, E_F/k_B$. The chemical potential of the condensate is [7]

$$\mu = -\frac{\hbar^2}{2ma_{3D}^2} + \frac{\pi\hbar^2 a_{3D} n}{m}, \tag{2.15}$$

where the first term is the binding energy per constituent of the bound molecule and the second term is a mean field contribution describing the repulsive interaction between the molecules in the gas. This simple mean field expression neglects correlations between different pairs or between one fermion and a pair.

BCS Regime In the regime of attractive interaction, where $1/(k_F^{3D} a_{3D}) < 1$, no two-body bound state exists. Nevertheless, fermions with opposite spin and momentum $\mathbf{k}$ and $-\mathbf{k}$ can form Cooper pairs on the surface of the Fermi sea, see Fig. 2.6. The size of the bound pairs is much larger than the inter-particle separation.

The pair formation is a pure many-body effect, facilitated by the presence of the non-interacting Fermi sea. This is described in a self-consistent way by the BCS theory [53]. All energy states, except a small fraction below and above the Fermi surface, are excluded from the scattering events due to the Pauli blocking. Cooper pairs exist even for arbitrarily weak interaction.

The fermions are either in a normal, non-paired state, or in a superfluid state consisting of Cooper pairs. In the BCS limit of weak attractive interaction $1/(k_F^{3D} a_{3D}) \to -\infty$, adding a Cooper pair to the superfluid costs $2\mu^{3D} \approx 2E_F^{3D}$. The binding energy $E_{B,BCS}^{3D}$ of a single Cooper pair equals half the gap Δ, which itself stabilizes the superfluid state. Compared to the Fermi energy, the superfluid gap Δ is exponentially small

$$\Delta/E_F \approx \frac{8}{e^2} e^{-\pi/2k_F^{3D}|a_{3D}|}. \tag{2.16}$$

Here, the gap parameter is given in units of the Fermi energy, which in the BCS limit is approximately $E_F^{3D} \approx \mu^{3D}$.

At low temperature, the gap is largest and vanishes when the gas reaches the critical temperature of the superfluid transition

$$T_c^{3D} \approx 0.28\, T_F^{3D} e^{\pi/k_F^{3D} a_{3D}}, \tag{2.17}$$

which is an analytical result and shows the strong dependence of T_c^{3D} on the density $k_F^{3D} \approx n^{1/3}$.

Unitary Regime Exactly on resonance, where $1/(k_F^{3D} a_{3D}) = 0$, the scattering length diverges and drops out of the description of the system. The scattering cross section is limited to $\sigma = 4\pi/(k_F^{3D})^2$. That leaves the Fermi energy $E_F^{3D} = \hbar^2 (k_F^{3D})^2$ as the only relevant energy scale and the inter-particle distance $1/k_F^{3D}$ as the only relevant length scale.

Therefore, all unitary Fermi gases are expected to exhibit universal thermodynamics whereby the microscopic details of the systems become irrelevant. For a unitary gas at zero temperature, all thermodynamic quantities can be expressed in terms of a single parameter ξ_B, which is called the Bertsch parameter[1]. It is universal constant defined as the energy of a system with unitary interaction in units of the free gas energy [8, 9, 54]. The thermodynamic equation of state is then of the simple form $\mu^{3D} = \xi_B E_F^{3D}$.

The universal behaviour becomes also apparent in the set of the so-called Tan relations [55–57]. They relate thermodynamic properties of the unitary gas to short-range correlations in terms of a single quantity named contact, which was measured via, e. g. radio-frequency (rf)- and Bragg-spectroscopy [58, 59].

In strongly interacting Fermi gases near a Feshbach resonance, one can realize very robust superfluids. The lifetime is relatively large due to Pauli statistics which strongly suppresses three-body recombination.

[1] Another commonly used quantity is the gain factor $\beta = \xi - 1$ [8].

2.4. 2D Fermi Gases

An extensive discussion of the peculiar features of 2D Fermi gases is beyond the scope of this chapter. Instead, we summarize a few important characteristics of 2D gases and point out that all 2D physics relevant for this work are discussed in detail in Ch. 6.

In 2D quantum gases, the role of fluctuations is significantly enhanced which strongly modifies superfluid properties and, e. g. forbids the formation of a true condensate at any finite temperature in accordance to the famous Mermin-Wagner-Hohenberg (MWH) theorem [35, 36]. The phase transition to a BEC is replaced by the BKT transition from the normal to a superfluid phase, which is strongly connected to the existence of bound vortex pairs. Each pair consists of two vortices with opposite phase winding. Above the critical temperature of the BKT phase transition, the pairs are dissociated and free vortices proliferate. The free vortices depict strong local phase fluctuations, which lead to a decay of the long-range order in the system on very short length scales. This is described by the decay of the first order correlation function, which changes from algebraically to exponentially when going form the superfluid to the normal phase. Below the critical temperature, phase fluctuations prevent the emergence of a condensate and the BKT superfluid is considered a quasi-condensate.

Generally, in contrast to the case of 1D and 3D, true condensation in 2D is only possible at zero temperature. In 1D, strictly speaking, no BEC can emerge even at zero temperature[1]. However, 1D systems are analytically solvable and in 3D, phase fluctuations are typically negligible at low temperatures. Hence, 2D systems are particularly hard to describe owing to the importance of fluctuations.

The fundamentally changed 2D scattering behaviour manifests itself in a logarithmic dependence of the 2D scattering length on the scattering energy instead of an energy independent scattering length in 3D. As a consequence, unlike in 3D, there is no unitary behaviour.

Due to the finite extent of 2D clouds in the experiments, the third dimension never becomes unimportant. In fact, both the 3D scattering length and the characteristic length l_z of a harmonic oscillator the strongly confined direction influence the scattering amplitude.

In analogy to the 3D case, we define the dimensionless interaction parameter
$\ln(k_F^{2D} a_{2D})$. As shown in Fig. 2.7. the Fermi gas is in the regime of strong interactions for $\ln(k_F^{2D} a_{2D}) \to 0$, corresponding to the situation where $k_F^{2D} \approx a_{2D}$, . For $\ln(k_F^{2D} a_{2D}) \to \infty$, the 2D Fermi gas is in the limit of a non-interacting Fermi gas. The opposite case $\ln(k_F^{2D} a_{2D}) \to -\infty$ depicts the limit of a non-interacting gas of deeply bound dimers. The regime where $\ln(k_F^{2D} a_{2D})$ is

[1] In presence of a trapping potential, a 1D quasi-BEC can emerge.

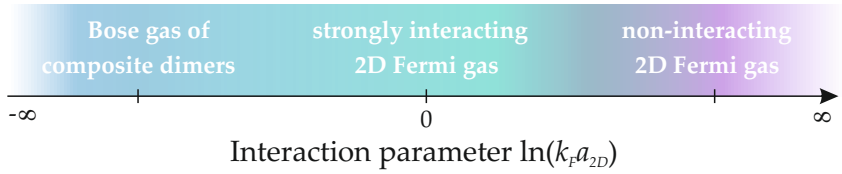

Figure 2.7.: Schematic phase diagram of ultracold 2D Fermi gases. The system is described by the dimensionless interaction parameter $\ln(k_F a_{2D})$. For $\ln(k_F a_{2D}) \to 0$, where $k_F^{3D} \approx a_{2D}$, the gas is strongly interacting. The BCS regime is described by positive interaction parameters. In the limit of $\ln(k_F a_{2D}) \to \infty$, the system approaches the ideal non-interacting 2D Fermi gas. In the opposite limit $\ln(k_F a_{2D}) \to -\infty$, the gas consists of non-interacting deeply bound composite dimers.

between -1 and 1, is called crossover.

Part I.

Experimental Setup

3. A Novel ^{6}Li Quantum Gas Experiment

Quantum gases have been in the focus of experimental physicists for decades, and yet, the production and probing of ultracold gases in an isolated environment is still an immensely challenging task. This particularly accounts for fermions since they are intrinsically harder to cool than bosons due to the Pauli-principle. However, the possibility to use Feshbach resonances to freely choose sign and strength of interactions renders fermions the ideal specimen for a broad range of intriguing phenomena, particularly in two dimensions.

This chapter presents the development process and realization of a novel quantum gas experiment which combines the fast and efficient production of degenerate 2D ^{6}Li quantum gases with the ability to image and probe the atomic clouds with very high resolution. We begin by introducing general consideration in Sec. 3.1 and give an overview of the apparatus and the cooling sequence in Sec. 3.2. Afterwards, Sec. 3.3 follows the evolution from hot to degenerate 2D gases and provides a detailed explanation of the essential parts and techniques.

Preface With advancing experimental techniques, modern quantum gas research increased its interest in the investigation of local properties. The implementation of high resolution imaging gave direct access to, e. g. in-situ density correlations and fluctuations.

Furthermore, in recent years a completely new generation of quantum gas experiments emerged, dedicated to the creation of low-dimensional quantum gases. Nowadays, 2D and 1D systems earn more and more interest due to their fundamentally different many-body physics and intriguing connections to solid state matter phenomena.

At the time of the development of our new apparatus, experiments with fermions were only few and no existing research group was able to locally resolve and manipulate 2D Fermi gases. We aimed to create an experiment to combine 2D fermionic quantum gases with an excellent degree of control and advanced optical systems to probe and manipulate the samples with very high resolution.

For the initial cooling, we choose a combination of a Zeeman slower and a 3D magneto-optical trap (MOT). The concept has proven to be reliable already, e. g. in an experiment which was under the advisory of *H. Moritz* in the group of *T. Esslinger*. We took inspiration from said experiment, yet, our apparatus

represents an augmented version in many regards. The high level of prior knowledge furthermore enabled us to prevent many difficulties during the design and realization process.

The main parts of the experiment were set up in three years by my colleague *W. Weimer* and me. The main vacuum chamber was designed by *F. Wittkötter*, who was a diploma student at that time. In the past two years, the group was joined by *J. Siegl* and *K. Hueck*, who built, e. g. the 1D optical lattice for the production of 2D gases. All of them contributed to this work by supporting measurements and by providing valuable input.

Extensive information about the design and assembly of our vacuum system, our high resolution imaging system, and the in-vacuo cooling resonator can be found in the thesis of *W. Weimer* [29]. Here, we give more detailed information on the Zeeman slower, the MOT, the transport dipole trap, and the laser system. Particular attention is given to the magnetic field setup which is presented in the succeeding Ch. 4.

3.1. General Considerations

Building a new quantum gas experiment requires several substantial and interdependent decisions regarding the choice of the atomic species, the vacuum design, and the cooling scheme. One of the main difficulties is to combine a vacuum system to produce pure and unperturbed atomic samples with the ability to get in proximity for the employment of high resolution imaging. In the following, we briefly explain the general design considerations and how we realized an excellent degree of control in an ultra-high vacuum (UHV) environment, i. e. the ability to probe and detect 2D atomic clouds on a submicron length-scale.

Proper Atomic Species Lithium is the lightest alkali metal and ^{6}Li, together with ^{40}K, the only radioactively stable fermionic species. Due to the small mass, the recoil energy $E_{rec} = \frac{\hbar^2 k^2}{2m}$ is about seven times larger for Lithium than for Potassium. This requires higher laser powers to prevent high tunnelling rates in an optical trap. On the other hand, the small mass enables us to study fast dynamics and allows for very efficient laser cooling, due to the high momentum transfer of scattered photons. Compared to ^{40}K, the natural abundance of ^{6}Li is very high, with respectively 7.5 % to 0.01 %, which adds a lot of headroom to the cooling procedure. The 300 G broad magnetic Feshbach resonance of ^{6}Li is highly advantageous with respect to physics regarding the BEC-BCS crossover and the unitary regime. The resonance is located at a magnetic field strength of 834 G, which is more than three times higher compared to the case of ^{40}K and thus requires larger magnetic coils or higher current strengths.

Lastly, preparation of the bosonic isotope ^{7}Li is possible with only a few changes to the laser system realizing sympathetic cooling of ^{6}Li with ^{7}Li if wanted. However, sympathetic cooling does not lead to lower temperatures. Thus, we decided to use a mixture of the two lowest hyperfine state of ^{6}Li and to employ a magnetic Feshbach resonance to tune the scattering behaviour between both states.

In summary, only the requirement of deep optical traps and strong magnetic fields are potential disadvantages. The former is a technical limitation which is more and more overcome while the latter is mainly an issue of the available space and cooling, which is both manageable. Due to the above mentioned advantages of ^{6}Li, it is the best suited fermionic species for the exploration of the BEC-BCS crossover. Finally, laser diodes for the ^{6}Li resonance wavelength of approximately 671 nm are relatively cheap and readily available.

Tailored Vacuum System The ideal vacuum chamber for a quantum gas experiment features an UHV environment to isolate the gaseous samples, simultaneously provides optimal optical access, and allows for the placement of magnetic coils and optics in short distances to the position of the atoms. This is not easy to accomplish since the corresponding requirements are not always compatible.

For instance, maintaining a good vacuum requires big pumps close to all relevant positions, which in turn reduces the available space for optics and magnetic coils. This makes it more difficult to generate strong magnetic fields and to perform high resolution imaging, since the corresponding space consuming components can easily interfere with the chamber dimensions. Moreover, the switching of magnetic coils causes vibrations so that all coils have to be isolated from the chamber. Additionally, in case of high current densities the magnetic coils generate a lot of dissipated power close to the chamber walls which eventually worsens the vacuum.

Many problems are circumvented by disentangling the preparation, i. e. the main part of the cooling sequence from the location where the actual experiments with the atomic samples are carried out. In our case, the final step towards a degenerate Fermi gas is done in a small, additional vacuum cell. This octagonal cell, to which we refer as the science cell, is connected to the main chamber with a small, 126 mm long tube. The separation from the main chamber provides us with enough space to implement magnetic coils and a high performance optical system.

All-Optical Cooling Strategy The slowing of atoms in a Zeeman slower and the trapping and subsequent cooling in a MOT is a common procedure. To reach quantum degeneracy in Fermi gases, further cooling is required.

While bosons scatter at low temperatures, the Pauli exclusion prevents identical fermions to collide and therefore to thermalize during evaporative

cooling. Instead, Fermi gases can be cooled sympathetically, i. e. with another species to enable collisions. Alternatively, one can prepare an equal mixture of two different hyperfine states to address a magnetic Feshbach resonance for optimal evaporative cooling.

In many experiments, the evaporative cooling is carried out after the atoms are transferred into a magnetic trap or optical dipole trap. Magnetic trapping allows for large capture volumes hence a simple atom transfer. But, the achievable densities are quite low compared to optical dipole traps. Therefore, the evaporation is less efficient. In the case of ^{6}Li, magnetic traps have another disadvantage. The required offset fields for sufficiently large scattering lengths in combination with a magnetic trap are likely to interfere and technically difficult to achieve. We employ an optical dipole trap to decouple the trapping of atoms and the tuning of the scattering length.

The atom transfer into the smaller volume of a dipole trap is more demanding. Also, the generation of deep optical traps requires high laser powers. We overcome both potential issues by using a ring resonator inside the vacuum. Two counter-propagating laser beams form a standing wave pattern with a high power enhancement and therefore very deep trap depths. The diverging eigenmode between two curved mirrors allows us to transfer the atoms into the resonator beam at a position where the beam diameter is large. We therefore reach a very high transfer efficiency of $\sim 60\,\%$.

High Resolution Optical System Our aim is the investigation of ultracold Fermi gases with an imaging resolution on the order of the relevant intrinsic length scales of the physical system, e. g. the Fermi wavevector, lattice constants, or the interparticle distance. Resolving these length scales, which are usually less than one micron, gives in-situ access to local properties of the gas, like local dynamics and correlations.

For that purpose, a microscope objective with a resolution of a several hundred nm at the wavelength of the imaging light is necessary. Such optical systems are very complex and their design is time consuming and costly. When the development of our new experiment begun, high performance imaging systems were existing in experiments with bosons but not with fermions, yet.

We put the idea further and implemented two identical microscope objectives in a symmetric arrangement above and below the atoms. These depict a very versatile tool, not only for high resolution imaging, but also for local manipulation of ultracold gases.

3.2. Apparatus Overview

This section provides an overview of the realized experimental setup. We briefly introduce the four main sections of the apparatus, namely the oven,

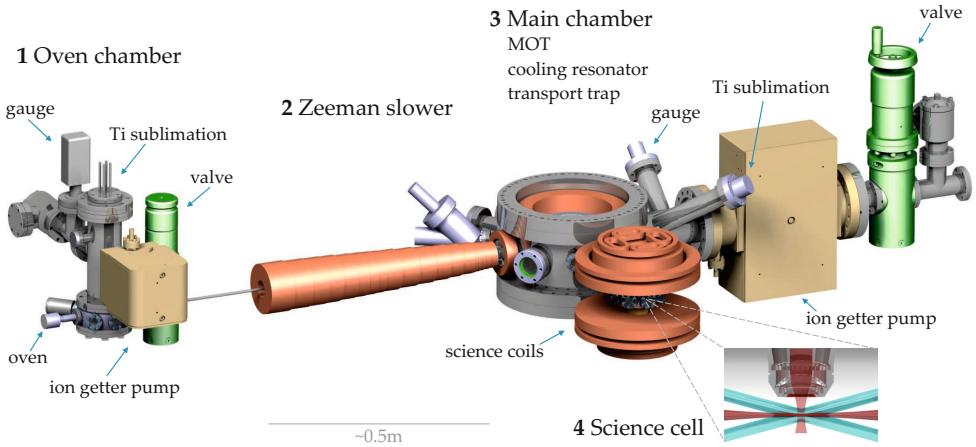

Figure 3.1.: Technical drawing of the experimental apparatus. We divide the setup into four main sections in correspondence to different steps throughout the experimental sequence. 1) The oven chamber consists of pumping devices, a vacuum gauge, and the small oven itself. 2) The tapered magnetic field coils of the Zeeman slower placed around a thin vacuum tube which connects the oven chamber with the main chamber. 3) In the main chamber, the slowed atoms are captured in the MOT and transferred into the in-vacuo resonator enhanced dipole trap to perform evaporative cooling. 4) The science cell is a small octagonal vacuum chamber which is placed between various magnetic field coils. The inset shows a sketch of the upper microscope objective above the position of the atoms. The horizontal red beam depicts the optical dipole trap to produce oblate atomic clouds. Two intersection laser beams generate the 1D optical lattice to prepare 2D Fermi gases.

Zeeman slower, main chamber and science cell. Afterwards, we summarize the cooling protocol and then proceed with a detailed discussion of the corresponding parts in Sec. 3.3.

The complete setup consists of one optical table for the laser system, one for the vacuum chamber, and a large quantity of electronic devices for monitoring and control. Both optical tables are located in the same laboratory which maintains a stable room temperature, air humidity, and minimum vibrations of the tables. Figure 3.1 shows a technical drawing of the apparatus, which can be divided into four main sections to reflect different steps throughout the cooling procedure and the preparation of ultracold Fermi gases:

1) The oven, where a hot gas of ^{6}Li is created.
2) The Zeeman slower, to slow the jet of hot atoms.
3) The MOT, to perform the first trapping and cooling.
4) The science cell, for the final preparation and experiments.

Cycling operation repeats the preparation of identical ultracold gases every $\sim 15\,\mathrm{s}$ with high reliability with respect to the achieved atom numbers and

cloud temperatures. At the end of each cycle, typically an absorption picture of the cloud is taken. This ultimately destroys the atomic sample and the preparation of the next cloud begins. We now take a closer look onto the separate sections of the experimental setup.

Oven The oven contains chunks of solid ^{6}Li and is constantly heated to $\sim 430\,°C$ to produce a high vapour pressure inside the steel vacuum chamber. The hot atoms leave the oven in a collimated jet and travel through the Zeeman slower towards the main chamber. The atom beam can be blocked by a mechanical shutter which is connected to a magnetic feed-through[1], see Fig. 3.2. A titanium sublimation pump[2] and an ion getter pump[3] compensate for the out-gassing at high temperatures. A differential pumping stage connects the oven to the Zeeman slower. With a length of 280 mm and an inner diameter of 4 mm, the thin vacuum tube leaves the pressure in the main chamber of 1.8×10^{-11} mbar unaffected by the pressure of 1×10^{-9} mbar in the oven vacuum chamber[4]. To secure the main chamber and for optional maintenance, the oven chamber can be separated from the main chamber with a Conflat (CF) 16 vacuum valve[5]. In the vicinity to where significant amounts of liquid or gaseous ^{6}Li is expected, nickel instead of copper gaskets are used for the vacuum flanges.

Zeeman Slower The jet of hot atoms leaves the differential pumping stage and travels through a 465 mm long tube with an inner diameter of 18 mm into the main chamber. Along their path, the atoms are slowed down with the help of a Zeeman slower. It consists of magnetic coils of decreasing diameter, placed around the vacuum tube over a length of 520 mm. Opposite to the location of the oven, on the other side of the main chamber, a laser beam enters the vacuum through a CF40 sapphire view-port. Atoms with an initial velocity of about $1000\,\mathrm{m\,s^{-1}}$ are slowed down by the scattering of photons from the counter-propagating laser beam. The tapered magnetic field constantly compensates for the changing Doppler shift to keep the atoms in resonance. With final velocities of about $50\,\mathrm{m\,s^{-1}}$ we are able to capture the atoms in the MOT.

Since the sapphire view-port is directly exposed to the atom beam, it might be necessary to replace it at a certain time. A CF40 valve[6] allows us to do so without destroying the vacuum inside the main chamber.

[1] Vacom MagiDrive MD16, www.vacom.de.
[2] Vacom Titansublimationspumpe DN40CF, www.vacom.de.
[3] Gamma Vacuum 25S-DI-2V-SC-N-N, www.gammavacuum.com.
[4] The pressure is monitored with a Pfeiffer PBR260 pressure gauge, www.pfeiffer-vacuum.de.
[5] VAT DN16, www.vatvalve.com.
[6] VAT Ganzmetall-Schieber DN40, www.vatvalve.com.

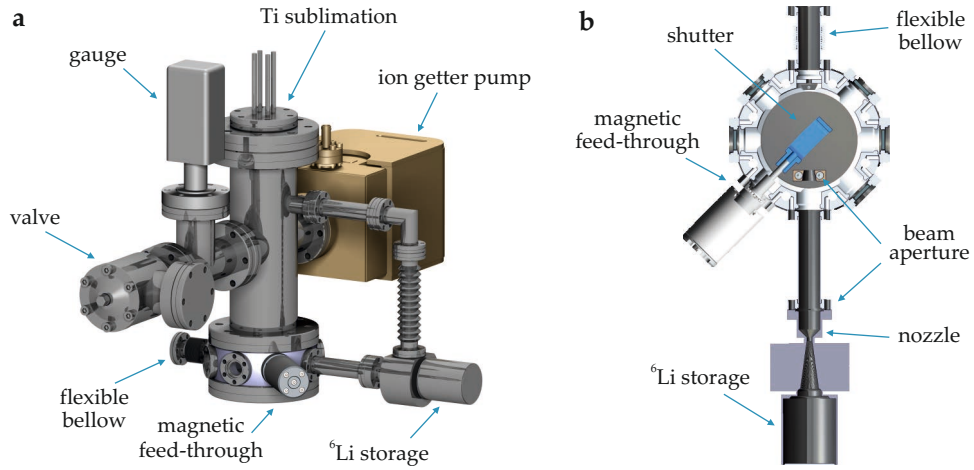

Figure 3.2.: a) Technical drawing of the oven vacuum chamber. The flexible bellow connects the oven chamber with the vacuum tube of the Zeeman slower. With a magnetic feed-through we can move a mechanical shutter inside the vacuum to block the atomic beam. b) Top-view (cut-away) of the oven, exposing the mechanical shutter and the beam apertures for the atom jet.

Main Chamber The MOT is located inside the main chamber, which is a large non-magnetic steel chamber with a diameter and height of 304 mm and 205 mm, respectively. As shown in Fig. 3.3, 16 different view-ports provide optical access for the six MOT beams, imaging, optical traps, the connection of the Zeeman slower, an optional 2D-MOT, vacuum pumps, and gauges[1]. The Zeeman slower is connected to a CF25 port opposite to a large CF100 port which accepts the main pumping stage consisting of a 100 l ion getter pump[2] and a titanium sublimation pump[3]. The two coils for the generation of the MOT field are recessed in the top and bottom CF100 view-ports. Two laser beams for the in-vacuo resonator enter the main chamber under an angle of $\sim 65°$ with respect to the Zeeman slower axis.

Perpendicular to the Zeeman slower axis, the beam of the moving dipole trap enters the main chamber. After the evaporation inside the cooling resonator is performed, the cold atoms are captured inside the dipole trap and transported into the science cell by moving the trap focus accordingly.

Science Cell The final preparation is carried out in a small, octagonal, non-magnetic steel vacuum chamber[4], which is depicted in Fig. 3.4. It is connected

[1]The pressure in the main chamber is monitored with a Varian UHV-24p Nude Bayard-Alpert gauge, now `www.agilent.com`.
[2]Gamma Vacuum 100L-DI-6D-SC-N-N, `www.gammavacuum.com`.
[3]Varian Mini Ti-Ball, now `www.agilent.com`.
[4]UKAEA CCFE Special Techniques, `www.ukaea.co.uk`.

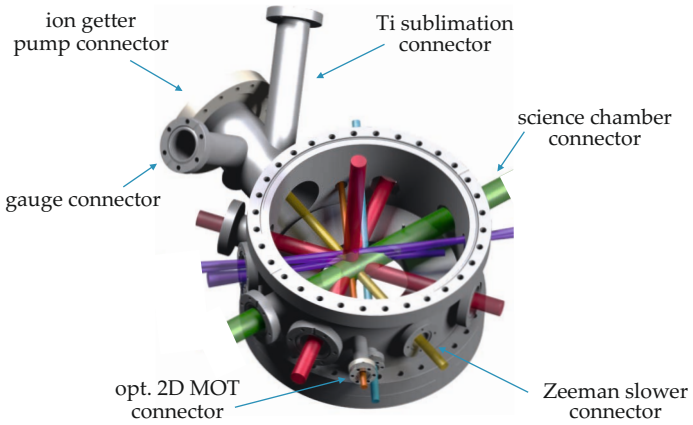

Figure 3.3.: Technical drawing of the main vacuum chamber. The large chamber consists of connectors for pumps, a vacuum gauge, and 16 view-ports to provide optical access. The different coloured laser beams depict the MOT light (red), the beam for the optional 2D MOT (orange), a possibility for imaging light (cyan), the Zeeman slower light (yellow), the moving dipole trap (green), and the light for the cooling resonator (velvet). The upper chamber part and the cooling resonator are not shown.

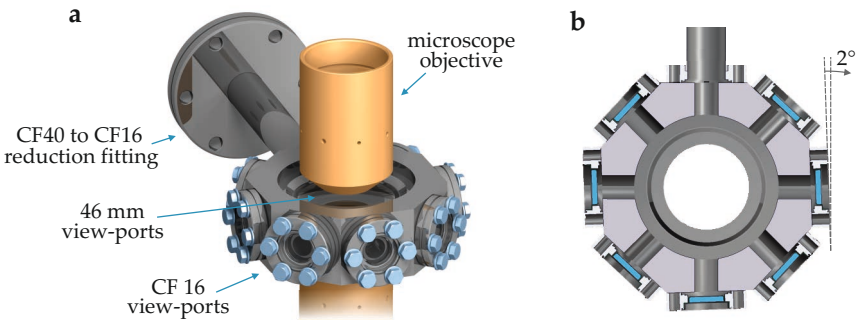

Figure 3.4.: a) Technical drawing of the science cell. A CF40 to CF16 reduction fitting connects the small octagonal cell to the main vacuum chamber. The top and bottom window feature a diameter of 46 mm. Seven CF16 view-ports are placed around the sides of the cell. b) Top-view (cut-away) of the science cell. The view-ports are tilted by 2° to avoid undesired back-reflections.

to a CF40 port at the main chamber with a 126 mm long tube with an inner diameter of 16 mm. A non-evaporable getter foil[1] is placed inside the connection tube to ensure a good vacuum in the science cell. The protruding design allows us to place magnetic coils in proximity to the atoms and to perform experiments without being limited by the dimensions of the main chamber.

The science cell is only 34 mm high, and the recessed top and bottom CF40 view-ports are separated by 8 mm and enable us to place the microscope objectives in minimum distance to the atoms. The thickness of the main view-ports is (4.00 ± 0.05) mm. Their surface quality is specified to be better than $\lambda/8$. Seven CF16 view-ports on the side of the cell provide excellent optical access from all directions. To prevent back-reflections, the view-ports on the side of the cell are tilted by 2°. All view-ports are anti-reflection coated for the wavelengths 532 nm, 590 nm, 760 nm, 780 nm and 1064 nm for incident angles from 0° to 30°.

3.3. Producing Ultracold 2D ^{6}Li Gases

In the following, we briefly outline the individual steps from the slowing of atoms in the Zeeman slower to the final evaporative cooling inside the science cell. Afterwards, we focus on the realization of the separate steps in our experimental setup. First, Sec. 3.3.1 introduces the laser system we employ for cooling and imaging of ^{6}Li. In Sec. 3.3.2 to 3.3.4, we present the all-optical cooling steps we employ inside the main chamber and science cell. The laser system for the moving dipole trap and the realization of ultracold 2D Fermi gases is presented in Sec. 3.3.5. Finally, an overview of our high performance imaging system is given in Sec. 3.3.6.

Experimental Sequence The experiment runs in cycling operation with a fast repetition rate, i. e. every ~ 15 s a 2D cloud is prepared, imaged and destroyed, and a new preparation begins.

At the end of the cooling procedure, we obtain atomic clouds with final temperatures of a few ten nK, which corresponds to a reduction of ten orders of magnitude. The cooling steps required to produce such cold gases are described in the following and sketched in Fig. 3.5.

- At a temperature of 430 °C, the atoms leave the oven with a mean velocity of roughly 1400 m s^{-1} and enter the Zeeman slower. The coils and laser light for the Zeeman slower and the MOT are switched on. A rotating magnetic feed-through closes a mechanical shutter in front of the oven nozzle when the MOT loading is finished.

[1] SAES Getters ST122/NFC/50-150/130X180/D, `www.saesgetters.com`, activated during the bake-out procedure.

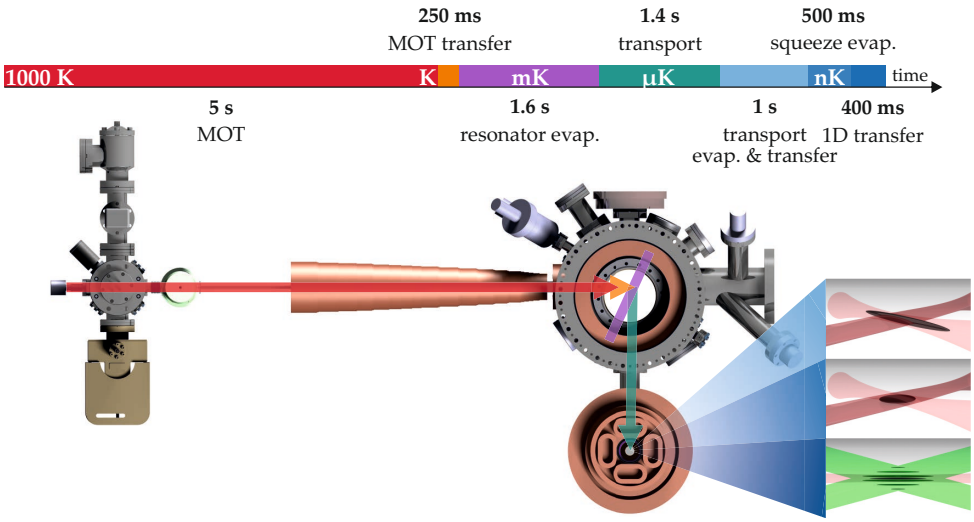

Figure 3.5.: Sketch of the all-optical cooling scheme. Different colours depict the sequential steps to produce ultracold 2D Fermi gases in our apparatus. The preparation starts in the oven with a hot gas of ^{6}Li. After 5 s, the MOT loading (red) is complete and the atoms are transferred (orange) into the cooling resonator enhanced dipole trap for the first evaporative cooling step (velvet). The cold gas is then transported into the science cell (green) and transferred into the squeeze dipole trap (bright blue) and evaporatively cooled (blue). The final step to generate the 1D optical lattice and to confine the ultracold atoms in a single anti-node of the corresponding interference pattern (dark blue). This simplified overview does not account for about 5 s in which, e. g. the actual experiments with the prepared cold gases are carried out.

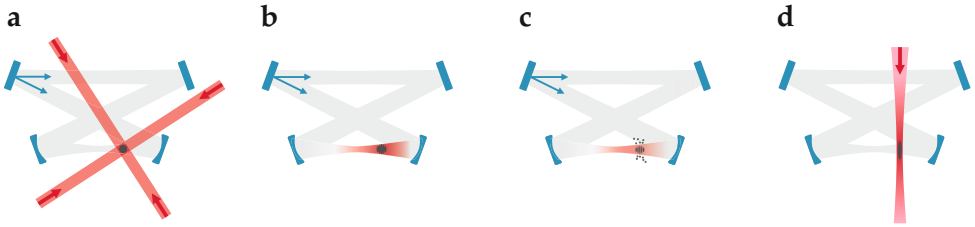

Figure 3.6.: Working principle of the resonator enhanced dipole trap. a) The MOT is loaded and two counter propagating laser beams are coupled into the cooling resonator. b) The atoms are transferred from the MOT into the standing wave interference pattern inside the resonator. c) Evaporative cooling is performed by lowering the power of both resonator laser beams. d) The cold atoms are transferred into the running wave dipole trap and transported into the science cell.

- The changing magnetic field of the Zeeman slower keeps the constantly slowed atoms in resonance with the counter-propagating laser light. The scattered photons decelerate the atoms down to $50\,\mathrm{m\,s^{-1}}$ so that they can be captured in the MOT.
- The MOT consists of six beams of near resonant laser light coming from all spatial directions and a magnetic quadrupole field. Together, they generate a spatially dependent radiation force restricting the atoms to the centre of the trap. The final MOT temperature is on the order of m K. After 5 s, approximately 30×10^6 atoms are captured, the loading is finished, and the Zeeman slower is switched off. Each half of the atoms is one of the two lowest hyperfine spin states.
- The laser light for the cooling resonator enhanced dipole trap is switched on during the MOT phase. To transfer the atoms into the standing wave pattern of the resonator beam, the MOT laser is tuned closer to the cooling transition to compresses the MOT volume. Simultaneously, the magnetic MOT centre is shifted by offset fields to ideally overlap with the resonator eigenmode. The high power enhancement of the resonator realizes a trap depth of $\sim 40\,\mathrm{mK}$ and thus a high transfer efficiency of 60 %, see Fig. 3.6.
- After the transfer, the MOT light is switched off and the polarity of one of the MOT coils is changed to create a magnetic offset field. With this, the interaction between the spin states is large enough to perform efficient evaporative cooling inside the resonator beam.
- The dipole trap which transports the atoms into the science cell is switched on and overlapped with the resonator mode at the position of the atoms. The beam power of the cooling resonator is lowered to perform evaporative cooling and finally, the beams are switched off to transfer the cold atoms into the several hundred µK deep running wave dipole trap. Typically, we are left with 1×10^6 atoms with a temperature on the order of 100 µK.
- The focussing lens of the transport dipole trap is positioned on an air-beared translation stage. Moving the lens over a distance of 326 mm transports the atoms into the science cell in $\sim 1\,\mathrm{s}$.
- The laser power of the transport trap is lowered from 2.4 W to 100 mW to perform further cooling[1]. We obtain 1×10^5 to 1×10^6 atoms with an approximate temperature of 100 µK.
- Afterwards, the atoms are transferred into the oblate squeeze dipole trap. Lowering the corresponding beam power from 400 mW to 20 mW results in atom numbers on the order of 1×10^5 at temperature of $\sim$ 100 nK. Experiments are either carried out with flat 3D gases inside the squeeze trap or, after transfer, in the 1D optical lattice.
- The blue-detuned 1D lattice is generated by two 532 nm laser beams

[1] For lower laser powers, the emergence of a elongated molecular BEC can be observed.

which form a standing wave interference pattern with a large lattice spacing. For the transfer into a single anti-node of the interference pattern, the power of the squeeze trap is increased to compress the atomic cloud. Afterwards, the squeeze trap is switched off and 1×10^5 atoms are prepared as a 2D cloud.

The final steps of the sequence may vary since they depend on the particular type of experiment. Either way, after approximately 15 s each cycle typically ends with the acquisition of an absorption image of the cloud. Resonant light casts a shadow of the spatial atom distribution onto a sensor and simultaneously destroys the atomic cloud.

3.3.1. Laser System for Cooling, Trapping and Imaging

The slowing, laser cooling, trapping and imaging of atoms is based on scattering events of photons. This requires resonant light, stable in frequency and intensity. In our laboratory, the corresponding laser system consists of several diode laser and electronics for temperature and frequency control. The entire setup is located on a separate optical table.

All lasers are external cavity diode lasers (ECDLs) in Littrow configuration with linewidths significantly below the natural ^{6}Li linewidth of $\Gamma = 5.9\,\mathrm{MHz}$. Piezo-actuated gratings enable us tune and stabilize the frequencies via proportional-integral (PI) control in a range of about 100 MHz. With output powers on the order of ten mW, the diode lasers seed tapered amplifiers (TAs) which generate 250 mW to 450 mW. This light is then distributed among different paths and finally in-coupled into single-mode polarization maintaining optical fibres which lead to the experiment. All output powers are actively stabilized by PI control and photo diodes which monitor the intensities on the experiment table.

The reference frequency for the MOT, the Zeeman slower and the imaging light is set by performing Doppler-free spectroscopy inside a 340 °C hot ^{6}Li vapour cell. The lower S orbital of ^{6}Li is split into two levels, one $F = 1/2$ and one $F = 3/2$ state which are separated by 228 MHz, see Fig. 3.7. With a Pound-Drever Hall (PDH) locking scheme, the reference laser is locked onto the transition of the crossover between the $^2S_{1/2}, F = 1/2$ and $F = 3/2$ to the $^2P_{3/2}$ state along the D2 line (approximately 671 nm). The splitting of the upper P orbital state is below the linewidth Γ and can therefore be treated as a single state. The P state sub-levels only splits further in presence of strong magnetic fields.

A common offset-lock technique is used to stabilize the laser for the MOT light with respect to the reference laser. The MOT laser seeds an individual TA and the amplified light is then split into two separate beams, the MOT cooler and repumper, to realize a closed cycling transition during MOT operation. Two acousto-optic modulators (AOMs) shift the frequencies of these two

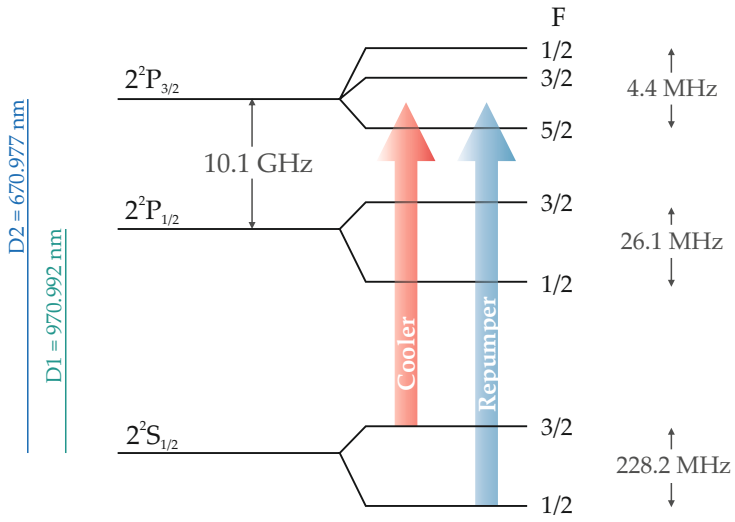

Figure 3.7.: Level scheme of ^{6}Li without an external magnetic field. Shown are the $2^2S_{1/2}$ ground state and the excited P state. The coloured vertical lines depict the transitions on the D2 line for our MOT cooling laser (red) and repumper laser (cyan). F depicts the different total angular momenta. The energy splitting of the $2^2P_{3/2}$ is smaller than the linewidth of ^{6}Li and therefore not resolvable. The given values are adapted from Ref. [49, 60].

beams ± 114 MHz. The crossover to which the reference laser is locked lies exactly between them. The cooler laser drives the $^2S_{1/2}, F = 3/2 \rightarrow {}^2P_{3/2}, F = 3/2$ transition and the repumper the $^2S_{1/2}, F = 1/2 \rightarrow {}^2P_{3/2}, F = 3/2$ transition. Our laser system is also prepared to cool bosonic ^{7}Li, which is also contained in the oven and the vapour cell of the spectroscopy.

An additional laser provides the seed light for the Zeeman slower TA and also generates the imaging light. While the Zeeman slower light drives the same transition as the cooler, the imaging light drives the repumper transition. Both are separately tunable in frequency. The imaging light can be tuned over a wide range of about 1 GHz to account for a wide range of magnetic field strengths. Two AOMs set frequency shifts of the imaging light of either 40 MHz or -400 MHz. Separate imaging fibres allow us to quickly change between different imaging axes and low or high field imaging.

Furthermore, for the creation of local potentials, there is a 780 nm light source, consisting of a diode-laser and a TA.

3.3.2. Zeeman Slower and Magneto-Optical Trap

After outlining the cooling and preparation of ^{6}Li quantum gases, we now turn to a detailed discussion of the individual parts of the experimental setup, beginning with the Zeeman slower and the MOT. Note that details about the realization of the corresponding magnetic fields are given in Ch. 4.

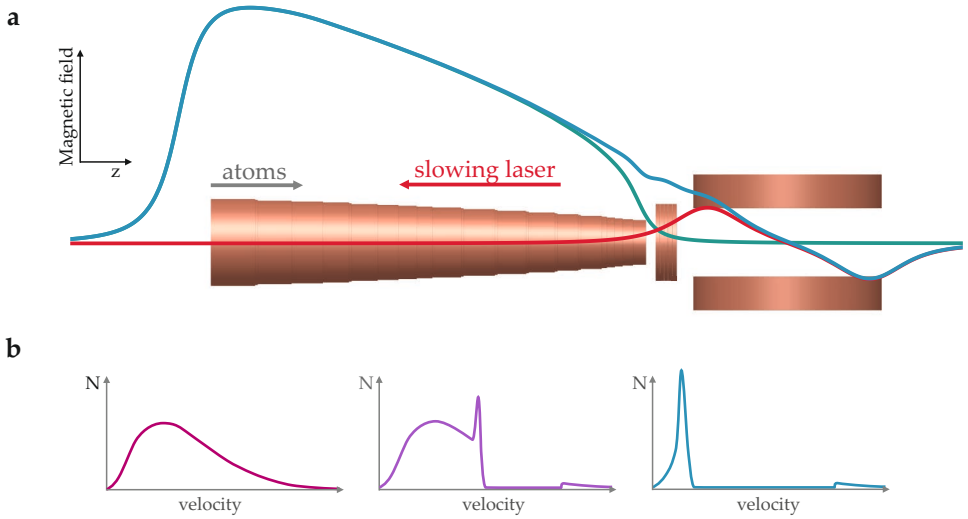

Figure 3.8.: Sketch of the Zeeman slower and the resulting magnetic field along the slower axis. a) The hot atoms enter the tapered magnetic field generated by the Zeeman slower coils and are constantly decelerated by counter propagating laser light. The green line denotes the calculated axial magnetic field of the Zeeman slower. The red line depicts the MOT field. The cyan line depicts the resulting sum of the fields generated by the Zeeman slower, the shim coil, and the MOT coils. b) Sketch of the increasingly compressed Boltzmann distribution of the atom velocity at three different positions along the slower axis.

Laser cooling of atoms is based on scattering events of resonant photons. The net momentum transfer slows the atoms down to a lower limit given by the recoil velocity $v_{rec} = \hbar k/m$, where m is the particle mass. The Zeeman slower, for instance, relies on this principle. If inter-particle scattering allows the atoms to re-thermalize we are not only able to reduce their velocity but also the temperature of an atomic cloud as it is realized in a MOT.

Zeeman Slower At a temperature of 400 °C, the hot atoms leave the oven with a mean velocity of $v \approx 1400\,\mathrm{m\,s^{-1}}$. To capture them in the MOT, they have to be slowed down by two orders of magnitude to $v \approx 50\,\mathrm{m\,s^{-1}}$. This can be realized with a Zeeman slower, which yields an atomic flux of up to $1 \times 10^{10}\,\mathrm{s^{-1}}$ [61].

The basic idea of a Zeeman slower is to constantly decelerate the atoms with the help of a counter-propagating laser beam, see Fig. 3.8. To maintain the radiation pressure along the atoms path, a decreasing magnetic field compensates for the changing Doppler shift $\delta_D = v\lambda/c$ of the atomic energy levels via the Zeeman effect, where λ is the wavelength of the slowing light, v the velocity of the atoms, and c is the speed of light. This decreasing field

is generated by tapered magnetic coils, placed around the vacuum tube in which the atoms travel from the oven into the main chamber.

Atoms with an initially lower velocity are addressed at a later position in the Zeeman slower. This leads to a compression of the velocity distribution and depicts the difference between the slowing and cooling of atoms.

To avoid losing decelerated atoms from the slowing process, the compensation of the Doppler shift has to be fulfilled over the entire length of the slower. Considering the imposed level shift by an external magnetic field B and the equations of motion of the atoms yields the ideal magnetic field slope

$$B(z) = \frac{\hbar}{\mu_B}\left[\delta_0 + \frac{1}{\lambda}\sqrt{v_{init}^2 - 2a_e z}\right], \tag{3.1}$$

where the resulting magnetic field is depicted in Fig. 3.8. The z-direction is the symmetry axis of the slower, μ_B is Bohr's magneton, λ the wavelength of the slowing light, $a_e = \kappa a_{max}$ is the effective deceleration, the constant $0 < \kappa \leqslant 1$, and v_{init} the initial velocity of the atoms.

If the detuning δ_0 between the slower light and the MOT cooler transition equals zero, the position where the atoms reach their final velocity v_{end} coincides with the centre of the MOT field. Choosing $\delta_0 > 0$ shifts the slower end beyond the MOT centre, but prevents the Zeemman slower light from perturbing the MOT due to resonant scattering.

In the limit of high laser intensity the maximum light force acting on the atoms is

$$F_{max} = m a_{max} = \frac{\hbar k \Gamma}{2}, \tag{3.2}$$

which determines the maximal deceleration a_{max}, with the linewidth $\Gamma = 5.9\,\mathrm{MHz}$ of the used transition and the wavenumber k. In the case of ^{6}Li, it follows $a_{max} \approx 2 \times 10^6\,\mathrm{m\,s^{-2}}$. This fairly large value makes the use of a Zeeman slower for ^{6}Li feasible. Typically, a deceleration of $\kappa\, a_{max} = 0.5 a_{max}$ is chosen to realize a robust operation, i. e. to be independent from random fluctuations of the light intensity and scattering rate.

In our experimental setup, the Zeeman slower light enters the vacuum chamber through a CF40 view-port opposite to the oven and is focussed onto the 4 mm oven nozzle over a distance of about 2 m. The circularly σ^+ polarized light drives the $2S_{1/2}, m_J = 1/2 \rightarrow 2P_{3/2}, m_J = 3/2$ transition with an available laser power of 80 mW. The slower frequency is detuned from the cooler laser by additional $\delta_0/(2\pi) = -36\,\mathrm{MHz}$.

The magnetic field coils of the Zeeman slower are operated with a current of 9.9 A at 48 V. This yields a maximum field strength of 1250 G at the beginning of the slower to address atoms with an initial velocity of up to $\sim 1000\,\mathrm{m\,s^{-1}}$.

Magneto-Optical Trap When the atoms are successfully decelerated by the Zeeman slower, they are captured in the MOT which corresponds to the first

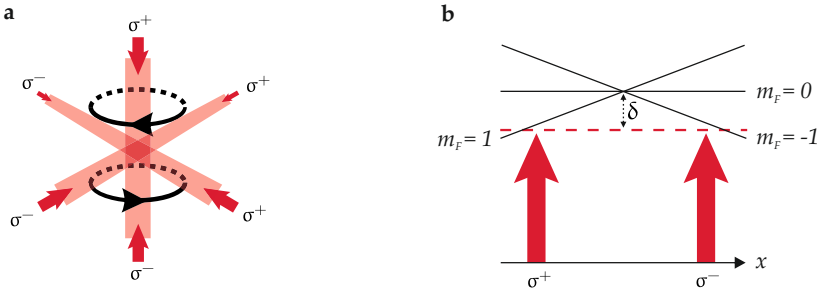

Figure 3.9.: Working principle of a MOT. a) Three pairs of counter-propagating laser beams intersect at the centre of a magnetic quadrupole field. This field is generated by two coils, which are operated with a current of opposite circular direction. b) Away from the local minimum at the MOT centre, the magnetic gradient field introduces a change of the atomic level shift. Due to the magnetic field and the polarization of the six laser beams, the atoms are only resonant with the laser beam counter propagating the direction in which the atoms move. This results in an effective restoring force which confining the atoms to the centre of the MOT. Here, the detuning of the MOT light is described by δ.

cooling step. At the end of the MOT phase, the temperature of the gas has already decreased by almost seven orders of magnitude. The lower temperature limit in the MOT is determined by the Doppler temperature $T_D = 140\,\mu K$ due to momentum transfer of re-emitted photons.

The experimental realization of a MOT consists of three orthogonal circularly polarized and near-resonant laser beams which illuminate the atoms in the main chamber from all spatial directions. Each beam exits through a view-port and is back reflected into the vacuum chamber by a mirror which is combined with a $\lambda/4$ retardation plate. Therefore, the incident pairs of beams are respectively σ^+ and σ^- polarized, as shown in Fig. 3.9 a.

Two magnetic coils are recessed in the top and bottom view-port of the main chamber. Their distance to the atoms is only 40.5 mm. During the MOT phase, the coils are operated in anti-Helmholtz configuration, i. e. the currents through the individual coils run in opposite circular direction. The generated magnetic quadrupole field is a gradient field with a minimum field strength in the centre.

The magnetic field and the polarization of the laser beams break the symmetry of the imposed radiation pressure. Atoms are only resonant with the beam which is coming from the direction in which the atoms travel, i. e. the atoms can only scatter a counter-propagating photon. Similar to the case of the Zeeman slower, the MOT light is red-detuned by a few line-widths $\Gamma \approx 5.9\,MHz$ to compensate for the Doppler effect. Thus, the atoms are slowed down to standstill in a shell around the centre of the MOT and then pushed

back, see Fig. 3.9 b.

With a detuning of approximately 5Γ, we obtain optimal loading performance with a MOT coil current of 63 A which generates in-plane magnetic field gradients of approximately $15\,\mathrm{G\,cm^{-1}}$. Since the cooling transition of ^{6}Li is not closed, after the absorption of a photon the atoms can relax from the $^2P_{3/2}$ state to the $^2S_{1/2}, m_J = -1/2$ state and become invisible for the cooler. Therefore, an additional repumper laser, which is overlapped with the cooler beam, re-excites the atoms to the $^2P_{3/2}$ state. A power of respectively 23 mW and 17 mW is available for cooler and repumper.

The lifetime of the atoms in the MOT is on the order of ten minutes, corresponding to the low background pressure of only 1.8×10^{-11} mbar in the main vacuum chamber. After 5 s MOT loading, we capture $\sim 30 \times 10^6$ atoms. In the last step of the MOT phase, the frequency of the cooler and repumper laser is tuned closer to the resonance to compress the MOT volume. Simultaneously, magnetic offset fields shift the zero field centre of the MOT field to overlap it with the resonator enhanced dipole trap. Switching off the MOT light completely transfers the atoms into the cooling resonator.

Comment on Loading Rates Our MOT is quite small compared to other ^{6}Li experiments which obtain loading rates up to two orders magnitude higher. Although the reason for this is still unknown, we could rule out many possible issues as discussed in the following.

First, we consider a possible limitation by the available laser power for the Zeeman slower light. Our design value for the effective deceleration of $0.5a_{max}$ yields a slowing light intensity I which equals the saturation intensity

$$I = I_{sat} = 2h\pi^2 \frac{\Gamma c}{3\lambda^3}. \tag{3.3}$$

For ^{6}Li, the resulting saturation intensity is $I_{sat} = 2.5\,\mathrm{mW\,cm^{-2}}$.

At the MOT position, the slowing laser beam has a diameter of about ≈ 20 mm, which equals the expected size of the slowed atom beam at that position. The available laser power of 80 mW for the slower light enables us to reach a maximum intensity of $18.0\,\mathrm{mW\,cm^{-2}}$, which would correspond to a deceleration of $\approx 0.9a_{max}$. Thus, the Zeeman slower light is no limiting factor.

This does not apply for the MOT light. Typical values for the power density of a ^{6}Li MOT are $10\,\mathrm{mW\,cm^{-2}}$ to $15\,\mathrm{mW\,cm^{-2}}$. This is about five times I_{sat} to fully saturate the resonance. However, the maximum power of 23 mW and 17 mW for our cooler and repumper laser yields only 60 % of the saturation intensity I_{sat}.

The clear limitation of the laser power is mainly due to the degradation of the performance of the corresponding 670 nm TA. On the timescale of months, we repeatedly observed an increasing loss of output power after the assembly of several TAs. We can only assume that there is a problem with the TA device

itself or with insufficient management of dissipated heat. Two measures are thus planed for the next downtime of the experiment. First, we will improve the laser system by using two separate TAs for cooler and repumper light. And second, the illumination of the atoms in the MOT will be optimized by adapting the shape of the MOT beams to the spread of the MOT volume, i. e. we reduce the beam size and therefore increase the intensity. Furthermore, a new mechanical design for the TA setup is finished and will be tested soon.

Above that, the direction of the atom beam itself was carefully adjusted. We also optimized the match of magnetic Zeeman slower and MOT field by installing a small shim coil between end of the Zeeman slower coils and main chamber.

Another possible issue might regard the applied magnetic fields. The magnetic centre of the MOT is shifted by magnetic offset fields during the loading, as well as for the transfer into the cooling resonator afterwards[1]. This results in a non-trivial asymmetric magnetic field configuration of the MOT. As a consequence, the wavefronts of the corresponding laser beams are tilted in respect to the magnetic field lines, which may be disadvantageous for the MOT loading performance. The same accounts for the Zeeman slower beam which has to match the angle of divergence of the hot atom jet.

Finally, the performance of the oven itself seems to be erroneous. We observed a reduction in atom flux over the past years. The reasons might be that ^{6}Li chemically reacted to form solid lithium-oxide Li_2O and -hydroxide LiOH. These obstructions are most likely located in proximity to the oven nozzle but at a position where we are unable to see and eliminate them.

We compensate for the reduced flux by operating the oven at higher temperatures of $(400 \text{ to } 440)\,^\circ\text{C}$. As a consequence, we increased the current in the Zeeman slower coils to adapt the magnetic field to the higher mean velocity of the atoms. The Zeeman slower now operates closer to a regime where $\kappa \leqslant 1$, i. e. where the effective deceleration is close to the maximum attainable deceleration of the atoms. So far, this was not disadvantageous for us.

However, a new oven is manufactured and will be assembled at the earliest opportunity. It features a less complicated design to minimize the chances for a blockage. Until then, our efficient preparation of the atomic samples compensates for the reduced atom numbers we start with.

3.3.3. Cooling Resonator and Transport Dipole Trap

In order to access lower temperature regimes, we employ optical dipole traps. Here, the Doppler temperature is not longer the lower limit. This makes the all-optical preparation of degenerate alkali gases so feasible.

[1] The Zeeman slower axis, which is shifted in respect to the geometric centre of the main chamber, prevents us from loading the MOT without the offset fields. Further informations are given in Ch. 4.4.

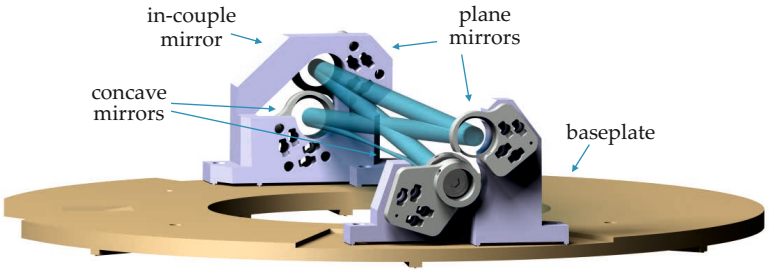

Figure 3.10.: Technical drawing of the cooling resonator. The mirror holders are positioned on a rigid steel baseplate inside the main vacuum chamber. The lower mirrors are convex and cause the resonator eigenmode to feature a minimum beam waist of (17.5×30) µm, which coincides with the geometric centre of the main chamber.

Cooling Resonator After the MOT phase, the atoms are transferred into the resonator enhanced dipole trap in the main chamber. The cooling resonator consists of four mirrors in bow-tie configuration placed on a monolithic steel baseplate inside the main chamber, as shown in Fig. 3.10. Two of the mirrors are curved, forming a resonator eigenmode. The minimum beam waist of (17.5×30.0) µm is located at the geometric centre of the chamber. The asymmetry of the resonating mode is due to the fact that all four mirrors define a plane which is tilted by 45° with respect to the baseplate. The round-trip length of the resonator is 87 cm which leads to a free spectral range of $\nu_{FSR} = 345\,\text{MHz}$ and a power enhancement of ~ 1300. A finesse of 3880 yields a bandwidth of 80 kHz.

A commercial Nd:YAG solid-state laser system[1] provides the laser light for the cooling resonator. Two beams, which are mode and polarization matched to the cycling eigenmode, are coupled into the resonator through the polished back of one of the plane mirrors, see Fig. 3.10. The incident angle of the two beams is such that they propagate in opposite directions within the resonator. The TEM_{00} mode is excited and a standing wave interference pattern is formed.

The resulting resonator power enhancement enables us to realize very deep trapping potentials to gain a high transfer efficiency from the comparatively hot MOT. Despite the high cycling power in the resonator, the mode volume at the centre is too small for sufficient transfer efficiencies. Thus, ideal overlap between MOT and cooling resonator eigenmode is obtained by shifting the MOT with magnetic offset fields, accordingly. The final transfer position is approximately 20 mm away from the centre of the main chamber, where the minimum beam waist of at the centre has increased to approximately ~ 400 µm.

The transfer is further optimized by compressing the MOT volume by tuning the cooler and repumper laser frequency closer to the resonance. In addi-

[1] Innolight Mephisto MOPA 25, `www.coherent.de`.

tion, the laser powers are lowered and finally switched off when the transfer is complete.

During the transfer, the incident power of the two 1064 nm resonator beams is 105 mW, which results in trap frequencies of $(10.000 \times 0.135 \times 0.080)$ MHz in axial and both radial directions. The resulting trap depth is about 40 mK at the centre. At the transfer position, the trap depth is about 175 µK corresponding to trap frequencies of $(650 \times 520 \times 290)$ kHz. With this, nearly 60 % of the atoms are loaded from the MOT volume into the oblate slices defined by the intensity maxima of the standing wave pattern. Then, the MOT light as well as the magnetic coils are switched off completely.

To perform evaporative cooling, the polarization of one of the MOT coils is inverted to change from anti-Helmholtz coil configuration to Helmholtz configuration. Now, the current through both solenoids has the same circular direction and creates a magnetic offset field with a strength of 210 G at the position of the atoms. The corresponding scattering length of $|a_{3D}| \approx 235\, a_0$ enables us to cool the atoms by reducing the beam powers in 1.6 s down to 8 mW[1].

Since the mechanical design of the cooling resonator is very stable, we have to take care mainly of the frequency stabilization of the in-coupled light. A 68 MHz modulation via an electro-optic modulator (EOM) creates sidebands on the laser light. Via PDH technique, an error signal is generated by detecting the beat signal of the carrier frequency with the modulated sidebands. The corresponding photo-diode (PD) detects one resonator beams reflected from the in-couple mirror. We stabilize the laser frequency to the resonator on a time-scale of 100 kHz. Additionally, the frequency of the laser itself can be tuned over a range of ±100 MHz with an internal piezo actuator to vary the length of the laser cavity. The resulting regulation frequency is about 20 kHz. Finally, we control the temperature of the Nd:YAG crystal directly which is rather slow but necessary to ensure that the laser frequency does not drift too far from resonance to lock on. The PI control for the intensity has a control speed of 10 kHz and acts on two AOMs in the laser beam paths of the in-coupled beams. Two photo diodes monitor each resonator beam individually via leaking light behind the curved mirror opposite to the in-couple mirror.

During the evaporative cooling, the power of the running wave transport dipole trap is ramped up. Both, resonator and transport trap, share the same laser light source. When the evaporation inside the cooling resonator is finished and the beams are finally switched off and the atoms are contained in the transport trap.

[1] One of the beam is switched off completely. Hence, the atoms are transferred from a running wave dipole trap into the transport dipole trap.The final trap frequencies are on the order of a few Hz.

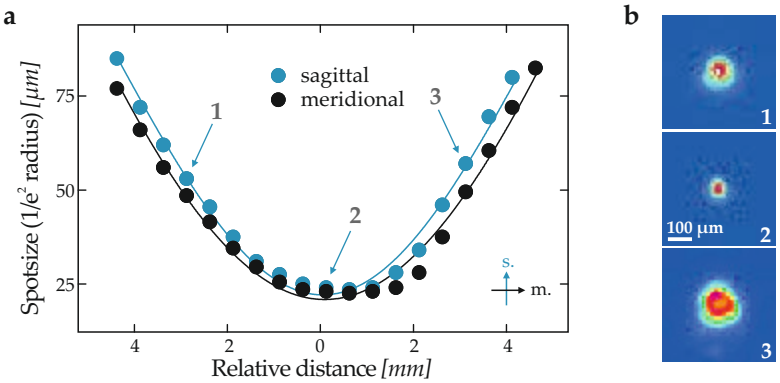

Figure 3.11.: Characterization of the transport dipole trap beam. a) Spotsize ($1/e^2$ radius) of the beam focus along its axis. The cyan circles depict the measured values in the sagittal plane, the black circles denote the measurements in the meridional plane. The solid lines are fit curves, yielding the minimum beam radius of 20.9 µm (sagittal) and 22.1 µm (meridional). b) False colour pictures of the obtained beam profiles corresponding to the marked data points.

Transport Dipole Trap One of the key features of many quantum gas experiments is the spatial separation of the main cooling steps and the position where the actual experiments are carried out. As a consequence, the atoms have to be transferred over a macroscopic distance which poses a considerable challenge.

There are different possibilities to realize the transport of atoms, e. g. using a moving magnetic trap generated by consecutively powered coils or magnetic coils mounted on a translation stage. A more common solution is to combine one or multiple lenses to create a tightly focussed optical dipole trap with a translation stage to move the focus and the atoms accordingly. Most alternatives are rather complex and thus yield numerous sources for possible optical aberrations. We opted for a simple and thus reliable design.

We realize the optical dipole trap by focussing a laser beam with a single achromatic lens on a high grade linear translation stage[1], see Table 3.1 for more details. The air beared translation stage is operated with cleaned pressured air[2] and powered by two 10 A switch power supplies[3] powering a brushless linear servo motor with Hall sensor based position feedback. The focussing lens has a focal length of 1000 mm and creates beam focus with a waist of ~ 22 µm ($1/e^2$ radius), see Fig. 3.11. It overlaps with the cooling resonator beam in the main chamber. After the atoms are transferred from the resonator into

[1] Dover AirGlide AG-350, `www.dovermotion.com`, operated with an Aerotech Ensemble ML-40 controller, `www.aerotech.com`.
[2] Water-seperator, grade AO pre- and grade AA high efficiency filter.
[3] Meanwell DRP-480-48, `www.meanwellusa.com`.

Transport Dipole Trap	
Focussing lens focal length	1000 mm
$1/e^2$ Beam waist radius	23 µm
Rayleigh length	1.8 mm
Trap frequencies (4 W)	$(8800 \times 8800 \times 90)$ Hz
Trap frequencies (20 mW)	$(400 \times 400 \times 5)$ Hz
Trap depth	290 µK (4 W)
PID control speed	5 kHz
Linear Stage	
Maximum available current	10 A
Specified max. peak current	14.2 A
Specified max. cont. current	4.5 A
Specified max. acceleration	$5\,\mathrm{m\,s^{-2}}$
Specified max. velocity	$1000\,\mathrm{m\,s^{-1}}$
Travel distance	326.35 mm
Maximum Travel distance, approx.	350.00 mm
Time of travel	1.4 s

Table 3.1.: Summarized properties of the transport dipole trap and the linear translation stage which is used to move the focussing lens. Specified values are given by the manufacturer.

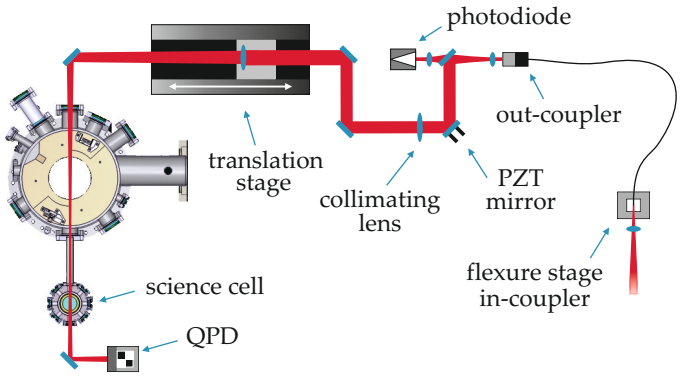

Figure 3.12.: Optical setup of the transport dipole trap beam. The 1064 nm laser beam is coupled into a bare fibre end which is fixed on a 6-axis translation table. The diverging out-coupled light is then reflected by two mirrors before being collimated. The leaking light behind the first mirror is used for the power regulation. The second mirror is piezo-actuated to employ position-control of the transport trap beam pointing. Moving the focussing lens with the linear translation stage transports the atoms from the main chamber into the science cell. Behind the science cell, the beam is focussed onto a QPD whose signal is used to control the piezo-actuated mirror.

the running wave dipole, the focus is moved over a distance of $\sim 326\,\mathrm{mm}$ in about 1 s to transport the atoms into the science cell.

In order to obtain an ideal focus profile, the transport dipole trap laser beam is coupled through a short optical fibre. The diverging out-coupled light is first reflected under $\sim 45°$ by two mirrors, and then passes an achromatic lens with a focal length of $f = 800\,\mathrm{mm}$, see Fig. 3.12. This lens is positioned on a small translation table to precisely collimate the beam in accordance to the diameter of the movable focussing lens of 50.8 mm.

Optical Fibre In case of a silica core optical fibre, a constant high laser power through-put is difficult to achieve, especially in sequential operation. This is mainly due to different thermalization time-scales of the involved optical elements. As a consequence, thermal drifts cause misalignment, i. e. worsen the coupling efficiency which can ultimately destroy the optical fibre. Nevertheless, with appropriate caution we are able to achieve output powers of 6 W with a coupling efficiency of at least 70 %.

Yet, special measures have to be taken. For in-coupling, the typically used angle-polished connector (APC) is not feasible because the connector and the ferrule are likely to be exposed to high dissipated powers from scattered light or light within the cladding. Furthermore, optimal mode-matching of the incident light beam with respect to the angled fibre tip is difficult to obtain. We therefore cleaved one end of the fibre and mounted the bare fibre end on

a six-axis flexure stage[1]. Thus, we are able to precisely move and tilt the fibre tip in all spatial directions with sub-micron accuracy.

Unfortunately, the first fibre did not withstand the high input powers and was destroyed in a distance of a few centimetres away from the bare end. To keep the downtime as short as possible, we replaced the fibre with a similar one, and opted to operate it at a lower output power of 2.5 W to reduce the danger of damaging the fibre.

However, the silica core fibre is about to be replaced by a hollow-core photonic crystal fibre[2], which allows us to obtain $\geqslant 95\,\%$ coupling efficiency with an input power of 10 W without significant thermalization issues. While one end is confectioned with a FC/APC connector the other end is cleaved, sealed and polished[3]. Thus, we can use the same coupling peripherals.

Operation and Stabilization Special care has to be taken so that the beam is not truncated along its path inside the vacuum chamber and to avoid back reflections. Both could cause losses during the transport. Furthermore, the acceleration of the trap focus must not exceed the time-scale given by the axial trap frequency to prevent non-adiabatic effects. For a laser power of 2.5 W, this time scale is on the order of 100 ms. The radial trap frequencies set the limit for vibrations and jitter perpendicular to the laser beam. Although there are no noticeable vibrations of the translation stage, the laminar air flow provided by the flow-boxes above the optical table, causes significant jitter of $\pm 2\,\mu$m of the focus position on the QPD. Therefore, we covered the optical beam path and reduced the vibrations to 0.5 µm and 0.3 µm in x- and y-direction. The residual jitter along the axial direction was determined to be on the order of a few 100 nm in amplitude, using the position feedback of the linear stage.

To obtain constant atom numbers, the pointing position of the transport trap beam is stabilized to the location of the Feshbach field maximum inside the science cell with a QPD. This diode is placed in a short distance behind the view-port of the science cell through which the transport trap beam exists. The position control features a piezo-actuated mirror in adequate distance to the 1000 mm lens, see Fig. 3.12. The position readout by the QPD is done while the reduction of the transport laser power for evaporation is halted for 100 ms at 100 mW. Regulation is possible on a timescale of 30 Hz.

Instead of transferring the atoms into the squeeze dipole trap we can continue the evaporation inside the transport trap to produce an elongated molecular BECs. Typically, the final laser power at the end of the evaporation is between 20 mW and 10 mW. Lowering the trap depth leads to spilling of particles, as shown in Fig. 3.13 a. We determined the corresponding trap fre-

[1] Thorlabs MBT616D Fiber Launch System, www.thorlabs.com.
[2] NKT Photonics LMA-PM-15, www.nktphotonics.com.
[3] Alphanov, www.alphanov.com.

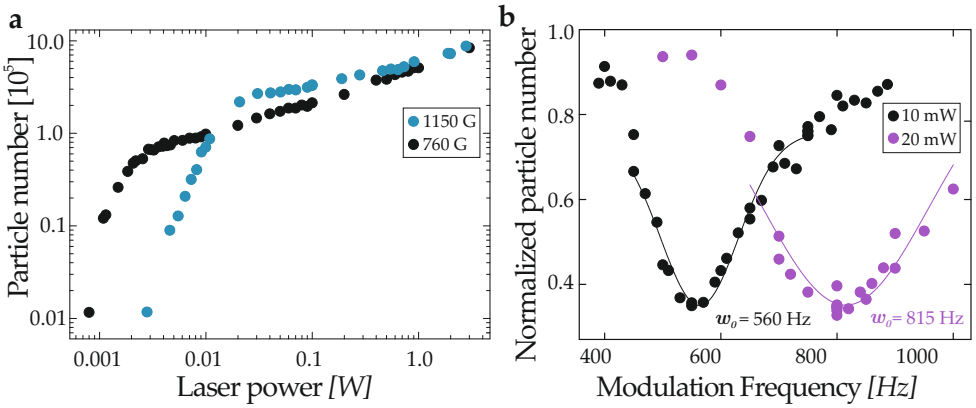

Figure 3.13.: a) Number of particles in the transport dipole trap as a function of the laser power. For low powers, we observe onset of spilling. Due to the formation of molecules there is an increase in the particle number at low powers. The measurement is performed for two different magnetic field strengths, corresponding to a gas consisting of dimers on the BEC side (760 G) and a Fermi gas on the BCS side (1150 G). Before imaging, we increase the trap power to 1 W and perform a magnetic field sweep to afield above the Feshbach resonance to dissociate all molecules. b) Parametric heating in the transport trap as a function of the beam power modulation frequency. The atom loss is caused by the excitation of the radial breathing mode. The measurement is performed at a magnetic field of 790 G for the beam powers $P = 10\,\mathrm{mW}$ and $P = 20\,\mathrm{mW}$. We modulated with an amplitude of $\leqslant 1\,\%\,P$ for 150 ms. The solid lines are Lorentzian fits yielding the maximum atom loss for a frequency of 560 Hz and 815 Hz. The corresponding trap frequency is 280 Hz and 409 Hz, respectively.

quencies via parametric heating to respectively 409 Hz and 280 Hz, as shown in Fig. 3.13 b.

Logarithmic Power Control During evaporation, the power in the transport trap is reduced by almost three orders of magnitude. A power control based on a linear power monitoring is not feasible since it works reliably either for high or for low powers. We employ a PI control using a photo diode with a logarithmic amplifier instead, which provides a feasible control signal over the whole laser power range with a control speed of 5 kHz.

The signal of the logarithmic photo diode amplifier is proportional to the logarithm of the measured laser power $\propto \log P$. For regulation, the PI control compares the measured laser power $\propto \log P$ with the logarithm of the set value $\log S$. The PI control acts on an AOM to regulate the laser power. Using the relative difference $\log P - \log S$ as a control signal does not work because the AOM has to compensate for the real difference in laser power. However, in case of small deviations the difference is

$$\log P - \log S \cong \frac{P - S}{S}. \tag{3.4}$$

Therefore, the control signal can be multiplied by S to create a feasible control signal.

3.3.4. Squeeze Dipole Trap and 1D Optical Lattice

In 1.4 s, the atoms are transported from the main chamber to their final position in the science cell. Here, the laser beam of the squeeze dipole trap enter the science cell perpendicular to the transport trap, both traps are overlapped, and the power of the transport trap is lowered to transfer the atoms into the oblate squeeze trap. After further cooling of the atoms, one either experiments with an oblate cloud, or an additional transfer into the 1D optical lattice is carried out.

The available space around the science cell is quite limited. Consequently, the required optics for trapping, i. e. for the realization of the squeeze trap and the 1D optical lattice, had to be integrated in a compact way without forfeiting their stability. We thus realized a rigid and yet compact setup on a separate, non-magnetic breadboard[1], which is shown Fig. 3.14. After the testing and adjustment of the optics, the breadboard was implemented into the experiment[2].

The breadboard is positioned between the magnetic coils without being in direct contact to either the vacuum chamber or the coils. All mechanical

[1] EP-GC 201, Erhard Hippe KG, `www.hippe.de`.

[2] A detailed description of the adjustment procedure can be found in the Master's Thesis of *K. Hueck* [62].

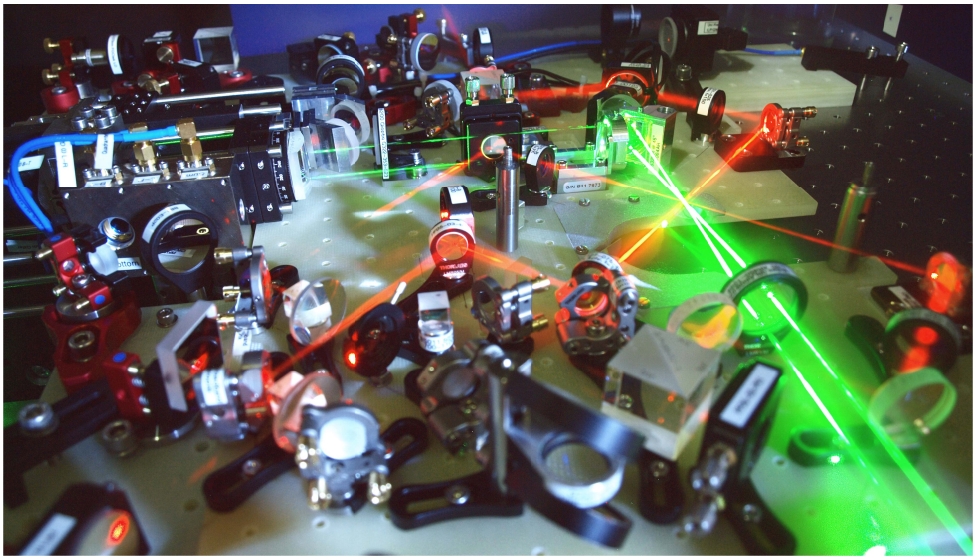

Figure 3.14.: Photograph of the compound breadboard which accommodates the optics providing the 1D lattice and the squeeze dipole trap. The picture was taken before the breadboard was integrated into the experimental setup. The green 532 nm laser beam of the lattice and two red 671 nm imaging beams are made visible using vaporized dry ice. Below the position where the beams cross, one can recognize the cut-out for the lower microscope objective.

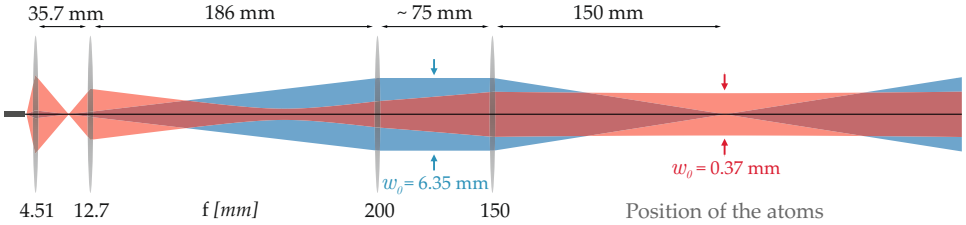

Figure 3.15.: Lens setup for the creation of the squeeze dipole trap. The cyan and red beam depict the sagittal and meridional beam axis, respectively. The sagittal beam extension is scaled down by a factor of ten.

mounts, many of which are custom-built, are non-magnetic and mostly non-metallic to ensure that they are unaffected by changing magnetic fields. For adjustment, piezo actuators are connected to all relevant mirrors and lenses.

Squeeze Dipole Trap The laser light for the red-detuned squeeze trap is provided by the same laser light source as the cooling resonator and the transport dipole trap. An optical fibre[1] delivers the 1064 nm laser light to the breadboard where it is out-coupled[2].

After the beam polarization is cleaned with a polarizing beam-splitter, a cylindrical lens focusses the laser light in the horizontal direction which results in a large horizontal beam waist. An achromatic lens with a focal length of 200 mm collimates the beam in the meridional plane. With this, we realize a highly elliptical beam waist with an aspect ratio of about $1:40$ with $1/e^2$ radii of $w_{x,y} = 370\,\mu m$ and $w_z = 10\,\mu m$, see Fig. 3.15 for a sketch of the lens setup. The small waist size w_z is limited by the optical system and aberrations which are mainly caused by misalignment.

An achromatic lens with a focal length of $f = 150\,mm$ is mounted on a linear translation stage[3] to adjust the focal position along the beam direction inside the science cell. The second last mirror in front of the science cell view-port, through which the squeeze beam enter, is mounted in a piezo-actuated mirror mount[4]. Tilting this mirror moves the focus up to $\pm 6\,mm$ up or down, and left or right, respectively.

The typical squeeze trap beam power during the transfer is 400 mW, which generates a 4 µK deep trap with trap frequencies of $(68 \times 68 \times 2300)$ Hz in x-, y-, and z-direction, respectively. To realize an ideal transfer, we apply a magnetic field strength close to the Feshbach resonance.

Finally, the atoms are loaded into the squeeze trap without significant losses. By lowering the laser power we perform evaporative cooling and

[1] Thorlabs PM980-XP, www.thorlabs.com.
[2] Toptica FiberDock 2V0, six axis, f=4.51 fibre-coupler, www.toptica.de.
[3] Newport Agilis AG-LS25, www.newport.com.
[4] Newfocus 8886 Pint Sized Corner Mount 12.7 mm, www.newport.com.

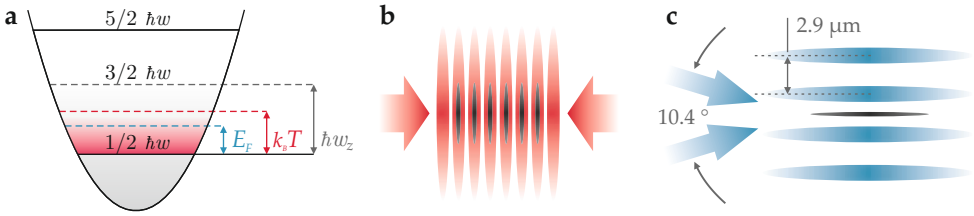

Figure 3.16.: a) Quasi-2D regime in an optical lattice. All movement along the strongly confined direction besides the zero-point motion is frozen out. This requires the Fermi energy E_F and thermal energy kT to be smaller than the excitation energy to the first excited state $E_F, k_B T \ll \hbar\omega_z$. b) Typical configuration of red-detuned 1D optical lattice. Two counterpropagating 1064 nm laser beams generate an interference pattern with a small lattice spacing of 532 nm. A stack of quasi-2D clouds is loaded. c) Our configuration consists of two blue-detuned laser beams which intersect under a steep angle to create an optical lattice with a lattice spacing of 2.9 µm. As a consequence, we create a single quasi-2D cloud trapped in a anti-node of the interference pattern.

set the atom number or temperature. At a final power of 20 mW, the radial trap frequencies are dominated by the curvature of the magnetic field. The resulting trap frequencies are $(32 \times 32 \times 500)$ Hz.

As high field seekers, ^{6}Li atoms are attracted by magnetic field maxima. As a consequence, the curvature of the magnetic offset field generates a highly radially symmetric confinement with a frequency of about 30 Hz at a field strength of 800 G[1]. To precisely control the beam power, a photo diode monitors the light leaking through one of the mirrors behind the view-port through which the beam exists the science cell. The corresponding PI control loop operates at a maximum speed of 17 kHz.

With a final power of 20 mW, the squeeze trap typically contains 20 000 atoms per spin state with a temperature on the order of $\leqslant 0.1\,T/T_F$. The oblate cloud can either be used for experiments or we continue with the preparation to realize a single 2D cloud by transferring the atoms into the 1D optical lattice.

1D Optical Lattice In order to achieve the 2D regime, excitations in one direction of motion have to be frozen out. Hence, the Fermi energy and the temperature have to be sufficiently low in respect to the confinement $E_F, k_B T \ll \hbar\omega_z$, where ω_z is the trap frequency of the strongly confined lattice direction, as illustrated in Fig. 3.16 a. The higher the trap aspect ratio of the vertical and the radial direction $\omega_z/\omega_r \gg 1$, the stronger is the 2D confinement. Note, that due to the finite radial extent of realistic experiments, even

[1] With a final power of 20 mW the resulting trap frequencies without magnetic confinement are $(15 \times 15 \times 500)$ Hz.

in the case of very strong confinements, the gas is said to be quasi-2D.

A convenient way to produce a 2D gas is to use a red-detuned light sheet [63]. However, the aspect ratio of the realizable radial and axial trap frequency is quite limited and the prepared atomic gases are therefore not far in the 2D regime. This is improved by using blue-detuned Hermite Gaussian laser beams [64] and 1D optical lattices. These are formed by the standing wave interference pattern of two counter propagating laser beams. Here, the trap frequency of the strong confinement easily exceeds typical energy scales of excitations. Thus, strong confinements and highly planar gases are realized. However, due to the small lattice spacing, typically many adjacent 2D planes are populated, see Fig. 3.16 b [65–72]. This easily causes an averaging of measured quantities and counteracts the advantages of high performance imaging systems.

Being interested in local properties, it is therefore desirable to address individual 2D planes [73,74] or prepare only a single 2D cloud. This can be done by decreasing the intersecting angle of the counter propagating lattice beams which results in a larger lattice spacing [75], as shown in Fig. 3.16 b.

We intersect two 532 nm laser beams under an angle of 10.4°, we create a lattice spacing of $532\,\mathrm{nm}/2\sin(10.4°/2) \approx 2.9\,\mu\mathrm{m}$, see Fig. 3.16 c. We are able to directly transfer the atoms from the squeeze dipole trap into a single layer of the 1D lattice with a high aspect ratio of $\omega_z/\omega_r \approx 1000$. Furthermore, since the atoms are confined inside an anti-node of the interference pattern of the blue-detuned laser light, scattering induced heating is strongly suppressed. In the radial direction, the 1D lattice is anti confining, which is particularly advantageous to perform evaporative cooling inside the lattice. However, radial confinement is typically provided by the highly symmetric magnetic offset field which is applied to set the inter-particle interaction.

Realization The 532 nm laser light for the 1D optical lattice is generated by a 1064 nm fibre-amplifier[1] and a frequency-doubling resonator[2]. Details about the laser system are presented in Sec. 3.3.5.

For a reliable realization of a single quasi-2D cloud, relative drift between the squeeze dipole trap and the optical lattice has to be avoided. A displacement of less than one micron is sufficient to populate two lattice layers. A constant performance thus requires a highly stable optical setup for the beam preparation and delivery of both, the squeeze and the lattice beams.

Therefore, a very rigid and compact setup in minimum proximity to the science vacuum cell was realized on the same non-magnetic breadboard which accommodates the squeeze trap optics, as shown in Fig. 3.14. The beam delivery is done with a highly stable fibre out-coupler[3], similar to the one of

[1] Nufern NuAmp PSFA-1064-50mW-50W-6-0, www.nufern.com.
[2] Evans & Sutherland, supplier for digital theatres and planetariums, www.es.com.
[3] Toptica FiberDock 2V0, www.toptica.de.

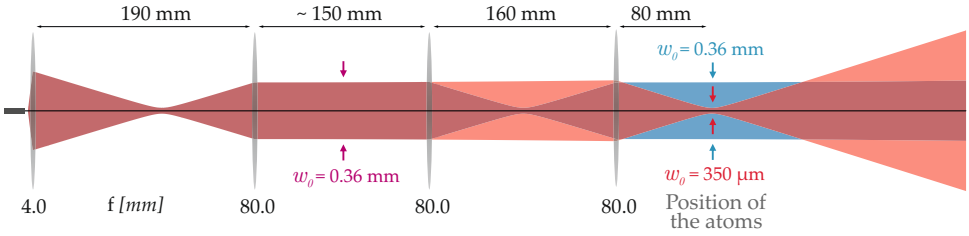

Figure 3.17.: Lens setup for the creation of the 1D lattice. The cyan and red beam depict the sagittal and meridional beam axis, respectively.

the squeeze dipole trap. Close to the out-coupler, the leaking light behind a mirror is used for the power monitoring for the PI control. An achromatic lens with a focal length of 80 mm collimates the beam with a diameter of about 360 µm. After a retardation waveplate and polarization cleaning, the beam is split into two by a second polarizing beam splitter.

The corresponding optics are placed in a monolithic mount to create a pair of parallel and phase-stable laser beams. These intersect inside the science cell to form the optical lattice. The polarization of both beams is equalized with an $\lambda/2$ waveplate and each beam profile is then changed to an elliptical shape by passing through a cylindrical lens.

The two elliptical beams are intersected with each other at the position of the atoms via a lens with a focal length of 150 mm, which is positioned between the cylindrical lens and the entrance view-port of the science cell. The beam divergence in the direction of the beam axis is adapted such that the optical lattice generates a symmetric radial confinement. In the horizontal direction perpendicular to the beam axis, the waist of the lattice beams is about 370 µm, similar to the waist of the squeeze beam to realize an ideal overlap of the two traps. The focussing lens is mounted on a piezo-actuated translation stage[1] to adjust the position of the focus by ± 3 mm. The lens setup for the creation of the 1D optical lattice is depicted in Fig. 3.17.

Protocol The starting point is an ultracold cloud consisting of balanced mixture of ^{6}Li atoms in the two lowest hyperfine states confined in the oblate squeeze dipole trap at a power of 20 mW. To transfer the atoms into the optical lattice, the squeeze beam power is ramped up to 1000 mW to compress the atomic cloud. The magnetic field is ramped from the evaporation field strength at the Feshbach resonance at 834 G to approximately 800 G in 100 ms. On the BEC side of the Feshbach resonance, the Fermi pressure is decreased and thus the mean interparticle distance and the vertical cloud extent is reduced.

Simultaneously, the laser power of the lattice beams are exponentially in-

[1] Newport Agilis AG-LS25, `www.newport.com`.

creased to 600 mW[1]. The vertical and radial trap frequencies of respectively 25 kHz and −19 Hz are realized and interlayer tunnelling is thus negligible. In 300 ms, the squeeze trap is switched off exponentially and the atoms are adiabatically transferred into a single anti-node of the optical lattice. The adiabacity of the lattice loading is verified by a return transfer into the squeeze dipole trap and subsequent temperature analysis.

The radial confinement is usually dominated by the magnetic confinement, i. e. $\omega_r \approx 30$ Hz for a magnetic field strength close to the Feshbach resonance. Our resulting aspect ratio of $\omega_z/\omega_r \approx 850$ exceeds the ratio of most comparable experiments. The highly stable optical setup provides us with quasi-2D Fermi gases with typically 30 000 atoms per spin state and temperatures of a few percent of the Fermi temperature T_F and condensate fractions of $\approx 50\,\%$.

For lattice beam powers $\geqslant 400$ mW, no significant tunnelling between individual layers can be observed. Lowering the beam power below 400 mW leads to noticeable losses on the relevant times scales, as shown in Fig. 3.18 a. However, finite squeeze beam powers significantly counteract. Instead of switching the squeeze off completely, maintaining a low power of only 30 mW causes an additional vertical confinement which is sufficient to suppresses the tunnelling almost completely, even for lattice powers down to 50 mW. As a result, for a lattice beam power of only 200 mW lifetimes of an atomic cloud on the BCS regime of ~ 15 s are restored. Towards the BEC regime, the lifetime decreases due to losses caused by decay of bound dimers into lower molecular states.

In Fig. 3.18 b, we show exemplary results of the determination of the radial trap frequency. We excite a sloshing mode of the atomic cloud in the planar direction by introducing a slight displacement of the squeeze trap with respect to the lattice. The resulting trap frequency accounts for both, the magnetic field curvature and the optical lattice.

Single Layer Verification It is important to have an explicit and reliable method to assure that we populate only one layer of the optical lattice. One obvious way would be to image the trapped cloud from the side, but the available optical system lacks the resolution to resolve multiple layers of atoms. However, we are able to directly determine the number of populated layers with the microscope objective based imaging in only one shot.

To optimize the single layer performance, the squeeze trap and the lattice are operated with a high laser power of respectively 400 mW and 600 mW. In the ideal case, the squeeze trap is perfectly aligned with a single anti-node between two intensity maxima of the 1D lattice, see Fig. 3.19 a.

The corresponding absorption image shows the tightly compressed cloud. Due to the fact that the axis of the squeeze trap is titled by approximately 1.5° in respect to the 1D optical lattice, the imaged cloud is elongated along the

[1]The lattice beam power is always given as the sum of both intersecting laser beams.

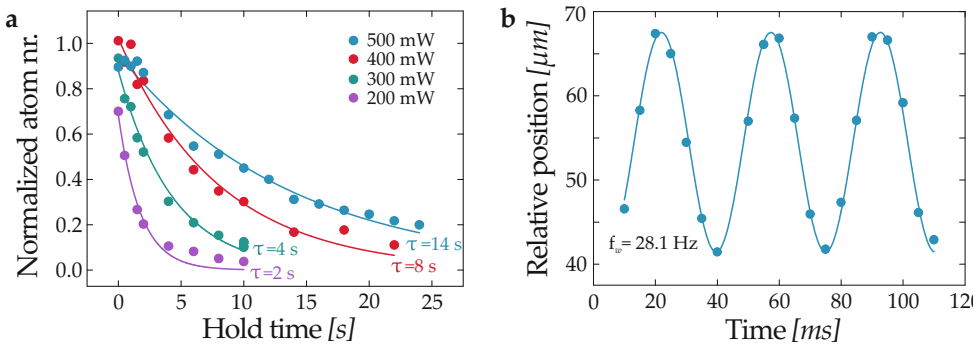

Figure 3.18.: a) Particle loss in the optical lattice as a function of time. The measurements are carried out at a magnetic field strength of 830 G. For typical beam powers of (500 to 600) mW, the lifetime is 14 s and higher. For lower power, the lifetime rapidly decreases. When the squeeze dipole trap is switched on simultaneously, long lifetimes on the order of 15 s are restored even for low lattice power such as 20 mW (not shown). b) Radial trap frequency of the 1D lattice. The measurement is carried out with a lattice power 700 mW at a magnetic field strength of 680 G. The sinusoidal fit yields a radial trap frequency of 28.1 Hz, resulting from the confinement of the optical lattice and the magnetic field curvature. We deduce a optical trapping frequency of −18 Hz.

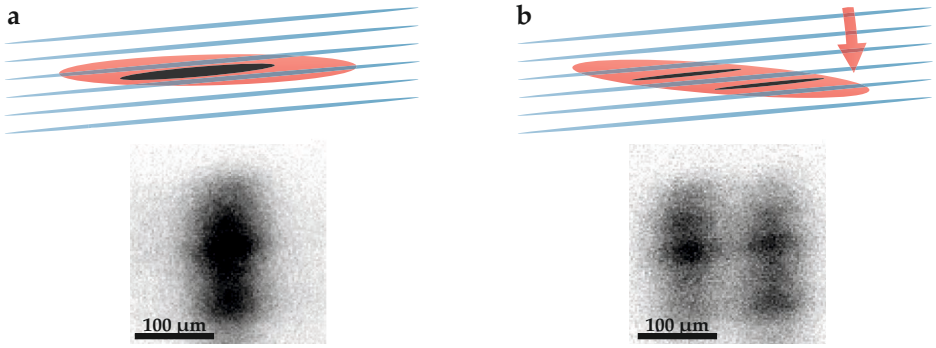

Figure 3.19.: Scheme to verify the preparation of a single quasi-2D cloud in the 1D optical lattice. a) Sketch of the ideal overlap of 1D lattice and squeeze dipole trap, where the cold gas is loaded into a single anti-node of lattice interference pattern. Accordingly, the absorption image shows a single cloud. b) Tilting the squeeze dipole trap leads to a relative displacement between both traps. As a result, the atomic cloud in the squeeze trap is separated and the atoms populate two lattice layers, which is clearly visible in the absorption image. The images are acquired with the squeeze trap operating at 500 mW and the lattice at 600 mW at a magnetic field strength of 715 G. The clouds are elongated along the tilting axis.

tilting axis.

When the beam of the squeeze trap is tilted so that the focus moves by half the lattice spacing, the atomic cloud is split in half by a maximum of the lattice interference pattern. The tilting angle causes a displacement of both clouds, see Fig. 3.19 b, which can be observed in the resulting absorption image. Without the tilt, the two resulting clouds would be axially aligned on top of each other and both cases would be difficult to distinguish. With a distance of about 100 µm between the two separate parts of the cloud we estimate the relative angle between the plane of the squeeze trap and the lattice to be $\sim 1.3°$.

For a qualitative optimization, three Gaussian curves are fitted to the vertical average of the obtained pictures. The optical lattice is vertically moved with the piezo-actuated mirror in front of the science cell entrance port to minimize the adjacent density peaks. In the optimal case, this simple analysis provides us with 85 % of the atoms in one single layer, which is most likely a lower bound. However, even with 15 % to 20 % in the adjacent layers, the influence on the experiments and the image analysis of the central layer is expected to be negligible. This method allows us to realize single layer preparation in only a few iterations.

3.3.5. 532 nm and 1064 nm Laser System

In the case of ^{6}Li, there are numerous commercial options to realize red-detuned optical dipole traps. However, this is not the case for blue-detuned traps, where the availability of well suited laser systems is only just increasing. In the following, we briefly present our 1064 nm laser system and a custom-built 532 nm laser system which consists of a high power amplifier and an external doubling resonator, which provides up to 50 W in continuous wave operation[1]. When this system was set up, it was the first laser system combining a fibre amplifier with an external doubler to produce 532 nm and to exceed the performance of available commercial systems by far.

Our 1064 nm light source is a commercial solid state system with an output power of up to 25 W[2] and a linewidth of 1 kHz. It is located on the main optical table and provides the laser light primarily for the cooling resonator, the transport dipole trap, and the squeeze trap.

A similar solid state laser is located on the optical table of the 671 nm laser system, see Sec. 3.3.1. Through an optical fibre, the laser provides the seed light for the amplifier which is part of the 532 nm setup. In front of the fibre in-coupler, an EOM generates sidebands with a modulation frequency of

[1] More details about the performance and adjustment of the 532 nm laser system can be found in the Bachelor's Thesis of *J. Thielking*, who tested the setup and developed the electronics for the frequency and temperature control of the doubling resonator [76].

[2] Innolight Mephisto MOPA 25, now `www.coherent.de`.

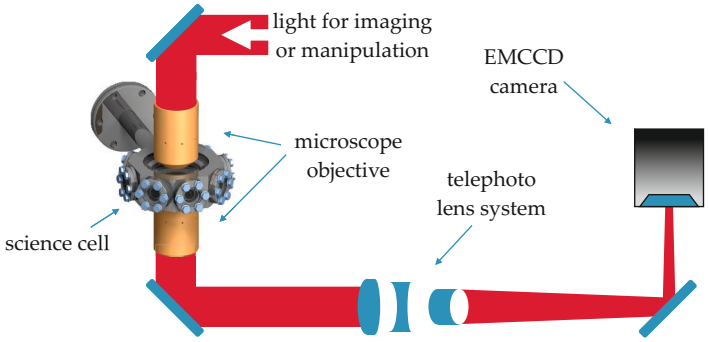

Figure 3.20.: Sketch of the high resolution microscope setup. Imaging light is guided through the upper objective onto the atoms and then focussed via the lower objective and a telephoto lens system onto the camera sensor. The upper microscope objective is also used for manipulation of the cold gases.

230 MHz for the PDH stabilization scheme of the resonator length. Below the main optical table, the seed light is fibre-coupled to the fibre amplifier[1].

The doubling resonator consists of four mirrors in bow-tie configuration and a doubling crystal. The optical elements are built into a monolithic housing which offers high thermal and mechanical stability. The out-couple mirror is reflection coated for the 1064 nm input light, and anti-reflection coated for the doubled 532 nm light. The running wave operation of the resonator protects the doubling crystal from being damaged by high intensity peaks of a standing wave interference pattern. One of the mirrors is piezo-actuated to vary the cavity length and controlled with the signal from the frequency lock.

With an input seed power of 100 mW the amplifier generates up to 50 W at a wavelength of 1064 nm. This light is then frequency-doubled in the doubling resonator[2]. The frequency doubling efficiency reaches up to 80 % and the resulting output light features a linewidth of 10 kHz.

Inside the birefringent LiB3O5 doubling crystal, the refractive index for the input frequency and the doubled output frequency are temperature dependent. Only at a certain crystal temperature, both frequencies stay in phase throughout the crystal. If this is the case, the wavelength conversion efficiency is very high. Otherwise, both wavelengths rapidly fall out of phase and thus the conversion efficiency is low. As a consequence, the performance is sensitive to temperature changes and the crystal is thus temperature controlled with a peltier element.

3.3.6. High Resolution Microscopes

Typically, at the end of each cycle an absorption image of the atomic cloud is taken. Our high numerical aperture (NA) optical system is highly advantageous in regard to in-situ measurements of local properties of quantum gases. Thus, we have access to dynamics, which would otherwise dissolve in typical TOF measurements. Imaging a single 2D quantum gas is particularly interesting since the extracted information is unobstructed by additional layers of atoms above and below the sample. Hence, avoiding the integration along the line-of-sight enables us to detect the smallest local changes and to probe the underlying physics in many-body systems.

The imaging setup consists of one microscope objective below the science cell and a telephoto lens in front of a high perfomance camera with a back-illuminated EMCCD[1] and a front window which is anti-reflection coated for (532, 670, 767 and 780) nm. A second identical objective is located above the atoms to realize, e. g. small local or mesoscopic potentials, see Fig. 3.20. Both microscope objectives are corrected for the science cell windows. When an absorption image is taken, a resonant imaging beam illuminates the atomic cloud through the upper objective and casts a shadow of the atoms. The light is then captured by the lower objective, collimated, and focussed by the telephoto lens onto the camera sensor.

The objectives have a NA of 0.62 which corresponds to a diffraction limited spatial resolution of 700 nm at the imaging wavelength of 671 nm. The attained field of view is about 150 µm. The air spaced lenses, which allow us to use high laser powers for the generation of additional optical lattices and micro-potentials, are anti-reflection coated for (532, 671, 780 and 1064) nm.

Both microscope objectives are mounted in non-magnetic resin tubes[2]. These protrude through the centre of the magnetic coil packages above and below the science cell. Outside the coils, each holder tube is mounted on a combination of precise translation tables. Coarse alignment of each objective can be done manually with a two-axis table[3] with a travel of 20 mm and a resolution of 10 µm. On top of that, a custom-design three-axis tilt-shift table enables us to align the tilt angle of the microscopes and also the coarse vertical direction. PI controlled positioning is carried out with a piezo-actuated three-axis table[4] with a motion range of 100 µm and nanometre accuracy.

Image Acquisition The image acquisition and analysis consists of several steps to reconstruct the density distribution of the atoms and, e. g. retrieve

[1] Nufern NuAmp PSFA-1064-50mW-50W-6-0, www.nufern.com.
[2] Evans & Sutherland, www.es.com, supplier for digital theatres and planetariums.
[1] Andor Ixon3 897, www.andor.com.
[2] Ultem 2300, 30 % glass reinforced polyetherimide.
[3] Owis KT 90- D56-MP, www.owis.eu
[4] Piezosystem Jena TRI-TOR 102, www.piezosystem.de.

the atom number or the gas temperature.

First, the atomic cloud is illuminated with resonant laser light of weak intensity I_0, either in-situ or after some TOF is applied. Depending on the column density of the particles, the optical density OD determines the normalized transmission intensity $I/I_0 = \exp(-OD)$ which is captured on the EMCCD sensor. In short succession, a second picture of the imaging beam is taken without the atoms. This contains all information about present fringes and inhomogeneities of the light itself to subtract them from the first picture. Finally, a dark picture without the imaging light is taken to take stray light and pixel errors into account.

When 2D images of 3D atomic clouds are acquired, the significant expansion along the line-of-sight causes the imaged atom density to be integrated along this direction. To reconstruct the 3D density distribution, one can employ the mathematical tool of inverse Abel transformation. In contrast, images of flat 2D clouds give direct access to the density.

4. Magnetic Field Setup

All quantum gas experiments today heavily rely on magnetic fields for a wide range of applications, e. g. the Zeeman effect, which describes the magnetically induced shift of atomic energy levels and which enables us to cool and trap atoms. External magnetic fields also change the atomic potential energy and thus give access to free control over the inter-particle interaction via magnetic Feshbach resonances.

This chapter presents the design process and the realization of our magnetic field setup. We give an overview of the magnetic coil setup and the general considerations of the development and the realization of our magnetic coils in Sec. 4.1 and 4.2. Detailed descriptions of the individual coils are given afterwards, beginning with the Zeeman slower in Sec. 4.3, followed by the coils around the main chamber in Sec. 4.4, and the coils around the science cell in Sec. 4.5. The last two Sections 4.6 and 4.7 are dedicated to the current control and interlock system, and the thermal stability of our setup.

4.1. Overview

The magnetic coil setup around the main and science chamber is depicted in Fig. 4.1. All coils are attached to a solid aluminium framework around the main and science chamber. It is convenient to distinguish three experimental phases corresponding to three different magnetic field configurations. The first one is the MOT phase, followed by the cooling phase inside the in-vacuo resonator, and the experimental phase in the science cell. Each phase is now briefly summarized and the corresponding coils are listed. Note that the focus is on the generated fields and that we do not repeat, e. g. the description of the cooling sequence given in Ch. 3.

1) MOT phase
    - Zeeman slower
    - MOT coils
    - shim coil
    - push coil

At the beginning of each cycle, the current of the Zeeman slower and the MOT coils is switched on and atoms are continuously captured in the MOT. The pair of MOT coils is operated with a current of opposing directions to generate a magnetic quadrupole field with zero field strength in the centre. For optimal

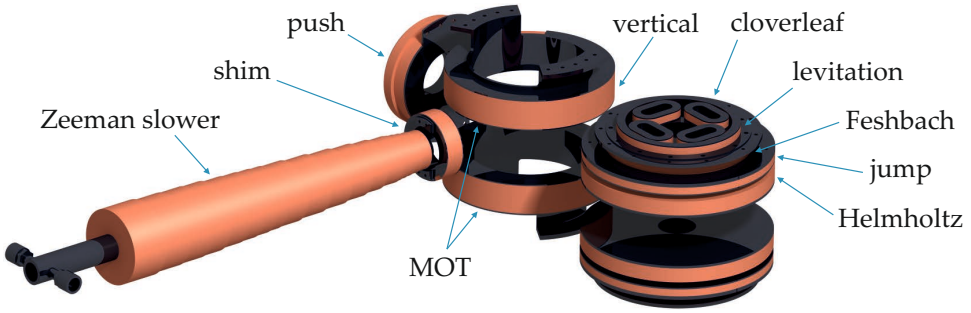

Figure 4.1.: Technical drawing of the magnetic coils in our experimental setup. During an experimental sequence the tapered Zeeman slower coils to the left, the shim, push and the pair of MOT coils are powered simultaneously. After the atoms are transported into the science cell, typically the Feshbach and Helmholtz coils are used for further preparation of the atomic sample and measurements.

performance, the magnetic field of the shim coil provides a smooth transition from the slower field into the MOT field. The axis of the Zeeman slower is shifted in respect to the centre of the main chamber. Therefore, during the loading the MOT centre is shifted onto the slower axis by an offset field which is created by the push coil.

2) Cooling resonator phase
   - MOT coils
   - shim coil
   - push coil

At the end of the MOT phase, the Zeeman slower coils are switched off and the current through the shim and push coil is increased. This shifts the MOT field minimum onto the transfer position of the cooling resonator beam, where the atoms are transferred into the resonator enhanced trap. When the transfer is complete, the magnetic fields for slowing and trapping are switched off.

Next, evaporative cooling inside the cooling resonator is performed. This only works if the atoms are able to re-thermalize when the trap depth is lowered. Since the ^{6}Li scattering length almost vanishes in absence of a magnetic field, we have to apply an external one. At 300 G, the scattering length has a local maximum of $|a_{3D}| = 300\,a_0$, which can be addressed by the MOT coils. Hence, the direction of the current in one of the MOT coils is changed. Instead of a quadrupole field with zero field at the centre, the coils now generate a field with the maximum magnetic field strength in the geometric centre.

When the evaporation is finished, the atomic cloud is transferred into the transport dipole trap and all fields in the main chamber are switched off.

3) Experimental Phase
   - Feshbach coils
   - Helmholtz coils
   - auxiliary coils

For further evaporation and experiments in the science cell, we have to control the scattering length over a wide range. Correspondingly, the magnetic field strength has to be changed over several 100 G around the Feshbach resonance at 834 G. Due to the coil geometry, the Feshbach field features a high field curvature. Therefore, an additional coil pair is placed around the Feshbach coils to generate highly homogeneous fields at the position of the atoms. We refer to them as Helmholtz coils.

The term auxiliary coils summarizes several smaller coils which are located around the science cell. There is a pair of smaller, so called jump coils, which feature a small inductance and can be used to quickly switch on magnetic fields. The levitation coils enable us to compensate the gravitational force which is felt by the atoms. Finally, eight small racetrack coils in groups of four above and below the science cell can be used to realize various field gradients along the atomic clouds.

4.2. Designing Magnetic Coils

For each required magnetic field configuration, the demands and constraints to the mechanical design have to be considered individually. Here, we introduce the fundamental field types employed in our experiment and then summarize the general considerations regarding the realization of magnetic coils.

4.2.1. Basic Field Types

The simplest possible field shape is the one created by a magnetic dipole, see Fig. 4.2. The magnetic dipole field is equal to the field created by a current carrying loop, or in a broader sense, a magnetic coil. The combination of dipoles generates more complex magnetic fields, e. g. two dipoles in an anti-parallel orientation generate a quadrupole field, which is employed in the MOT. In the experimental setup, depending on the coil dimensions, the distance, and the current, we generate a quadrupole gradient field with a zero field centre, or a field with a central finite strength. For the latter, the coils are said to be in Helmholtz configuration.

Helmholtz Configuration Consider two identical coils with radius r which are separated from each other by a distance d on the same axis. If the strength and circular direction of the current I is the same in both coils, a field of finite

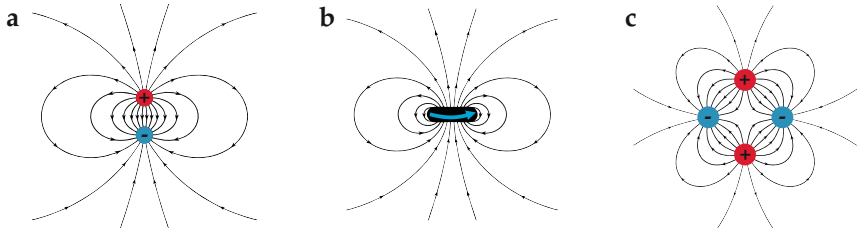

Figure 4.2.: Basic magnetic field types. a) A dipole field is the simplest magnetic field possible. b) A dipole field is generated by a current carrying loop, and in a wider sense, by a magnetic coil. c) The combination of two dipole fields results in a quadrupole field, which is employed in the MOT. It can be generated by two coils in anti-Helmholtz configuration.

strength at the symmetric centre is generated. For distances $d > r$ or $d < r$, the axial field component between both coils features a local minimum or maximum.

For $d = r$, the coils are said to be in Helmholtz configuration and the axial field is homogeneous along the centre region at $d/2$. To realize homogeneous fields with real coils, e. g. our Helmholtz coils, the finite extent and the centre of mass of the winding packages has to be considered.

For $d \ll r$, magnetic fields with high field strength and high curvature are generated, like it is the case with our Feshbach coils[1].

Anti-Helmholtz Configuration In anti-Helmholtz configuration, the current I in both coils is of the same strength but of different circular direction. The individual fields are thus different in sign and cancel between the coils. This generates a quadrupole field, which is a gradient field with zero field at the centre. The gradients are determined by the distance d, the radii r and the current I. This field configuration is employed in our MOT.

4.2.2. Realization

The implementation of magnetic coils in an environment with typically very limited space gives rise to particular constraints. Depending on the required field shape and strength, the feasibility of the coil design has to be considered and adapted, which is a iterative process to find the best possible realization. The complexity depends on the application, i. e. the design of a MOT field is far less sensitive than the one of a magnetic trap.

[1] The coil naming convention is not to be confused with the actual coil configuration. Both, Feshbach and Helmholtz coils operate almost in Helmholtz configuration. The term Feshbach coils refers to the Feshbach resonance, which is addressed with high magnetic field strength, regardless the field curvature. The term Helmholtz coils refers to the ideal Helmholtz configuration or field, since these coils are designed to generate highly homogeneous fields with zero curvature.

In the following, the main design aspects are briefly discussed. This involves our coil holders, the type of wire we use, and the coil mounts.

Coil Holder and Winding Process All of our magnetic coils are wound around aluminium coil holders. They offers high thermoconductivity, rigidity and machinability[1]. Sandblasting and black anodizing reduces the danger of reflective surfaces in the vicinity to laser beams.

The winding process was done by a specialized company[2]. The minimum possible wall thickness for an aluminium ring holder was specified with 1.5 mm. Below 1.0 mm, the constantly applied torque during the winding process leads to deformation of the material. Our coil holders feature a u-profile to realize a good guiding of the wire during the winding and therefore a high quality of the winding package with an optimal fill factor. The side of the holder which is facing the vacuum chamber is as thin as possible, i. e. (1.0 to 1.5) mm. This enables us to place the coils in proximity to the chamber walls.

Note that it is not necessary to use coil holders to stabilize the winding package. It is possible to use a removable holder and stabilize the coil by casting it into an epoxy resin, which improves the thermal conductance of the winding package significantly which is of particular importance for the cooling of larger coils. Typically, the adhesive Araldite F is used, which offers a high heat resistance to withstand high power consumptions when high current strengths are used[3].

The resin can also be used in combination with coil holders, as we did in the case of the Zeeman slower coils. All remaining coils were wound via wet winding, where liquid resin is added during the process. The finished coils are wrapped in a few layers of a resin soaked sheet for resilience and stabilization.

Hollow Copper Wire Almost all coils are wound with a hollow conductor[4] which features a (4×4) mm profile. The central bore has a diameter of 2.5 mm and the resulting current carrying area is thus 11.1 mm^2. The copper is covered with an insulating sheet of slightly fluctuating thickness, which adds (0.8 to 1.0) mm to the edge length.

A bending radius for (4×4) mm wire of 30 mm should not be undercut. Otherwise, the flow of the cooling water is likely to be significantly reduced by the compressed bore. In this regard, large winding packages, i. e. long

[1] All holders and associated parts were manufactured in the university workshop.
[2] OSWALD Elektromotoren GmbH, `www.oswald.de`.
[3] While Araldite F offers a heat stability up to 200 °C the corresponding hardener withstands temperatures of at least 150 °C.
[4] This type of wire is manufactured by an extrusion process of high purity oxygen-free copper with high electrical and thermal conductivity.

wires, reduce the water flow as well and make high powered booster pumps necessary[1].

For some applications, hollow conductors are not feasible. Conventional round or flat wire is the convenient choice for small coils and for coils which are operated with low currents or with very short duty cycles.

Ohmic Heating In the case of high magnetic field strengths, high current densities are required. Thus, a high fill factor and therefore a good winding quality is favourable. Additionally, a minimum distance to the position of the atoms is advantageous. Since quantum gases are bound to an UHV environment, the dimensions of the vacuum chamber limits the distance and higher currents are necessary for compensation. This increases the power dissipation due to Ohmic heating, which is problematic because it enhances out-gassing of the vacuum chamber walls.

As a rule of thumb, current densities of about $10\,\mathrm{A\,mm^{-2}}$ require water cooling. In case of current densities of around $5\,\mathrm{A\,mm^{-2}}$, the use of heatsinks and fans, peltier elements is typically sufficient. Below $5\,\mathrm{A\,mm^{-2}}$, purely passive cooling can be sufficient, depending on the material of the coil holder and available airflow The duty cycle plays an important role when the appropriate cooling measures have to be considered.

In most cases, passive cooling is insufficient and water cooling is the best choice. It is typically realized by the implementation of water channels into the coil holder. But in case of large coils, this lacks a homogeneous cooling of the winding package and thus high temperature gradients from the outer to the inner regions of the winding package develop. The use of hollow core wires omits this problem[2].

Calculating Magnetic Fields The magnetic field design was mainly done with the Windows application BiotSavart[3] and the programming language Mathematica[4]. In either case, the calculation of the resulting magnetic field of a given current carrying wire or loop is realized by the implementation of the Biot Savart law

$$\mathbf{B} = \frac{\mu_0}{4\pi} \int_C \frac{I\mathbf{l} \times \mathbf{r}}{|\mathbf{r}|^3}, \tag{4.1}$$

which describes the magnetic field $\mathbf{B}$ at position $\mathbf{r}$ being generated by a current $I\mathbf{l}$ along an arbitrary path C. The quantity μ_0 is the magnetic constant.

With the software BiotSavart, arbitrary conductor configurations in 3D space can be simulated to calculate the resulting magnetic fields. In combination with the 3D computer-aided design (CAD) drawing of the apparatus

[1] In our case it is a Wilo MVI 206-1/25/E/1-230-50-2, `http://www.wilo.de`.

[2] Note that Bitter type coils, which consist of thin conductive plates and insulating helically stacked spacers, allow for an even more effective water cooling [77].

[3] Ripplon Software Inc., `www.ripplon.com`.

[4] Wolfram Research Inc., `www.wolfram.com`.

it is a straight forward yet meticulous work to optimize the coil dimensions and achievable field shapes and strengths.

Mathematica allows us to address a broader range of tasks, such as the simulation of the deceleration of an atomic beam in the tapered magnetic field of the Zeeman slower. Hence, our slower design was carried out with a modified version of an existing code [78] to account for the shifted MOT field position and the Zeeman slower field shimming, see Sec. 4.1 and 4.4.

4.3. Zeeman Slower

The Zeeman slower coil generates a tapered magnetic field along the slower axis. This compensates for the changing Doppler shift of the constantly slowed atoms which travel towards an anti-propagating laser beam. The working principle of slowing atoms is presented in Sec. 3.3.2. Here, we present the technical aspects of different Zeeman slower types and discuss the realization of our Zeeman slower coils.

4.3.1. General Considerations

The task of slowing atoms can be accomplished with three types of Zeeman slower coil configurations. Consider the direction $\hat{z}$ to be the symmetry axis of the Zeeman slower coil. Depending on the slower type, the magnetic field B_z, which compensates for the changing Doppler shift along the axis, either decreases, increases or features a zero-crossing towards the end of the slower, see Fig. 4.3.

Whether the field strength has to decrease or increase towards the position of the MOT is determined by the employed slowing transition. Typically, transitions with $|\Delta m_F| \pm 1$ are used, which feature an opposite sign of the corresponding atomic Zeeman shift. It determines the polarisation of the slowing light to be σ^+ or σ^-, respectively.

The ideal field of Zeeman slower coils along the symmetry axis is described by[1]

$$B(z) = \frac{\hbar}{\mu_B}\left[\delta_0 + \frac{1}{\lambda}\sqrt{v_{init}^2 - 2a_e z}\right]. \tag{4.2}$$

Where μ_B is Bohr's magneton, λ is the wavelength of the slowing light, δ_0 is the frequency detuning of the slowing laser in respect to the MOT cooling laser, $a_e = \kappa a_{max}$ the effective deceleration of the atoms and v_{init} the maximum initial velocity. The quantity κ depends on the ratio $s_0 = I/I_{sat}$ of the intensity I of the slowing laser we use, and the saturation intensity I_{sat} of the slowing transition

$$\kappa = \frac{s_0}{1+s_0}. \tag{4.3}$$

[1] Here, we repeat Eq. 3.1 for convenience.

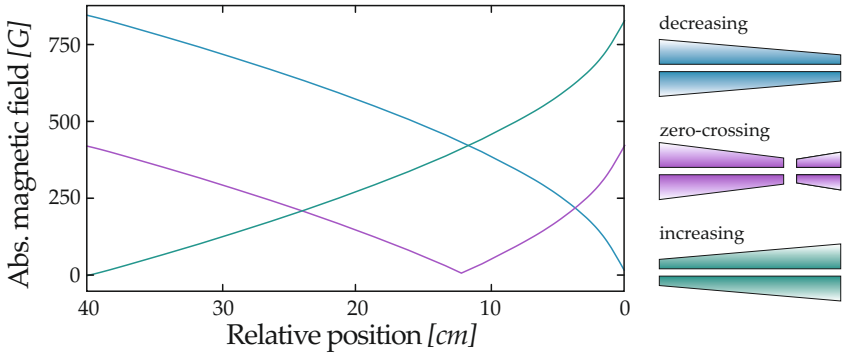

Figure 4.3.: Sketch of ideal axial magnetic fields of different Zeeman slower types. The green line depicts the field generated by an increasing slower, the velvet line depicts the field of a zero-crossing slower. We use the decreasing type, which is denoted by the blue line. The curves are calculated using Eq. 4.2.

A typical design value for the deceleration is $a_e = 0.5 a_{max}$, thus $I = I_{sat}$, to make the slowing process largely independent from fluctuations of the scattering rate which results in a robust performance.

The difference between maximum and minimum of the Zeeman slower field strength ΔB_z determines the highest velocity of atoms which can be slowed. ΔB_z and the length L of the slower define the slope of the Zeeman slower field. Steep slopes yield a strong deceleration a_e, where its maximum value $a_{max} = \hbar k \Gamma / 2m$ is given by the maximum photon scattering rate $\gamma = 1/\Gamma$ and the atoms mass m. It is important that the change of the magnetic field is smaller than the Doppler shift at any time, i. e.

$$\mu_B \frac{\partial B}{\partial \mathbf{z}} v(\mathbf{z}) \leqslant \hbar \mathbf{k} a_e, \tag{4.4}$$

otherwise, the atoms are lost from the slowing process.

The resonance condition for the counter-propagating light and the atoms at the end of the slower determines the detuning δ_0. For obvious reasons this is significantly different for the decreasing and increasing Zeeman slower. For the latter, the lowest velocities are reached at the highest field strength where the Zeeman shift is large. Therefore, the detuning δ_0 with respect to the bare atomic, as well as to the MOT transition, has to be large. This is an advantage, since light induced heating of the atoms in the MOT is negligible. In addition, the abrupt end of the resonance condition for the atoms prevents them from being eventually pushed back towards the slower. On the other hand, the MOT can be easily perturbed by the strong Zeeman slower field.

The magnetic field of a Zeeman slower also introduces a quantization axis for the atoms. This prevents the atoms from getting pumped into a dark state, which would exclude them from the slowing cycle. However, this is

not fulfilled for the magnetic field zero crossing of the zero-crossing Zeeman slower. Here, an additional laser repumps the atoms from the dark state.

Our Decision We use a decreasing Zeeman slower for the following reasons. Since we employ the $2^2S_{1/2}, m_F = 1/2 \rightarrow 2^2P_{3/2}, m_F = 3/2$ transition, where $\Delta m_F = +1$, the light of the slowing beam has to be σ^+ polarized. The necessary detuning δ_0 is technically easy to realize and the light can still be far enough detuned from the MOT light to prevent noticeable heating. Increasing δ_0 shifts the position where the atoms reach their lowest velocities away from the Zeeman slower coils. With a light species like ^{6}Li, we can easily ensure that this position is still covered by the capture volume of the MOT, which is not possible for heavier atoms. The deceleration of heavier atoms and atoms with longer lived excited states is generally more difficult, since both reduce the possible deceleration significantly.

For initial velocities of approximately $1000\,\mathrm{m\,s^{-1}}$ and a design length of about $0.5\,\mathrm{m}$, the required maximum field strength is below $1000\,\mathrm{G}$ and thus relatively easy to accomplish. Another advantage is the absence of noticeable magnetic disturbance of the MOT field due to the small field strength at the end of the slower.

A short distance between Zeeman slower and MOT keeps the divergence of the atom beam small. Strongly diverged atomic beams would eventually exceed the capture volume of the MOT. Finally, we were already experienced in the design process and the utilization of a decreasing Zeeman slower. Therefore, the time needed for development and manufacturing was presumably short.

Other methods to slow atoms are, for instance, using a chirped laser to compensate for the Doppler shift of the atoms, which prevents continuous loading. It is furthermore possible but very inefficient and time consuming to load a ^{6}Li MOT from a hot background gas. An appropriate alternative is the 2D MOT which employs transversal cooling while the atoms are decelerated to realize high fluxes with a compact design [79].

4.3.2. Realization

To accomplish the analytically ideal parameters with a Zeeman slower coil in an experimental setup is neither easy, nor necessarily practical. Thus, we first identify the mechanical constraints, calculate the field of a feasible slower coil and then simulate the performance of the design. In the following, the considerations regarding the dimensions of the slower, the required field strengths and the realization of the winding package are briefly presented. Afterwards, the results of the numerical simulations and a comparative characterization of the manufactured Zeeman slower are given.

General Considerations The length L of the Zeeman slower coil is determined by the initial and the final velocity, v_{init} and v_{end}, and the effective deceleration a_e, as

$$L = \frac{v_{init}^2 - v_{end}^2}{2a_e}. \tag{4.5}$$

Reorganization of Eq. 4.5 yields that the longer the Zeeman slower, the higher the possible initial velocities v_{init}. Thus, a larger fraction of atoms could be captured in the MOT. Despite being favourable, a very long Zeeman slower has two important downsides. It is not only very space consuming, it also causes strong divergence of the atom beam due to randomly re-emitted photons. The repeatedly scattered photons cause the atoms to perform a random walk in momentum space, which increasingly broadens the atom jet along the slower. Especially for long slower coils, where a long time of flight eventually results in a beam size which exceeds the capture radius of the MOT.

In our case, the best compromise between end velocity and beam broadening is a Zeeman slower length of about 0.5 m. This assumes an end velocity of $v_{end} \approx 50\,\mathrm{m\,s^{-1}}$, an initial velocity of $v_{init} = 1000\,\mathrm{m\,s^{-1}}$, and an effective deceleration of $a_e = 0.5a$. The velocity of the atoms exiting the Zeeman slower should be smaller than the capture velocity of the MOT, $v_{end} \leqslant v_{capture}$, where

$$v_{capture} = \sqrt{\frac{\hbar k \Gamma}{4m}}\, r. \tag{4.6}$$

For our parameters, i. e. for a radius of $r = 15\,\mathrm{mm}$ of the MOT laser light, Eq. 4.6 yields a capture velocity of $50\,\mathrm{m\,s^{-1}}$. Finally, to minimize the broadening of the atom beam, the end of the slower coil should be in proximity to the main chamber and the MOT field, hence a compact mount is required.

The vacuum tube, which is encased by the slower coils, must be large enough to prevent the slowed atoms from colliding with the wall. Close to the oven, the outer diameter of our differential pumping tube is 6 mm. It ends where the atoms begin to be decelerated and the divergence of the beam begins to increase, due to the onset of resonant light scattering. From here, the outer diameter of the vacuum tube is 22 mm, which determines the inner diameter of the coil holder of the Zeeman slower.

The coil holder, which is placed directly around the vacuum tube, features a double wall. The inner construction is segmented into two channels along the tube and joined at one end. The cooling water connections are located close to the oven. The diameter of the inner tube is (32.0×3.0) mm and the one of the outer tube (35.0×1.5) mm.[1] To prevent vibrations of the vacuum chamber, the coil holder is not in contact with the vacuum tube. The smallest diameter of the coil windings is 70 mm, set by the water cooled holder.

Combining Eq. 4.2 and 4.5 yields that for a given length and capture velocity of the MOT, the maximum field strength is determined by the initial

[1] The declaration is *outer diameter* $\times$ *wall thickness*.

velocity of the atoms. We want to address an initial velocity of approximately $1000\,\mathrm{m\,s^{-1}}$, which in our case requires a field strength of about 900 G. Additionally, the slope of the field along the Zeeman slower axis should provide an exact compensation for the changing Doppler shift at any position, as shown in Eq. 4.4.

Finally, a fail safe design is more important than for any other coil, since in case of a malfunction, the exchange of the Zeeman slower would be impossible without disassembling the oven chamber and therefore opening the vacuum chamber. Instead of a single wire or separate coils placed side by side along the axis, we use multiple individual stacked winding packages of (1×3) mm flat wire to minimize potential issues: if an individual coil fails, we are able to compensate for it with the remaining windings without causing a significant change of the slowing field shape. Each winding starts at the front, goes to the end and to the front again. The distance to the front is reduced with each of these double layers. Furthermore, in contrast to separate solenoids along the axis, this winding technique gives us precise control over the field slope.

Simulated and Manufactured Slower The simulation of our Zeeman slower accounts for all constraints mentioned above and assumes a winding package consisting of 14 stacked coils in 34 layers in total with a length of 0.52 m. The parameters were optimized to be consistent with the ideal slower parameters given by the analytic description.

At the MOT position, the $1/e^2$ atom beam diameter is estimated to be well below 20 mm and thus matches the size of the MOT. With a red-detuning of $\delta_0/(2\pi) = -36\,\mathrm{MHz}$ to the MOT transition, the simulation yields that almost 20 % of the atoms which leave the oven are slowed and thus an atomic flux of about $1 \times 10^{10}\,\mathrm{s^{-1}}$ can be achieved.

The corresponding calculated magnetic field of the final design is depicted in Fig. 4.4 a. Here, in addition the field sum, the individual fields of the slower coils, the shim coil, and the MOT field are shown. The maximum field strength is reached at a distance of about 80 mm from the back end of the slower coils, where the slowing process begins. For comparison, Fig. 4.4 a shows the ideal slowing field as well, and furthermore Hall probe measurements of the realized magnetic field.

The slope of the Zeeman slower field transitions smoothly into the MOT field with negligible deviations from the ideal field slope. Therefore, the compensation of the changing Doppler shift of the atoms remains fulfilled.

Due to the distance between the end of the slower and the MOT coils, the smooth transition requires a compensation field which is provided by the shim coil. The shim coil has a length of 25 mm and consists of only 14 turns of (4×4) mm hollow conductor. It is mounted in a distance of 11 mm from the front of the slower coils.

As shown in Fig. 4.4 b, deviations of the simulated deceleration from the

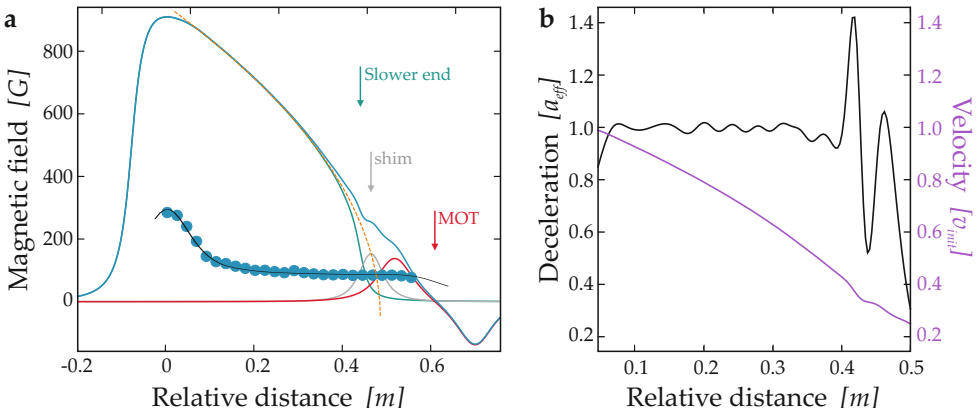

Figure 4.4.: a) Measurement and calculation of the magnetic Zeeman slower field as a function of the relative distance to the position of the maximum field strength. The solid cyan line depicts the resulting magnetic field sum of the slower field (solid green line), the field generated by the shim coil, and the MOT field (solid red line). The calculated field of an ideal slower is shown as the dashed orange line. The arrows mark the position of the end of the slower coils and the centre of the shim and MOT coils, respectively. Hall-sensor measurements of the magnetic field (cyan circles) are carried out 9 cm off-axis with the slower operated at 5 A. The result is in very good agreement with the corresponding calculated field (solid black line). b) The black line is the simulated deceleration of the atoms in units of the effective deceleration $a_{eff} = 0.5\, a_{max}$. A significant deviation from the ideal value is noticeable only where the Zeeman slower field transitions into the MOT field, see text. The purple line depicts the simulated velocity of the atoms in units of the initial velocity v_{init}.

Zeeman slower	
Identification number (ID)	QM-00175
Manufacturer serial number (SN)	900456
Coil length	518 mm
Coil weight, approx	21 kg
Wire diameter, without isolation	(3×1) mm
Wire length	788 m
Turns	3918
Minimum number of layers	10
Maximum number of layers	34
Minimum winding radius	35 mm
Resistance	4870 mΩ
Operating voltage	48 V
Operating current	9.9 A
Maximum field strength	1250 G
Total power dissipated, approx.	480 W
Temperature near oven	47 °C
Temperature near chamber	29 °C
Duty cycle	35%

Table 4.1.: Summarizing overview of the Zeeman slower properties. The given ID corresponds to our group internal registry. All values regarding the operation of the slower coils correspond to a typical experimental sequence, as described in Ch. 3. Note that the shim coil properties are listed separately in Table 4.2.

ideal value become recognizable at the transition point between Zeeman slower and the MOT field. These ripples are inevitable due to the limited possibilities to position the shim coil, and tolerable since the design value a_e leaves a wide safety margin. Apart from that, the deceleration along the slower axis features only negligible oscillations, which are mainly caused by the beginnings and endings of the individual windings. All specifications of the final Zeeman slower are given in Table 4.1.

Manufacturing For the winding process, two discs were clamped on the holder to prevent the wire of from slipping. These supports defined the exact start and end for the winding package and were removed later.

In order to maximize the thermal conductance of the coils, the entire wind-

ing package is vacuum casted in Araldite F, see also Sec. 4.2.2. The 14 layers result in 28 wire leads which had to be sealed individually. For this reason, a complex casting form had to be built. The first casting attempt failed and several leads were ripped off. Hence, the manufacturer improved the casting form design and was able to produce the slower, yet in a time consuming and complicated process.

With a final weight of approximately 21 kg, the implementation of the Zeeman slower coil into the experiment was a delicate process. A reliable wire rope hoist was constructed to slide the heavy weight carefully over the vacuum tube. It is also noteworthy that even so we are using the smallest available vacuum flange[1] to connect the vacuum tube with the oven chamber, a problem occurred regarding the fit of vacuum tube and Zeeman slower holder. Small deformations of the water cooled coil holder, which were most likely caused during the winding process, obstructed the assembly at first. To fix this, we had to reduce the diameter of the flange by about $(1 \text{ to } 2)$ mm by grinding.

4.4. Main Chamber Field Configuration

After the deceleration in the Zeeman slower, the atoms are captured in the MOT, whose working principle is presented in Sec. 3.3.2. During the MOT loading, a coil pair generates a magnetic quadrupole field in the main chamber. When the MOT loading is finished, the MOT field centre is overlapped with the cooling resonator beam and the atoms are transferred into the standing wave dipole trap. To perform evaporative cooling we switch the polarity of the upper MOT coil to generate a Feshbach field.

The magnetic field setup for the MOT and the cooling inside the resonator consists of five different coils: two MOT coils and three additional offset coils to shift the MOT field centre in all three spatial directions. The shim coil of the Zeeman slower acts as one of the offset coils. In the following, the magnetic field configuration for the MOT loading, the transfer into the cooling resonator and the evaporation inside the resonator dipole trap are presented.

4.4.1. Magneto-Optical Trap Loading

During the MOT loading, the two MOT coils generate a quadrupole field. The vacuum tube of the Zeeman slower is connected to the main chamber with an offset of 18.5 mm in the y-direction to the geometric centre of the chamber. The push coil is employed to shift the MOT centre onto the slower axis, as shown in Fig. 4.5.

[1] Microflange CF 10.

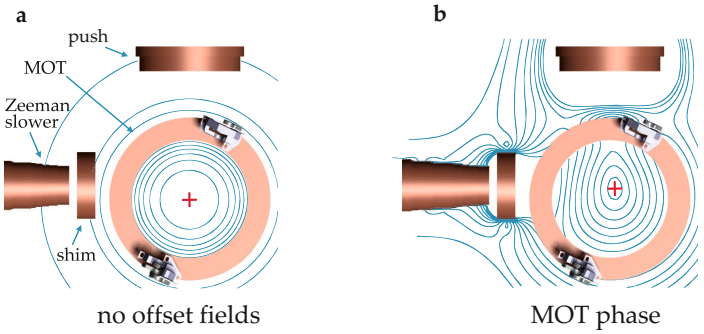

Figure 4.5.: Contour plot of the magnetic field generated in the main chamber. a) The red cross marks the centre of the MOT field. Without additional offset fields, the field centre coincides with the geometric centre of the main chamber. b) During the MOT loading, the magnetic offset field shifts the MOT field minimum onto the Zeeman slower axis.

MOT Coils The MOT coils are recessed in the top and bottom view-ports of the main chamber to reduce the distance between the coils to 81 mm to conveniently generate lateral field gradients of (10 to 20) G cm^{-1}.

The width of the recess determines the inner and outer coil radii. The design also requires an axial wire exit port in the coil holder. The final coils consist of 48 turns, which results in a length of the winding package of 40 mm and a width of ~ 25 mm. Due to the recess, increasing the number of turns is only possible by adding height and does not significantly increase the available field strengths. The MOT coils are wound with (4×4) mm hollow core wire to operate the coils with currents of up to 100 A without difficulties. The optimal loading perfomance is achieved with a current of 63 A and lateral field gradients of 17 G cm^{-1}. A typical duty cycle of 65 % leads to an increase of the coil temperature by only one degree Celsius to 22 °C.

During the MOT loading, a small offset field is applied to adjust the position of the MOT in the vertical z-direction. The field is generated by a coil which is directly wound onto the upper MOT coil and consists of ~ 75 turns of round wire with a diameter of 1.25 mm. It is powered with only 0.5 A to shift the centre of the MOT about 450 µm downwards.

Push Coil The push coil is placed around the CF40 main chamber view-port, through which the transport dipole trap enters, and consists of 49 turns of (4×4) mm hollow core wire. The winding package features two different outer radii. Further away from the main chamber, the radius of the winding package increases from (75 to 110) mm. With this, we realize the maximum number of turns, hence the highest achievable field strengths, without obstructing the neighbouring view-ports. The distance from the coil to the centre of the main chamber is 176 mm.

	MOT	Shim	Push	Vertical
ID	QM-00130-1	QM-00130-2	QM-00130-3	-
Manufacturer SN	900449/50	900543	900457	-
Wire diameter	(4×4) mm	(4×4) mm	(4×4) mm	1.25 mm
Turns per coil	48	14	49	100
Resistance per coil	45 mΩ	6 mΩ	25 mΩ	-
Operating voltage	9.1/8 V	3.3/7.5 V	9.8/9.3 V	1.0 V
Operating current	63.0/55.5 A	124.0/280 A	190/180 A	0.5 A
Total power diss.	600 W	400 W	1900 W	1 W
Temperature	22 °C	23 °C	29 °C	22 °C
Duty cycle	40 %	36 %	36 %	40 %
Distance to centre	40.5 mm	132 mm	176 mm	40.5 mm
Field gradient $\partial_{\hat{x}}\mathbf{B}$	$20\,\mathrm{G\,cm^{-1}}$	-	-	-
Field gradient $\partial_{\hat{y}}\mathbf{B}$	$13\,\mathrm{G\,cm^{-1}}$	-	-	-
Field gradient $\partial_{\hat{z}}\mathbf{B}$	$-33\,\mathrm{G\,cm^{-1}}$	-	-	-

Table 4.2.: Overview of the properties of the magnetic coils which are placed around the main vacuum chamber. The given resistance corresponds to the coil winding package only, i. e. it does not account for cables. The operating current and voltage includes cables and components of the circuitry, e. g. protective diodes. If two values are given, they correspond to the MOT loading phase and the cooling resonator transfer phase, respectively. The voltage corresponds to the first current value. The distance to the centre depicts the minimum distance of the winding package to the geometric centre of the main chamber. The given magnetic field gradients are calculated. Since the shim coil is important for both said phases, it is listed here.

The push coil enables us to shift the MOT field centre by $100\,\mu\mathrm{m\,A^{-1}}$. A current of 190 A generates the offset field during the MOT loading. The mean temperature of the push coil is below 23 °C. Table 4.2 summarizes the properties of the MOT and offset coils.

Performance While the gradients of the MOT field are isotropic for the not shifted case, applying the push field introduces an anisotropy. The resulting magnetic field gradients are $13\,\mathrm{G\,cm^{-1}}$ and $20\,\mathrm{G\,cm^{-1}}$ in x- and y-direction.

We estimate the radius of the MOT volume in direction i, depending on the corresponding gradient $\frac{\partial B}{\partial i}$ and the detuning δ_0

$$r_{\mathrm{MOT},i} = \frac{\hbar\delta_0}{\mu_B \frac{\partial B}{\partial i}}. \tag{4.7}$$

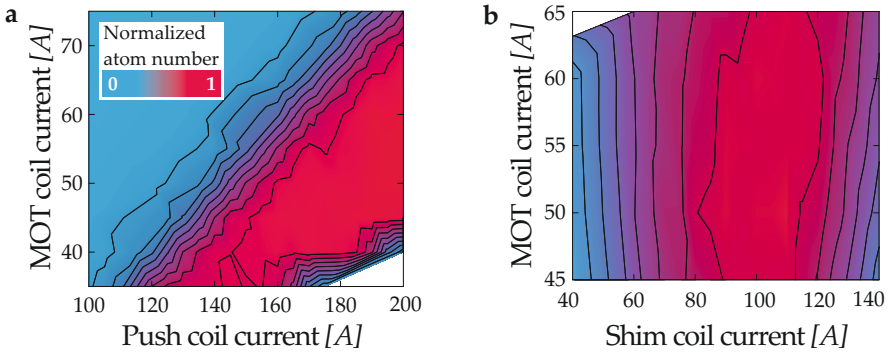

Figure 4.6.: Normalized atom number in the MOT as a function of the current through the MOT and offset coils. a) For stronger MOT fields, the push coil current has to be increased to shift the MOT field centre onto the Zeeman slower axis. The measurement is carried out with the shim coil powered with 95 A and the slower with 9.5 A. b) The performance of the MOT for shim coil currents is largely independent of the current through the MOT coils. The measurement is carried with the push powered with 195 A and the slower with 9.5 A.

This results in an elongated MOT volume with an extent of 17 mm and 10 mm in x- and y-direction. Hence, with a final radius of about 10 mm, the beam of slowed atoms is expected to stay well inside the capture radius of the MOT.

To adjust the optimal MOT position, we determine the atom number in the MOT depending on the current MOT coils and the offset coils, as shown in Fig. 4.6. Stronger MOT fields and thus larger gradients compress the MOT volume and result in higher densities. This leads to heating since two-body losses and the probability for the re-absorption of emitted photons from the atomic cloud are increased. For higher MOT currents, the required offset field strength increases accordingly while the inevitable asymmetry of the MOT remains unchanged. Smaller MOT field gradients result in more dilute cloud densities and a shallower trap so that captured atoms are more vulnerable to off-resonant light scattering by the slowing beam.

4.4.2. Cooling Resonator Loading

When the MOT loading is finished, the atoms are transferred into the resonator enhanced dipole trap to perform evaporative cooling, see Sec. 3.3.3. During the transfer, the Zeeman slower coils are switched off and the current through the MOT and offset coils are changed according to an optimal transfer efficiency.

When no additional offset fields are applied, the MOT field minimum coincides with the centre of the chamber and thus with the centre of the resonator beam. This is due to the recessed design of the MOT coils and the symmetry

of the main chamber. At the centre position, the beam waist of the resonator beam features a minimum, and transferring the atoms into the centre of the resonator beam thus results in extremely low transfer efficiencies. We therefore refrain from this option and perform the transfer at a position where the diameter of the resonator beam has increased to $\sim 400\,\mu m$, instead.

The axis of the cooling resonator is tilted to the y-axis of the chamber by about $25°$, which results in optimal design transfer coordinates of $x = 8.5\,mm$ and $y = 18.5\,mm$ with respect to the geometric chamber centre. While the y-offset is already applied during the MOT loading, we realize the offset in x-direction with the shim coil of the Zeeman slower. This requires a fairly high current of $280\,A$ due to the small size of the coil.

Finally, about $60\,\%$ of the atoms are transferred from the MOT into the standing wave resonator dipole trap for the subsequent evaporative cooling step.

4.4.3. Evaporation in the Resonator Dipole Trap

The ^{6}Li scattering length of the lowest two hyperfine states features a local maximum of $|a_{3D}| = 300\,a_0$ at a magnetic field strength of $300\,G$. For efficient evaporation in the main chamber, we address this maximum with the MOT coils.

When the resonator transfer is finished, all magnetic fields in the main chamber are switched off. Then, the polarity of the upper MOT coil is changed via insulated-gate bipolar transistor (IGBT) h-bridges, and the current through both is switched on again[1]. With the MOT coils in Helmholtz configuration, we are able to generate a magnetic Feshbach field with its maximum at the centre of the chamber.

We obtain optimal evaporation performance with a coil current of $55.5\,A$ to generate a maximum field strength of $\sim 210\,G$, with lateral field gradients lower than $1.5\,G\,cm^{-1}$. Therefore, despite the fact that the atoms are trapped in the standing wave dipole trap roughly $20\,mm$ away from the centre, they are exposed to a fairly similar field strength.

Due to the complex nature of evaporative cooling in a standing wave dipole trap, we have reason to believe that the efficiency can be further improved. During evaporation, the standing wave interference pattern only allows hot atoms to escape in the direction of small trap frequencies, i. e. orthogonal to the beam axis. It is conceivable that an additional vertical magnetic field gradient, generated by, e. g. increasing the current through only one the MOT coils, improves the evaporation efficiency. This is yet to be tested.

[1] The IGBT setup in presented at the end of this chapter in Sec. 4.6.

4.5. Science Chamber Field Configuration

Once the cooling procedure in the main chamber is finished, the atoms are transported into the science cell, where the preparation of quantum degenerated atomic clouds is continued. For the final evaporation and experiments, several different magnetic field configurations can be generated in the science cell for manifold applications. Thus, a nested and compact coil holder accommodates 16 coils in total.

The Feshbach coils allow us to address a wide range of interaction strengths around the Feshbach resonance at 834 G, with field strengths up to 1400 G. A set of Helmholtz coils provides highly homogeneous fields with negligible gradients along the extent of the samples. In addition, there is a pair of jump coils, levitation coils and eight small racetrack coils, called cloverleaf coils. These are located below and above the metal cell, outside the science coil packages. In the following, we present details about the different coils and their specific tasks.

4.5.1. Feshbach and Helmholtz Coils

The mechanical constraints to the coil construction are as follows. The minimum distance between the science coil holders is determined by the dimensions of the science cell and by the fact that we want to maintain the optical access through the top and bottom science cell window from the side, i. e. under a steep angle from in between the coil holders. This leads to a minimum distance between the coil holders of about 60 mm.

The minimum winding radii of the coils is determined by the microscope objectives. To place them at the centre of the coil holders and to maintain lateral freedom of movement, the inner radii is chosen to be 25 mm.

The winding packages of the Feshbach coils feature two different outer radii, as shown in Fig. 4.7. The resulting coils feature the maximum possible number of current carrying turns within a cone from the position of the atoms, to contribute to the maximum field strength regardless the field curvature. As a consequence, we are able to place the Helmholtz coils around the Feshbach coils to conveniently achieve an optimal position to generate highly homogeneous fields, since their distance to the atoms is similar to their radii, see also Sec. 4.2.

Both, Helmholtz and Feshbach coils, consist of (4×4) mm hollow conductor to achieve high current densities and to maintain optimal cooling properties. The outer radius of a Feshbach coil is 91.5 mm and 66.5 mm, where the total height is 59 mm. The inner radius of the Helmholtz windings is 66.5 mm, which extends to a outer radius of 126.5 mm. The height of a Helmholtz coil is 20 mm. Feshbach fields of $7.9\,\mathrm{G\,A^{-1}}$ are realized with large gradients of $0.83\,\mathrm{G\,cm^{-1}\,A^{-1}}$ along the atomic cloud. The homogeneous Helmholtz field features gradients of only $0.017\,\mathrm{G\,cm^{-1}\,A^{-1}}$, see Table 4.3 for further details.

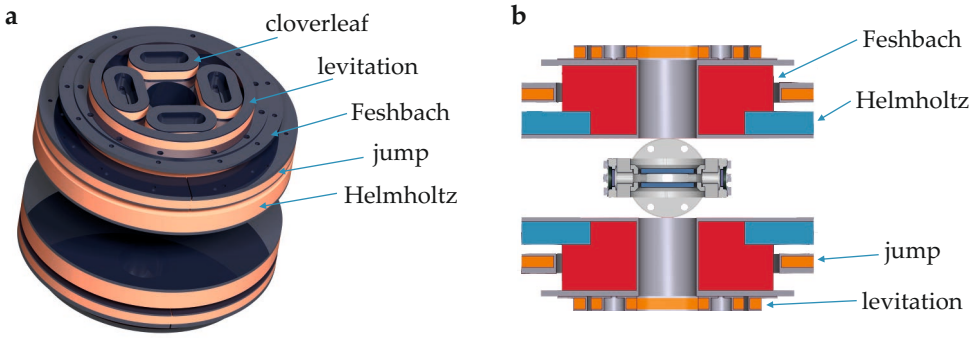

Figure 4.7.: Technical drawing of the magnetic coils which are positioned around the science chamber. a) Isometric view. The science vacuum chamber is hidden underneath the large coil packages. b) Section view of the science chamber coils. The Helmholtz coils, which are wound around the Feshbach coils, are depicted in cyan. The Feshbach coils are depicted in red, and all auxiliary coils in orange.

	Feshbach	Helmholtz
ID	QM-00130-4/-5	QM-00130-4/-5
Manufacturer SN	900460/61	900560/61
Wire diameter	(4×4) mm	(4×4) mm
Turns per coil	146	54
Resistance per coil	80 mΩ	50 mΩ
Inductance per coil	470 µH	145 µH
Maximum voltage	30 V	15 V
Maximum current	165 A	99 A
Total power diss.	4.4 kW	1.5 kW
Temperature	32.5 °C	23 °C
Duty cycle	10%	10%
Field strength	$7.9\,\mathrm{G\,A^{-1}}$	$4.7\,\mathrm{G\,A^{-1}}$
Field gradient $\partial_{\hat{x},\hat{y}}\mathbf{B}$	$8.32\,\frac{\mathrm{mG}}{\mathrm{A\cdot mm}}$	$0.17\,\frac{\mathrm{mG}}{\mathrm{A\cdot mm}}$
Field gradient $\partial_{\hat{z}}\mathbf{B}$	$-16.6\,\frac{\mathrm{mG}}{\mathrm{A\cdot mm}}$	$0.33\,\frac{\mathrm{mG}}{\mathrm{A\cdot mm}}$

Table 4.3.: Properties of the Feshbach and Helmholtz coils around the science chamber. The given maximum values are limited by the corresponding power supplies, listed in Table 4.5. The given magnetic field gradients are calculated.

Zero-Curvature Feshbach Fields The ^{6}Li hyperfine states we are using in the experiment are high field seekers, i. e. they are attracted by strong magnetic fields. As a consequence, the of the magnetic Feshbach field generates a horizontal magnetic trapping potential. At field strengths between (700 to 1000) G, the resulting horizontal trap frequencies are ~ 30 Hz, where the high radial symmetry is typically advantageous for experiments.

However, for evaporative cooling in the 1D optical lattice, it is favourable to realize Feshbach fields with a negligible radial confinement. The reason is that due to the blue-detuned lattice, the hot atoms could easily leave the trap in the radial direction, since they are neither restrained by a magnetic nor an optical potential. Moreover, the anti-confining lattice promotes the evaporation in the radial direction.

Instead of using the dedicated Feshbach coils, one way to realize a zero-curvature field is to employ the Helmholtz coils, which are designed to generate highly homogeneous fields. However, we are currently limited by the available power supply, which provides a maximum current of 99 A to generate a maximum field strength of 480 G. A further reduction of the radial confinement could be achieved by the employment of an appropriate power supply, which is planned for the near future. Until then, a convenient option to reach field strengths of (700 to 1000) G is to power the Feshbach and Helmholtz coils simultaneously. This combination generates a field of the required strengths with radial trap frequencies reduced by $\sim 40\,\%$.

Miscellaneous The direction of the current through the upper Helmholtz coil can be changed to generate and to superimpose a quadrupole field with the evaporation field which is generated by the Feshbach coils. We employ a current of 10 % of the Feshbach coil current during evaporation to shift the field maximum about 1 mm downwards. With this, we compensate for a vertical displacement of the science coils.

4.5.2. Auxiliary Coils

In addition to the Feshbach and Helmholtz coils, various smaller coils for specific tasks are placed above and below the science cell. They all consists of round cooper wire with a diameter of 1.25 mm and were wound by ourselves.

There are two groups of four racetrack coils each. An individual racetrack coil consists of 45 turns with a profile of (10×10) mm and an size of approximately (20×40) mm. They enable us to generate arbitrary field gradients at the position of the atoms. In a configuration, where the current in two neighbouring racetrack coils is of the inverse direction in regard to the opposing two coils, maximum gradients of 7.2 mG mm^{-1} A^{-1} are realized.

Around the four racetrack coils, there are levitation coils to provide 2.1 G A^{-1} to compensate for the gravitational drag on the atoms. Finally, on top of the Helmholtz coils and around the Feshbach coils, there is a pair of so-called

	Jump	Levitation	Cloverleaf
Wire diameter	1.25 mm	1.25 mm	1.25 mm
Turns per coil	130	70	45
Resistance per coil	1.25 Ω	-	-
Maximum current	10 A	10 A	10 A
Distance to centre	62.5 mm	103.0 mm	103.0 mm
Field gradient $\partial_{\hat{x},\hat{y}}\mathbf{B}$	0.9 $\frac{\text{mG}}{\text{A}\cdot\text{mm}}$	-	7.2 $\frac{\text{mG}}{\text{A}\cdot\text{mm}}$
Field gradient $\partial_{\hat{z}}\mathbf{B}$	1.8 $\frac{\text{mG}}{\text{A}\cdot\text{mm}}$	-	7.2 $\frac{\text{mG}}{\text{A}\cdot\text{mm}}$

Table 4.4.: Summary of the auxiliary coil properties. The distance to the centre depicts the minimum distance of the winding package to the geometric centre of the main chamber. The maximum current is limited by the purely passive cooling. The given magnetic field gradients are calculated. The missing values were not determined.

jump coils. They feature a low inductance of 6.9 mH to realize fast changes of the magnetic field strength with up to $9\,\text{G}\,\text{A}^{-1}$. All details about the auxiliary coils are summarized in Table 4.4.

4.6. Current Control and Interlock System

Realizing magnetic fields for various applications requires a large set of different power supplies and the ability to precisely control and switch currents. Here, we briefly summarize our current control methods and the safety measures we take.

The main coils, i. e. the MOT, offset, Feshbach and Helmholtz coils, are powered by high performance switch power supplies. The Zeeman slower coils, and all coils consisting of 1.25 mm round wire, are connected to smaller devices, as listed in Table 4.5.

All power supplies are remotely controlled from the experiment control computer. An analogue input signal enables us to set the current and power off the supplies directly on a time scale of about 30 Hz. This is slow compared to typical time scales in a quantum gas experiment and can be increased significantly by using an external switching method, for instance, an IGBT. With IGBTs, we realize switching speeds on the order of 1 kHz, see Fig. 4.8. Furthermore, IGBTs offer low power consumption and a high robustness.

IGBT h-bridges are employed to change the direction of the current through a coil, e. g. in the case of one of the MOT and the Helmholtz coils. In some cases, the circuitry to operate the magnetic coils contains an additional protective diode to prevent fault currents. Varistors secure the IGBTs against

Power supply	Load	I_{max}	V_{max}	ID
Delta SM15-200D	MOT	200 A	15 V	QM-00116-3
Delta SM15-200D	Helmholtz/push	200 A	15 V	QM-00116-2
Delta SM30-200	Feshbach	200 A	30 V	QM-00116-4
Delta SM15-400	Shim	400 A	15 V	QM-00116-1
EA PS3065-10B	Zeeman slower	10 A	65 V	QM-00091
Statron 16V/64A	Z push	10 A	65 V	QM-00183-1
EA PS3065-10B	IGBT driver	16 A	64 V	QM-00072-2
Delta 5 U 15-15B	IGBT driver	0.2 A	±15 V	QM-00201

Table 4.5.: List of the power supplies and the corresponding loads. For each power supply, the rated maximum current and voltage is given.

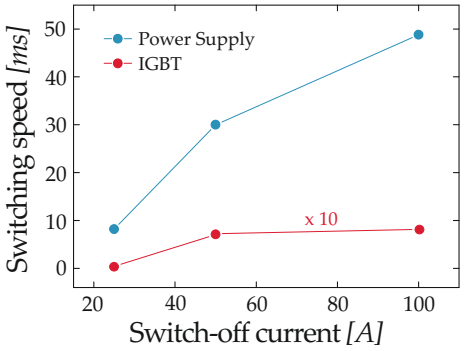

Figure 4.8.: Switching speed obtained with a Delta SM15-200D power supply and an IGBT. The time in ms denotes the duration in which a given current has asymptotically decreased to zero. The time is given as a function of the switched current strength. Regulating currents with the power supply is rather slow compared to the external switching method via an IGBT, which results in switching speeds on the order of 1 kHz. For illustration purposes, the given IGBT times are increased by a factor of ten.

high induction voltages after rapidly switching off coil currents. For the same reason, the coils are equipped with varistors and furthermore fuses to limit the maximum possible current.

Fast switching of IGBTs requires a driver board which provides the appropriate gate voltage and gate current. Therefore, the drivers output stage features an operational amplifier to provide up to 20 V and 3 A. For galvanic isolation, the trigger signals at the input stage are fed through opto-couplers. As a consequence, each IGBT is powered by its own, decoupled power supply.

A hard wired logic realizes the correct triggering of the various IGBTs. For switching of the IGBT gate driver, two transistor-transistor logic (TTL) signals to are connected to a comparator (AND) module. The combination of both allows us to address each IGBT separately, and also to change the configuration of an h-bridge. When an h-bridge realizes a certain current direction, the corresponding IGBTs are controlled in pairs. Therefore, neither the bypassing of current nor an unintentional powering of more than one coil is possible.

Safety measures are realized by an interlock system which is based on a field programmable gate array (FPGA) combined with a real-time processor[1]. It employs fifteen temperature sensors, water flow meters and leak sensors to control the cooling system. Visual feedback and control is maintained with a LabView based graphical user interface (GUI).

4.7. Thermal Stability

Many optical components of the experimental setup, particularly the squeeze dipole trap and the 1D optical lattice, are constant thermal environment. Only then, constant atom numbers, high transfer efficiencies, and a reliable preparation of a single 2D atomic cloud is possible.

Despite an optimal cooling of the magnetic coils, the dissipated heat of the coils and the power supplies cause the experiment to be fully thermalized only after a few hours of operation. This long time-scale was significantly reduced by implementing a pre-heater to the water supply of the Feshbach coils and the Zeeman slower. Together with an additional active heat shield on the lower surface of the optical table of the experiment, the temperature stability was significantly improved.

The pre-heater consists of three separate water circuits with PI controls and copper heat exchangers, each powered by 900 W heating foils. The heater unit is secured with its own water leakage sensors, sensors connected to the global interlock system, and several temperature sensitive circuit breakers. A timer switch starts the heating procedure four to five hours prior to the beginning of the experiments. The temperature of the Feshbach- and the Zeeman slower coils is increased to 30 °C and the surroundings thermalize.

[1] National Instruments, www.ni.com, CompactRIO chassis 9114 and controller 9022.

During operation, a water cooled heat shield prevents the various power supplies below the optical table to heat the table which otherwise causes significant temperature fluctuations of $\pm 1\,°C$ on the table surface. The heat shield consists of a water cooled intermediate ceiling covered with a $12\,\mu m$ aluminium foil. This reduces the temperature increase on the table surface by a factor of two and thus makes temperature fluctuations negligible. A constant temperature difference of $12\,°C$ in respect to below the table is maintained and we obtain thermally stable operation of the apparatus in approximately one hour.

Part II.

Results

5. Critical and Sound Velocity in 3D Fermi Gases

This chapter supplements work reported in the following publication: W. Weimer, K. M., V. P. Singh, J. Siegl, K. Hueck, N. Luick, L. Mathey, and H. Moritz, "The critical velocity in the BEC-BCS crossover", see Ref. [80], and closely follows the presentation therein. The discussion can be found in greater detail in the Thesis of W. Weimer [29].

Frictionless flow of charged or neutral particles is one of the most striking macroscopic phenomena arising from quantum physics. Its appearance is remarkably widespread, ranging from superconductivity in solids to superfluidity in liquids and dilute gases with flow of either bosonic or fermionic particles. Here, we map out the critical velocity in the crossover from BEC to BCS superfluidity with ultracold ^{6}Li gases by moving a small attractive potential along lines of constant column density. In the same samples, we measure the speed of sound v_s by exciting density waves and compare the results to the measured values of v_c. We perform numerical simulations in the BEC regime and find very good agreement, validating the approach.

Section 5.1 briefly motivates and relates our results to previous work. The measurement procedure, our results, and simulations are presented in Sec. 5.2 The conclusion is given in Sec. 5.3.

5.1. Motivation and Previous Work

For technological applications, stability against thermal fluctuations or external perturbations is crucial. The corresponding quantities, i. e. critical temperature and critical velocity, are typically highest in the strongly correlated regime, where the interactions stabilizing the many-body state are particularly strong. Attaining a full understanding of the underlying microscopic mechanisms in this regime is one of the major challenges of modern physics. Ultracold atomic gases have emerged as an excellent platform to study the influence of microscopic physics on macroscopic observables [8,81–85]. Frictionless flow of charged or neutral particles is one of the most striking macroscopic phenomena arising from quantum physics. Here, we explore the stability of superfluids against external perturbation in the crossover from Bose-Einstein condensation (BEC) of composite bosons to BCS pairing of fermions. An obstacle consisting of a small attractive potential is moved through an oblate su-

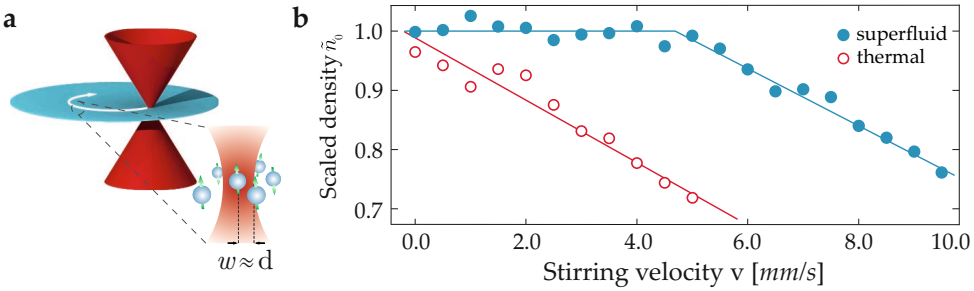

Figure 5.1.: A red detuned laser beam with waist w moves through the cloud with velocity v, where the obstacle size is on the order of the inter-particle separation d (inset). After stirring, the column integrated density $\tilde{n}_0(v)$ at the centre of the cloud is reduced for $v > v_c$ compared to the unperturbed value, indicating heating. For a superfluid gas (blue circles), the critical velocity v_c can be determined from a bilinear fit (blue line) and in a thermal cloud (red circles and line), no critical velocity can be observed. The data is acquired at $B = 806\,G$, $a = 13500\,a_0$ with $\tilde{n}_0 = 1.11\,\mu m^{-2}$, $N = 6100$ for the superfluid.

perfluid gas. Above a critical velocity heating is observed, as shown in Fig. 5.1. For a point-like weak perturbation, the Landau criterion $v_c = \min_p(\epsilon(p)/p)$ makes the direct connection between the critical velocity v_c as a macroscopic observable and the microscopic excitations of the system with energy $\epsilon(p)$ and momentum p. One source of heating is the excitation of phonons. For these excitations, the Landau criterion predicts that the critical velocity equals the sound velocity v_s, which can be calculated within the Bogoliubov approximation for a weakly interacting Bose gas. Consequently, we measure v_s as well by exciting and tracking density modulations. The obtained results are compared to the critical velocities. In the strongly correlated regime, where theoretical predictions only exist for the speed of sound, our measurements of v_c provide a testing ground for theoretical approaches.

Previously, v_c has been measured in ultracold Bose and Fermi gases. Three-dimensional [86] and two-dimensional [85] weakly interacting BECs were probed with moving repulsive obstacle potentials and critical velocities of 110 % and 60 % of the Bogoliubov sound velocity were found. It is expected that vortex excitations limited v_c [87] since the healing length was much smaller than the obstacle size. In Fermi gases, v_c was determined in the BEC-BCS crossover by subjecting the cloud to a moving optical lattice [88]. A comparison with theory was performed at the universal point yielding $v_c \approx 70\,\% v_s$. The precise microscopic excitation mechanism is not fully understood yet, but theoretical analyses [89–91] suggested that it is quite different from the one relevant in our measurements. In the crossover, v_s was measured as well [92–94]. However, in those experiments no comparison to v_c was made.

5.2. Experiment

Due to the high optical resolution and low densities achieved in our apparatus, it is finally possible to manipulate and probe superfluids on their intrinsic length scales. The obstacle size is on the order of the healing length in the BEC regime, the coherence length in the BCS regime, and the inter-particle separation in the crossover.

We prepare ^{6}Li atoms with mass m in a balanced mixture of the two lowest hyperfine states with a similar procedure as described in Ref. [95]. Ultimately, the atoms are trapped in a highly elliptical optical dipole trap with a beam waist of $10\,\mu m \times 370\,\mu m$ and a wavelength of 1064 nm. Typical trap frequencies are $\omega_z \approx 2\pi \cdot 550\,Hz$ and $\omega_r \approx 2\pi \cdot 30\,Hz$ in the vertical and radial direction. The radial confinement is mainly caused by the curvature of a radially symmetric magnetic field. We adjust the final evaporation to obtain a constant line of sight integrated central density of $\tilde{n}_0 = (1.15 \pm 0.05)\,\mu m^{-2}$ per spin state. Depending on the interaction strength, this corresponds to a total atom number N of 2500 to 14 000 per spin state. We estimate the systematic errors on atom numbers and densities to be approximately $\pm 20\,\%$.

Although the vertical confinement dominates, effects caused by reduced dimensionality are negligible since $E_F/\hbar\omega_z > 4.2$ in all measurements, where the Fermi energy E_F and wavevector k_F are defined as $E_F = \hbar^2 k_F^2/2m = \hbar(\omega_r^2\omega_z \cdot 6N)^{1/3}$. A measure for the temperature T is provided by the observed condensate fractions in the BEC regime of approximately 80 %. Since we observe no significant heating during magnetic field ramps, we use the theory in Ref. [96] to estimate the temperature in the BCS regime, yielding values of $T/T_F \approx 7\,\%$.

5.2.1. Measurements

In the actual stirring experiment, a red-detuned laser beam forms an attractive potential. This obstacle traces out a circular trajectory with speed v and radius $r = 10\,\mu m$ along lines of constant column density $\tilde{n}(r) \approx \tilde{n}_0$ within the superfluid core.

The beam has a wavelength of 780 nm and is focused to a waist w of $2.4\,\mu m \times 1.9\,\mu m$, a size comparable to the interparticle distance $d = n^{-1/3} \approx 1.5\,\mu m$ at unitarity. The relative column integrated density increase in the focus is approximately 85 %. The corresponding beam powers were adjusted depending on the interaction strength.

The stirring sequence proceeds as follows: first, the scattering length a is set to the desired value by ramping the magnetic field to a value between 750 G and 890 G close to a broad Feshbach resonance, followed by 50 ms thermalization time. Next, the power of the moving obstacle beam is linearly ramped up within 10 ms and the gas is stirred for 200 ms before the power is linearly ramped down in 5 ms. After 100 ms thermalization time the magnetic field is ramped to 680 G in 100 ms and an in-situ absorption image of the atoms is

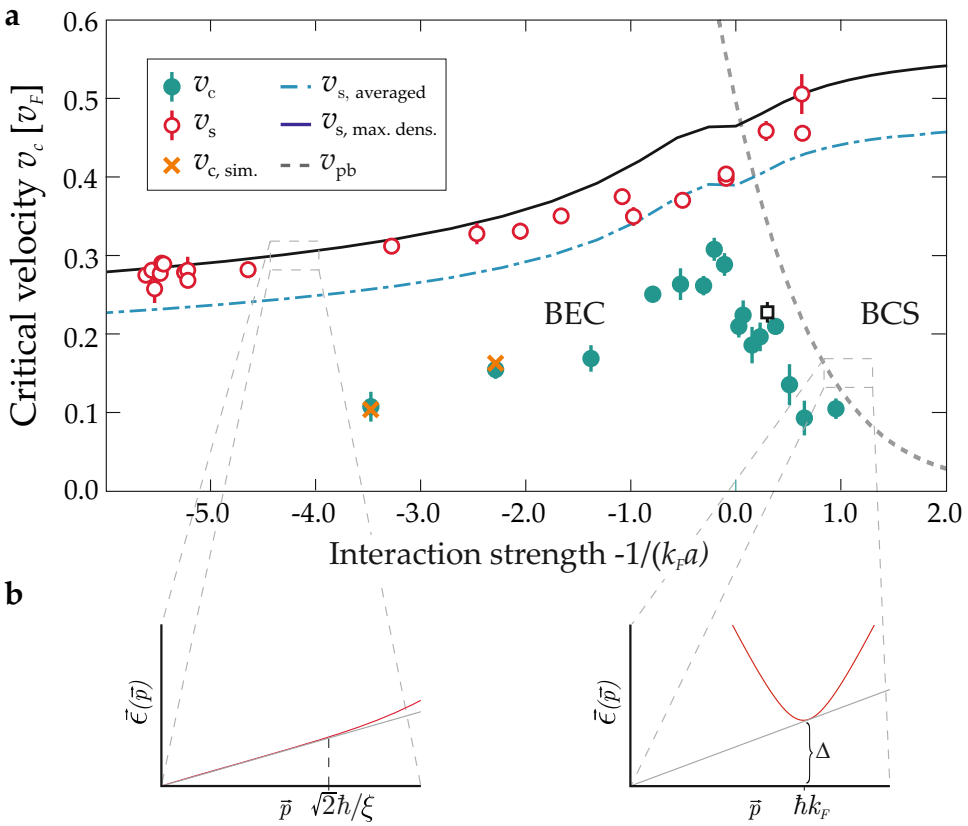

Figure 5.2.: a) Critical velocity v_c (green filled circles) and speed of sound v_s (red open circles) in units of the Fermi velocity v_F throughout the BEC-BCS crossover. The error bars correspond to the fit errors. A statistical error for v_c (black open square) was determined from five measurements. The simulated critical velocities are marked with crosses. The solid (dot-dashed) curve is the theory prediction for v_s assuming that the maximum (column averaged) density is relevant for sound propagation, see main text. The pair breaking velocity v_{pb} providing an upper bound for v_c in the BCS regime is plotted with a dashed line. b) Dispersion relations for the BEC and the BCS limiting cases (red) and the tangent to this curve from the origin to visualize the Landau criterion (grey).

acquired.

This sequence is typically repeated ten times for each speed v and extract the radially averaged and line of sight integrated density distribution $\tilde{n}(r)$ from the mean of those datasets, accounting for optical saturation effects [97]. Since the gas is well in the BEC regime at the time of imaging, we determine the central column density $\tilde{n}_0(v)$ as well as the condensate fraction from a bimodal fit. Heating is indicated by a reduction in either, yet $\tilde{n}_0(v)$ is the more robust measure since evaporation upon heating can occur in our trap of finite depth.

We observe a significant reduction in $\tilde{n}_0(v)$ and hence heating only above a threshold velocity which we identify with the critical velocity as shown in Fig. 5.1. The exact value is obtained from a fit with a continuous bilinear function [88]. It has a constant value of $\tilde{n}_0$ below v_c and decreases linearly above, see blue line in Fig. 5.1. The figure also shows that stirring within the thermal region of the cloud leads to heating for all obstacle speeds.

The critical velocities for different interaction strengths $-1/(k_F a)$ throughout the whole BEC-BCS crossover and far into the BEC regime is determined and plotted in units of the Fermi velocity v_F in Fig. 5.2 a. Qualitatively, the data shows a maximum of v_c close to $1/(k_F a) = 0$ and a decrease towards the BEC and the BCS side of the resonance, in agreement with Ref. [88]. The absolute values range between $1.7\,\mathrm{mm\,s^{-1}} \leqslant v_c \leqslant 6.3\,\mathrm{mm\,s^{-1}}$.

For comparison we also measure the speed of sound v_s by creating a small density excess in the centre of the gas, releasing it and tracking the maximum of the outgoing circular density wave. Here, the stirrer beam is placed at the centre of the gas, its power is adiabatically raised to values between $7\,\mu\mathrm{W}$ and $40\,\mu\mathrm{W}$ in $100\,\mathrm{ms}$ and suddenly switched off.

5.2.2. Results and Discussion

Our main results are shown in Fig. 2: they consist of measurements of v_c, v_s, and a detailed comparison with theory in the entire crossover. The results for v_s are in very good agreement with the theoretical prediction. In the BEC regime, the critical velocity is found to be significantly smaller than v_s but in excellent agreement with numerical simulations. The simulations take all experimental details into account and allow us to determine the origins of the reduction. Having validated the method in the BEC regime, our results in the strongly correlated regime may provide valuable benchmarks for theory. In the BCS regime, pair-breaking excitations are expected to limit v_c and our results are in qualitative agreement.

To compare the experimental results with theoretical predictions, it is convenient to consider three regimes, the BEC, the strongly correlated regime, and the BCS regime. In the latter ($-1/(k_F a) > 1$), superfluids are formed from loosely bound Cooper pairs. The excitation spectrum is sketched in the r. h. s. of Fig. 5.2 b. Pair breaking excitations limit the critical velocity to

$m v_{pb}^2 = \left(\Delta^2 + \mu^2\right)^{1/2} - \mu$ [98].

The pair breaking velocity v_{pb} is plotted as the dashed line in Fig. 5.2 a, where we determined the gap Δ and the chemical potential μ at $T = 0$ by solving the mean field gap the number equations numerically [9, 99]. The curve can be extended into the strongly correlated regime, where no simple theoretical description exists. Here, the mean field approach can at least provide a rough estimate for v_c and our data appears to be in qualitative agreement. We expect temperature effects to be small since $T/T_c < 0.5$ [100].

Before discussing the strongly correlated regime in depth, which is theoretically largely inaccessible and hence particularly interesting, we benchmark our experiment against theory. In the BEC regime ($-1/(k_F a) < -1$), the gas forms a molecular BEC of tightly bound dimers. Within Bogoliubov theory the dispersion relation is linear at low momenta with a slope v_s, see l. h. s. of Fig. 5.2 b, and v_c should equal v_s. The measured sound velocities are in very good agreement with the two theoretical predictions shown in Fig. 5.2 a. When the sound wavelength is large compared to the vertical extent of the cloud, the wave effectively probes the column averaged density (dot-dashed line), provided the gas is fully hydrodynamic [101–103]. Otherwise, the wavefront observed should be the one travelling with the speed determined by the maximum density along the z-direction (solid line).

Since the gas is only partially hydrodynamic in the vertical direction, we expect the experimental data to lie between the two curves. We note that the measurements of v_s presented here probe a new regime since all previous experiments determining v_s were performed in prolate gas clouds [92–94] described by effectively one-dimensional hydrodynamics [101–103].

The theory curves for v_s are obtained by taking thermodynamic derivatives [104] of the equation of state calculated in numerically exact zero-temperature quantum Monte Carlo simulations[1] [105]. The homogeneous theory is applied using the local density approximation: the density distribution in the trap, given by the equation of state, is used to calculate k_F and v_F of the corresponding trapped clouds[2].

Temperature effects should be small since the temperatures in the experiment are smaller than the mean field energy in the BEC regime and the Fermi temperature in the BCS regime [106].

We now turn to the strongly correlated regime. Due to the lack of a small parameter, perturbation theories are inaccurate and the quasi-particle description breaks down. Hence, the velocities v_s and v_{pb} associated with phonon creation and Cooper pair breaking excitations can only provide upper limits for v_c. We are not aware of a prediction for v_c, even at the universal point where $|a| \to \infty$.

[1] The change of slope at $1/k_F a = 0$ is an artefact of the parametrization used to approximate the QMC data analytically.

[2] Please note that the commonly accepted definition of k_F used also here is not trivially connected to the density.

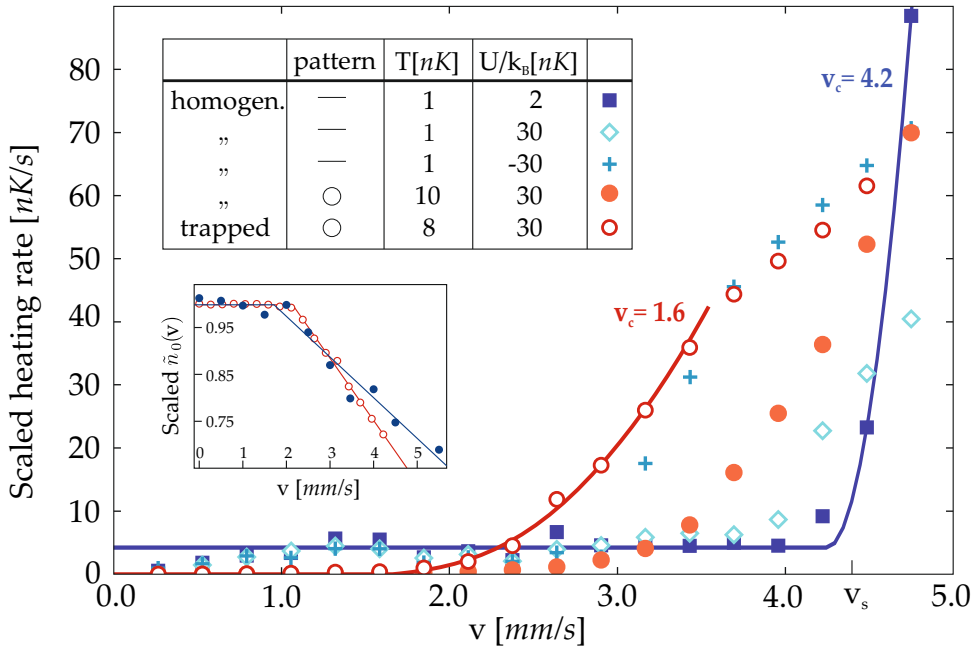

Figure 5.3.: Simulated heating rates normalized by the stirrer depth U^2. The complexity is gradually increased: blue squares depict the idealized case of a very cold homogeneous sample stirred with linear pattern. The relative density excess η in the weak stirrer potential $U = k_B \cdot 2\,\mathrm{nK}$ is only 3 %. For all datasets, the Bogoliubov result for v_s is $4.4\,\mathrm{mm\,s^{-1}}$. The red open circles depict a simulation of the experimental case: a trapped sample is stirred circularly with a stirrer of realistic depth. A lower temperature is chosen for technical reasons. Here, the y-axis scaling factor is one. In the inset, the results for the heating observed in the central column density $\tilde{n}_0(v)$ are compared. We find very good agreement between the experimental (blue filled circles) and the simulated results (red open circles). The bilinear fits to extract v_c are shown with solid lines. In the inset $U = k_B \cdot 35\,\mathrm{nK}$.

The largest value for v_c we observe is $v_c = 0.31(2)\,v_F$, close to the universal point, see Fig. 5.2. Reference [88] found a value of $v_c = 0.31\,v_F$ using a different excitation mechanism. These values are considerably smaller than the corresponding $v_s \approx 0.40(1)\,v_F$ we measure and the theory prediction $v_s = \xi_B^{1/4}/\sqrt{3}\,v_F = 0.45\,v_F$[1] [9] employing the local density approximation.

Very recently, a critical velocity of $v_c = 0.42^{+0.05}_{-0.11}\,v_F$ was observed in an elongated ^{6}Li gas oscillating with respect to a ^{7}Li BEC [107]. Here, the onset of heating is predicted to occur for a relative velocity that equals the sum of the individual sound velocities [108].

5.2.3. Simulations

In order to understand the critical velocity in the BEC regime, we perform simulations and identify the factors reducing v_c. These are the finite temperature, the inhomogeneous density profile along the strongly confined direction, the circular instead of linear motion of the stirrer, and to a lesser degree the finite depth of the obstacle potential. We use a classical field method, which is the limiting case of the truncated Wigner method used in Ref. [109]. The time evolution of an ensemble of complex-valued fields is calculated using classical equations of motion. The initial states are generated from a grand canonical ensemble via a classical Metropolis algorithm. We employ a real-space representation on a lattice with $60 \times 60 \times 3$ ($140 \times 140 \times 11$) sites for the simulation of homogeneous (trapped) systems. The discretization length is $1\,\mu m$.

All simulations are performed with the same stirring time, stirrer beam size, dimer-dimer scattering length $a_{DD} = 0.6 \times 3634\,a_0$, and density $n_{3D} = 0.486\,\mu m^{-3}$ (and column density in the trapped case) as the experimental data point at $-1/k_F a \approx -3.5$. When choosing all remaining parameters, i. e. temperature, confining potential, stirrer depth, and motion in accordance with the experiment, we reproduce the experimentally measured v_c. To disentangle the various features of the system that influence these measurements, it is instructive to start with an idealized case: a homogeneous gas at a low temperature of 1 nK, stirred along a linear path. In this case, the heating rate increases steeply at a critical velocity which is approximately v_s as shown in Fig. 5.3.

To determine v_c, the fit function $A \cdot \left(v^2 - v_c^2\right)^2 / v + B$ is used for $v > v_c$ [110], with the free parameters A, B and v_c. The simulated heating rates are in good agreement with the second order perturbation theory that predicts a scaling with U^2. Moreover, by increasing the stirrer depth U, we observe that the extracted v_c is slightly reduced.

These results demonstrate that we work with relatively weak perturbations and that vortex excitations do not limit v_c [87], in contrast to previous ex-

[1] The Bertsch parameter $\xi_B = 0.37$ is determined in [51, 54].

periments in 3D [86] and 2D atomic BECs [85]. The simulations also show that attractive stirrer potentials are preferable to realize a stirrer. For larger repulsive potentials [85,86] the inherent density reduction strongly reduces the observed critical velocity as shown in Fig. 5.3.

Next, the effects of the finite experimental temperature and of the circular motion of the stirrer are investigated. The simulations show that both features reduce v_c by approximately 15 %. Having both present simultaneously causes a small further reduction of v_c. The reduction at finite temperature might be due to vortex-antivortex excitations, or rotonic precursors of them. As the temperature is increased above the mean field energy, density fluctuations increase and vortices can nucleate at points of minimal density. That the circular motion can reduce v_c can be seen in perturbation theory performed in momentum space: here, the motion of the perturbation consists of a distribution of velocities rather than a single velocity.

Finally, we perform a simulation of an inhomogeneous system in a trap, with a realistic temperature and a circular stirring motion. The simulated critical velocity of $1.6(1)$ mm/s agrees excellently with the experimentally measured value of $1.7(3)$ mm/s, see Fig. 5.2. We believe that the additional reduction of 39 % with respect to the homogeneous simulation result is mainly due to probing lower density regions along the stirrer axis. The results for the central column densities are in good agreement as well, see inset of Fig. 5.3, considering the experimental signal to noise.

5.3. Conclusion

In conclusion, we have demonstrated the breakdown of superfluidity due to moving obstacle across the BEC-BCS transition, for the first time in close analogy to Landau's Gedankenexperiment. We compare the results with theoretical predictions throughout and achieve quantitative understanding in the BEC regime by performing numerical simulations. Pointlike defects also play a role in strongly correlated high temperature superconductors. The experiment presented here provides the opportunity to isolate relevant effects in a very clean and controllable environment. Of particular interest for future studies are strongly correlated two-dimensional superfluids.

6. Theory of 2D Fermi Gases

The high degree of recent experimental and theoretical interest in 2D Fermi gases stems from the fact that their physical properties are strikingly different from the 3D case. As a consequence, 2D Fermi gases remain one of the least understood interacting many-body systems. Theoretical predictions for the 2D BEC-BCS crossover are rare and sometimes even contradictory.

The purpose of this chapter is twofold. First, we present and discuss the peculiar physics of strongly confined quantum gases. Second, we introduce the available theory aiming to describe these systems. This lays the foundation for the benchmark against the experimental results given in Ch. 7.

In Section 6.1, we focus on the particularly different scattering behaviour in true and quasi-2D gases. Following basic arguments we demonstrate the absence of a 2D BEC in Sec. 6.2. Instead, there is the BKT phase transition which replaces condensation in 3D gases. The qualitative difference to the physics in 3D systems is the increased importance of phase fluctuations, who are in the focus of Sec. 6.3. Sec. 6.4 summarizes the progress of theory and compares different predictions of the 2D BEC-BCS crossover.

6.1. Scattering Problem

One of the striking properties of 2D quantum gases is the drastically changed collisional behaviour. In contrast to the 3D and 1D case, where collisions are entirely defined by the s-wave scattering length and the particle mass, planar scattering behaviour depends on the relative momentum.

Due to its profound importance for the understanding of 2D quantum gases, we discuss the scattering problem in some detail. First, we examine the homogeneous system, then we discuss the quasi-2D case of realistic experiments, where scattering is dominantly determined by the confinement strength of the trapping potential perpendicular to the 2D plane. We emphasize the characteristic features and point out where divergences occur. Parts of this chapter follow the discussion in Ref. [39, 111].

6.1.1. Genuine 2D Fermi Gases

We consider an equal mixture of a two-component gas of fermions in the theoretical case of a purely 2D geometry. Our first task is to model the interactions in a convenient way. Although it is tempting to proceed similarly to the case of a 3D system, i. e. by introducing a contact potential and formulating a

coupling term $g\delta(\mathbf{r})$ for the contact interaction, it is in general not possible to describe 2D interactions in this simple fashion. The collisional processes are more involved and thus we cannot directly transpose the formalism from 3D to lower dimensions. We have to turn to an energy dependent coefficient, as we will see in this section.

To give a conclusive outlook let us summarize the main results of the following discussion.

- We consider low energy s-wave scattering and choose an ansatz consisting of an incoming plane wave and an outgoing circular wave to solve the s-wave Schrödinger equation.
- The solution of the Schrödinger equation logarithmically diverges for small energies $k \ll 1$. As a consequence, the interaction is always repulsive in contrast to the 3D case with repulsive and attractive interaction.
- Analogous to the 3D case, the optical theorem yields the scattering cross section σ. While in the limit of small energies $k \to 0$, the 2D cross section tends to infinity $\lim_{k\to 0} \sigma = \infty$, the 3D cross section tends to a_{3D}^2.
- Using the partial wave expansion we find the phase shift of scattered s-waves to express the scattering amplitude $f(k)$. For $k \to 0$, the 2D scattering amplitude tends to zero, whereas in the 3D case, $f(k)$ approaches minus the 3D scattering length $-a_{3D}$.

Schrödinger Equation of Relative Motion In general, the low-energy scattering is described by the scattering amplitude for elastic collisions and the scattering cross section. The starting point to obtain both quantities is the 2D Schrödinger equation for two particles interacting via an isotropic short-range local potential $V(\mathbf{r})$ at an energy E [39, 112]. The centre-of-mass and the relative motion are separable and the former drops out of the scattering problem, simplifying the formalism. The Schrödinger Equation of relative motion reads

$$-\frac{\hbar^2\nabla^2}{2m_r}\Psi(\mathbf{r}) + V(\mathbf{r})\Psi(\mathbf{r}) = E\Psi(\mathbf{r}), \tag{6.1}$$

where the reduced mass of two particles of identical mass is $m_r = m/2$. We assume that the interaction potential only depends on the interparticle distance $r = |\mathbf{r}|$, where $\mathbf{r}$ is the relative coordinate of the two scatterers.

The evaluation of the 2D collisional problem requires that the range of the scattering potential $V(r)$ decays sufficiently fast. For alkali atoms, this is fulfilled since the effective potential range R is approximately described by the van der Waals tail of the potential $V(r) \approx -C_6/r^6$. At distances $r \gg R$, there is

no noticeable contribution of the potential so that we can omit the interaction and the relative motion is free[1].

A suitable wavefunction ansatz $\Psi(\mathbf{r})$ solves Eq. 6.1. At interparticle distances in the asymptotic limit $r \to \infty$, the scattering state, i. e. the wavefunction of colliding atoms, is a superposition of the incident plane and scattered circular wave

$$\Psi(\mathbf{r}) \approx e^{i\mathbf{kr}} - f(k,\theta)\sqrt{\frac{i}{8\pi k}}\frac{e^{ikr}}{\sqrt{r}}, \tag{6.2}$$

where $\mathbf{k}$ is the incident wave vector and the wave is defined by $E = \hbar^2 k^2/(2m_r)$. The amplitude of the scattered wave $f(k,\theta)$ is the scattering amplitude. θ denotes the angle between the direction of the incoming and the scattered wave. For convenience, we restrict this discussion to forward scattering assuming $\theta = 0$. The pre-factor $\sqrt{i/(8\pi k)}$ accounts for the conservation of the probability density of the outgoing circular plane wave in 2D.

Since the effective range R of the interaction potential is much shorter than the average interparticle spacing $1/k$ and the thermal de Broglie wavelength λ_{dB}, we consider the interaction to be effectively a contact interaction. The scattering amplitude at low energy is dominated by the contribution from the isotropic s-wave scattering.

Low-Energy Wavefunction Before we deduce the scattering amplitude and its connection to the scattering cross section, we can already identify characteristic properties from the low-energy wavefunction.

The scattering potential is assumed to be isotropic, hence we can separate the
Schrödinger equation 6.1 into the radial and angular part. The former is decomposed into separate equations for each quantum number l of the angular momentum. To find the s-wave scattering amplitude $f(\mathbf{k})$ one has to solve the $l = 0$ Schrödinger equation 6.1 for the relative motion. In the limit where $r \gg 1/k$ and $r \gg R$, the solution is the s-wavefunction

$$\Psi_s(k,\mathbf{r}) = J_0(k|r|) - \frac{i\,f(k)}{4}H_0(k|r|). \tag{6.3}$$

The outgoing wave is described by the Bessel function J_0 and the Hankel function H_0. From the asymptotic behaviour of the Hankel function we can already infer a meaningful characteristic feature of the 2D scattering problem: for distances $r \gg R$ and vanishingly small energies $k \ll 1$, the Hankel function, and thus the whole wavefunction, diverges logarithmically.

In this case, the free relative motion is basically free and the wavefunction is $\Psi_s \propto \ln(r/a)/\ln(1/ka)$. Here, $a > 0$ is a characteristic constant of dimension

[1] A Coulomb type potential $\propto 1/r$, for instance, would prevent the definition of a characteristic length scale R, because one cannot find a spatial region in which the strength of the interaction potential is significantly lowered.

length that depends on the detailed shape of the potential $V(\mathbf{r})$ and can be identified with the scattering length.

The probability density $|\Psi_s(k)|^2$ of finding two atoms at a given separation always increases with r, as the condition $r > a$ is always reached. This is only different in the case of an existing bound state for very large scattering lengths $a \to \infty$.

This means, as a direct consequence of the 2D kinematics particles favour to be separated, i. e. they repel each other. This exclusively repulsive interaction is fundamentally different from the 3D case, where both attractive and repulsive interaction is possible.

Scattering Cross Section We consider the 2D total scattering cross section, which is the area of dimension length in which two colliding atoms interact

$$\sigma(k) = \frac{1}{k}\mathrm{Im}\, f(k,0) \tag{6.4}$$

$$= \frac{|f(k)|^2}{4k}. \tag{6.5}$$

Equation 6.4 is the well-known optical theorem, relating the forward scattering amplitude to the total cross section of the scatterer[1]. Due to flux conservation, the imaginary part of the scattering amplitude depicts the change in flux from the incoming plane wave. In other words, the cross section denotes the amount by which the forward probability current is lessened by a scattering event.

Even without an exact expression for the scattering amplitude, we immediately see that for $k \to 0$ the cross section in Eq. 6.5 tends to infinity

$$\lim_{k\to 0} \sigma = \frac{|f(k)|^2}{4k} \to \infty. \tag{6.6}$$

This is different to the situation in 3D, where $\sigma(k \to 0)$ asymptotically approaches a constant value $\sim a_{3D}^2$.

Scattering Amplitude To find the dimensionless scattering amplitude, we decompose the wavefunction of the incident and the scattered state into separate waves for each quantum number l, which is the partial wave expansion[2]. The scattered states experience a phase shift $\delta_l(k)$ relative to the incoming wave at distances larger than the potential range. Generally, outside the potential range, the solution of the Schrödinger equation will be a superposition of all these partial waves.

[1] Generally, the total cross section is $\sigma(k,\theta) = \frac{1}{8\pi k}\int d\theta\, |f(k,\theta)|^2$ and the differential cross section $d\sigma/d\theta = |f(k)|^2/(8\pi k)$.

[2] The partial wave expansion for the scattering amplitude is $f(\mathbf{k}) = \Sigma_{l=0}^{\infty}(2-\delta_{l0})\cos(l) f_l(k)$. The Kronecker delta δ accounts for the degeneracy within the partial wave and should not be confused with the phase shift [113].

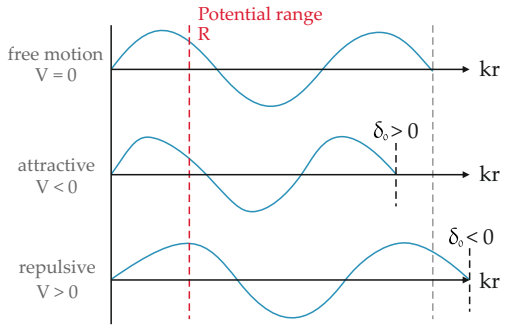

Figure 6.1.: Sketch of the phase shift of a scattered wavefunction outside the scattering potential. The dashed red line depicts the effective potential range R. In case of an attractive potential $V < 0$, the scattered state experiences a phase shift $\delta_0 > 0$ with respect to the unperturbed wave ($V = 0$). For $V > 0$, i. e. for repulsive interaction, a phase shift of the opposite direction $\delta_0 < 0$ occurs.

In the low energy limit of s-wave scattering one considers the first $l = 0$ term in the expansion and compare the general wavefunction 6.2 with the partial wave to identify

$$f(k) = \frac{4}{i - \cot \delta_0(k)}. \tag{6.7}$$

Thus, the scattering amplitude is related to the phase shift of the s-wave. In the limit $r \gg R$, the only effect of the scattering potential is to retard the wave by a fixed phase shift so that the spherical wave fronts are shifted in regard to the unperturbed plane wave, see Fig. 6.1.

An effective range expansion of $\cot \delta_0(k)$ yields the low energy behaviour [111, 112, 114]

$$\cot \delta_0(k) = \frac{2}{\pi} \ln(ka) + O(k^2). \tag{6.8}$$

With this, the scattering amplitude is [8, 39]

$$f(k) = \frac{2\pi}{\ln(ka) + i\pi/2}. \tag{6.9}$$

In the limit of small energies, the 2D scattering amplitude tends to zero, $\lim_{k \to 0} f(k) = 0$. This contrasts the behaviour in 3D, where the scattering amplitude at zero energy equals the negative scattering length $-a_{3D}$. This low-energy behaviour has important consequences which are summarized below.

- The energy region where $k \approx 1/a$ corresponds to the resonance with a peak in $|f(k)|$, which decreases with increasing or decreasing k. The

scattering rate peaks accordingly[1]. In this case are both, the real and imaginary part of $f(k)$ important. Since the resonance behaviour is of logarithmic scale, the decrease in α by a factor of 2 requires the energy $E(k)$ to change by factor of 20.

- When $ka \gg 1$, the scattering amplitude is real and negative and its magnitude increases with decreasing k.
- In the opposite limit, where $ka \ll 1$, we may omit the imaginary part in Eq. 6.9. The scattering amplitude becomes real and positive and increases with increasing k. Interestingly, the denominator in Eq. 6.9 diverges logarithmically at low energies, and thus the definition of the scattering length becomes ambiguous[2].

For weak interactions, due to Pauli blocking, only atoms at the Fermi surface contribute. The coupling strength can then be parametrized by the mean-field parameter

$$\tilde{g}_{MF}^{2D} = -\frac{4\pi\hbar^2/m}{\ln(k_F a_{2D})}. \tag{6.10}$$

The limit of zero interaction corresponds to $a_{2D} \to \infty$, different to the 3D case where an infinite scattering length denotes the regime of strongest interaction. In the mean field approximation of the 2D case however, the regime of strong interaction arises for $\ln(k_F a_{2D}) = 0$. In the strongly interacting regime the mean field expansions in powers of $1/\ln(k_F a_{2D})$ breaks down.

6.1.2. Quasi-2D Fermi Gases

Under realistic experimental conditions, the atomic motion in a 2D system is not strictly planar and we refer to the gas as a quasi-2D system.

In order to realize a quasi-2D quantum gas, the motion along one direction has to be frozen out. This is typically realized with a 1D optical lattice, where in the other two directions the atoms are much more weakly and in all experiments so far harmonically trapped. The energy level spacing in the strongly confined direction z exceeds the Fermi energy and therefore all relevant energies are well below the excitation energy from the ground state to the first excited state $E_F, k_B T \ll \hbar\omega_z$, where ω_z is the confinement frequency in z-direction.

[1] The rate α equals the intensity of the scattered wave times a pre-factor. The average of $\alpha(k)$ over the momentum distribution of atoms, multiplied by the number of atom pairs in a unit area, gives the number of scattering events in this area per unit time.

[2] In fact, a definition different to Eq. 6.8 for the 2D scattering length can be found in the literature. The widely used $a_{2D} = \frac{a}{2}e^{\gamma}$ stems from the collisions between hard discs with radius a, see Ref. [39].

The extension of the gas perpendicular to the quasi-2D plane remains finite and the third dimension still plays a role as the particles exhibit zero-point motion in the confined direction. However, the strong confinement introduces a new length scale, the harmonic oscillator length $l_z = \sqrt{\hbar/m\omega_z}$, which is typically much larger than the range of the van der Waals type interactions R. Therefore, when $r \ll l_z$, i. e. for short range two-body interaction, the wavefunction of colliding atoms is determined by 3D scattering potentials. Even when the gas is energetically and predominantly kinematically 2D, the collisional dynamics remain governed by 3D properties and the 3D scattering length never becomes irrelevant.

Schrödinger Equation for the Relative Motion We consider a harmonic potential $V(z) = \frac{1}{2}m\omega_z^2 z^2$ in the direction perpendicular to the 2D plane. Again, the centre-of-mass motion and the relative motion are separable and the non-interacting two-body problem in relative coordinates reduces to the harmonic oscillator equation

$$-\frac{\hbar^2\nabla^2}{m_r}\psi(\mathbf{r}) + (V(r) + V(z))\psi(\mathbf{r}) - \frac{\hbar\omega_z}{2}\psi(\mathbf{r}) = E\psi(\mathbf{r}), \tag{6.11}$$

which is satisfied by the wavefunction of the relative motion $\psi(\mathbf{r})$ (6.2). The solution of the quasi-2D scattering problem contains two length scales, the characteristic length of the scattering potential a_{3D}, and the extension l_z of the wavefunction in the z-direction.

Scattering Amplitude We limit our attention to the case of short range interactions $R \ll l_z$ and low-energy s-wave scattering where $kR \ll 1$. To determine the quasi-2D scattering amplitude, one can express the solution of the Schrödinger Equation 6.11 through the Green's function and finds [39]

$$f(k) = \frac{4\pi}{\sqrt{2\pi}l_z/a_{3D} - \ln(\pi/B\cdot k^2 l_z^2) + i\pi}. \tag{6.12}$$

Where $B = 0.905$. In the limit $l_z \gg |a_{3D}|$, the vertical extend is much larger than the characteristic scattering length scale. Hence, the influence of the vertical confinement is negligible, the logarithmic term in Eq. 6.12 is unimportant, and the scattering amplitude becomes independent of the energy. Under any other condition, the scattering amplitude is energy dependent regardless of the value of a_{3D}, i. e. there is no unitary limit as in the 3D case. At a fixed ratio a_{3D}/l_z, there is a resonance behaviour in the energy dependence of the quasi-2D scattering amplitude $f(k)$ in Eq. 6.12, as shown in Fig. 6.2. Typically, experiments exploit a different kind of resonance behaviour. While $f(k)$ logarithmically depends on the particle energy and is quite similar to the resonance in 2D, there is an additional power law dependence on the ratio a_{3D}/l_z. For positive scattering lengths $a_{3D} > 0$, this behaviour is shown in Fig.

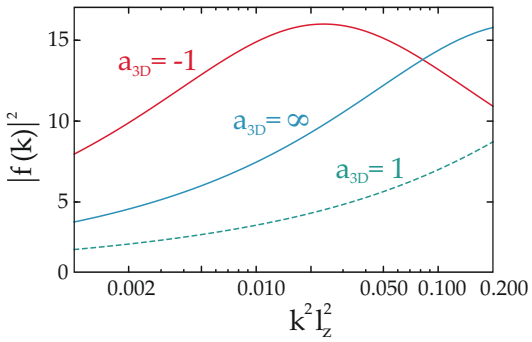

Figure 6.2.: Absolute square of the scattering amplitude $|f(k)|^2$ as a function of $k^2l_z^2$ at fixed ratios a_{3D}/l_z. In the case $a_{3D}/l_z = 1$ and $a_{3D}/l_z = \infty$, there is always $E/E_B \ll 1$ and $f(k)$ increases with k^2. For $a_{3D}/l_z = -1$ there is a logarithmic-scale resonance in the behaviour of $|f(k)|^2$.

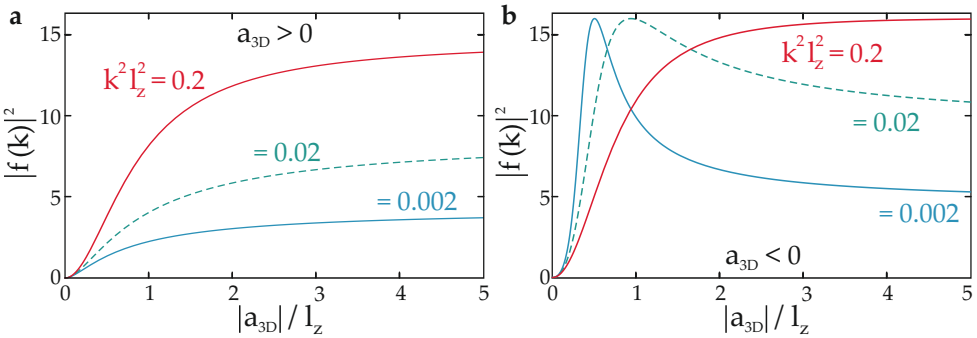

Figure 6.3.: Absolute square of the scattering amplitude $|f(k)|^2$ as a function of a_{3D}/l_z at fixed $k^2l_z^2$. a) For positive scattering lengths $a_{3D} > 0$, $|f(k)|^2$ always increases with increasing ratio a_{3D}/l_z. b) For negative scattering lengths $a_{3D} < 0$, there is a pronounced resonance behaviour as a function up to $k^2l_z^2 = 0.02$.

6.3 a. For $a_{3D} < 0$ and fixed values up to $k^2 l_z^2 = 0.02$, there is a pronounced resonance behaviour as a function of a_{3D}/l_z, see Fig. 6.3 b.

- If the 3D scattering is positive and large, e. g. close to a Feshbach resonance, the logarithmic term in Eq. 6.9 causes a reduction of the scattering amplitude.
- For small positive 3D scattering lengths, $l_z/a_{3D} \gg 1$, the 3D dimer, with a size of $\sim a_{3D}$, fits well within the confining potential and is only weakly influenced by the harmonic confinement[1]. As the scattering length is increased, the 2D features in the relative motion of atoms become pronounced which is described by the logarithmic term in Eq. 6.12.
- For negative a_{3D}, the logarithmic term can lead to a strong increase in the scattering amplitude.
- In the limit of small negative scattering length, $l_z/a_{3D} \ll -1$, the dimer spreads out in the 2D plane and the relative motion of atoms is therefore strongly influenced by the tight confinement.

In summary, there is a subtle difference between resonant scattering which arises from 2D kinematics as in pure 2D systems, and the enhanced scattering that results from the finite extent of the gas in the confined direction.

Scattering Length Comparing the 2D scattering amplitude 6.9 to the scattering amplitude of the quasi-2D case in Eq. 6.12 yields the scattering length [39, 115]

$$a_{2D} = l_z \sqrt{\frac{\pi}{B}} e^{-\sqrt{\frac{\pi}{2}} \frac{l_z}{a_{3D}}}, \tag{6.13}$$

where $B = 0.905$ and a_{2D} has the dimension length. Alternatively, a_{2D} can be found from the binding energy of 3D molecules [116, 117].

Eq. 6.13 is a valid in the BEC regime where $a_{3D} < 0$ and a dimer exists also in the 3D case. However, as long as the confinement strength exceeds the scattering energy, i. e. $k l_z \ll 1$, Eq. 6.13 is a valid approximation in the BCS regime, where no 3D bound state exists. The behaviour of a_{2D} as a function of the magnetic field strength, i. e. of the 3D scattering length is shown in Fig. 6.4.

We define the dimensionless 2D interaction parameter $\ln(k_F a_{2D})$. Positive values correspond to the BCS regime and $\ln(k_F a_{2D}) < 0$ depicts the BEC regime. It is generally assumed that the crossover occurs at $\ln(k_F a_{2D}) = 0$, which is consistent with the mean-field chemical potential $\mu = E_F - E_B/2$ being

[1] In the BEC limit, dimers will always be smaller than the confinement length. They become 3D bosons confined to a quasi-2D geometry.

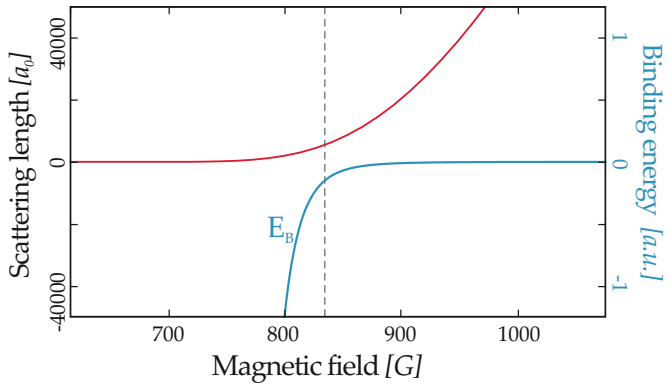

Figure 6.4.: 2D scattering length and binding energy as a function of the external magnetic field. The magnetic Feshbach resonance, which is depicted as the dashed grey line, is located at $B = 834.15\,G$. The s-wave scattering length a_{2D} (red solid line) is exponentially small for magnetic field strengths smaller than the resonance. For higher field strengths, a_{2D} rapidly increases. The molecular binding energy E_B^{2D} is depicted as the solid cyan line. Because a 2D bound state always exists, regardless the sign and strength of interaction, the binding energy is always finite $E_B^{2D} < 0$. On the l. h. s. of the resonance, the binding energy strongly increases.

zero. However, numerical simulations show that the chemical potential in fact vanishes at $\ln(k_F a_{2D}) \approx 0.5$ [40, 118].

The quasi-2D interaction parameter is sensitive to changes in the density n through the Fermi wave vector k_F, and the 2D scattering length, which is usually set by a_{3D}, i. e. through the magnetic Feshbach resonance. Thus, changing either n or a_{2D} enables us to address the quasi-2D resonance. In fact, an inhomogeneous density distribution provided, the crossover between BEC and BCS regime is realized within the same quantum gas. Depending on the confinement strength, the dependence of $\ln(k_F a_{2D})$ on the density n or the magnetic field in terms of a_{3D} varies, see Fig. 6.5. The weaker the 2D confinement, the more pronounced is the dependence on the 3D scattering length, whereas changes in the density become insignificant. While the interaction in a 2D system is always repulsive for low energy collisions, in a quasi-2D gas where $l_z \gg a_{3D}$, the sign of the interparticle interaction is the same as in 3D case.

The coupling strength may be parametrized by the dimensionless mean-field interaction parameter

$$\tilde{g}_{2D} = \frac{4\pi\hbar^2/m}{\sqrt{2\pi}l_z/a_{3D} + \ln(B/\pi k^2 l_z^2)}. \tag{6.14}$$

When the denominator is zero, a pole in Eq. 6.14 occurs, which may be associated with the appearance of a confinement-induced resonance (CIR). At the

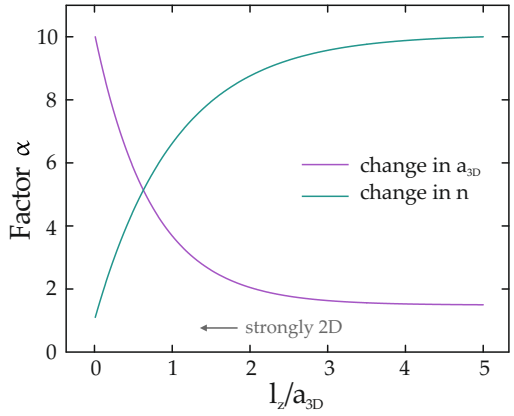

Figure 6.5.: Schematic behaviour of dependence of the 2D interaction parameter $\ln(k_F a_{2D})$ on the ratio l_z/a_{3D}. The quantity α denotes the factor which is required to change $\ln(k_F a_{2D})$ by the same amount either due to a variation in the density n or the 3D scattering length a_{3D}. The velvet solid line depicts the variation in a_{3D} and the green solid line depicts the variation in n. For $l_z/a_{3D} \ll 1$, the gas is deep in the 2D regime and the interaction parameter dominantly depends on the density n. In the opposite limit, towards the regime where the gas behaves like its 3D counterpart, the 3D scattering length becomes important.

simplest level, a CIR refers to any resonantly enhanced scattering resulting from strong confinement.

Setting the denominator in Eq. 6.14 to zero and solving for the 3D scattering length yields

$$a_{3D} = -\frac{\sqrt{2\pi} l_z}{\ln(B/(\pi k^2 l_z^2))}. \tag{6.15}$$

For our experimental parameters we expect the CIR to be located at a magnetic field strength of $B \approx 838\,\mathrm{G}$ and an interaction parameter of $\ln(k_F a_{2D}) \approx 0.7$, respectively.

Limit of Weak Confinement With increasing energy $E_B \gg \hbar\omega_z$, the regime continuously transforms to ordinary 3D scattering[1].

In particular, if $|a_{3D}| \ll l_z$ the quasi-2D regime is practically absent and for a large range of energies, the imaginary and logarithmic terms in Eq. 6.12 are negligible. In this case, the scattering amplitude can be approximated by

$$f(k) \approx \sqrt{8\pi} a_{3D}/l_z \equiv g_{MF}^{2D} \ll 1. \tag{6.16}$$

[1] For $|a_{3D}| \geqslant l_z$ the approximate crossover between the quasi-2D and 3D dominated regime is reached when $E \approx 0.1\hbar\omega_z$ [39].

Here the coupling constant g_{MF} is independent of energy and the resulting dimensionless coupling constant $\tilde{g}_{MF}^{2D} = \frac{\hbar^2}{m} g_{MF} \ll 1$, hence, the gas is weakly interacting. At very low densities, the dimensionless coupling constant $\tilde{g}_{MF}^{2D}$ should be replaced by the density dependent parameter (6.14).

Bound State There is always a bound diatomic molecular state in 2D. The reason is that the 2D scattering length is always positive, independent of the sign and strength of a_{3D}, and independent of the ratio l_z/a_{3D} [111, 114].

For $l_z/a_{3D} \ll -1$, when the dimer spreads out in the 2D plane, the dimer binding Energy is approximately $E_B^{2D} = \hbar^2/(m a_{2D}^2)$. In the vicinity of the 3D resonance, the dimer binding energy becomes a universal value in units of the confinement energy $E_B^{2D} = 0.244\,\hbar\omega_z$. Further, the 2D scattering length (6.13) can be replaced by $a_{2D} = \hbar/\sqrt{m E_B^{2D}}$.

Above the Feshbach resonance, i. e. in our case for fields strengths $B > 834\,G$, where no 3D bound state exists and the binding energy of the induced bound state is very weak $E_B^{2D} \ll \hbar\omega_z$, the dimer binding energy can be found with the relation [8]

$$\frac{l_z}{a_{3D}} = \int_0^\infty \frac{du}{\sqrt{4\pi u^3}} \left(1 - \frac{2u e^{-u E_B^{2D}/\hbar\omega_0}}{1 - e^{-2u}}\right). \tag{6.17}$$

In the BEC limit $\ln(k_F a_{2D}) \ll 0$, where the size of deeply bound molecules is smaller than l_z, the binding energy approaches the known 3D value $E_B^{3D} = \hbar^2/(m a_{3D}^2)$.

6.2. Phase Diagram

The kind of order a system can possess is determined by its dimensionality. One of the most distinct properties of uniform 2D quantum gases is that no true BEC can emerge at finite temperatures, and even more profoundly that there is a different type of phase transition instead. This BKT type transition yields the formation of a quasi-condensate and is strongly connected to the existence of bound and unbound vortices in the gas.

In this section, we show that the condition for the emergence of a BEC is strikingly different in 3D and 2D. We then discuss the nature of the BKT phase transition and the distinct role of vortices.

6.2.1. Bose-Condensation in Reduced Dimensions

Bose condensed gases at very low temperatures are typically characterized by the presence of a condensed and a thermal part of the cloud. The former corresponds to the macroscopic occupation of the lowest quantum state, whereas the latter refers to particles in thermally excited states. To these is referred to

as thermal condensate depletion[1]. In liquid ^{4}He, the condensate depletion is up to 90% [119]. In anisotropic weakly interacting dilute 3D quantum gases, the condensate depletion is usually below one percent, hence negligible.

For quantum gases in lower dimensions, the situation changes dramatically. In the following, we calculate the number of particles of finite momentum k, which do not occupy the condensate ground state in 3D and 2D, and find that no 2D BEC exists at finite temperature.

The starting point of our purely classically treatment is the free, d-dimensional ideal Bose gas consisting of N particles of the same spin with the single particle energy $E_{\mathbf{p}} = \mathbf{p}^2/(2m)$, where $\mathbf{p}$ is the momentum vector and m the particles mass. The energy level occupation at a given temperature T is determined by the Bose distribution function $f(E_{\mathbf{p}}, T, N)$.

For a sufficiently large system size V, the total particle number N is given by the sum of the particles N_0 in the ground state and the excited particles, given by the integral of $f(E_{\mathbf{p}}, T, N)$ over all momenta

$$N = N_0 + N_{exc} \tag{6.18}$$

$$= N_0 + V \int_{-\infty}^{\infty} d^d p \, \frac{f(E_{\mathbf{p}}, T, N)}{(2\pi\hbar)^d}. \tag{6.19}$$

In the following, we will show that at low temperature, the number of particles in the excited states in 3D becomes finite. As a consequence, additional particles accumulate in the ground state, forming a BEC. In 2D, only at zero temperature a 2D condensate can form.

To our convenience, we transform the integral from to spherical coordinates via

$$\int_{-\infty}^{\infty} dx_1 \dots dx_d = \int_0^{\infty} dr \, S_d r^{d-1}, \tag{6.20}$$

where we have given the surface of the d-dimensional unit sphere using the Gamma function Γ,

$$S_d = \frac{2\pi^{d/2}}{\Gamma(d/2)}. \tag{6.21}$$

Due to its formal similarity to the Bose distribution function, it is convenient to introduce the generalized Zeta function

$$\zeta_\nu(z) = \frac{1}{\Gamma(\nu)} \int_0^{\infty} dx \, \frac{x^{\nu-1}}{z^{-1} e^x - 1}. \tag{6.22}$$

With this, the number of particles in Eq. 6.19 can be rewritten as

$$N = N_0 + \frac{V}{\lambda^d} \zeta_{d/2}(z), \tag{6.23}$$

[1]Even at zero temperature, where thermal excitations are absent, there is quantum depletion of the condensate due to interaction effects, see Sec. 6.3.

with the thermal de Broglie wavelength $\lambda = \sqrt{2\pi\beta\hbar^2/m}$, the inverse temperature $\beta = 1/(k_B T)$, and the fugacity $z = e^{\beta\mu}$ with the chemical potential μ.

When the temperature T is changed, the chemical potential μ will adapt to conserve the total number of particles. Above the critical temperature $T > T_c$, the chemical potential μ is negative. When the temperature approaches T_c, μ goes to zero. Lowering the temperature further, i. e. $T < T_c$, μ remains zero and the number of condensed particles N_0 increases as the number of excited particles N_{exc} decreases. That means, the maximum number of particles in excited states N_{exc}^m is reached and all excess particles $N_0 = N - N_{exc}^m$ will then occupy the ground state and form a condensate. In this case, the $\zeta_{d/2}(z)$-function reduces to the Riemann zeta function $\zeta(d/2)$ so that

$$N_{exc}^m = \frac{V}{\lambda^d}\zeta(d/2). \tag{6.24}$$

The critical condition for the formation of a 3D BEC follows from Eq. 6.24 as

$$n\lambda^3 \simeq \zeta(3/2) \simeq 2.612, \tag{6.25}$$

where $n = N/V$ is the density. The quantity $n\lambda^d$ is also referred to as degeneracy parameter which depicts the critical phase-space density for condensation.

The calculation of the parameter for the 2D Bose gas requires special caution, since when $d = 2$ is chosen, the ζ-function in Eq. 6.24 diverges due to its pole at $z = 1$. A sum expansion for the limit of respectively $z \to 1$ and $\mu \to 0$ yields the degeneracy parameter

$$n\lambda^2 \simeq \lim_{\mu\to 0^-} \ln(-\beta\mu). \tag{6.26}$$

The logarithmic divergence of $n\lambda^2$ at all finite temperatures signals that the formation of a BEC is impossible in the limit of a large system, except at exactly $T = 0$. In other words, the conservation of the particle number does not require the BEC ground state to be occupied as the atom number diverges for $\beta \to 0$. The underlying physical reason is that the emergence of the BEC is precluded by long-wavelength phase fluctuations, see Sec. 6.3.2. Similar arguments apply in the 1D case, where no Bose-condensation can occur even at zero temperature.

The generalization from the ideal to the interacting gas is formulated in the MWH theorem [34–36], which states that there is no spontaneous symmetry breaking in a 2D equilibrium system at finite temperature with short-range interactions. As a consequence, there is no transition from a disordered to an ordered phase and no true 2D BEC emerges. We conclude that phase fluctuations play a crucial role in 2D, as they are sufficient to prevent the development of long-range order (LRO), which makes the population of a macroscopic eigenstate and the formation of a true BEC impossible at finite temperature.

However, the system undergoes a different type of phase transition which is described within the BKT theory. This transition happens at a critical temperature $T_{BKT} < T_c$ without the necessity of an long-range ordered phase [37, 38].

The presence of a harmonic trapping potential restores the divergence problem of the free 2D gas due to the changed density of states. However, the situation remains particularly different to the 3D case: the cloud density at the trap centre formally diverges $n \to \infty$, which means that in the harmonic potential condensation should only occur when the density at the trap centre is infinitely large.

6.2.2. BKT Phase Transition

For a temperature below T_{BKT}, a 2D superfluid phase exists without requiring the presence of a BEC with a phase coherent over a distance on the order of the system size.

Instead, the phase is coherent over a much smaller distance [38, 120–122] and thus the signature of the BKT superfluid is disentangled from Bose condensation. It rather appears in long-range correlations in the so-called quasi-condensate.

The critical temperature T_{BKT} is determined by [123]

$$T_{BKT} = \frac{\pi}{4} n_{sf}(T_{BKT}), \tag{6.27}$$

where $n_{sf}(T)$ is the superfluid density[1] as a function of the temperature. At the critical temperature the superfluid density is the only thermodynamic quantity which shows a discontinuity[2], jumping from 0 to the universal value $4/\lambda_{dB}^2$ [123–126]. The BKT transition thus occurs when the superfluid density $n_{sf}\lambda_{dB}^2 = 4$ while an experimental method to determine of the corresponding T_{BKT} has yet to be found.

For the case $\ln(k_F a_{2D}) \ll 1$, an analytical analysis for the transition temperature of a weakly interacting gas of composite dimers yields [127]

$$\frac{T_{BKT}}{T_F} = \frac{1}{2}\left[\ln\left(\frac{A}{4\pi}\ln\left(\frac{4\pi}{k_F^2 a_{2D}^2}\right)\right)\right]^{-1}, \tag{6.28}$$

where $A = 380 \pm 3$. In the limit $\ln(k_F a_{2D}) \to -\infty$, the critical temperature approaches $T_{BKT} \to 0$. In the experiment, one typically obtains $T_{BKT}/T_F \approx 0.1$

In the BCS limit $\ln(k_F a_{2D}) \gg 1$, the critical temperature can be estimated from the mean field temperature at which the gap vanishes [128, 129]

$$\frac{T_{BKT}}{T_F} = \frac{1}{\pi k_F a_{2D}}. \tag{6.29}$$

[1] n_{sf} refers to the superfluid fermion density which is twice the superfluid pair density.

[2] The BKT transition is often said to be of infinite order because no thermodynamic quantity shows a discontinuity at the transition point.

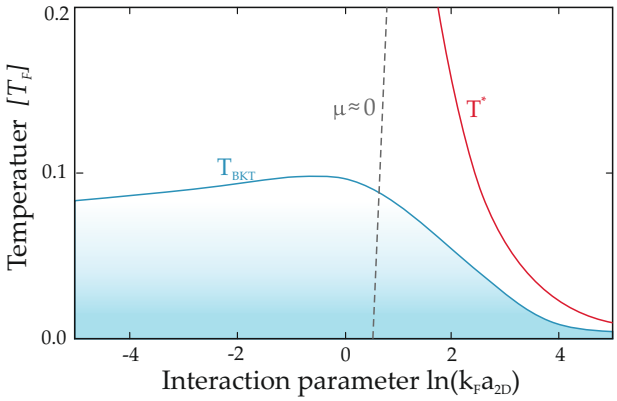

Figure 6.6.: Phase diagram of a strictly 2D Fermi gas in the BEC-BCS crossover. The critical temperature T_{BKT} is depicted as the solid cyan line. It corresponds to an interpolation between the two known limits, see text. The solid red line depicts the critical temperature T^* for the onset of pairing without superfluidity. The pseudogap region is expected to be bound by T_{BKT} and T^*. The dashed grey line depicts the situation where $\mu \sim 0$. The figure is adapted from Ref. [113].

T_{BKT} is set by the lowest energy scale in the system, which is the pair dissociation energy. Figure 6.6 shows the 2D phase diagram in the BEC-BCS crossover with an interpolation of T_{BKT} for the corresponding limits.

For temperatures above T_{BKT}, a pseudogap state can exist, allowing for the existence of pre-formed pairs but no emergence of long-range coherence. For temperature above the pairing temperature $T > T^*$, the paired state fully evolves into the normal state.

The microscopic mechanism of the BKT phase transition is associated with the presence of vortices. At the centre of a vortex, the density is $n = 0$ and increases over the vortex healing length ξ. These vortices are topological points with a phase winding of a multiple of 2π and represent local phase defects. In the normal phase of a 2D gas, disordered free vortices proliferate in the gas and cause an exponential decay of the first-order correlation function g_1.

Below the critical temperature T_{BKT}, the formation of bound vortex pairs is favourable, see Fig. 6.7. Each pair consists of vortices with an opposite phase circulation so that the local phase perturbation is negligible. The correlation function g_1 decays algebraically, which is characteristic for the phase fluctuating BKT phase and the existence of a quasi-condensate.

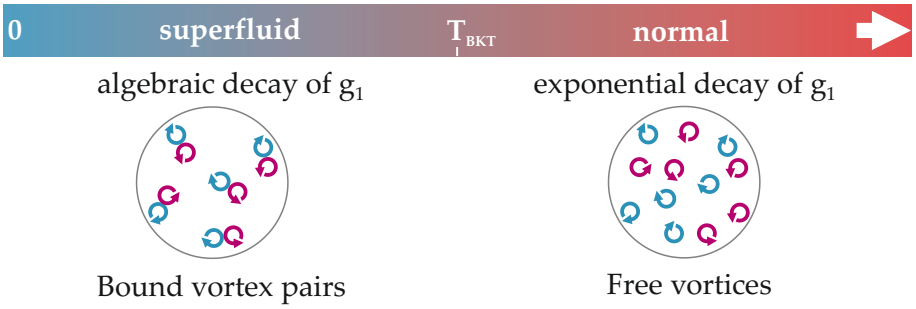

Figure 6.7.: Sketch of the evolution of vortices along the BKT transition. For temperatures $T < T_{BKT}$, a superfluid phase exists. Vortices are present only in bound pairs which do not destroy the quasi-longrange order in the gas. This is signalled by algebraic decay of the first-order correlation function g_1. For $T > T_{BKT}$, vortices proliferate freely and represent strong phase disturbances, causing the correlation function g_1 to decay exponentially.

6.3. Phase Fluctuations

The recent interest in low-dimensional quantum gases stems from the fact that their physical properties are strikingly different from the 3D case, which is primarily due to the enhanced importance of phase fluctuations[1] [130–133]. In 3D, the influence of fluctuations is in general small and the phenomenon of superfluidity is closely related to the formation of a BEC[2]. While the 3D BEC is a prime example for a coherent state, the coherence properties change significantly in lower dimensions. Here, the phase does not evolve into a fully coherent state and only a quasi-condensate emerges. Phase fluctuations in the homogeneous 1D case preclude a true condensate at any temperature, and only allow for a 2D BEC at zero temperature, according to the MWH theorem.

The occurrence of order in a many-body system directly manifests itself in the correlation functions.

6.3.1. Correlations

Bose-condensation is understood as the macroscopic occupation of one single-particle quantum state. First, we introduce the basic tools to investigate the order of a system and then study the role of fluctuations in all three relevant dimensions.

Correlation Function The occurrence of LRO in a many-body system directly manifests itself in the normalized first order or one-particle correlation

[1] Density fluctuations are negligible at low temperatures typical for quantum gas experiments.
[2] In 3D, phase fluctuations only play a role very close to the critical temperature.

function

$$g_1(\mathbf{r}', \mathbf{r}'') = \frac{\langle \hat{\psi}^\dagger(\mathbf{r}')\hat{\psi}(\mathbf{r}'')\rangle}{\langle \hat{\psi}^\dagger(\mathbf{r}')\hat{\psi}(\mathbf{r}')\rangle \langle \hat{\psi}^\dagger(\mathbf{r}'')\hat{\psi}(\mathbf{r}'')\rangle}. \tag{6.30}$$

where $\hat{\psi}^\dagger$ and $\hat{\psi}$ are the bosonic field operators. The g_1-function tells us whether the presence of two particles at a position $\mathbf{r}'$ and $\mathbf{r}''$ is correlated, i. e. it describes the loss of phase coherence over a distance $r = |\mathbf{r}' - \mathbf{r}''|$. Equation 6.30 yields values between zero and one, for respectively a completely uncorrelated and a perfectly coherent state. In a classical system, the correlation function is zero for large distances, whereas in a quantum gas, g_1 can remain finite.

In the thermodynamic limit, the first-order correlation function is given by the Fourier transform of the momentum distribution of the gas, which can thus be studied equivalently.

In a 2D BKT superfluid below the critical temperature T_{BKT}, the algebraic decay of the correlation function is due to long-wavelength phase fluctuations. These destroy the condensate without preventing the emergence of the superfluid. The gas still admits finite regions where the phase is well correlated, but with relatively weak phase correlations between different regions. For temperatures above T_{BKT},g_1 decays exponentially.

Correlations are also visible in the one-particle density matrix

$$\rho(\mathbf{r}', \mathbf{r}'') \equiv \langle \hat{\psi}^\dagger(\mathbf{r}')\hat{\psi}(\mathbf{r}'')\rangle, \tag{6.31}$$

which gives the amplitude for removing a particle at the position $\mathbf{r}'$ and creating another at $\mathbf{r}''$. In case of $\mathbf{r}' = \mathbf{r}''$, the density matrix equals the particle density $n(\mathbf{r}')$, so that the density matrix is normalized through the condition $\int d\mathbf{r}\, \rho(\mathbf{r}', \mathbf{r}') = N$, where N denotes the total number of particles.

The density matrix is Hermitian and can thus be diagonalized with real eigenvalues. The coherence of the system, manifests itself in the off-diagonal elements of ρ [20,134]. If one of the eigenvalues is on the order of the number of particles $\langle N\rangle$ and all other eigenvalues are on the order of one, ρ is said to have off-diagonal long range order (ODLRO). In this case, the system is called Bose condensed and for large separations we find a non-vanishing condensate density.

6.3.2. Thermal Fluctuations

To study the existence of an ordered phase, we first investigate its stability against classical excitations. The lowest lying excitations in a BEC are phonons, i. e. sound modes.

In the following, we calculate the mean square of thermal phase fluctuations associated with a mode of wave vector $\mathbf{q}$, as it is discussed in Ref. [119,135,136]. The relevant modes are those which are occupied the most, i. e. the modes

with low energy. We will see that this deviation diverges in dimensions lower than 3D.

In the limit of a large volume $V_d \to \infty$ of a uniform d-dimensional Bose gas at finite temperature $T \neq 0$ in thermal equilibrium, we consider the phase ϕ of the condensate wave function

$$\phi(\mathbf{r}) = \sum_{\mathbf{q}} \phi_{\mathbf{q}} e^{i\mathbf{q}\mathbf{r}}. \tag{6.32}$$

Since $\mathbf{v} = \frac{\hbar}{m}\nabla\phi$, we relate the phase ϕ of the mode to the corresponding velocities $\mathbf{v}_{\mathbf{q}} = i\phi_{\mathbf{q}}\frac{\hbar\mathbf{q}}{m}$. The mode occupancy is given by the Planck function $1/(e^{\epsilon_q/kT}-1)$, thus for $kT \gg \epsilon_{\mathbf{q}}$, the mean kinetic energy in the mode is $kT/2 = mnV_d/2 \cdot \langle \mathbf{v}_{\mathbf{q}}\mathbf{v}_{\mathbf{q}}^* \rangle$. It follows that

$$\langle |\phi_{\mathbf{q}}|^2 \rangle = \frac{mkT}{N\hbar^2}\frac{1}{q^2}. \tag{6.33}$$

We assume the different modes to be independent and thus write for the phase variance

$$\langle \phi^2 \rangle = \sum_{\mathbf{q}<\mathbf{q}_{cut}} \langle |\phi_{\mathbf{q}}|^2 \rangle . \tag{6.34}$$

Relevant are all wavevectors smaller than a cut-off wavevector $q < q_{cut}$. Above $q < q_{cut}$ the approximations fail. This either occurs when the thermal energy becomes comparable to the phonon energy associated with $\mathbf{q}$ and the full Bose-distribution must be used, or because the energy dispersion is not longer linear in the wavevector $\mathbf{q}$. Both effects suppress the occupation of modes above the cut-off so strongly that they do not contribute significantly to the phase deviations.

Changing from summation to integration yields

$$\langle \phi^2 \rangle \simeq \frac{mkT}{N\hbar^2}\frac{V_d}{(2\pi\hbar)^d}\int_{1/L}^{q_{cut}} \frac{d^d q}{q^2}. \tag{6.35}$$

Here, the lower boundary $1/L$ of the integral is determined by the system size and the upper bound is given by the cut-off wavevector q_{cut}. For $d = 3$, the integral in Eq. 6.35 converges at its lower boundary for $L \to \infty$. Due to the cut-off, the entire integral is finite. For $d \leqslant 2$, the integral diverges at its lower boundary $q \to 0$. Hence, in the 1D and 2D case, long-wavelength phase fluctuations destroy the phase coherence. The particular cases yield:

- In 3D, the integral converges at long wavelengths, which means that LRO is retained and a BEC emerges.

- In 2D, the integral diverges logarithmically as

$$\langle \phi^2 \rangle \propto \frac{T}{T_c^{2D}} \ln(q_{cut} L). \tag{6.36}$$

  Hence, the phase fluctuations diverge in the thermodynamic limit where $L \to \infty$. The critical temperature $T_c^{2D} = 2\pi\hbar^2 n_{2D}/(mk)$ for the non-interacting gas marks the point where the de Broglie wavelength is comparable to the interparticle separation and quantum degeneracy sets in. n_{2D} is the 2D particle density. At zero temperature, there is no divergence.

- In 1D, the phase fluctuations diverge as well, but with a linear behaviour

$$\langle \phi^2 \rangle \propto \frac{T}{T_c^{1D}} L, \tag{6.37}$$

  where n_{1D} is the corresponding particle density and $T_c^{1D} = \hbar^2 n_{1D}/(mk)$ the critical temperature.

Phase Fluctuations in the Density Matrix We now answer the question how phase fluctuations affect the one-particle density matrix in Eq. 6.31 [135]. Consider a system at finite temperature in thermal equilibrium with the classical wavefunction [137]

$$|\psi(\mathbf{r})| e^{i\phi(\mathbf{r})}. \tag{6.38}$$

Since the density matrix is a non-local property, the global phase $\phi(\mathbf{r})$ contributes. We rely on the fact that the energy of the system can be considered as the one of a collection of independent harmonic oscillators, so that the canonical coordinates and momenta have Gaussian distribution [135]. At large separations r, the density matrix then simplifies to

$$\rho(\mathbf{r}', \mathbf{r}'') = \langle |\psi(\mathbf{r}')||\psi(\mathbf{r}'')| e^{i(\phi(\mathbf{r}') - \phi(\mathbf{r}''))} \rangle \tag{6.39}$$

$$= |\psi|^2 e^{-\langle (\phi(\mathbf{r}') - \phi(\mathbf{r}''))^2 \rangle / 2} \tag{6.40}$$

We consider the mean square phase fluctuations in the exponent of Eq. 6.40 and find using Eq. 6.32

$$\langle (\phi(\mathbf{r}') - \phi(\mathbf{r}''))^2 \rangle = 2 \sum_{\mathbf{q} < \mathbf{q}_{cut}} \langle |\phi_{\mathbf{q}}|^2 \rangle \left[1 - \cos(\mathbf{q}\mathbf{r})\right]. \tag{6.41}$$

For $q \to 0$, the cosine term behaves like $[1 - \cos(\mathbf{q}\mathbf{r})] \propto q^2$. Analogous to the discussion of Eq. 6.35, we now distinguish the behaviour of the density matrix for different spatial dimensions.

- In 3D, the density matrix $\rho(x) \simeq n_c^{3D}(1 + 1/x)$ decreases to a constant value at large separations, i. e. LRO establishes and a BEC emerges.

- In 2D, for large r, the sum in Eq. 6.41 is cut off at small q by the cosine function, which introduces an effective lower limit at $q \sim 1/r$. The length r is assumed to be much greater than the characteristic length given by the cut-off wavevector, i. e. $r \gg r_{cut}$ with $r_{cut} \equiv 1/q_{cut}$. For the the long-wavelength limit we can now use the result 6.33 in Eq. 6.41 and obtain

$$\langle(\phi(\mathbf{r}') - \phi(\mathbf{r}''))^2\rangle \simeq \frac{mkT}{\pi\hbar^2 n}\int_{1/r}^{1/r_{cut}} \frac{dq}{q} \simeq \nu \ln(r/r_{cut}). \tag{6.42}$$

  where the length r_{cut} may be identified with the correlation length ξ. The behaviour of the density matrix is thus given by

$$\rho(\mathbf{r}) \propto e^{-\langle(\phi(\mathbf{r}')-\phi(\mathbf{r}''))^2\rangle/2} \propto \left(\frac{r}{\xi}\right)^{\nu}, \tag{6.43}$$

  where $\nu \propto T/T_c^{2D}$. Due to thermal phase fluctuations, the density matrix tends algebraically to zero for large r. No fully coherent BEC exists and the density n_c is identified with a quasi-condensate density, except at $T = 0$, where there can be a 2D condensate.

- In 1D, the density matrix decays exponentially $\rho(x) \simeq n_c^{1D} e^{-x\frac{T_c^{1D}}{T}}$, so that not even a quasi-condensate exists and the system is in the normal state.

So far, we have only considered long-wavelength excitations of the form of sound modes. In 2D quantum gases, vortices represent an additional type of excitation. For temperatures above T_{BKT}, it is their unbinding and free proliferation which causes the density matrix decay to change from algebraically to exponentially $\propto e^{-|r|/d_\nu}$, with the mean vortex separation $d_\nu \propto L/\sqrt{N_\nu}$, N_ν being the number of vortices [135]. The corresponding BKT transition temperature is substantially lower than the critical temperature for quantum degeneracy $T_{BKT} = T_c^{2D}/4$.

6.3.3. Quantum Fluctuations

To extend the investigation of phase fluctuations to quantum effects we allow for particles of finite momenta even at zero temperature. For a quantitative description of the fluctuations on the quantum level we consider a condensate represented by the order parameter $\hat{\psi}(\mathbf{r})$. The decomposition[1] of the quantum gas order parameter reflects the mathematical representation of the condensate and uncondensed fraction of the atoms

$$\hat{\psi}(\mathbf{r}) \simeq \langle\hat{\psi}(\mathbf{r})\rangle + \delta\hat{\psi}(\mathbf{r}). \tag{6.44}$$

[1]The decomposition of such an operator representation may be called fluctuation expansion or Bogoliubov shift.

The fluctuation operator $\delta\hat{\psi}(\mathbf{r})$ describes both, thermal and quantum fluctuations, i. e. quantized excitations (quasi-particles) of the atom field. If the fluctuating states are orthogonal to the condensate state, the field operator acquires an expectation value which is the macroscopic condensate wave function. Therefore, the first term in Eq. 6.44 yields a classical wave function $\Psi_c(\mathbf{r})$ that describes the macroscopic state of condensed atoms

$$\langle\hat{\psi}(\mathbf{r})\rangle = \Psi_c(\mathbf{r}). \tag{6.45}$$

This replacement of an operator with an ordinary complex number is the Bogoliubov replacement, which is valid at very low temperatures where a large number of atoms is condensed $N_c \simeq N$, where N is the total number of atoms in the system.

When the condensate contribution can be treated as a classical field, we are able to formulate the order parameter (6.44) alternatively as

$$\hat{\psi}(\mathbf{r}) \simeq \sqrt{n_c(\mathbf{r})}\, e^{i\hat{\phi}(\mathbf{r})}, \tag{6.46}$$

where we focus on fluctuations in phase and all the operator dependence is contained in the phase operator $\hat{\phi}(\mathbf{r})$ which permits a precise treatment of the phase fluctuations[1].

Again, the determination of the one-particle density matrix clarifies whether the density n_c describes a true condensate or a quasi-condensate.

$$\rho(\mathbf{r}', \mathbf{r}'') = \sqrt{n_c(\mathbf{r}')n_c(\mathbf{r}'')}\, e^{-\langle(\hat{\phi}(\mathbf{r}')-\hat{\phi}(\mathbf{r}''))\rangle/2}. \tag{6.47}$$

In order to calculate the exponent in Eq. 6.47, the Bogoliubov-de Gennes equations and the Bogoliubov transformation of the phase operator $\hat{\phi(\mathbf{r})} = 1/\sqrt{4n_c(\mathbf{r})}\sum_{j=1}^{\infty} f_j^+ \hat{a}_j + \text{h.c.}$ is required, where $\hat{a}$ is the annihilation operator of the mode j and $f_j^+ = v_j + u_j$ is the wavefunction in terms of Bogoliubov amplitudes with the energy ϵ_j. We directly discuss the results without presenting an explicit calculation and refer to Ref. [135, 138] instead.

The one-particle density matrix (6.47) accounts for fluctuations in phase even at zero temperature and thus goes beyond the classical result (6.40).

- In 3D weakly interacting gases, quantum fluctuations are strongly suppressed and virtually absent, i. e. there is no significant influence on the coherent BEC ground state.

- In 2D, the phase fluctuations converges for large separation $\mathbf{r}' - \mathbf{r}''$, thus quantum fluctuations do not destroy the BEC, unlike thermal fluctuations do.

[1] To account for fluctuations in the density, one would substitute the density operator $\hat{n}(\mathbf{r}) = n_c(\mathbf{r}) + \delta\hat{n}(\mathbf{r})$.

- In 1D, the zero-point phase fluctuations behave like the thermal ones do in 2D. Even at zero temperature, there is no BEC in a homogeneous 1D gas.

In summary, 2D fluctuations are mainly of thermal origin and true Bose-condensation is only possible at zero temperature. At finite temperature, the one-particle correlation function decays algebraically and there is a quasi-condensate[1]. The phase fluctuations in 1D are dominantly of quantum origin, hence even at zero temperature condensation is impossible.

6.4. Equation of State

Full knowledge of the thermodynamics of the gas provided, the equation of state determines any thermodynamic quantum gas quantity under a given condition, relating well defined macroscopic variables as the gas temperature T, pressure P, or energy E. A full description of all peculiar effects in 2D quantum gases is a difficult task for theories.

In this section, we first give an incomplete overview of the theoretical work concerning the BEC-BCS crossover in 2D Fermi gases. We then consider the intuitive description of simple Mean Field Theory (MFT) to discuss the 2D BEC-BCS crossover qualitatively. This lays the foundation to extend the overview to more sophisticated approaches, which will be benchmarked against our experiment in the succeeding chapter. This section therefore ends with a comparative summary of the corresponding theory predictions for the 2D equation of state in the BEC-BCS crossover.

6.4.1. Theory Overview

The role of strong interactions makes an exact analytical descriptionof the equation of state in the crossover impossible so far. We briefly show that even in the case of a weakly interacting Bose gas, theory results are incomplete and contradictory.

The dimensionless 2D coupling constant $\tilde{g}_{MF}^{2D}$ corresponding to the weakly interacting 2D Bose gas is described by the Gross-Pitaevskii theory in which all particles are considered to be in the condensate. Unlike in the 3D and 1D case, the coupling constant is density dependent thus the construction of a precise theory is difficult.

In the BEC regime, where $\ln(k_F a_{2D}) \ll 1$, we consider the boson chemical

[1]The direct connection between the one-particle density matrix and the momentum distribution via Fourier transformation allows us to equivalently discuss the quantum condensate depletion. In fact, the depletion and the expectation value of phase fluctuations are identical quantities.

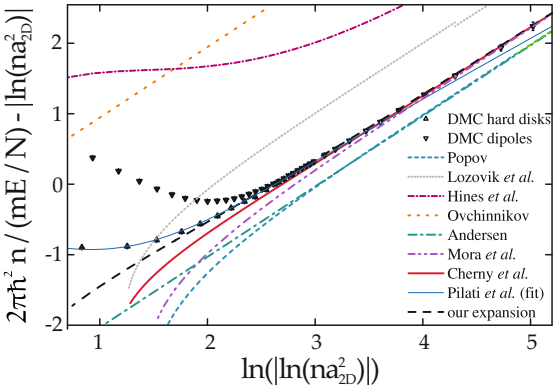

Figure 6.8.: Beyond mean field corrections in the energy per particle of a 2D Bose gas. Symbols denote QMC calculations. The lines depict different equations of state. The figure is adapted from the same Ref. [141], see the same and references therein for a comprehensive overview and comparison.

potential μ_{MF} in terms of a density dependent coupling constant [133, 139]

$$\mu_{MF} = \tilde{g}_{MF}^{2D} n = \frac{4\pi\hbar^2 n/m}{|\ln(na_{2D}^2)|}. \tag{6.48}$$

Integration yields the energy per particle equation of state

$$\frac{E}{N} = \frac{4\pi\hbar^2}{mna_{2D}^4}\Gamma(0, 2|\ln(na_{2D}^2)|), \tag{6.49}$$

Here, the solution of the integral over μ is given by the incomplete Gamma function $\Gamma(a,x)$, which is a generalization of the Gamma function for integrals which are bound by a finite value. The leading contribution of Eq. 6.49 was already obtained by *M. Schick* in 1971 [140]. In order to go beyond mean field accuracy, the incomplete Γ-function is expanded around the dilute limit $na_{2D}^2 \to 0$. The expansions of Eq. 6.49 results in logarithmically small terms which are significant for the study of beyond mean field effects. This strongly contrasts the 3D dilute gas, which is perfectly described by the leading order MFT term. For the 2D Bose gas, there is an ongoing search for higher order terms and thus numerous theoretical work, as shown in Fig. 6.8. For further details see Ref. [141] and references therein.

We now briefly summarize the evolution of theoretical approaches to point out the arising problems and to emphasize the crucial importance of complementary experimental work. Our starting point is the early work on the 3D BEC-BCS crossover from which we progress to the achievements in 2D.

Early Crossover Approaches The equation of state of a 3D Bose gas dates back to the year 1956, when the first mean field correction was obtained

by *T. D. Lee* and *C. N. Yang* [142]. The first systematic study of the BEC-BCS crossover at zero temperature was developed 1969 by *D. M. Eagles* [11] and *A. J. Leggett* [12] to explore superconductivity beyond weak interactions. Based on mean field equations, a smooth evolution from the BCS side of the resonance into the regime where pairs are tightly bound in real space[1] was developed. They used a standard BCS ground state as a variational ansatz, which gives a qualitative description of the crossover and provides a correct description in the deep BCS regime.

Thermal excitation of collective modes were outside the range of these theories, until 1985, when *P. Nozières* and *S. Schmitt-Rink* developed a generalized BCS theory, often referred to Nozières and Schmitt-Rink (NSR) approach [13]. This diagrammatic perturbation method is applicable at finite temperatures and includes the effects of pairing fluctuations around the Fermi edge. Improvements based on the NSR approach added quartic (Gaussian) phase and density fluctuations around a mean field saddle point within time-dependent Ginzburg-Landau theory and successfully reproduced density profiles, collective excitations and critical temperatures in the crossover [99, 143–145].

Most of these studies fail at strong coupling, and while the BCS MFTs incorrectly[2] predict a dimer-dimer scattering length $a_d^{3D} = 2a^{3D}$ instead of $0.6a^{3D}$, the extension including Gaussian pair fluctuations results in a more accurate scattering length of $a_d^{3D} = 0.75a^{3D}$. The equation of state was derived including fluctuations on the Gaussian level in different ways [146–150], and benchmarked against experiments and simulations [105, 151–154], achieving an overall good agreement with experiment.

Two Dimensions and the BKT Transition The zero temperature case in 2D was theoretically first investigated by *K. Miyake* [128] and later by *M. Randeria* [114, 155]. Most of the finite temperature analyses are based on different extensions of the NSR approach [156], e. g. T-matrix methods[3].

These methods account for fluctuations on the Gaussian level, which indeed destroy LRO and thus are in agreement with the MWH theorem. However, Gaussian fluctuations are inadequate to describe the BKT transition, thus the related jump of the superfluid density is not reproduced and divergences in the fluctuation contribution at low temperature occur. Those problems are remedied by taking higher interaction orders into account, e. g. with an effective interaction between pair fluctuations [157].

Later, the BKT phase transition became accessible for an extended mean

[1] Due to the fact, that this evolution shows no non-analytic behaviour, e. g. a symmetry-change, it is called crossover.

[2] The dimer-dimer scattering length $a_d^{3D} = 0.6a^{3D}$ is the solution of four-body calculations [39].

[3] The T-, or transition-matrix method was introduced to solve the scattering problem in a more convenient way instead of dealing with the scattering states explicitly by replacing the bare two-body interaction potential. The matrix elements are directly related to the scattering amplitudes and describe the outcome of a collision process.

field treatment which included phase fluctuations via path integral formalisms[1] in 2D [129, 158] and quasi-2D [159–162].

Finding the 2D equation of state along the entire BEC-BCS crossover is particularly challenging and thus analytical solutions are rare. In the corresponding limits, one can resort to perturbative methods based on the 2D Fermi liquid theory [163] and the equation of state for a 2D Bose gas of dimers [139,140]. Ab-initio QMC simulations at zero temperature provide the most reliable results [164, 165], which are proven to agree with experiments [115, 166].

However, we first discuss the qualitatively but not quantitatively correct mean field approach, since it already offers an intuitive picture of the BEC-BCS crossover in 2D.

6.4.2. Mean Field Description

In this section, we will first derive the chemical potential μ and also obtain the gap parameter Δ as a function of the interaction parameter $\ln(k_F a_{2D})$. The aim is to calculate the energy per particle E/N, which is sometimes the more intuitive quantity compared to μ. Due to the large contribution from the binding energy E_B, it is convenient to subtract it from the energy density E/N. In mean field description, we find the constant relation $E/N - E_B = 1$, which shows that MFT cannot predict the crossover correctly.

MFT approximates a weakly interacting gas by assuming every particle to be independent and by replacing interactions by a mean field. Generally, this replacement can be performed in different ways, but none is expected to be quantitatively accurate. The dimer-dimer scattering length is predicted incorrectly, and for strong interactions, the ground state energy is too large compared to experiments and simulations. Thus, MFT only provides an upper bound on the energy.

In the following, we sketch the derivation of the chemical potential and the gap parameter, following Ref. [159, 167], and restrict ourselves from detailed calculations to focus on the results which are relevant for this work.

The typical 2D BCS Hamiltonian is ($\hbar \equiv 1$) [159]

$$H = \int dx^2 \Psi_\sigma^\dagger(\mathbf{x}) \left(-\frac{\nabla^2}{2m} - \mu \right) \Psi_\sigma(\mathbf{x}) + g \int dx^2 \Psi_\uparrow^\dagger(\mathbf{x}) \Psi_\downarrow^\dagger(\mathbf{x}) \Psi_\downarrow(\mathbf{x}) \Psi_\uparrow(\mathbf{x}). \quad (6.50)$$

The operator $\Psi_\sigma(\mathbf{x})$ represents the finite temperature Fermi field, $\mathbf{x} = \mathbf{r}, t$, where $\mathbf{r}$ is a 2D vector, and $\sigma = \uparrow, \downarrow$. The chemical potential μ fixes the density $n = N/V$, where V is the systems volume. The attractive potential is $U_0 = g\delta(\mathbf{x} - \mathbf{x}')$. The Hamiltonian (6.50) is solved by rewriting it in terms

[1] The Feynman path-integral method is a generalization of the classical Lagrange and Hamilton formalism to quantum mechanics. It is a non-perturbative representation of the grand-canonical partition function. The systems dynamics are determined by the so-called action. According to the principle of least action the minimum of the functional is determined.

of a partition function $Z(V,\mu,T)$. The so-called Hubbard-Stratonovich transformation allows condensation regardless whether its due to Cooper pairs or local pairs. From the analysis of the Hamiltonian (6.50) follows the gap equation

$$-\frac{1}{g} = \frac{1}{V}\sum_{\mathbf{k}} \frac{1}{2E_{\mathbf{k}}} \tanh\left(\frac{E_{\mathbf{k}}}{2T}\right) \tag{6.51}$$

where $E_{\mathbf{k}} = \sqrt{\xi_{\mathbf{k}} + \Delta}$ is the excitation spectrum and $\xi_{\mathbf{k}} = \frac{\mathbf{k}^2}{2m} - \mu$. According to Ref. [168], the gap equation at zero temperature yields

$$-\frac{1}{g} = \frac{1}{2V}\sum_{\mathbf{k}} \frac{1}{\sqrt{\xi_{\mathbf{k}}^2 + \Delta^2}} = \frac{m}{4\pi}\int_{-x_0}^{\infty} dz \frac{1}{\sqrt{1+z^2}}, \tag{6.52}$$

where the integrand is $z = \frac{\hbar^2}{2m\Delta} - x_0$, and x_0 is the interaction parameter $1/\ln(k_F a_{2D})$. The δ-function of the interaction leads to a UV divergence of the gap equation. In 3D, where a bound state exists only on the repulsive side of the resonance, one must choose an appropriate cut-off. In 2D, where a finite bound state energy exists for any coupling strength, the divergence can be eliminated by subtracting the bound state equation

$$-\frac{1}{g} = \frac{1}{V}\sum_{\mathbf{k}} \frac{1}{\mathbf{k}^2/m + E_B} = \frac{m}{2\pi}\int_{-x_0}^{\infty} dz \frac{1}{2z + 2x_0 + E_B/\Delta} \tag{6.53}$$

from the gap equation. After performing the integration of the difference of Eq. 6.52 and Eq. 6.53 we arrive at

$$\frac{E_B}{\Delta} = \sqrt{1+x_0^2} - x_0. \tag{6.54}$$

The number equation is given by

$$n = \frac{1}{V}\sum_{\mathbf{k}} \left(1 - \frac{\xi_{\mathbf{k}}}{E_{\mathbf{k}}} \tanh\left(\frac{E_{\mathbf{k}}}{2T}\right)\right) \tag{6.55}$$

$$= \frac{m}{2\pi}\left(\sqrt{\mu^2+\Delta^2} + \mu + 2T\ln\left[1 + \exp\left(-\frac{\sqrt{\mu^2+\Delta^2}}{T}\right)\right]\right). \tag{6.56}$$

At zero temperature, the interaction parameter is related to the gap parameter Δ/E_F and the chemical potential μ/E_F in units of the Fermi energy E_F by

$$\frac{\Delta}{E_F} = \frac{2}{x_0 + \sqrt{1+x_0^2}}, \quad \frac{\mu}{E_F} = \frac{2x_0}{x_0 + \sqrt{1+x_0^2}}. \tag{6.57}$$

With these two equations we finally obtain

$$\mu = E_F - \frac{E_B}{2}, \tag{6.58}$$

$$\Delta = \sqrt{2E_F E_B}. \tag{6.59}$$

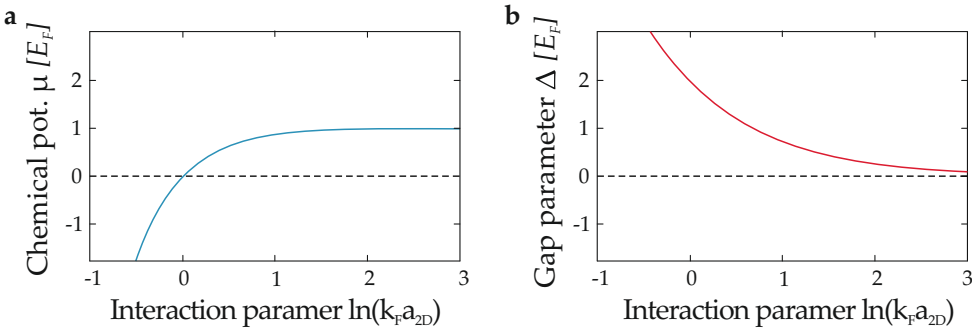

Figure 6.9.: Mean field chemical potential μ and gap parameter Δ in the crossover. a) In the BCS regime, where $\ln(k_F a_{2D}) > 0$, the chemical potential μ almost equals the Fermi energy E_F. For $\ln(k_F a_{2D}) \to 0^+$, μ decreases due to the increasing pairing energy and is zero when the interaction parameter is zero. b) The gap is exponentially small in the BCS regime and $\Delta = 2E_F$ when $\ln(k_F a_{2D}) = 0$. For stronger attraction, the gap increases.

These simple zero temperature results were already found in Ref. [128, 155].

Far in the BCS regime of weak attraction where $\ln(k_F a_{2D}) \gg 1$, the chemical potential is $\mu \simeq E_F$, see Fig. 6.9 a. The two-body binding energy $E_B \ll E_F$ and the gap $\Delta \ll E_F$ are very small thus the pair size is much larger than the interparticle spacing $1/k_F$. Just beyond the pairing threshold, the obtained result is identical to the one of BCS theory of Cooper pairs. In the BCS regime, the gap becomes exponential small, see Fig. 6.9 a. However, the binding energy stays finite since in 2D a bound state always exists. In the 3D case, the gap closes completely and equally the superfluid phase vanishes because no pairs are left to contribute

In the BEC regime of strong attraction where $\ln(k_F a_{2D}) \ll 1$, there is a deeply bound two-particle state so that $|E_B| \ll E_F$, and the gas consists of essentially non-interacting composite bosons. The chemical potential here is $\mu \simeq -|E_B|/2$, which is one half the energy of pair dissociation for tightly bound pairs. This means that the binding energy of fermion pairs is nearly identical to the two-body binding energy.

For $\ln(k_F a_{2D}) \to 0$, the chemical potential μ decreases due the increasing pairing energy and equals zero when the interaction parameter reaches zero. This point corresponds to $\mu = 0$ and signals a distinct change in the quasi-particle excitation spectrum $E_{\mathbf{k}} = \sqrt{(\epsilon_{\mathbf{k}} - \mu)^2 + \Delta^2}$ and marks the natural crossover. It may be viewed as analogous to the 3D unitary point $1/(k_F a_{3D}) = 0$. We note that this picture is insufficient since the mean field chemical potential is finite with $\mu > 0$ at the 3D crossover point. Furthermore, QMC simulations showed that the point in 2D where the chemical potential vanishes is more on the attractive side of the 3D resonance at $\ln(k_F a_{2D}) \approx 0.5$ [40, 118].

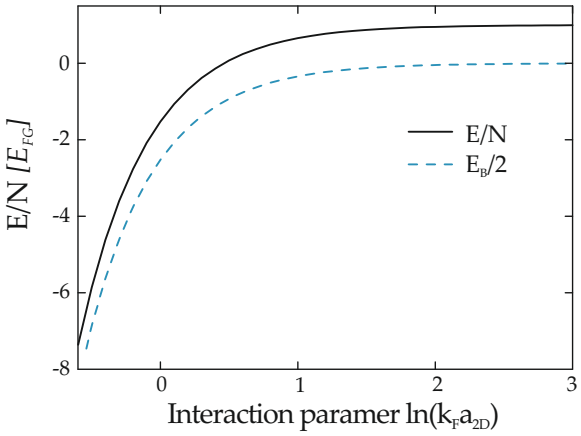

Figure 6.10.: Mean field prediction of the equation of state as a function of the 2D interaction parameter $\ln(k_F a_{2D})$. The solid black line is the mean field result. In the BCS limit, the energy per particle E/N approaches the energy per particle of a non-interacting Fermi gas $E_{FG} = \hbar^2 k_F^2/(4m) = E_F/2$. The cyan green dashed line is the molecular binding energy $E_B/2 = E/N - 1$.

Equation of State in Mean Field Approximation The energy per particle is connected to the chemical potential by the thermodynamic relation $\mu = \frac{\partial E}{\partial N}$. With the definition of the Fermi energy $E_F = \hbar^2 k_F^2/(2m)$, the energy per particle in units of the energy of a free Fermi gas $E_{FG} = E_F/2$ is

$$\frac{E}{NE_{FG}} = 1 - \frac{8}{(a_{2D} k_F)^2}, \tag{6.60}$$

which is shown in the BEC-BCS crossover in Fig. 6.10.

In the BCS regime, the energy per particle approaches the energy of a non-interacting Fermi gas E_{FG}. On the BEC side, where bound dimers exist, the particle energy increases exponentially. The analytically predicted dimer-dimer interaction scales only with density rather than being appropriately renormalized by quantum effects, thus all higher orders are missed by MFT. The mean field energy is only determined by the binding energy of the dimers. In fact, subtracting the two-body binding energy from the energy per fermionic particle results in a constant value for any interaction parameter, signalling the inadequacy of MFT.

6.4.3. Beyond Mean Field Approaches

MFT provided us with a qualitative description of the chemical potential in the crossover. However, it fails in predicting the correct binding energy E_B and it is consequently unable to predict the corrected energy per particle $E/N - E_B$. We now extend our discussion to beyond mean field methods, which will be compared to the experimental results in the next chapter. The most reliable

results are given numerical QMC simulations, which are presented at the end of this section. Before we discuss these, we will compare two perturbative methods, which are applicable in the two limits of the BCS and BEC regime.

Weakly Interacting Fermi Liquid In 1950, *L. D. Landau* developed the Fermi liquid (FL) theory that allows us to derive perturbative expressions that connect the thermodynamic properties of a weakly interacting Fermi gas to those of an ideal Fermi liquid [163, 169–171].

We consider a homogeneous zero temperature 2D Fermi gas with weak attractive short-range interaction where $\ln(k_F a_{2D}) \gg 1$. The equation of state for the energy per particle is the one of a normal attractive FL in perturbative expansion

$$\frac{E_{FL}}{NE_{FG}} = 1 + 2g + A_2 g^2. \tag{6.61}$$

The coefficient $A_2 = 3 - 4\ln 2$ of the second order term depends on the chosen 2D coupling constant $g = -1/(2\ln(k_F a_{2D}))$ [165]. Note that the first order term is already different to the simplest mean field result, see Eq. 6.60. The exact value results from claiming a consistent g and energies for both, the weakly interacting regime as well as the strongly repulsive regime[1].

To emphasize many-body effects beyond the mean field contribution we subtract the two-body contribution arising from the molecules. The resulting equation of state $E_{FL}/N + |E_B|$ in units of E_{FG} is shown as the solid orange line in Fig. 6.11. Towards the BCS limit of a non-interacting Fermi gas, the FL theory agrees well with QMC results, which are depicted as the black circles[2]. Approaching the resonance $\ln(k_F a_{aD}) \to 0^+$, the difference between both methods becomes significant as the predictions within FL theory diverge. We also show the results obtained via MFT. These cannot predict crossover behaviour correctly due to the lack of a correct binding energy E_B.

Weakly Interacting Gas of Dimers In the BEC limit where $\ln(k_F a_{2D}) \ll -1$, we consider the equation of state of a 2D gas of weakly interacting composite bosons [139, 140].

We follow Ref. [113, 172] and sketch the perturbative expansion of the energy per particle. Consider the total energy $E = -E_B N_d + E_d$, where E_d is the energy of a repulsive Bose gas consisting of $N_d = N/2$ bosons. The grand potential

$$\Omega = E_d - \mu_d N_d \tag{6.62}$$

[1] Despite a similar coupling constant, there are different values of the coefficient A_2 given in the literature. In addition to the value obtained within second-order perturbation theory presented here, $A_2 = (3 - 4\ln 2) \simeq 0.06$ [170, 171], recent QMC calulations find the value $A_2 \simeq 0.17$ [40].

[2] The complete numerical QMC results are presented at the end of this section.

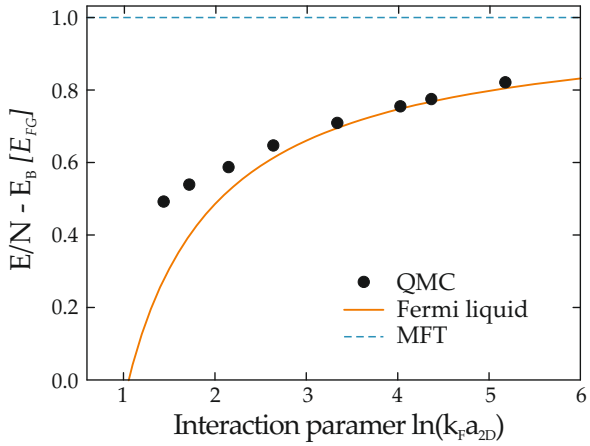

Figure 6.11.: The equation of state in the 2D BCS regime, corrected by the molecular binding energy $E_B/2$. The prediction within Fermi liquid theory is depicted as the solid orange line. For $\ln(k_F a_{aD}) \gg 1$, the perturbative FL results approach the energy of a non-interacting Fermi gas E_{FG}. For comparison, we also show results from recent QMC calculations (black circles) and the MFT results (dashed cyan line). Towards the crossover, where $\ln(k_F a_{aD}) \to 0^+$, the FL results diverge and increasingly deviate from the numerical calculations. MFT cannot the predict the crossover at all, due to the lack of a correct binding energy prediction, see Sec. 6.4.2.

in Bogoliubov approximation is

$$\Omega = \frac{2m\mu_d^2}{16\hbar^2\pi}\left(1-2\ln\left(\frac{1}{2m\mu_d\alpha^2 a_{2D}^2}\right)\right), \tag{6.63}$$

with the boson chemical potential $\mu_d = 2\mu + E_B$. The factor α accounts for the modified dimer-dimer scattering in case of deeply bound composite bosons instead of the collision of individual fermions. The derivative of the grand potential Ω with respect to μ yields the two-particle density n_d

$$-\frac{\partial\Omega}{\partial\mu_d} \equiv n_d = \frac{2m\mu_d}{4\pi\hbar^2}\ln\left(\frac{4\pi}{2m\mu_d\alpha^2 a_{2D}^2}\right). \tag{6.64}$$

Rearranging Eq. 6.64 provides us with the leading order term of the chemical potential

$$\mu_d \simeq \frac{2\pi\hbar^2 n_d}{m}\frac{1}{\ln\left(\frac{1}{n_d\alpha^2 a_{2D}^2}\right)}\left[1-\frac{\ln\ln\left(\frac{1}{n_d\alpha^2 a_{2D}^2}\right)}{\ln\left(\frac{1}{n_d\alpha^2 a_{2D}^2}\right)}\right], \tag{6.65}$$

where $n_d = n/2$ is the dimer density and $m_d = 2m$ the dimer mass. At zero temperature and considering Eq. 6.62, one arrives at the equation of state [40, 113, 172]

$$\frac{E/N - |E_B|}{NE_{FG}} = \frac{1}{2}g_d\left(1+g_d\left[\ln(\pi g_d)+2\gamma+1/2\right]\right). \tag{6.66}$$

Similar to the perturbative FL approach, the coupling constant $g_d = -1/\ln(n_d\alpha^2 a_{2D}^2)$ has to be chosen appropriately [40]. We parametrize Eq. (6.66) in terms of the interaction parameter $\ln(k_F a_{2D})$ and show the result as the solid cyan line in Fig. 6.12. Surprisingly, the perturbative expansion of the composite boson equation of state is applicable beyond the point where $\ln(k_F a_{2D}) = 0$. Over the whole range, it is in reasonable agreement with the numerical QMC results.

Quantum Monte Carlo Simulations It is tempting to interpolate the results in the weak interacting limits to derive an analytical description for the BEC-BCS crossover. However, in order to obtain an accurate prediction of the equation of state throughout the crossover, we have to turn to numerical simulations [164, 165], which have proven to agree with experiments [115, 166].

The zero temperature QMC technique approaches the microscopic properties of the 2D Fermi gas, based on the grand canonical many-body Hamiltonian in a cubic volume $V = L^3$ with periodic boundary conditions. One introduces a function $f(\mathbf{R},\tau) = \phi_T(\mathbf{R})\Psi(\mathbf{R},\tau)$, where $\Psi(\mathbf{R},\tau)$ denotes the wave function of the system. A trial function $\phi_T(\mathbf{R})$ is evolved in imaginary time $\tau = it/\hbar$, according to the Schrödinger equation. Finally, finite size analysis is carried out to extrapolate the results to the thermodynamic limit $V \to \infty$.

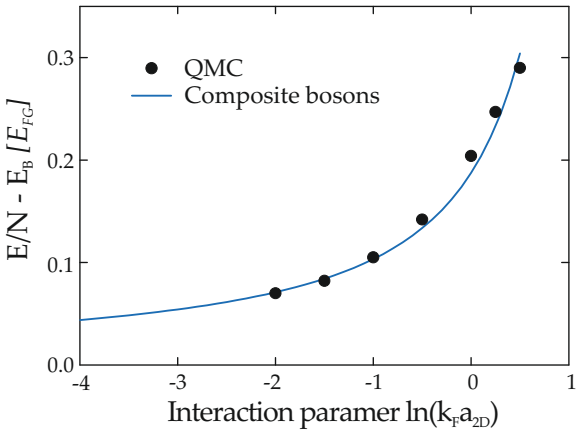

Figure 6.12.: The equation of state $E/N - E_B$ in the BEC-BCS crossover. Results for 2D gas of weakly interacting composite bosons are depicted as the solid blue line. For $\ln(k_F a_{2D}) \to \ll 0$, as the dimers get tightly bound and the binding energy increases, the perturbative predictions approach zero. Numerical QMC results are depicted as black circles.

The results of the QMC simulations along the entire crossover are reported as the black circles in Fig. 6.13, which is the central figure of this section. The solid grey line is a fit to the QMC data

$$\epsilon(x) = \alpha + \beta \arctan(\gamma \cdot (x - \delta)), \tag{6.67}$$

with the coefficients $\alpha \simeq 0.41$, $\beta \simeq 0.33$, $\gamma \simeq 0.62$ and $\delta \simeq 1.09$. The results obtained from FL theory and the equation of state of composite bosons in the BEC regime are shown as well.

To summarize, the QMC results provide us with the most reliable prediction of the crossover behaviour. In the next Chapter 7, we compare the presented theory approaches to the measured 2D speed of sound. Unsurprisingly, the inaccurate mean field description wont be able to describe our results.

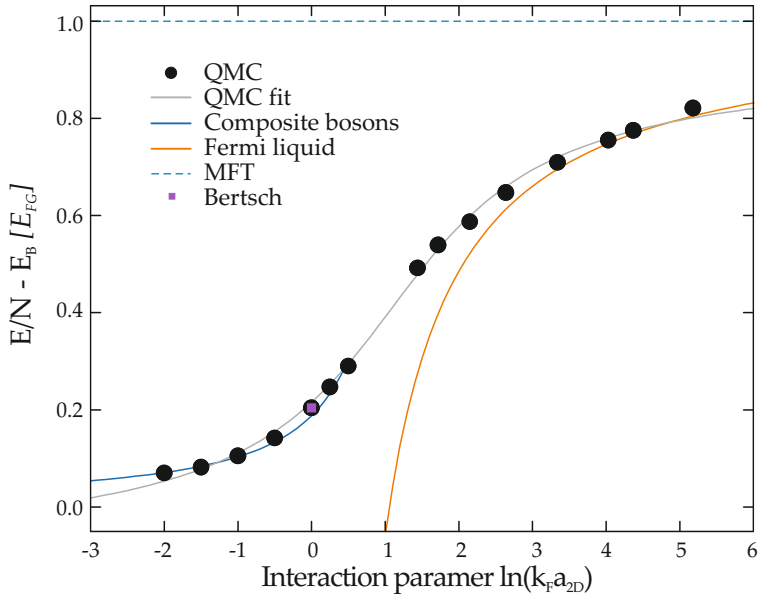

Figure 6.13.: Comparison of different equations of state as a function of the interaction parameter $\ln(k_F a_{2D})$. The dashed cyan line are the MFT results, the solid blue line depicts the equation of state of composite bosons, and the solid orange line the prediction within FL theory. The solid grey line is a fit to the numerical results (black circles), see text. While the FL results rapidly diverge towards the resonance $\ln(k_F a_{aD}) \to 0^+$, the equation of state for composite bosons is applicable even beyond the crossover $\ln(k_F a_{aD}) = 0$. Additionally, we show the prediction at $\ln(k_F a_{aD}) = 0$ using the Bertsch parameter (velvet square). The energy per particle reaches a universal value at the 2D resonance ($\ln(k_F a_{2D}) \simeq 1$). After subtracting the binding energy it is $E/N - E_B = 0.204 E_F/2$.

7. Exploring the Thermodynamics of 2D Fermi Gases

The BEC-BCS crossover in 2D Fermi gases presently attracts considerable interest and yet, comprehensive understanding is still lacking. Full knowledge of the thermodynamics, i. e. the equation of state, would yield a complete representation and full description of the system, and automatically account for all its peculiarities. A crosscheck of the equation of state is afforded by studying the dynamic response of the system, i. e. measuring the speed of sound. Here, we present the first results on the speed of sound in 2D Fermi gases in the BEC-BCS crossover, and compare it to the predictions of the equation of state . Furthermore, we present preliminary results on the pressure equation of state, from which we obtain the sound velocity as well.

Section 7.1 of this chapter recaptures the distinct features of 2D Fermi gases and elaborates on the possibility to use the speed of sound to probe these systems. After a preview of our results in Sec. 7.2, an overview of experimental work is given in Sec. 7.2. Section 7.3 presents the speed of sound measurements and concludes with an extensive comparison with theoretical predictions of the speed of sound derived from different equation of state models. Our results beyond the speed of sound, i. e. the pressure equation of state, are presented in Sec. 7.4. A recently developed method to measure the temperature of interacting 2D Fermi gases is discussed in Sec. 7.5. We conclude and draw the attention to open questions and arising controversies in Sec. 7.6, emphasizing the importance of advancing the knowledge of these systems with experiments.

7.1. Motivation

The BEC-BCS crossover physics in 2D systems are remarkably different. The preceding chapter elucidated that this is mainly due to the BKT phase transition, the fundamentally changed scattering behaviour and the enhanced importance of phase fluctuations. Overall, the variety of peculiarities and great diversity of physical phenomena causes the strong growth in experimental and theoretical effort to understand the thermodynamic and superfluid properties of 2D Fermi gases.

Yet, on the theoretical side, analytical and numerical methods predicting the thermodynamics in 2D BECs of composite bosons and ultracold gases of Cooper pairs are inconsistent. Now, the ability to realize single layer 2D

Fermi gases close to a Feshbach resonance provides us with the possibility to test the theoretical predictions.

Naturally, the question arises how these rich but complicated systems can be studied adequately. One obvious and appealingly simple answer is a direct measure of response to, e. g. a small local perturbation. A well suited example is a density wave which propagates with the speed of sound. The density wave can be generated by the creation and the sudden release of a local density excess. Being a collective excitation it captures all characteristics of the 2D BEC-BCS crossover and is thus sensitive to scattering, trap and temperature effects, and superfluid properties.

Here, we present measurements of the sound velocity for a wide range of interaction parameters $\ln(k_F a_{2D})$ in a strongly confined Fermi gas. The realization of a single 2D quantum system enables us to conduct high precision experiments. Our studies thus offer the possibility to explore the 2D thermodynamics, to test theories, and to invalidate some of them. While this chapter focuses on the speed of sound, we additionally present our preliminary results on the pressure equation of state. From this, we extract the speed of sound and find it in excellent agreement with the results of the response experiments.

7.2. Our Observations and Previous Work

The first low-dimensional BEC was created in 2001 in the group of *W. Ketterle* [63]. Less than a decade later, *A. Turlapov* and colleagues prepared the first two-dimensional Fermi gas [173]. Since then, experiments by the groups of *M. Köhl*, *M. Zwierlein*, and *J. Thomas* aimed for a deeper understanding of the quasi 2D Fermi gas crossover physics [116, 174–177]. However, the number studies of the thermodynamic properties in the BEC-BCS crossover in 2D Fermi gases remains limited. The behaviour of collective excitations, i. e. the breathing and quadrupole mode has been studied in [45]. *C. Vale* and colleagues investigated the influence of dimensionality [178] and conducted first measurements of the thermodynamic equation of state by analysing in-situ density profiles [166]. Recent work of the group of *A. Turlapov* follows a similar approach and covers the investigation of the ground state pressure of the gas along the crossover [115] in good agreement with theory [40].

So far, the speed of sound had not been measured in 2D Fermi gases. In 3D BECs, early sound velocity experiments were carried out in the group of *W. Ketterle* [179]. The speed of sound in a BEC at high temperatures was investigated by *P. van der Straten* and colleagues [180], and was measured as well in the BEC-BCS crossover by *J. Thomas* and others [92–94]. Recently, *R. Grimm* and co-workers studied the second sound in a resonantly interacting 3D Fermi gas [93, 94]. Theoretical work has mainly been done on 3D gases [101, 181–183] and on dilute 2D Bose gases [184] and recently on unitary 2D

Fermi gases [185].

Overall, the exploration of the phase diagram of ultracold 2D Fermi gases has only just begun. Many unresolved questions exist, e. g. regarding the critical temperature for the BKT phase-transition, the FFLO phase in spin imbalanced systems, or the nature of the pseudo-gap regime. Another prime example is the general role of interactions, as recent experiments on dynamical gas properties yield contradictory results. While spin transport measurements [44] are in agreement with theory, the observation of an undamped breathing mode [45] surprisingly indicates the opposite case of interaction effects much weaker than expected.

Against this background, our results are an important addition to the first direct analyses of the 2D Fermi gas in the BEC-BCS crossover and the understanding of these systems. The speed of sound represents a powerful probe providing important information on key thermodynamic quantities and also on the systems dynamic behaviour and interactions. Moreover, the sound velocity is sensitive to the superfluid fraction, and should in principle enable us to probe the BKT phase boundary [184] and directly determine the critical temperature for BKT superfluidity. Besides, engineering first sound experiments potentially paves the road to the excitation and observation of second sound. This has never been measured in 2D [182], and so far, we could not observe sufficient evidence.

Preview We take a brief look ahead on the experimental results, with the main focus being on the speed of sound measurements in Sec. 7.3. One possible representation of the equation of state is given by the relationship between the chemical potential μ and the density n. The sound velocity is then determined by the derivative of this equation of state as

$$v_s^2 = \frac{n}{m}\frac{\partial \mu}{\partial n}. \tag{7.1}$$

In the experiment, we realize a single 2D ^{6}Li quantum gas, strongly confined in a blue-detuned 1D optical lattice at the lowest attainable temperatures. The effective aspect ratio of our trap exceeds most of the ratios of aforementioned experiments by far, we thus work with pure, cold, and strongly confined 2D quantum systems.

Making use of a broad Feshbach resonance and a high degree of control over particle densities, we map out the BEC-BCS crossover measuring the speed of sound v_s. After the creation and sudden release of a local density excess in the centre of the cloud, we track the outward propagation of the resulting density wave, see Fig. 7.1. The method is similar to the one we employed in the 3D experiments, see Ch. 5. The covered distance of the peak density after a certain delay time τ yields the speed of sound directly. We follow this procedure for various interaction parameters $\ln(k_F a_{2D})$, where

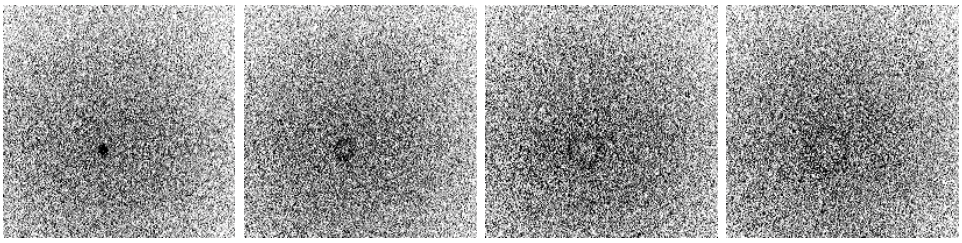

Figure 7.1.: Denstiy wave in a 2D gas for different propagation times. A small attractive potential creates a density excess in the superfluid centre of the cloud. Suddenly switching off the potential releases a density wave which propagates outwards in a circular symmetric way. The peak density travels with the speed of sound and is extracted by image analysis. For each value of the interaction parameter $\ln(k_F a_{2D})$ we acquire ten of these snapshots. The images show clouds with an interaction parameter of $\ln(k_F a_{2D}) = 0.8$, a particle number of 35 000, and a central density of about $1.7 \times 10^{12}\,\mathrm{m}^{-2}$.

a_{2D} is the 2D scattering length and the Fermi wave vector $k_F = \sqrt{4\pi n_0}$, with the central cloud density n_0.

The experimental results are shown in Fig. 7.2. The sound velocity v_s, given in units of the Fermi velocity $v_F = \hbar k_F/m$, is smallest on the BEC side, where $\ln(k_F a_{2D}) \leqslant 0$, and increases monotonously when we cross the 2D resonance, where $\ln(k_F a_{2D}) = 0$[1], towards the BCS regime, where $\ln(k_F a_{2D}) \geqslant 0$.

Here, we show two theory comparisons. The first is the sound velocity prediction within MFT including phase and amplitude fluctuations [41], which is depicted as the horizontal line in Fig. 7.2. Clearly, it is not in accordance with our data even at the qualitative level and emphasizes the difficulties of theory to capture interaction and pronounced fluctuation effects. The currently best suited tools to describe 2D Fermi gases in the BEC-BCS crossover are numerical techniques, such as QMC simulations. The speed of sound, derived from a fit to a recent QMC equation of state [40, 165] is in very good agreement with our results.

In addition, we show the speed of sound extracted from the experimental pressure equation of state, which is obtained from in-situ 2D density profiles. The excellent agreement of the results of both methods, the measurement of direct response and the equation of state, confirms the high precision and reliability of the experiment. In the following, the speed of sound measurements are explained and discussed.

[1] Despite its imprecise nature, which is discussed in Ch. 6, the term *resonance* is used throughout this chapter.

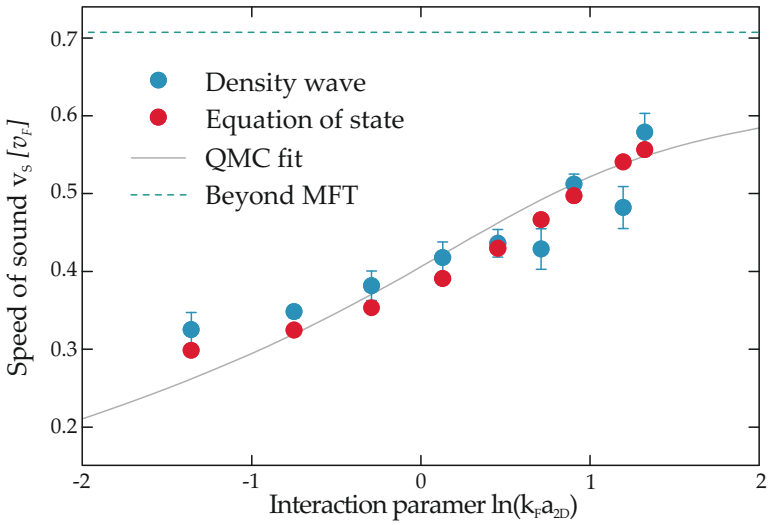

Figure 7.2.: The speed of sound in 2D Fermi gases in the BEC-BCS crossover. The cyan circles show the results of the direct measurement via the excitation of density waves. The error bars are due to the scatter of the density peak position for different propagation times. Early speed of sound results which we derive from the measured equation of state are depicted as the red circles. The two experimental results are in excellent agreement. The solid grey line shows the sound velocity we derived from a fit to recent numerical calculations of the equation of state [40, 165]. The dashed green line is a sophisticated mean field prediction which accounts for phase and amplitude fluctuations [41].

7.3. Speed of Sound

First, we present the experimental procedure to measure the sound velocity and discuss the experimental parameters. We then present the complete results including the different theory approaches presented in Ch. 6. Before we summarize at the very end of this section, we introduce the foundations for the thermodynamic nature of the speed of sound and develop a way to derive the sound from a given equation of state.

Sound velocity experiments were hitherto exclusively done in highly elongated 3D quantum gases by generating a perturbation in the centre of the trap using a focussed blue-detuned laser beam. As presented in Ch. 5 and Ref. [80], our group was the first to create a point like density excitation in a highly oblate Fermi gas using a red-detuned beam to measure the speed of sound together with the superfluid critical velocity throughout the crossover.

Here, we take this method further and present the first report of a direct and precise measurement of the sound velocity in the BEC-BCS crossover in a 2D cloud, strongly confined in a single layer of a 1D lattice.

7.3.1. Sound Wave Excitation

The preparation of the 2D clouds follows Ch. 3. Details about the blue-detuned 1D optical lattice and its alignment procedure can be found in the corresponding Sec. 3.3.4. In short, an ultracold gas, consisting of a balanced mixture of ^{6}Li atoms in the lowest two hyperfine states, is prepared in the already highly oblate squeeze dipole trap. We lower the laser power of the squeeze trap from 400 mW to 20 mW to perform evaporative cooling. The evaporation is done at a magnetic field close to the 3D scattering resonance at 834 G. By ramping up the power of the squeeze laser beam to 1000 mW, the cloud is compressed. Simultaneously, the 1D optical lattice beam power is increased to a total power of 600 mW. Switching off the squeeze trap transfers 85 % of the atoms into a single anti-node of the optical lattice, loading only an insignificant fraction into adjacent layers.

The excitation laser beam has a wavelength of 780 nm and is pointed at the centre of the 2D cloud through the upper microscope objective. The beam power is ramped up linearly in 100 ms to approximate values between (100 to 350) µW at the position of the atoms. The beam power is chosen such that a consistent density excess is created for different values of the interaction parameter in the crossover. Suddenly switching off the beam causes a density perturbation which spreads outwards as a circularly symmetric wave in the 2D cloud. After a certain delay τ from the moment of the excitation, an absorption image of the cloud is taken.

Figure 7.1 shows in-situ density profiles recorded after different delay times τ. To determine the speed of sound v_s, we analyse an average of several absorption images taken for different delay times τ and extract the distance

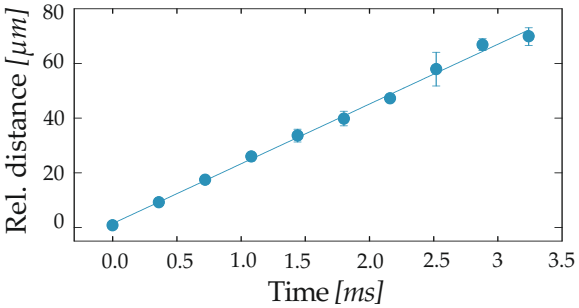

Figure 7.3.: Evolution of the density wave maximum as a function of the propagation time. The slope of the linear fit curve is identified with the speed of sound. The resulting absolute sound velocity is $v_s = (21.8 \pm 0.9)\,\mathrm{mm\,s^{-1}}$ and $v_s/v_F = 0.58 \pm 0.02$, respectively. The measurement is carried out in a 2D cloud with a central density of $1 \times 10^{12}\,\mathrm{m^{-2}}$ at a magnetic field strength of 889 G. The interaction parameter is $\ln(k_F a_{2D}) = 1.3$.

between cloud centre and peak positions, as shown in Fig. 7.3. The linear sound propagation is fitted with a linear function where the slope is identified with v_s.

We measure the speed of sound as a function of the dimensionless interaction parameter $\ln(k_F a_{2D})$. The magnetic field strength is thus ramped in a few ten ms to a value between (730 to 890) G, which corresponds to a change of the 2D scattering length $a_{2D} = (1000 \text{ to } 20\,000)\,a_0$[1]. The 2D scattering length is calculated as $a_{2D} = \frac{2}{e^\gamma} l_0 \sqrt{\frac{\pi}{B}} e^{-\sqrt{\pi/2}\, l_0/a_{3D}}$ with the Fermi wave vector $k_F = \sqrt{4\pi n_0}$ and the central cloud density n_0, which is directly accessible in the 2D geometry.

Since we keep the atom number constant at $N = 24\,000 \pm 1000$ for each data point, the atomic clouds get more dilute with increasing Fermi pressure towards the BCS regime. Thus, the central density decreases from $n_0 = 1.8 \times 10^{12}\,\mathrm{m^{-2}}$ within the BEC regime to $n_0 = 1.0 \times 10^{12}\,\mathrm{m^{-2}}$ in the BCS regime.

The interaction parameter is consequently determined by changing the magnetic field B and also due to the variation in the density n. With this, the interaction parameter covers the range of $\ln(k_F a_{2D}) = -1.36$ to $\ln(k_F a_{2D}) = 1.32$. Reaching further into the BEC regime is impractical due to a reduction of the lifetime, which is caused by three-body losses[2]. On the BCS side, we are limited by weak response signals due to the low density. Nevertheless, we intended to extend the measurements to magnetic field strengths of ≈ 930 G, but a forced downtime prevented us from doing so.

Ultimately, the absolute sound velocity changes from $v_s \approx 16\,\mathrm{mm\,s^{-1}}$ in the BEC regime to $v_s \approx 22\,\mathrm{mm\,s^{-1}}$ in the BCS regime. A first glance at the

[1] Correspondingly, the 3D scattering length changes from $a_{3D} = (-2700 \text{ to } 9000)\,a_0$.

[2] The dimers are very deeply bound so that they start to decay into lower (rotational and vibrational) states, releasing energy which can cause a third constituent to escape the trap.

results was given in Fig. 7.2, and we turn to the complete analysis in the next Sec. 7.3.2. But first, we discuss the relevant experimental parameters in the following paragraphs, to substantiate our observations.

Excitation Beam Since the atom number is kept constant along the crossover, the cloud density is significantly reduced in the BCS regime. Therefore, larger beam radii and thus an increased potential size appeared to be favourable for the excitation of a density wave, assuming that the beam power is increased accordingly. Since the available laser power is limited, we opted for an intermediate beam size, providing sufficient signal in both, the BEC and BCS regime. The $1/e^2$ radius of the excitation beam focus is thus $3.6\,\mu m \times 2.8\,\mu m$ and remains unchanged for all measurements.

Excitation Beam Power Sound propagation is inherently dependent on the density of its medium. Consequently, when the density excess is too large, corresponding to high excitation beam powers, the sound velocity is expected to increase due to the locally increased density. Beyond linear response, precise determination becomes ambiguous.

To avoid these effects we ensure that we stay in a regime of small perturbations and choose the excitation power accordingly low, i. e. for each value of the interaction parameter, we balance the response signal against the excitation beam power. As a result, the laser power was changed from $100\,\mu W$ in the BEC regime to roughly $350\,\mu W$ in the BCS regime. For higher excitation beam powers the observed speed of sound v_s/v_F significantly increases, as it is exemplary shown in Fig. 7.4.

Local Density Over the distance the propagating density wave is tracked, the local density essentially remains constant. This prevents the sound wave from changing its velocity during the propagation through the cloud, which greatly simplifies the analysis[1].

Far in the BEC (BCS) regime, the region of constant density has a radius of $r \approx 30\,\mu m$ ($75\,\mu m$), whereas the corresponding Gaussian width is $w_{BEC} \approx 80\,\mu m$ ($w_{BCS} 115\,\mu m$).

Temperature In each experimental realization, the 2D quantum gas is prepared at the lowest attainable temperature, which is typically below 10 % of the Fermi temperature T_F.

After changing the magnetic field and adapting the particle number, we conduct a temperature measurement before the actual sound measurements

[1] The case of a less homogeneous density profile may give rise to interesting experimental implications. In less uniform density profiles, the interaction parameter $\ln(k_F a_{2D})$ becomes spatially dependent, and one could, in principle, observe the crossover from the BEC to a BCS regime in a single realization.

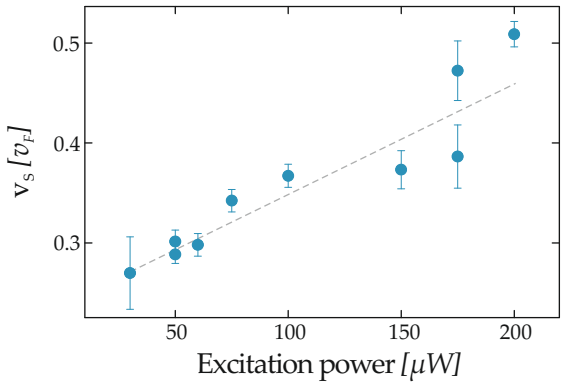

Figure 7.4.: Dependency of the measured sound velocity v_S on the excitation beam power, estimated at the atoms position. The correct speed of sound is expected to be measured only in the limit of low beam powers. For higher beam power, i. e. a deeper potential, the sound velocity increases due to the increase in the local density. The dashed grey line is a linear fit to the data, which was obtained in 2D clouds with an interaction parameter between $\ln(k_F a_{2D}) = -2.1$ and $\ln(k_F a_{2D}) = -2.2$.

are carried out[1]. We do this by an adiabatic ramp of the magnetic field well into the BEC regime and applying a short TOF inside the weak harmonic trap, generated by the magnetic Feshbach field. In short, we map the initial momentum distribution to the spatial domain, so that the low momentum fraction of the quasi-condensate collapses and gives rise to a pronounced display of the thermal atoms. By fitting a Gaussian curve to the thermal wings, we determine the condensate fraction and can thus extract the temperature, details are found in Sec. 7.5.

Throughout the BEC-BCS crossover, we obtain temperatures ranging from (18 to 22) nK and 6 % to 8 % of the Fermi temperature.

Image Analysis For each delay τ we take the averaged density profile $\bar{n}$ of ten absorption images or more. To enhance the visibility of the small density excess in $\bar{n}$, we subtract a reference picture $\bar{n}_0$, which we obtain by smoothing an averaged density profile of the unperturbed cloud. The profile $\bar{n}^* = \bar{n} - \bar{n}_0$ depicts a clearly visible density modulation. This profile $\bar{n}^*$ is divided into four quadrants which are evaluated individually, taking the radial average and determining the peak position. The distance between peak positions and the cloud centre as a function of time τ yields the speed of sound v_s.

In a few particular cases, the density wave does not propagate with perfect circular symmetry, most likely caused by, e. g. jitter of trap optics. To obtain

[1]Since we are keeping the atom number constant by adapting the atom number before the evaporative cooling is carried out, we already expect a slight difference in the final temperature.

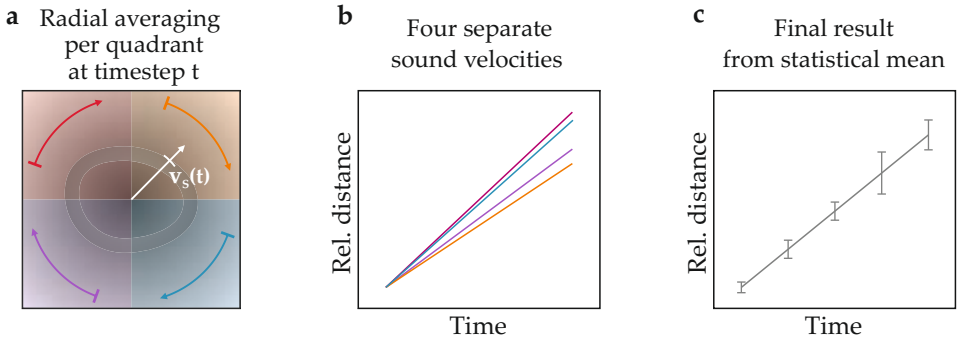

Figure 7.5.: Schematic of the image analysis to determine the speed of sound. a) For each propagation time t, the averaged and normalized density picture is divided into four quadrants to account for an asymmetric density wave propagation. Each quadrant is radially averaged. b) We evaluate all time steps t and obtain four linear fit curves, representing the speed of sound per quadrant. Significant outliers can be easily accounted for. c) The mean of the separate sound velocities gives us the final result.

reliable and reproducible results, we take radial averages of the four cloud quadrants, as sketched in Fig. 7.5. This enables us to determine the speed of sound separately and to identify and exclude outliers. The error bars in Fig. 7.3 are due to the different sound velocities we obtained in the four quadrants.

Furthermore, another type of image analysis was developed to avoid the influence of local density variations even more. Here, the cloud density profile is divided into slices of basically arbitrary number, which are then radial averaged individually. From the obtained density profiles, the local speed of sound as a function of the increasing distance and the local density is evaluated. We could not observe a noticeable difference between the results of both methods.

7.3.2. Results and Discussion

In general, the speed of sound as a thermodynamic phenomenon depends on the many-body physics and the quantum statistics of the system. Sound propagation is therefore expected to change with the scattering length a_{2D}, the strength of the vertical confinement, and the density of its medium. However, the behavioural change is smooth — as it is true for any thermodynamic quantity along the crossover from the BEC to the BCS regime.

Figure 7.6 depicts our measured speed of sound and the full set of results we have obtained from the theory which was discussed in Ch. 6. The sound velocity in terms of the Fermi velocity v_s/v_F is shown as a function of the 2D interaction parameter in the range $\ln(k_F a_{2D}) = -1.36$ to 1.32. A measure of the statistical uncertainty is shown at $\ln(k_F a_{2D}) \approx 0.7$, where the given speed of sound value $v_s/v_F = 0.44 \pm 0.05$ is the average of five separate measurements. The given error is the standard deviation. The error of the remaining data is determined by the image and fit analysis, as discussed in Sec. 7.3.

The corresponding absolute velocities range from $v_s \approx 16\,\mathrm{mm\,s^{-1}}$ in the BEC regime, to $v_s \approx 22\,\mathrm{mm\,s^{-1}}$ in the BCS regime. On the BEC side, where $\ln(k_F a_{2D}) < 0$, the measured speed of sound is about 30 % of the Fermi velocity and increases monotonously by approximately a factor of two towards the BCS side, $\ln(k_F a_{2D}) > 0$.

The data is in remarkably good agreement with the sound velocity results from our pressure equation of state (red circles), see Sec. 7.4. This has important indications. Achieving identical results with two different methods does confirm the high overall quality of our experimental data. Moreover, it justifies the assumption that we are in the weak response limit. Finally, it verifies that our equation of state yields a corrects description of our quantum gases.

Theory Comparison We now comment on the comparison of the experimental results to theory. Afterwards, the thermodynamic definition of the sound velocity is presented to derive the speed of sound from the equation of state, see Ch. 6.

The simplest MFT prediction yields $v_s/v_F = 1/\sqrt{2}$ (dashed green line) [155], based on BCS theory [12], which is not in accordance with the experiment, as shown in Fig. 7.6. This is unsurprising, since this method is a rather strong approximation, completely disregarding fluctuations in phase and amplitude. However, there is a significantly more advanced mean field approach, which adds variations to the gap equation, accounting for fluctuations in amplitude and phase [41]. It is intriguing that this approach yields the same result as the simple mean field approach, namely $v_s/v_F = 1/\sqrt{2}$. Clearly, even advanced mean field techniques cannot describe our data[1].

[1] Even though the stated theory result is valid at zero temperature, no noticeable change for

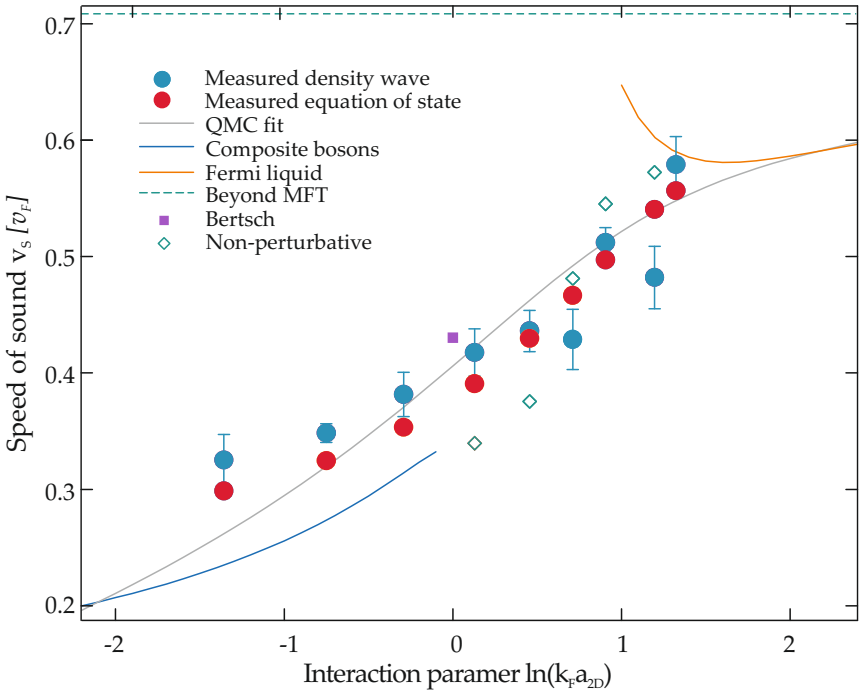

Figure 7.6.: Comparison of sound velocities obtained via different experimental and theoretical methods in the BEC-BCS crossover. This figure shows the main result of this chapter. The results which we obtained via density wave propagation are shown as the cyan circles. The red circles show preliminary results from the measured equation of state. The two different methods are both in very good agreement with the sound we derived from a fit to numerical QMC equation of state results (solid grey line) [40,165]. In the BEC regime, we show the sound velocity which results from a perturbative equation of state calculation for composite bosons (solid blue line) [140]. In the opposite limit, we derive the speed of sound from the equation of state calculated within FL theory (solid orange line) [163]. The green open diamonds depict results from a non-perturbative approach [186]. The dashed green line is a beyond mean field result accounting for phase and amplitude fluctuations [41]. See Ch. 6 for more information about the presented theory. The velvet square depicts the sound velocity prediction using the Bertsch parameter ξ_B for a unitary 2D Fermi gas.

The best agreement with the experiment is obtained by the speed of sound, which is derived from the fit to the equation of state from numerical QMC simulations (solid grey line) [40, 165]. The fact that the QMC simulation is a zero temperature method suggests that the experimental data is not influenced by pronounced finite temperature effects. Although, temperature effects might explain the noticeable residual deviations in the BEC regime.

On the BEC side, the interparticle attraction is strong and the gas is characterized by weakly interacting dimers. Going beyond MFT, perturbation methods yields the equation of state for composite bosons [140]. The derived sound velocities (solid blue line) are systematically smaller than the experimental results. It is worth noting that the equation of state for composite bosons gives reasonable results up to $\ln(k_F a_{2D}) = 0$, where the agreement with our data seems to improve.

On the BCS side, we derive the speed of sound from the equation of state calculated within FL theory (solid orange line) [163]. Towards the resonance, the predicted speed of sound diverges. However, the results from the FL equation of state agrees well with the QMC results. Note that in the BCS limit, where $\ln(k_F a_{2D}) \to \infty$, the MFT and Fermi liquid result match.

Along the crossover, we furthermore obtain a reasonable agreement from the comparison to a non-perturbative path-integral formalism (green open diamonds) [186]. Interestingly, the predicted speed of sound seems to match with the one from the equation of state for composite Bosons and from Fermi liquid theory towards $\ln(k_F a_{2D}) \to 0^{-,+}$.

In case of unitary interaction, the sound velocity at zero temperature in a d-dimensional Fermi gas is predicted to be $v_s/v_F = \sqrt{\xi/d}$, where ξ is the Bertsch parameter $\xi_B = 0.37$ measured in 3D [51, 54]. The result (velvet square) is in good agreement with the measurements.

7.3.3. Model

The preceding discussion requires us to understand the speed of sound as a thermodynamic quantity. In this section, we introduce the hydrodynamic two-fluid model from *L. Landau* and *L. Tisza* [187, 188] and develop a way to derive the sound velocity from the equations of state which are presented in Ch. 6.

The two-fluid model yields a convenient description of the speed of sound in 2D. It is based on a normal component, which behaves like an ordinary fluid, and a superfluid component with zero viscosity and zero entropy, both co-existing in one liquid. At zero temperature, the entire liquid is superfluid and above a certain critical temperature, the entire liquid is in the normal state. The total density of the liquid is the sum of the independent densities of superfluid and normal component $\rho = \rho_s + \rho_n$.

any temperature $T_{BKT} > T > 0$ was found numerically [41].

To apply the two-fluid model, the thermal component has to be in the collisional limit where the gas constituents collide frequently so that hydrodynamics apply[1]. In a Fermi liquid, the collision time $\tau \propto T^2$ strongly decreases at low temperatures T and the hydrodynamic limit is only reached for modes of low frequency ω such that $\tau\omega \ll 1$ [189]. The existence of a trapping potential gives rise to a lower limit to the sound mode frequency, i. e. the hydrodynamic regime is not necessarily achieved. However, it was shown that the assumption of the collisional limit holds in a wide range of temperature and interaction [145, 190–192]. In a strongly interacting Fermi gas, the scattering length is much larger than the interparticle spacing, thus collisions are generally more effective and the thermal component easily enters the hydrodynamic regime. Far on the BEC side, the weakly interacting thermal component of the BEC is very dilute and the assumption of being in the collisional regime becomes doubtful.

The two-fluid hydrodynamic equations of motion describe the systems dynamics of both, Bose or Fermi gases, in three and two dimensions [184, 189]

$$\frac{\partial \rho}{\partial t} + \nabla \mathbf{j} = 0, \qquad \frac{\partial s}{\partial t} + \nabla(s\mathbf{v}_n) = 0, \tag{7.2}$$

$$m\frac{\partial \mathbf{v}_n}{\partial t} = -\nabla(\mu + V_{ext}), \qquad \frac{\partial \mathbf{j}}{\partial t} = -\nabla P - n\nabla V_{ext}. \tag{7.3}$$

With the entropy density s, the current density $\mathbf{j} = \rho_s \mathbf{v}_s + \rho_n \mathbf{v}_n$, the mass density ρ, and the chemical potential μ. The trapping potential is denoted by V_{ext} and $s = S/N$ is the entropy density. From Eq. 7.2 and 7.3 we can predict the existence of two sound velocities. Assuming a tight confinement in the vertical direction without additional confinement in the 2D plane, the two velocities are given by the two non-negative solutions of

$$u^4 - \frac{T}{m}\left(\frac{1}{nT\kappa_S} + \frac{\bar{s}^2 n_s}{\bar{c}_V n_n}\right)u^2 + \frac{T^2\bar{s}^2 n_s}{m^2 \bar{c}_V n_n n T \kappa_T} = 0. \tag{7.4}$$

Here, the 2D thermodynamic quantities are the specific heat at constant volume $\bar{c}_V$, the entropy density $\bar{s}$, the superfluid and normal densities n_s and n_n, and the isothermal and adiabatic compressibility κ_T and κ_S, respectively [184]. The two solutions of Eq. 7.4 are respectively the first and second sound u_1 and u_2, where $u_1 > u_2$.

In general, the first speed of sound u_1 denotes a density modulation where superfluid and normal component are in phase, see Fig. 7.7, and is essentially an iso-entropic wave. The second sound u_2 corresponds to a local entropy or temperature perturbation manifested as an isobaric wave with the normal and superfluid components oscillating with opposite phase. At zero temperature

[1] Hydrodynamic behaviour is characterized by a mean free path of the atoms smaller than the systems size. Then, the properties of the gas are strongly influenced by inter-particle collisions.

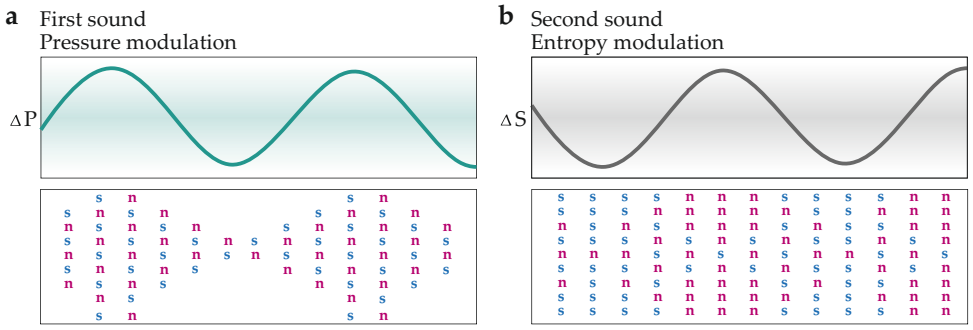

Figure 7.7.: Two-fluid description of first and second sound. The symbols in the lower pictures depict schematically the normal and superfluid density component. The total density is represented by the sum along a column. a) In case of first sound, the excitation is a pressure modulation ΔP associated with a density wave. The two components move in phase with each other. b) Second sound describes fluctuations in entropy ΔS, driven by temperature changes in the normal fluid. Normal and superfluid component are out of phase, such that the density remains constant. The figure is adapted from Ref. [193]

second sound does not exist and as it depends on the superfluid fraction, u_2 vanishes above the critical temperature. First sound exists at zero temperature, in both, the BEC and BCS regime.

Finite temperatures cause a coupling between density and temperature oscillations, i. e. the two sound velocities mix. In general, this coupling can be described in terms of the Landau-Placzek ratio $(\bar{c}_P - \bar{c}_V)/\bar{c}_V$, where $\bar{c}_P$ and $\bar{c}_V$ are the heat capacities at constant pressure and density. To simplify the discussion, we assume the temperature to be sufficiently low $T \to 0$. Then, the entropy carrying thermal component vanishes and the heat capacities become equal, $\bar{c}_P = \bar{c}_V$. Therefore, the Landau-Placzek ratio equals zero and the coupling between first and second sound is insignificant.

According to Landaus hydrodynamic equations, the first sound $u_1 = v_s$ is then well represented by the isothermal sound defined by the isothermal compressibility κ_T, as

$$v_s^2 = \frac{1}{mn}\frac{1}{\kappa_T} = \frac{1}{m}\left.\frac{\partial P}{\partial \rho}\right|_T \tag{7.5}$$

$$\backsimeq \frac{n}{m}\left.\frac{\partial \mu}{\partial n}\right|_T . \tag{7.6}$$

Equation 7.6 connects the speed of sound v_s to the chemical potential μ. It is valid at zero and finite temperature for a trapped 2D system [41]. Below, we use Eq. 7.6 to derive the speed of sound from the theoretical 2D equation of state predictions, see Ch. 6.

Mean Field Theory The speed of sound as a fundamental thermodynamic phenomenon is directly connected to the equation of state. Yet again, it is instructive to begin with the appealingly simple mean field picture at zero temperature [155]. In Sec. 6.4.2, we found $\mu = E_F - \frac{E_B}{2}$ for the chemical potential within 2D MFT. This is valid in the entire crossover. With this chemical potential, the speed of sound is

$$v_s^2 = \frac{n}{m}\frac{\partial}{\partial n}\left(E_F - \frac{E_B}{2}\right). \tag{7.7}$$

We express the speed of sound in terms of the Fermi velocity v_F, using the Fermi energy $E_F = \hbar^2\pi n/m$, and arrive at

$$\frac{v_s}{v_F} = \frac{1}{\sqrt{2}}. \tag{7.8}$$

This is the result we know from the discussion in Sec. 7.3.2, which is identical to the one obtained within the beyond MFT formalism taking phase and amplitude fluctuations into account [41].

Note that the simple MFT substantially overestimated the effective dimer-dimer interaction in the BEC regime, see Ch. 6. The effective chemical potential only describes the gas correctly in the limit of a non-interacting Fermi gas[1]. We naïvely try to find a statement about the BEC regime by introducing a boson chemical potential $\mu_d = 2E_F = 2\mu + E_B$ [113]. This, however, produces the same result $1/\sqrt{2}$, i. e. we will not improve our description on the grounds of MFT.

Equation of State We now turn to the speed of sound derivation from more accurate crossover theories including higher order perturbative expansions and QMC quantum simulations. The corresponding equations of state, which are discussed in Ch. 6, can generally be expressed in the form

$$E/N - |E_B|/2 = \epsilon(x)E_{FG}, \tag{7.9}$$

which is the energy per particle, or energy density E/N. Here, the two-body bound state energy $|E_B|/2$ is again subtracted to expose the many-body corrections. E_{FG} is the energy of a free non-interacting Fermi gas.

We write $\epsilon(x)$ as a function of the interaction parameter $\ln(k_F a_{2D})$. It follows for the chemical potential

$$\mu(x) = \frac{\partial\epsilon(x)}{\partial N}NE_{FG} + \epsilon(x)N\frac{\partial E_{FG}}{\partial N} + \epsilon(x)E_{FG} \tag{7.10}$$

$$= \frac{\partial\epsilon(x)}{\partial x}\frac{NE_{FG}}{2N} + 2\epsilon(x)E_{EG}. \tag{7.11}$$

[1] The result for a non-interacting 3D Fermi gas can be identified with the Bogoliubov-Anderson mode similar to the sound velocity $v_s^{3D}/v_F^{3D} = 1/\sqrt{3}$.

The first term in Eq. 7.10 is deduced by expanding the partial derivation $\frac{\partial}{\partial N}$ and taking the first derivative $\frac{\partial}{\partial x}\ln(k_F a_{2D})$. To determine the speed of sound, we use Eq. 7.6 and the thermodynamic relation $\mu = \frac{\partial E}{\partial N}$. We formulate the total energy E by multiplying $\epsilon(x)$ with E_{FG} and the total atom number N. This finally gives an expression to derive the speed of sound v_s from the equation of state $\epsilon(x)$

$$v_s^2 = \frac{v_F^2}{8}\left(\frac{1}{2}\frac{\partial^2}{\partial x^2}\epsilon(x) + 3\frac{\partial}{\partial x}\epsilon(x) + 4\epsilon(x)\right). \tag{7.12}$$

With Eq. 7.12, we calculated all theoretical speeds of sound which are shown in Fig. 7.6.

To derive the sound velocity from the experimental pressure equation of state, we follow a similar approach. As it is shown in Sec. 7.4, we fit the normalized pressure P_T/P_0 with a typically used arctan-function, where the pressure is a function of the interaction parameter $x = \ln(k_F a_{2D})$. We thus obtain an analytical representation $\eta(x)$ of our pressure equation of state. Using the thermodynamic relation in Eq. 7.5, we get

$$v_s^2 = v_F^2\left(\frac{1}{4}\frac{\partial}{\partial x}\eta(x) + \frac{1}{2}\eta(x)\right). \tag{7.13}$$

7.4. Equation of State

Understanding the thermodynamics of 2D Fermi gases along the BEC-BCS crossover is particularly challenging, see Ch. 6. Despite the complexity of these systems, all microscopic and macroscopic properties are encapsulated within a single thermodynamic equation of state, yielding access to any thermodynamic quantity under a given condition. Due to the preliminary status of our results on the equation of state, this section is kept deliberately short.

7.4.1. Experimental Procedure

One strategy to obtain the equation of state experimentally is to analyse in-situ absorption images of the atomic cloud [194]. This gives direct access to the 2D density distribution $n(\mathbf{r})$. With these pictures, we are able to determine, e. g. the isothermal pressure $P(V)|_T = P_T(V)$ and the compressibility $\kappa(V)|_T = \kappa_T(V)$ without requiring knowledge of the gas temperature or the chemical potential.

The 2D clouds are prepared as reported in Sec. 7.3. We acquire the mean of ten absorption images of identical 2D gases at a certain value of the interaction parameter $\ln(k_F a_{2D})$ in the BEC-BCS crossover.

Towards the BCS regime, the Fermi pressure increases, and the lateral spread of the 2D clouds becomes larger and eventually exceeds the field of view of the microscope objective. To avoid losing important information,

the microscope objective is positioned such that a lateral shift of the objective of about 100 µm enables us to take two different sets of pictures. Each contains the central region and adjacent low-density wings. After averaging, the images are combined to obtain a 2D density profile $n(\mathbf{r})$.

7.4.2. Pressure and Compressibility

In the next step, we deduce the local density $n(V)$ by calculating the shape of the harmonic trapping potential $V(\mathbf{r}) = \frac{m}{2}\omega_{\mathbf{r}} r^2$. The lateral trap frequencies $\omega_x/2\pi = 27\,\mathrm{Hz}$ and $\omega_x/2\pi = 29\,\mathrm{Hz}$ are determined experimentally via parametric heating. Both, the potential $V(\mathbf{r})$ and local density $n(V)$ are contained in a $n \times n$ matrix, from which we obtain a vector representation, where each density value is assigned to a potential strength.

Pressure Numerical integration of $n(V)$ over the potential yields the local isothermal pressure

$$P_T(V) = \int_V^\infty n(\tilde{V})\,d\tilde{V}. \tag{7.14}$$

In Fig. 7.8 a, we show the resulting pressure $P_T(V)/P_0$, normalized by the pressure per spin state $P_0 = \pi\hbar^2 n^2/m$ of an ideal 2D Fermi gas of the same local density, as a function of the trapping potential. The two curves depict data for two different interaction parameters $\ln(k_F a_{2D}) \approx -1.36$ (red circles) and $\ln(k_F a_{2D}) \approx 1.32$ (cyan circles). The former corresponds to a gas far in the BEC regime, whereas the latter depicts a cloud on the BCS side of the resonance.

At the centre of the cloud, where the potential energy is smallest and the density is highest, the normalized pressure of the Bose gas is $0.16\,P/P_0$. Going outwards, as the gas is more dilute, the pressure tends to the value of the ideal Fermi gas $P_T(V) = P_0$. In the opposite case of a fermionic gas of loosely bound Cooper pairs, the central pressure is higher $0.51\,P/P_0$, and changes only gradually over different potential depths.

The central pressure along the BEC-BCS crossover is shown in Fig. 7.8 b. It rises monotonously towards the BCS side as the fermionic character of the gas becomes dominant. The green line is a fit to the data, using the formula given in Eq. 6.67 with the additional boundary condition that the fit approaches the pressure of a non-interacting Fermi gas in the corresponding limit $\ln(k_F a_{2D}) \to \infty$. We compare our results to the pressure equation of state which we derived from the numerical QMC data (grey line), and find excellent agreement with the experiment. The prediction from the composite boson equation of state is depicts as the blue line, see Sec. 6.

With the thermodynamic relation $v_s^2 = \frac{\partial P}{\partial \rho}\Big|_T$ (Eq. 7.5), we extract the isothermal speed of sound and find excellent agreement with the results from the

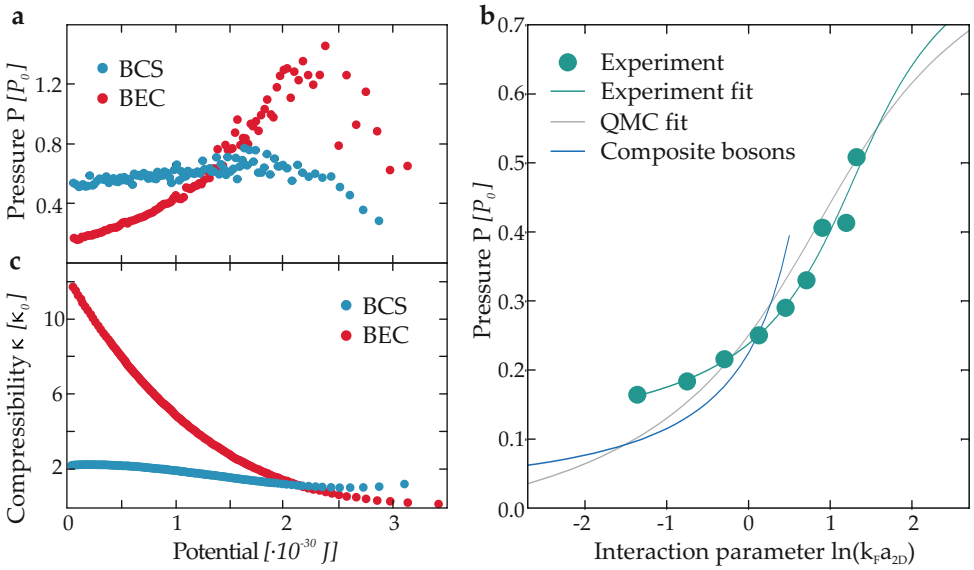

Figure 7.8.: Preliminary results on the 2D equation of state in the BEC-BCS crossover. a) The cyan circles depict the normalized pressure as a function of the trapping potential for a 2D cloud in the BCS regime. The dimensionless interaction parameter is $\ln(k_F a_{2D}) = 1.32$. The position of the smallest potential energy is at the centre of the cloud, i. e. the region of highest density is on the l. h. s. of the plot. The red circles show the pressure in the BEC regime, where the interaction parameter is $\ln(k_F a_{2D}) = -1.36$. b) The results of the pressure equation of state in the crossover are depicted as the green circles. The green line shows a fit to the data. The obtained pressure equation of state from the fit to the numerical QMC results is shown as the grey line. Additionally, the blue line depicts the prediction we obtain from the equation of state for composite bosons. c) The normalized compressibility of the 2D cloud in the BEC and BCS regime.

response experiments, as shown in Sec. 7.3.2. Note that the calculation of the sound velocity from the QMC pressure equation of state and from the corresponding energy density equation of state yield the same result, and thus validates the sound derivation from the experimental equation of state.

In addition to the local pressure, the density $n(V)$ gives access to the local compressibility of the gas

$$\kappa_T(V) = \frac{1}{n}\frac{\partial n(\tilde{V})}{\partial \tilde{V}}, \tag{7.15}$$

which describes the relative change in density in respect to a change in pressure.

In Fig. 7.8 c, we show the normalized isothermal compressibility $\kappa_T(V)/\kappa_0$, where $\kappa_0 = m/(2\pi\hbar^2 n^2)$ is the compressibility of an ideal Fermi gas of the same local density. The curves depict the same two values of the interaction parameter as in the case of the normalized pressure. The normalized compressibility the gas of composite bosons (red circles) is significantly higher than in the interacting gas on the BCS side (cyan circles), where, as expected, the compressibility is higher than that of an ideal Fermi gas without interactions.

The equation of state is subject to ongoing investigations, and in future work we may extend the studies to temperature dependent properties as the onset of superfluidity. In this regard, precise knowledge of the gas temperature is of great importance. Therefore, thermometry of 2D Fermi gases is in the focus of the following section.

7.5. Thermometry

Measuring the temperature of a strongly interacting Fermi gas is notoriously difficult since the corresponding density profile is not known. One method is to adiabatically transform the gas to a weakly interacting Fermi gas by a quick magnetic field ramp deep into the BEC regime [195]. In both cases, one subsequently fits the density profile of a non-interacting gas to the thermal wings of the cloud to access the gas temperature.

Here, we measure the temperature of 2D Fermi gases of arbitrary interaction by combining the iso-entropic formation of deeply bound dimers with a short TOF. During the TOF, the gas expands in a weak harmonic trap, which enables us to probe the initial momentum distribution. As a consequence, the fraction of thermal atoms is more pronounced and hence easier to identify in the momentum space representation. Inter-particle interactions are suddenly switched off by the rapid expansion in the beforehand strongly confinement direction. Therefore, the momentum distribution is not altered and resembles the one of the trapped gas. Note that the method presented here was also realized in Heidelberg very recently [196] and used to determine the phase diagram of a strongly interacting Fermi gas [197].

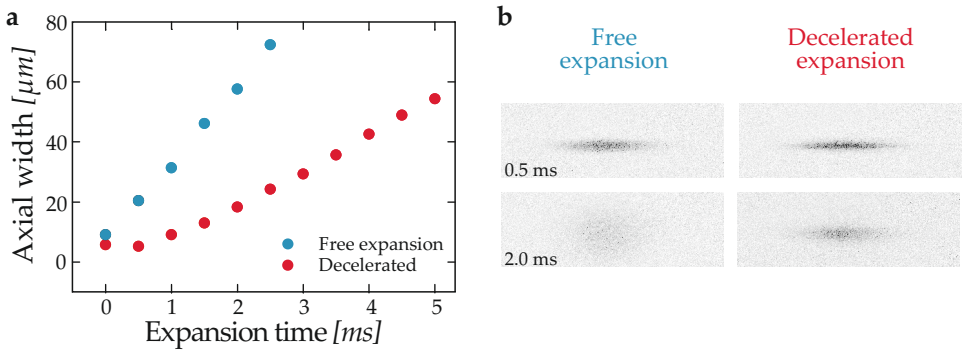

Figure 7.9.: Reduction of the cloud expansion during TOF. a) Due to the strong confinement of the 1D optical lattice in axial direction, the corresponding cloud width rapidly increases during TOF. Applying a confinement pulse by switching on the red-detuned squeeze dipole trap for 200 µs with 100 mW leads to a significant reduction of the cloud width (red circles). The cyan circles depict the axial width after free expansion. b) Corresponding absorption images, taken from the side after after 0.5 ms and 2.0 ms, respectively. The measurement is carried out at a magnetic field strength of 711 G.

7.5.1. Experimental Procedure

First, a 2D cloud is prepared with a certain value of the interaction parameter $\ln(k_F a_{2D})$. To perform the momentum space mapping, we adiabatically ramp the magnetic field to a field strength of 711 G to form a more weakly interacting gas consisting of tightly bound molecules.

Then, the 1D optical lattice is immediately switched off. The strong vertical confinement with a trap frequency of 25 kHz causes the gas to expand rapidly and to lower its density abruptly. Therefore, interaction effects are negligible during the TOF, so that the atoms ballistically expand in the residual weak harmonic trap which is generated by the radial symmetric magnetic field. Since the atoms trajectories are according to their initial momenta, the motion during the TOF corresponds to a translation from the position to the momentum space. After exactly one quarter of the time period of the remaining magnetic potential $t_{1/4} = 1/4(\omega_{trap}/2\pi) \approx 7\,\text{ms}$, the spatial position of each particle represents its initial momentum.

There is a drawback of the rapid decrease in density during the applied TOF. The obtained imaging signal decreases as the atoms quickly leave the short depth-of-field of the high NA microscope objective. We counteract this by limiting the vertical cloud expansion by switching on an additional confinement only a moment after the release from the optical lattice and only for a short amount of time.

This additional confinement is generated by the optical squeeze dipole trap, which is pulsed on with a power of 100 mW for 200 µs after a ballistic

expansion for 250 µs. This short pulse slows down the atoms in the vertical direction and increases the imaging signal significantly. Figure 7.9 shows a comparison of the axial cloud extent with and without the confinement pulse applied. Due to the insignificant influence of the low powered squeeze dipole trap on the radial confinement, the ballistic expansion is not expected to be perturbed.

Finally, after a time $t_{1/4}$ we take an absorption image of the cloud. The spatial distribution now represents the mapped in-situ momentum distribution. The low momentum fraction collapses into the centre and gives rise to a clearly visible bimodal distribution with pronounced thermal wings.

7.5.2. Results

To access the temperature, we fit the momentum distribution of an ideal Bose gas $\propto \exp(-p^2/(2mk_BT))$ to the thermal fraction of the momentum profile. To obtain reliable results, it is important to evaluate the exact extent of the thermal fraction. This is done by minimizing the Gaussian fit uncertainty in dependence of the interval of the outer cloud region which is modelled by the fit function. If the fitted region includes a noticeable non-thermal fraction, the goodness of the fit decreases. Therefore, we are able to determine the optimal fit radii[1].

The resulting cloud temperatures are very consistent along the crossover. The absolute values range from (18 to 22) nK corresponding to 6 % to 8 % of the Fermi temperature T_F.

7.6. Summary

The presented results provide precise information about the thermodynamics of 2D Fermi gases in the regime crossover and help to establish a better understanding where reliable predictions are rare. The main part of this chapter focussed on the speed of sound results in 2D, which are in very good agreement with the sound velocity we derived from recent numerical QMC calculations, while perturbation theories are in qualitative agreement with our data and MFT cannot reproduce the experiment. We furthermore measured the pressure equation of state in the crossover and found the results to be in very good agreement with corresponding results from simulations. The speed of sound we derived from our equation of state data and the results from the direct response experiments are in very good agreement. In addition, we presented preliminary studies of the temperature of 2D Fermi gases and the determination of the quasi-condensate fraction in the BEC-BCS crossover.

[1] More details can be found in the Master's thesis of *N. Luick* [198].

8. Conclusion and Perspectives

Over the years, the investigation of ultracold atomic Fermi gases developed a new level of scientific rigor. Experiments became more and more advanced and reached the technical accuracy for precise studies of quantum gases on a fundamental level. However, this does not necessarily imply that there are less questions left to be addressed. On the contrary, we are nowadays faced with quite the opposite: with studies of increasing accuracy, new surprising effects are found [45, 199].

In this work, we have presented an apparatus for high-resolution studies of ultracold Fermi gases. The experimental setup incorporates a high precision optical system for manipulation and imaging of atomic clouds. The broad magnetic Feshbach resonance of ^{6}Li enabled us to precisely map out the critical velocity v_c in the entire crossover from fermionic to bosonic superfluidity, as presented in Ch. 5. We created a small attractive potential and dragged it along the atomic cloud to demonstrate the breakdown of superfluidity, for the first time in close analogy to Landau's Gedankenexperiment. Numerical simulations in the BEC regime validated the experiment and the high precision measurements made it possible to isolate relevant effects reducing v_c. We furthermore measured the speed of sound in the BEC-BCS crossover and compared it to the critical velocity.

Being directly connected to the dynamics of a many-body system, the sound velocity serves as a benchmark for the equation of state, which is a powerful tool to describe the equilibrium properties of a physical system. Here, quasi-2D Fermi gases are of particular interest. As a direct and profound consequence of the reduced dimensionality, the underlying physics change dramatically. To unravel the open questions it is desirable to perform high precision studies of local properties of 2D systems. In this regard, it is of great importance that we are able to realize isolated single layer clouds under strong confinement deep in the 2D regime. In Ch. 7, we presented the first measurements of the speed of sound in quasi-2D Fermi gases in the BEC-BCS crossover. To benchmark the inconsistent theory predictions for the 2D equation of state, we calculated the corresponding sound velocities and compared them to our measurement. We found very good agreement with recent numerical calculations and were able to invalidate a sophisticated mean field approach. Furthermore, preliminary results on the 2D pressure equation of state were presented. As a crosscheck, we derived the speed of sound from the measured equation of state and found it to be in excellent agreement with the results of the direct method.

The results presented in this work provide valuable input to the development of a comprehensive understanding of the 2D thermodynamics in the BEC-BCS crossover. Where reliable quantitative theories are still missing, quantum gas experiments are able to pioneer the work to bring forth both, theory and experiment. In conclusion, 2D Fermi gases still offer a vast range for possible studies, and we like to mention selected topics which appear the most interesting to us in the following.

Role of Interactions in 2D Recent measurements of dynamical properties appeared to observe that the effect of interactions is much weaker than theoretically predicted. Interactions in 2D gases break the otherwise expected scaling symmetry [200, 201]. One consequence of this broken symmetry is the damping of the breathing mode. Surprisingly, this could not be observed in the experiment [45], and thus indicates only a very weak role of interactions[1]. In contrast, recent spin diffusivity measurements are in accordance with the theoretical predictions [44].

Our apparatus might allow us to probe the spin-diffusivity and the viscosity with different methods, possibly providing new insights into this issue.

Imbalanced 2D Fermi Gases In this work, we emphasized the lack of understanding of quasi-2D Fermi gases, and yet, we have only considered the spin-balanced case. The imbalanced case, featuring a minority and a majority spin species, gives rise to exotic phases. One example is the superfluid FFLO phase, which shows a deformed Fermi surface due to Cooper pairs with finite momenta [42, 43].

Experimental verification the 2D FFLO superfluid is still missing. So far, it has only been observed in condensed matter bulk superconductors [203]. Due to the non-vanishing momenta of the Cooper pairs, the FFLO phase should display density modulations, which should be resolvable with our imaging system. The preparation of highly imbalanced quasi-2D Fermi gases is already possible, as shown in Fig. 8.1.

Mesoscopic 2D Systems We aim to realize mesoscopic systems by imprinting local potentials onto a quasi-2D Fermi gas, creating a small, isolated system of intermediate length-scale. Our experimental setup already provides us with different methods to create arbitrary potential structures.

For instance, using a 2D acousto-optic deflector (AOD) we are in principle able to prepare a ring of attractive potential minima. Ideally, we would populate each minimum with a single atom of alternating spin. The high resolution microscope should enable us to remove one of the atoms in the 1D spin chain. After some evolution of the system over time, the resulting

[1] In the same experiment, the quadrupole mode was observed to be strongly damped, which could be later explained by anisotropy of the trap and temperature effects [202].

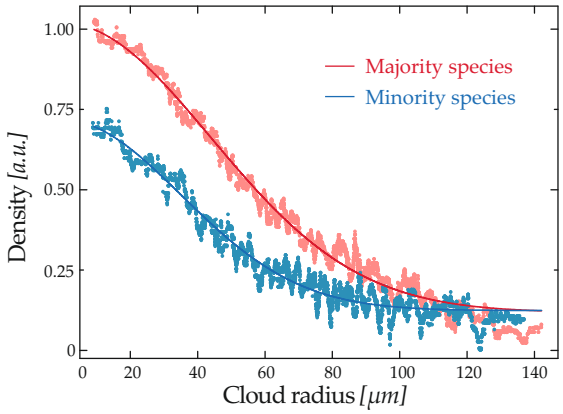

Figure 8.1.: Averaged density profile of an imbalanced 2D Fermi gas. The red circles depict the majority hyperfine state species, the cyan circles the minority species. The ratio is roughly $70:30$ and the total atom number is $14\,000$ atoms. The solid lines are fit curves yielding $1/e^2$ radii of $88\,\mu m$ and $70\,\mu m$ for the majority and minority, respectively. Identical clouds are prepared at a magnetic field strength of $760\,G$ and both species are imaged sequentially.

hole and the spin excitation should have separated and we could observe the phenomenon of spin-charge separation in real space for the first time [32].

With a similar technique, we could realize smaller Hubbard type systems ranging from plaquettes to some 10 by 10 sites. These can be understood as building blocks for quantum simulation of the 2D Fermi Hubbard model [204]. It is expected to describe fundamental aspects of high-temperature superconductors (HTSC) [16, 19, 205], whose existence has been motivating research for decades, and yet, thorough understanding of the underlying processes is still lacking.

The repulsive side of the Hubbard model phase diagram gives rise to the anti-ferromagnet (AFM) phase. So far, experiments were unable to establish the AFM phase ordering. This is mainly due to the major challenge currently to reach low enough temperatures in experiment. This particularly holds for quasi-2D gases, where the strong strong confinement is typically provided by red detuned optical lattices. The inherent trapping in the radial directions makes evaporation in 2D difficult. In this regard, our blue-detuned optical lattice should enable us to achieve the required temperature regime.

BKT Phase Transition The BKT phase transition has only been successfully observed in quasi-2D Bose gases [206]. Yet, local properties are beyond the scope of the applied method, since it probes the self-interference of the entire superfluid. A different way to investigate the BKT transition is to study the correlations in the systems, as the algebraic decay of LRO is characteristic for the BKT superfluid. Furthermore, theory predicts that the corresponding

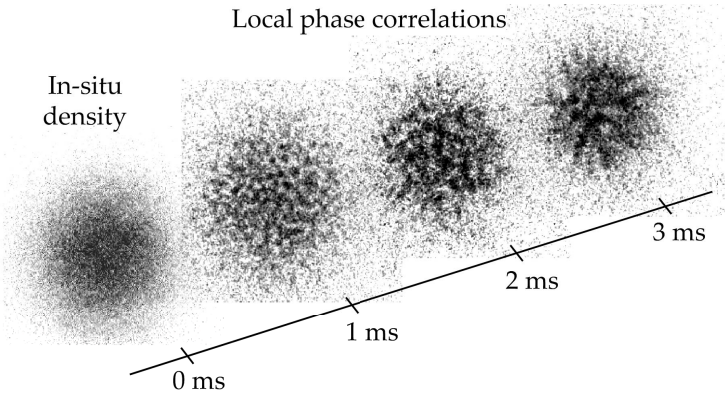

Figure 8.2.: Free expansion as a probe of phase correlations. A 2D Fermi gas consisting of ^{6}Li dimers is released from the tight axial confinement and expands in a shallow magnetic trap. After short expansion times density ripples develop. They give access to the initial in-situ phase correlations.

scaling exponent is directly connected to the superfluid density.

Only recently, we have realized the first spatially resolved studies of phase correlations in 2D Fermi gases. This fundamental quantity is the ideal tool to locally resolve the BKT phase transition for the first time.

We probe the phase correlations after a short TOF of a 2D cloud on the BEC side of the Feshbach resonance. During the expansion, fluctuations transform into density fluctuations, as shown in Fig. 8.2. The spatial correlation analysis allows us to locally access phase fluctuations in areas of specific density. In high density regions, we observe evidence for algebraic decay of phase correlations predicted for the superfluid phase in 2D, whereas towards outer regions of low density there is evidence for the phase transition where phase correlations decay on much shorter length scales.

List of Figures

List of Tables

Acronyms

AFM anti-ferromagnet

AND comparator

AOD acousto-optic deflector

AOM acousto-optic modulator

APC angle-polished connector

BCS Bardeen-Cooper-Schrieffer

BEC Bose-Einstein condensate

BKT Berezinskii-Kosterlitz-Thouless

CAD computer-aided design

CF Conflat

CIR confinement-induced resonance

ECDL external cavity diode laser

EOM electro-optic modulator

EMCCD electron-multiplying charged-couple device

FFLO Fulde-Ferrell-Larkin-Ovchinnikov

FL Fermi liquid

FPGA field programmable gate array

GUI graphical user interface

HTSC high-temperature superconductors

ID Identification number

IGBT insulated-gate bipolar transistor

LDA local density approximation

LRO long-range order

MFT Mean Field Theory

MOT magneto-optical trap

MWH Mermin-Wagner-Hohenberg

NA numerical aperture

NSR Nozières and Schmitt-Rink

OD optical density

ODLRO off-diagonal long range order

PD photo-diode

PI proportional-integral

PDH Pound-Drever Hall

QPD quadrant photodiode

QMC Quantum Monte Carlo

rf radio-frequency

SN serial number

TA tapered amplifier

TOF time of flight

TTL transistor-transistor logic

UHV ultra-high vacuum

1D one-dimensional

2D two-dimensional

3D three-dimensional

Bibliography

[1] B. DeMarco and D. S. Jin, "Onset of Fermi Degeneracy in a Trapped Atomic Gas," *Science*, vol. 285, no. 5434, pp. 1703–1706, 1999.

[2] S. Jochim, M. Bartenstein, A. Altmeyer, G. Hendl, S. Riedl, C. Chin, J. Hecker-Denschlag, and R. Grimm, "Bose-Einstein condensation of molecules.," *Science*, vol. 302, no. 5653, pp. 2101–3, 2003.

[3] C. A. Regal and D. S. Jin, "Measurement of Positive and Negative Scattering Lengths in a Fermi Gas of Atoms," *Phys. Rev. Lett.*, vol. 90, no. 23, p. 230404, 2003.

[4] M. W. Zwierlein, C. A. Stan, C. H. Schunck, S. Raupach, S. Gupta, Z. Hadzibabic, and W. Ketterle, "Observation of Bose-Einstein Condensation of Molecules," *Phys. Rev. Lett.*, vol. 91, no. 25, p. 250401, 2003.

[5] C. Chin, R. Grimm, P. Julienne, and E. Tiesinga, "Feshbach resonances in ultracold gases," *Rev. Mod. Phys.*, vol. 82, no. 2, pp. 1225–1286, 2010.

[6] W. Zwerger, *The BCS-BEC Crossover and the Unitary Fermi Gas. Lecture Notes in Physics.* Springer, 2011.

[7] W. Ketterle and M. W. Zwierlein, "Making, probing and understanding ultracold Fermi gases," *ArXiv Prepr.*, no. June 2006, pp. 20 – 30, 2008.

[8] I. Bloch, J. Dalibard, and W. Zwerger, "Many-body physics with ultracold gases," *Rev. Mod. Phys.*, vol. 80, no. 3, pp. 885–964, 2008.

[9] S. Giorgini, S. Stringari, and L. P. Pitaevskii, "Theory of ultracold atomic Fermi gases," *Rev. Mod. Phys.*, vol. 80, no. 4, pp. 1215–1274, 2008.

[10] M. R. Schafroth, S. Butler, and J. Blatt *Helv. Phys. Acta*, pp. 30–93, 1957.

[11] D. M. Eagles, "Possible Pairing without Superconductivity at Low Carrier Concentrations in Bulk and Thin-Film Superconducting Semiconductors," *Phys. Rev.*, vol. 186, no. 2, pp. 456–464, 1969.

[12] A. J. Leggett, "Cooper Pairing in Spin-Polarized Fermi Systems," *J. Phys.*, vol. 7, no. 41, pp. 7–19, 1980.

[13] P. Nozières and S. Schmitt-Rink, "Bose Condensation in an Attractive Fermion Gas : From Weak to Strong Coupling Superconductivity," *J. Low Temp. Phys.*, vol. 59, no. 3/4, pp. 195–211, 1985.

[14] P. Kapitza, "Viscosity of Liquid Helium below the Lambda point," *Nature*, vol. 141, p. 74, 1938.

[15] J. F. Allen and A. D. Misener, "Flow of Liquid Helium II," *Nature*, vol. 141, p. 75, 1938.

[16] E. Dagotto, "Correlated electrons in high-temperature superconductors," *Rev. Sci. Instrum.*, vol. 66, no. 3, pp. 763–840, 1994.

[17] D. C. Tsui, H. L. Stormer, and A. C. Gossard, "Two-Dimensional Magnetotransport in the Extreme Quantum Limit," *Phys. Rev. Lett.*, vol. 48, no. 22, pp. 1559–1562, 1982.

[18] A. Damascelli, "Angle-resolved photoemission studies of the cuprate superconductors," *Rev. Mod. Phys.*, vol. 75, pp. 473–541, 2003.

[19] P. A. Lee and X.-G. Wen, "Doping a Mott insulator: Physics of high-temperature superconductivity," *Rev. Mod. Phys.*, vol. 78, no. 1, pp. 17–85, 2006.

[20] C. N. Yang, "Concept of Off-Diagonal Long-Range Order and the Quantum Phases of Liquid He and of Superconductors," *Rev. Mod. Phys.*, vol. 84, no. 4, pp. 694–702, 1962.

[21] M. V. Feigel'man, V. B. Geshkenbein, and A. Larkin, "Pinning and creep in layered superconductors," *Phys. C*, vol. 167, no. 1-2, pp. 177–187, 1990.

[22] N. D. Gemelke, X. Zhang, C. L. Hung, and C. Chin, "In situ observation of incompressible Mott-insulating domains in ultracold atomic gases.," *Nature*, vol. 460, no. 7258, pp. 995–8, 2009.

[23] T. Müller, B. Zimmermann, J. Meineke, J.-P. Brantut, T. Esslinger, and H. Moritz, "Local Observation of Antibunching in a Trapped Fermi Gas," *Phys. Rev. Lett.*, vol. 105, no. 4, p. 040401, 2010.

[24] W. S. Bakr, A. Peng, M. E. Tai, R. Ma, J. Simon, J. I. Gillen, S. Fölling, L. Pollet, and M. Greiner, "Probing the superfluid-to-Mott insulator transition at the single-atom level," *Science*, vol. 329, no. 5991, pp. 547–50, 2010.

[25] I. Bloch, J. Dalibard, and S. Nascimbène, "Quantum simulations with ultracold quantum gases," *Nat. Phys.*, vol. 8, no. 4, pp. 267–276, 2012.

[26] D. Stadler, S. Krinner, J. Meineke, J.-P. Brantut, and T. Esslinger, "Observing the drop of resistance in the flow of a superfluid Fermi gas.," *Nature*, vol. 491, no. 7426, pp. 736–9, 2012.

[27] J.-P. Brantut, J. Meineke, D. Stadler, S. Krinner, and T. Esslinger, "Conduction of ultracold fermions through a mesoscopic channel.," *Science*, vol. 337, no. 6098, pp. 1069–71, 2012.

[28] J.-P. Brantut, C. Grenier, J. Meineke, D. Stadler, S. Krinner, C. Kollath, T. Esslinger, and A. Georges, "A thermoelectric heat engine with ultracold atoms.," *Science*, vol. 342, no. 6159, pp. 713–5, 2013.

[29] W. Weimer, *Probing superfluid properties in strongly correlated Fermi gases with high spatial resolution*. Institute of Laser-Physics, University of Hamburg, 2014.

[30] B. Paredes, A. Widera, V. Murg, O. Mandel, S. Fölling, I. Cirac, G. V. Shlyapnikov, T. W. Hänsch, and I. Bloch, "Tonks-Girardeau gas of ultracold atoms in an optical lattice," *Nature*, vol. 429, no. 6989, pp. 275–7, 2004.

[31] T. Kinoshita, T. Wenger, and D. S. Weiss, "Observation of a one-dimensional Tonks-Girardeau gas.," *Science*, vol. 305, no. 5687, pp. 1125–8, 2004.

[32] J. M. Luttinger, "An Exactly Soluble Model of a Many-Fermion System," *J. Math. Phys.*, vol. 4, no. 9, p. 1154, 1963.

[33] T. Giamarchi, *Quantum Physics in One Dimension*. Oxford: Oxford University Press, 1991.

[34] R. E. Peierls, "Suppl. II," *Helv. Phys. Acta.*, vol. 7, 1934.

[35] D. Mermin and H. Wagner, "Absence of Ferromagnetism or Antiferromagnetism in One- or Two-dimensional Isotropic Heisenberg Models," *Phys. Rev. Lett.*, vol. 17, no. 22, pp. 1133–1136, 1966.

[36] P. Hohenberg, "Existence of long-range order in one and two dimensions," *Physical Review*, vol. 158, no. 2, 1966.

[37] V. L. Berenzinskii, "Destruction of Long-range Order in One-dimensional and Two-dimensional Systems Possessing a Continious Symmetry Group. II. Quantum Systems," *Sov. Phys. JETP*, vol. 34, pp. 610–616, 1973.

[38] J. M. Kosterlitz and D. J. Thouless, "Ordering, metastability and phase transition in two-dimensional systems," *Solid State Phys.*, vol. 6, pp. 1181–1203, 1973.

[39] D. S. Petrov and G. V. Shlyapnikov, "Interatomic collisions in a tightly confined Bose gas," *Phys. Rev. A*, vol. 64, no. 1, pp. 1–14, 2001.

[40] G. Bertaina and S. Giorgini, "BCS-BEC Crossover in a Two-Dimensional Fermi Gas," *Phys. Rev. Lett.*, vol. 106, no. 11, p. 110403, 2011.

[41] L. Salasnich, P. A. Marchetti, and F. Toigo, "Superfluidity, sound velocity, and quasicondensation in the two-dimensional BCS-BEC crossover," *Phys. Rev. A*, vol. 053612, pp. 1–7, 2013.

[42] P. Fulde and R. A. Ferrell, "Superconductivity in a strong spin-exchange field," *Physical Review*, vol. 135, no. A550, 1964.

[43] A. Larkin and Y. Ovchinnikov, "Inhomogeneous state of superconductors," *JETP*, vol. 47, no. 762, 1965.

[44] M. Koschorreck, D. Pertot, E. Vogt, and M. Köhl, "Universal spin dynamics in two-dimensional Fermi gases," *Nature*, vol. 9, no. 7, pp. 405–409, 2013.

[45] E. Vogt, M. Feld, B. Fröhlich, D. Pertot, M. Koschorreck, and M. Köhl, "Scale Invariance and Viscosity of a Two-Dimensional Fermi Gas," *Phys. Rev. Lett.*, vol. 108, no. 7, p. 070404, 2012.

[46] M. Inguscio, S. Stringari, and C. E. Wieman, *Bose-Einstein Condensation in Atomic Gases*. Amsterdam: IOS Press, 1999.

[47] A. J. Moerdijk, B. J. Verhaar, and A. Axelsson, "Resonances in ultracold collisions of 6Li, 7Li, and 23Na," *Phys. Rev. A*, vol. 51, no. 6, pp. 4852–4861, 1995.

[48] M. Bartenstein, A. Altmeyer, S. Riedl, R. Geursen, S. Jochim, C. Chin, J. Denschlag, R. Grimm, A. Simoni, E. Tiesinga, C. Williams, and P. Julienne, "Precise Determination of 6Li Cold Collision Parameters by Radio-Frequency Spectroscopy on Weakly Bound Molecules," *Phys. Rev. Lett.*, vol. 94, no. 10, p. 103201, 2005.

[49] M. E. Gehm, "Properties of Li-6." 2003.

[50] C. H. Schunck, M. W. Zwierlein, C. A. Stan, S. M. F. Raupach, and W. Ketterle, "Feshbach resonances in fermionic 6Li," *Phys. Rev. A*, vol. 71, no. 4, p. 045601, 2005.

[51] G. Zürn, T. Lompe, A. N. Wenz, S. Jochim, P. Julienne, and J. Hutson, "Precise Characterization of 6Li Feshbach Resonances Using Trap-Sideband-Resolved RF Spectroscopy," *Phys. Rev. Lett.*, vol. 110, no. 13, p. 135301, 2013.

[52] C. A. R. Sá de Melo, "When fermions become bosons: Pairing in ultracold gases," *Phys. Today*, vol. 61, no. 10, pp. 45–51, 2008.

[53] J. Bardeen, L. N. Cooper, and J. R. Schrieffer, "Theory of Superconductivity," *Phys. Rev.*, vol. 108, no. 5, pp. 1175–1204, 1957.

[54] M. Ku, A. T. Sommer, L. W. Cheuk, and M. W. Zwierlein, "Revealing the superfluid lambda transition in the universal thermodynamics of a unitary Fermi gas," *Science*, vol. 335, no. 6068, pp. 563–7, 2012.

[55] S. Tan, "Energetics of a strongly correlated fermi gas," *Annual Physics*, vol. 323, pp. 2952–2970, 2008.

[56] S. Tan, "Large momentum part of a strongly correlated fermi gas," *Annual Physics*, vol. 323, pp. 2971–2986, 2008.

[57] S. Tan, "Generalized virial theorem and pressure relation for a strongly correlated fermi gas," *Annual Physics*, vol. 323, pp. 2987–2990, 2008.

[58] E. Kuhnle, S. Hoinka, P. Dyke, H. Hu, P. Hannaford, and C. J. Vale, "Temperature Dependence of the Universal Contact Parameter in a Unitary Fermi Gas," *Phys. Rev. Lett.*, vol. 106, no. 17, pp. 21–24, 2011.

[59] R. J. Wild, P. Makotyn, J. M. Pino, E. A. Cornell, and D. S. Jin, "Measurements of Tan's Contact in an Atomic Bose-Einstein Condensate," *Phys. Rev. Lett.*, vol. 108, no. 14, p. 145305, 2012.

[60] E. Arimondo, M. Inguscio, and P. Violino, "Experimental determinations of the hyperfine structure in the alkali atoms," *Rev. Mod. Phys.*, vol. 49, no. q, pp. 31–76, 1977.

[61] W. D. Phillips and H. Metcalf, "Laser Deceleration of an Atomic Beam," *Phys. Rev. Lett.*, vol. 48, no. 9, pp. 596–599, 1982.

[62] K. Hueck, *Erzeugung uns Untersuchung von ultrakalten, zweidimensionalen Fermi-Gasen*. Institute of Laser-Physics, University of Hamburg, 2013.

[63] A. Görlitz, J. Vogels, A. Leanhardt, C. Raman, T. Gustavson, J. R. Abo-Shaeer, A. Chikkatur, S. Gupta, S. Inouye, T. Rosenband, and W. Ketterle, "Realization of Bose-Einstein Condensates in Lower Dimensions," *Phys. Rev. Lett.*, vol. 87, no. 13, p. 130402, 2001.

[64] N. L. Smith, W. H. Heathcote, G. Hechenblaikner, E. Nugent, and C. J. Foot, "Quasi-2D confinement of a BEC in a combined optical and magnetic potential," *J. Phys. B At. Mol. Opt. Phys.*, vol. 38, no. 3, pp. 223–235, 2005.

[65] C. Orzel, A. K. Tuchman, M. L. Fenselau, M. Yasuda, and M. A. Kasevich, "Squeezed states in a Bose-Einstein condensate.," *Science*, vol. 291, no. 5512, pp. 2386–9, 2001.

[66] S. Burger, F. S. Cataliottu, C. Fort, P. Maddaloni, F. Minardi, and M. Inguscio, "Quasi-2D Bose-Einstein condensation in an optical lattice," *Europhys. Lett.*, vol. 1, no. 57, pp. 1–6, 2002.

[67] M. Köhl, H. Moritz, T. Stöferle, C. Schori, and T. Esslinger, "Superfluid to Mott insulator transition in one, two, and three dimensions," *J. Low Temp. Phys.*, vol. 138, no. 3-4, pp. 635–644, 2005.

[68] O. Morsch and M. Oberthaler, "Dynamics of Bose-Einstein condensates in optical lattices," *Rev. Mod. Phys.*, vol. 78, no. 1, pp. 179–215, 2006.

[69] I. Spielman, W. D. Phillips, and J. Porto, "Mott-Insulator Transition in a Two-Dimensional Atomic Bose Gas," *Phys. Rev. Lett.*, vol. 98, no. 8, p. 080404, 2007.

[70] K. J. Günter, T. Stöferle, H. Moritz, M. Köhl, and T. Esslinger, "p-Wave Interactions in Low-Dimensional Fermionic Gases," *Phys. Rev. Lett.*, vol. 95, no. 23, p. 230401, 2005.

[71] X. Du, Y. Zhang, and J. E. Thomas, "Inelastic Collisions of a Fermi Gas in the BEC-BCS Crossover," *Phys. Rev. Lett.*, vol. 102, no. 25, p. 250402, 2009.

[72] G. Modugno, F. Ferlaino, R. Heidemann, G. Roati, and M. Inguscio, "Production of a Fermi gas of atoms in an optical lattice," *Phys. Rev. A*, vol. 68, no. 1, p. 011601, 2003.

[73] D. Schrader, I. Dotsenko, M. Khudaverdyan, Y. Miroshnychenko, A. Rauschenbeutel, and D. Meschede, "Neutral Atom Quantum Register," *Phys. Rev. Lett.*, vol. 93, no. 15, p. 150501, 2004.

[74] S. Stock, Z. Hadzibabic, B. Battelier, M. Cheneau, and J. Dalibard, "Observation of Phase Defects in Quasi-Two-Dimensional Bose-Einstein Condensates," *Phys. Rev. Lett.*, vol. 95, no. 19, p. 190403, 2005.

[75] Z. Hadzibabic, S. Stock, B. Battelier, V. Bretin, and J. Dalibard, "Interference of an Array of Independent Bose-Einstein Condensates," *Phys. Rev. Lett.*, vol. 93, no. 18, p. 180403, 2004.

[76] J. Thielking, *Stabilisierung der Frequenzverdopplung eines Nd:YAG-Hochleistungsfaserlasers*. Institute of Laser-Physics, University of Hamburg, 2012.

[77] D. O. Sabulsky, C. V. Parker, N. D. Gemelke, and C. Chin, "Efficient continuous-duty Bitter-type electromagnets for cold atom experiments.," *Rev. Sci. Instrum.*, vol. 84, no. 10, p. 104706, 2013.

[78] B. Zimmermann, *Microscopy of Ultra-cold Fermionic Lithium*. ETH Zurich, 2010.

[79] T. Tiecke, S. Gensemer, A. Ludewig, and J. Walraven, "High-flux two-dimensional magneto-optical-trap source for cold lithium atoms," *Phys. Rev. A*, vol. 80, no. 1, p. 013409, 2009.

[80] W. Weimer, K. Morgener, V. P. Singh, J. Siegl, K. Hueck, N. Luick, L. Mathey, and H. Moritz, "The critical velocity in the bec-bcs crossover." arXiv:cond-mat/1408.5239v1, accepted in Phys. Rev. L., 2014.

[81] R. Onofrio, C. Raman, J. Vogels, J. R. Abo-Shaeer, A. Chikkatur, and W. Ketterle, "Observation of Superfluid Flow in a Bose-Einstein Condensed Gas," *Phys. Rev. Lett.*, vol. 85, no. 11, pp. 2228–2231, 2000.

[82] C. Raman, M. Köhl, R. Onofrio, D. S. Durfee, C. Kuklewicz, Z. Hadzibabic, and W. Ketterle, "Evidence for a Critical Velocity in a Bose-Einstein Condensed Gas," *Phys. Rev. Lett.*, vol. 83, no. 13, pp. 2502–2505, 1999.

[83] M. W. Zwierlein, J. R. Abo-Shaeer, A. Schirotzek, C. H. Schunck, and W. Ketterle, "Vortices and superfluidity in a strongly interacting Fermi gas.," *Nature*, vol. 435, no. 7045, pp. 1047–51, 2005.

[84] A. Ramanathan, K. C. Wright, S. R. Muniz, M. Zelan, W. T. Hill, C. J. Lobb, K. Helmerson, W. D. Phillips, and G. K. Campbell, "Superflow in a Toroidal Bose-Einstein Condensate: An Atom Circuit with a Tunable Weak Link," *Phys. Rev. Lett.*, vol. 106, no. 13, p. 130401, 2011.

[85] R. Desbuquois, L. Chomaz, T. Yefsah, J. Léonard, J. Beugnon, C. Weitenberg, and J. Dalibard, "Superfluid behaviour of a two-dimensional Bose gas," *Nature*, vol. 8, no. 9, pp. 645–648, 2012.

[86] W. Ketterle, D. S. Durfee, and D. M. Stamper-Kurn, "Making, probing and understanding Bose-Einstein condensates," *Arxiv Prepr.*, 1999.

[87] J. S. Stieß berger and W. Zwerger, "Critical velocity of superfluid flow past large obstacles in Bose-Einstein condensates," *Phys. Rev. A*, vol. 62, no. 061601, pp. 1–4, 2000.

[88] D. E. Miller, J. K. Chin, C. A. Stan, Y. Liu, W. Setiawan, C. Sanner, and W. Ketterle, "Critical velocity for superfluid flow across the BEC-BCS crossover," *Phys. Rev. Lett.*, vol. 99, no. 070402, 2007.

[89] G. Watanabe, F. Dalfovo, F. Piazza, L. P. Pitaevskii, and S. Stringari, "Critical velocity of superfluid flow through single-barrier and periodic potentials," *Phys. Rev. A*, vol. 80, no. 5, p. 053602, 2009.

[90] Y. Yunomae, I. Danshita, D. Yamamoto, N. Yokoshi, and S. Tsuchiya, "Current-induced instability of superfluid Fermi gases in optical lattices," *J. Phys. Conf. Ser.*, vol. 150, no. 3, p. 032128, 2009.

[91] G. Watanabe, F. Dalfovo, L. P. Pitaevskii, and S. Stringari, "Effects of periodic potentials on the critical velocity of superfluid Fermi gases in the BCS-BEC crossover," *Phys. Rev. A*, vol. 83, no. 3, p. 033621, 2011.

[92] J. Joseph, B. Clancy, L. Luo, J. Kinast, A. Turlapov, and J. E. Thomas, "Measurement of Sound Velocity in a Fermi Gas near a Feshbach Resonance," *Phys. Rev. Lett.*, vol. 98, no. 17, p. 170401, 2007.

[93] M. Horikoshi, S. Nakajima, M. Ueda, and T. Mukaiyama, "Measurement of universal thermodynamic functions for a unitary Fermi gas," *Science*, vol. 327, no. 5964, pp. 442–5, 2010.

[94] L. A. Sidorenkov, M. K. Tey, R. Grimm, Y.-H. Hou, L. P. Pitaevskii, and S. Stringari, "Second sound and the superfluid fraction in a Fermi gas with resonant interactions.," *Nature*, vol. 498, no. 7452, pp. 78–81, 2013.

[95] B. Zimmermann, T. Müller, J. Meineke, T. Esslinger, and H. Moritz, "High-resolution imaging of ultracold fermions in microscopically tailored optical potentials," *New J. Phys.*, vol. 13, no. 4, p. 043007, 2011.

[96] L. Carr, G. V. Shlyapnikov, and Y. Castin, "Achieving a BCS Transition in an Atomic Fermi Gas," *Phys. Rev. Lett.*, vol. 92, no. 15, p. 150404, 2004.

[97] G. Reinaudi, T. Lahaye, Z. Wang, and D. Guéry-Odelin, "Strong saturation absorption imaging of dense clouds of ultracold atoms.," *Opt. Lett.*, vol. 32, no. 21, pp. 3143–5, 2007.

[98] R. Combescot, M. Kagan, and S. Stringari, "Collective mode of homogeneous superfluid Fermi gases in the BEC-BCS crossover," *Phys. Rev. A*, vol. 74, no. 4, p. 042717, 2006.

[99] M. Marini, F. Pistolesi, and G. C. Strinati, "Evolution from BCS superconductivity to Bose condensation: analytic results for the crossover in three dimensions," *Eur. Phys. J. B*, vol. 1, no. 2, pp. 151–159, 1998.

[100] B. Mühlschlegel, "Die thermodynamischen Funktionen des Supraleiters," *Zeitschrift fur Phys.*, vol. 155, no. 3, pp. 313–327, 1959.

[101] P. Capuzzi, P. Vignolo, F. Federici, and M. P. Tosi, "Sound propagation in elongated superfluid fermionic clouds," *Phys. Rev. A*, vol. 73, no. 2, p. 021603, 2006.

[102] G. Bertaina, L. P. Pitaevskii, and S. Stringari, "First and Second Sound in Cylindrically Trapped Gases," *Phys. Rev. Lett.*, vol. 105, no. 15, p. 150402, 2010.

[103] T. Ghosh and K. Machida, "Sound velocity and multibranch Bogoliubov spectrum of an elongated Fermi superfluid in the BEC-BCS crossover," *Phys. Rev. A*, vol. 73, no. 1, p. 013613, 2006.

[104] N. Manini and L. Salasnich, "Bulk and collective properties of a dilute Fermi gas in the BCS-BEC crossover," *Phys. Rev. A*, vol. 71, no. 3, p. 033625, 2005.

[105] G. Astrakharchik, J. Boronat, J. Casulleras, and S. Giorgini, "Equation of State of a Fermi Gas in the BEC-BCS Crossover: A Quantum Monte Carlo Study," *Phys. Rev. Lett.*, vol. 93, no. 20, p. 200404, 2004.

[106] H. Heiselberg, "Sound modes at the BCS-BEC crossover," *Phys. Rev. A*, vol. 73, no. 1, p. 013607, 2006.

[107] I. Ferrier-Barbut, M. Delehaye, S. Laurent, A. T. Grier, M. Pierce, B. S. Rem, F. Chevy, and C. Salomon, "A mixture of bose and fermi superfluids." Science 1255380 Published online, 17 July 2014.

[108] Y. Castin, I. Ferrier-Barbut, and C. Salomon, "The Landau critical velocity for a particle in a Fermi superfluid," *ArXiv Prepr.*, p. 13, 2014.

[109] A. C. Mathey, C. W. Clark, and L. Mathey, "Decay of a superfluid current of ultracold atoms in a toroidal trap," *Phys. Rev. A*, vol. 90, no. 2, p. 023604, 2014.

[110] G. Astrakharchik and L. P. Pitaevskii, "Motion of a heavy impurity through a Bose-Einstein condensate," *Phys. Rev. A*, vol. 70, no. 1, p. 013608, 2004.

[111] L. D. Landau and E. M. Lifshitz, *Quantum Mechanics: Non-Relativistic Theory, Course of Theoretical Physics Vol. 3*. New York: Pergamon, 1989.

[112] S. K. Adhikari, "Quantum scattering in two dimensions," *Am. J. Phys.*, vol. 362, no. 1986, pp. 362–367, 2008.

[113] J. Levinsen and M. M. Parish, "Chapter 1 Strongly interacting two-dimensional Fermi gases," in *World Sci. Rev.*, ch. 1, 2014.

[114] M. Randeria, J.-M. Duan, and L.-Y. Shieh, "Superconductivity in a two-dimensional Fermi gas: Evolution from Cooper pairing to Bose condensation," *Phys. Rev. B*, vol. 41, no. 1, pp. 327–343, 1990.

[115] V. Makhalov, K. Martiyanov, and A. Turlapov, "Ground-State Pressure of Quasi-2D Fermi and Bose Gases," *Phys. Rev. Lett.*, vol. 112, no. 4, p. 045301, 2014.

[116] M. Feld, B. Fröhlich, E. Vogt, M. Koschorreck, and K. Michael, "Observation of a pairing pseudogap in a two-dimensional Fermi gas," *Nat. Phys.*, vol. 480, no. 75, 2011.

[117] B. Fröhlich, M. Feld, E. Vogt, M. Koschorreck, M. Köhl, C. Berthod, and T. Giamarchi, "Two-Dimensional Fermi Liquid with Attractive Interactions," *Phys. Rev. Lett.*, vol. 109, no. 13, p. 130403, 2012.

[118] V. Ngampruetikorn, J. Levinsen, and M. M. Parish, "Pair Correlations in the Two-Dimensional Fermi Gas," *Phys. Rev. Lett.*, vol. 111, no. 26, p. 265301, 2013.

[119] K. Huang, *Statistical Mechanics*. Michigan: John Wiley and Sons, 1991.

[120] N. N. Bogoliubov, *Statistical Physics Part 2, Selected Works, Part II: Quantum and Statistical Mechanics*. New York: Gordon and Breach, 1991.

[121] E. M. Lifshitz and L. P. Pitaevskii, *Statistical Physics, Part 2*. New York: Pergamon, 1980.

[122] V. N. Popov, *Functional Integrals in Quantum Field Theory and Statistical Physics*. Dordrecht: Reidel, 1983.

[123] D. R. Nelson and J. M. Kosterlitz, "Universal Jump in the Superfluid Density of Two-Dimensional Superfluids," *Phys. Rev. Lett.*, vol. 39, no. 19, pp. 1201–1205, 1977.

[124] I. Rudnick, "Critical Surface Density of the Superfluid Component in 4He Films," *Phys. Rev. Lett.*, vol. 40, no. 22, pp. 1454–1455, 1978.

[125] D. J. Bishop and J. D. Reppy, "Study of the Superfluid Transition in Two-Dimensional 4He Films," *Phys. Rev. Lett.*, vol. 40, no. 26, pp. 1727–1730, 1978.

[126] J. Noh, J. Lee, and J. Mun, "Observation of the universal jump across the Berezinskii-Kosterlitz-Thouless transition in two-dimensional Bose gases," *arXiv*, pp. 1–5, 2013.

[127] D. S. Petrov, M. A. Baranov, and G. V. Shlyapnikov, "Superfluid transition in quasi-two-dimensional Fermi gases," *Phys. Rev. A*, vol. 67, no. 031601, pp. 1–4, 2003.

[128] K. Miyake, "Fermi Liquid Theory of Dilute Submonolayer 3He on Thin 4He II Film," *Prog. Theor. Phys.*, vol. 69, no. 6, pp. 1794–1797, 1983.

[129] S. S. Botelho and C. A. R. Sá de Melo, "Vortex-Antivortex Lattice in Ultracold Fermionic Gases," *Phys. Rev. Lett.*, vol. 040404, pp. 1–4, 2006.

[130] W. J. Mullin, "Bose-Einstein condensation in a harmonic potential," *J. Low Temp. Phys.*, vol. 106, no. 5-6, pp. 615–641, 1997.

[131] T.-L. Ho and M. Ma, "Quasi 1 and 2D Dilute Bose Gas in Magnetic Traps: Existence of Off-Diagonal Order and Anomalous Quantum Fluctuations," *J. Low Temp. Phys.*, vol. 115, no. 1/2, pp. 61–70, 1999.

[132] D. S. Petrov, G. V. Shlyapnikov, and J. T. M. Walraven, "Regimes of Quantum Degeneracy in Trapped 1D Gases," *Phys. Rev. Lett.*, vol. 85, no. 18, pp. 3745–3749, 2000.

[133] D. S. Petrov, M. Holzmann, and G. V. Shlyapnikov, "Bose-Einstein Condensation in Quasi-2D Trapped Gases," *Phys. Rev. Lett.*, vol. 84, no. 12, pp. 2551–2555, 2000.

[134] O. Penrose and L. Onsager, "Bose-Einstein Condensation and Liquid Helium," *Phys. Rev.*, vol. 104, no. 3, pp. 576–584, 1956.

[135] C. Pethick and H. Smith, *Bose-Einstein Condensation in Dilute Gases*. Cambridge: Cambridge University Press, 2001.

[136] E. L. Wolf, *Graphene: A New Paradigm in Condensed Matter and Device Physics*. Oxford: Oxford University Press, 2014.

[137] L. D. Landau and E. M. Lifshitz, *Bose Einstein Condensation*. Cambridge: Cambridge University Press, 1995.

[138] H. T. C. Stoof, *Ultracold Quantum Fields*. Bristol: Canopus Publishing, 2009.

[139] E. H. Lieb, R. Seiringer, and J. Yngvason, "A Rigorous Derivation of the Gross-Pitaevskii Energy Functional for a Two-dimensional Bose Gas," *Commun. Math. Phys.*, vol. 224, no. 1, pp. 17–31, 2001.

[140] M. Schick, "Two-Dimensional System of Hard-Core Bosons," *Phys. Rev.*, vol. 3, no. 3, pp. 1067–1073, 1971.

[141] G. Astrakharchik, J. Boronat, J. Casulleras, I. Kurbakov, and Y. Lozovik, "Equation of state of a weakly interacting two-dimensional Bose gas studied at zero temperature by means of quantum Monte Carlo methods," *Phys. Rev. A*, vol. 79, no. 5, p. 051602, 2009.

[142] T. D. Lee and C. N. Yang, "Many-Body Problem in Quantum Mechanics and Quantum Statistical Mechanics," *Phys. Rev.*, vol. 105, p. 1119, 1956.

[143] C. A. R. Sá de Melo, M. Randeria, and J. R. Engelbrecht, "Crossover from BCS to Bose Superconductivity: Transition Temperature and Time-Dependent Ginzburg-Landau Theory," *Phys. Rev. Lett.*, vol. 71, no. 19, pp. 3202–3205, 1993.

[144] J. R. Engelbrecht, M. Randeria, and C. A. R. Sá de Melo, "BCS to Bose crossover: Broken-symmetry state," *Phys. Rev. B*, vol. 55, no. 22, pp. 15153–15156, 1997.

[145] H. Hu, A. Minguzzi, X. Liu, and M. P. Tosi, "Collective Modes and Ballistic Expansion of a Fermi Gas in the BCS-BEC Crossover," *Phys. Rev. Lett.*, vol. 3, no. November, pp. 3–6, 2004.

[146] A. Bulgac, J. E. Drut, and P. Magierski, "Spin 1/2 Fermions in the Unitary Regime: A Superfluid of a New Type," *Phys. Rev. Lett.*, vol. 96, no. 9, p. 090404, 2006.

[147] R. B. Diener, R. Sensarma, and M. Randeria, "Quantum fluctuations in the superfluid state of the BCS-BEC crossover," *Phys. Rev. A*, vol. 77, no. 2, p. 023626, 2008.

[148] R. Haussmann, W. Rantner, S. Cerrito, and W. Zwerger, "Thermodynamics of the BCS-BEC crossover," *Phys. Rev. A*, vol. 75, no. 2, p. 023610, 2007.

[149] P. Pieri, L. Pisani, and G. C. Strinati, "BCS-BEC crossover at finite temperature in the broken-symmetry phase," *Phys. Rev. B*, vol. 70, no. 9, p. 094508, 2004.

[150] Q. Chen, J. Stajic, and K. Levin, "Thermodynamics of Interacting Fermions in Atomic Traps," *Phys. Rev. Lett.*, vol. 95, no. 26, p. 260405, 2005.

[151] J. Carlson, S.-Y. Chang, V. R. Pandharipande, and K. E. Schmidt, "Superfluid Fermi Gases with Large Scattering Length," *Phys. Rev. Lett.*, vol. 91, no. 5, p. 050401, 2003.

[152] S.-Y. Chang, J. Morales, V. R. Pandharipande, D. G. Ravenhall, J. Carlson, S. C. Pieper, R. B. Wiringa, and K. E. Schmidt, "Neutron Matter: A Superfluid Gas," *Nucl. Phys. A*, vol. 746, pp. 215–221, 2004.

[153] S.-Y. Chang and V. R. Pandharipande, "Ground-State Properties of Fermi Gases in the Strongly Interacting Regime," *Phys. Rev. Lett.*, vol. 95, no. 8, p. 080402, 2005.

[154] G. Astrakharchik, J. Boronat, J. Casulleras, and S. Giorgini, "Momentum Distribution and Condensate Fraction of a Fermion Gas in the BCS-BEC Crossover," *Phys. Rev. Lett.*, vol. 95, no. 23, p. 230405, 2005.

[155] M. Randeria, J.-M. Duan, and L.-Y. Shieh, "Bound States, Cooper Pairing, and Bose Condensation in Two Dimensions," *Phys. Rev.*, vol. 62, no. February, pp. 981–984, 1989.

[156] S. Schmitt-Rink, C. Varma, and A. E. Ruckenstein, "Pairing in Two Dimensions," *Phys. Rev. Lett.*, vol. 63, no. 4, pp. 445–448, 1989.

[157] S. Traven, "Superfluidity of a Two-Dimensional Dilute Attractive Fermi Gas," *Phys. Rev. Lett.*, vol. 73, no. 25, pp. 3451–3454, 1994.

[158] E. Babaev and H. Kleinert, "Nonperturbative XY-model approach to strong coupling superconductivity in two and three dimensions," *Phys. Rev. B*, vol. 59, no. 18, pp. 83–89, 1999.

[159] V. P. Gusynin, V. M. Loktev, and S. G. Sharapov, "Pseudogap phase formation in the crossover from Bose-Einstein condensation to BCS superconductivity," *J. Exp. Theor. Phys.*, vol. 88, no. 4, pp. 685–695, 1999.

[160] J.-P. Martikainen and P. Törmä, "Quasi-Two-Dimensional Superfluid Fermionic Gases," *Phys. Rev. Lett.*, vol. 95, no. 17, p. 170407, 2005.

[161] W. Zhang, G.-D. Lin, and J.-M. Duan, "Berezinskii-Kosterlitz-Thouless transition in a trapped quasi-two-dimensional Fermi gas near a Feshbach resonance," *Phys. Rev. A*, vol. 78, no. 4, p. 043617, 2008.

[162] A. M. Fischer and M. M. Parish, "BCS-BEC crossover in a quasi-two-dimensional Fermi gas," *Phys. Rev. A*, vol. 88, no. 2, p. 023612, 2013.

[163] P. Bloom, "Two-dimensional Fermi gas," *Phys. Rev. B*, vol. 12, no. 1, pp. 125–129, 1975.

[164] G. Bertaina and S. Giorgini, "Density profiles of polarized Fermi gases confined in harmonic traps," *Phys. Rev. A*, vol. 79, no. 013616, 2011.

[165] G. Bertaina, "Two-dimensional short-range interacting attractive and repulsive Fermi gases at zero temperature," *Eur. Phys. J. Spec. Top.*, vol. 217, no. 1, pp. 153–162, 2013.

[166] A. A. Orel, P. Dyke, M. Delehaye, C. J. Vale, and H. Hu, "Density distribution of a trapped two-dimensional strongly interacting Fermi gas," *New J. Phys.*, vol. 13, no. 11, p. 113032, 2011.

[167] V. M. Loktev and S. G. Sharapov, "Superconducting Condensate Formation in Metallic Systems with Arbitrary Carrier Density," *ArXiv Prepr.*, no. 1, p. 49, 1997.

[168] E. Babaev and H. Kleinert, "Crossover from Weak- to Strong-Coupling Superconductivity and to Normal State with Pseudogap," *arXiv*, 1998.

[169] J. R. Engelbrecht and M. Randeria, "New Collective Mode and Corrections to Fermi-Liquid Theory in Two Dimensions," *Phys. Rev. Lett.*, vol. 65, no. 8, pp. 1032–1035, 1990.

[170] J. R. Engelbrecht, M. Randeria, and L. Zhang, "Landau f function for the dilute Fermi gas in two dimensions.," *Phys. Rev. B. Condens. Matter*, vol. 45, no. 17, pp. 10135–10138, 1992.

[171] J. R. Engelbrecht and M. Randeria, "Low-density repulsive Fermi gas in two dimensions: Bound-pair excitations and Fermi-liquid behaviour," *Phys. Rev. B*, vol. 45, no. 21, pp. 419–434, 1992.

[172] C. Mora and Y. Castin, "Ground State Energy of the Two-Dimensional Weakly Interacting Bose Gas: First Correction Beyond Bogoliubov Theory," *Phys. Rev. Lett.*, vol. 102, no. 18, p. 180404, 2009.

[173] K. Martiyanov, V. Makhalov, and A. Turlapov, "Observation of a Two-Dimensional Fermi Gas of Atoms," *Phys. Rev. Lett.*, vol. 105, no. 3, p. 030404, 2010.

[174] B. Fröhlich, M. Feld, E. Vogt, M. Koschorreck, W. Zwerger, and M. Köhl, "Radio-Frequency Spectroscopy of a Strongly Interacting Two-Dimensional Fermi Gas," *Phys. Rev. Lett.*, vol. 106, no. 10, pp. 16–19, 2011.

[175] A. T. Sommer, L. W. Cheuk, M. Ku, W. S. Bakr, and M. W. Zwierlein, "Evolution of Fermion Pairing from Three to Two Dimensions," *Phys. Rev. Lett.*, vol. 108, no. 4, pp. 1–5, 2012.

[176] M. Koschorreck, D. Pertot, E. Vogt, B. Fröhlich, M. Feld, and M. Köhl, "Attractive and repulsive Fermi polarons in two dimensions.," *Nature*, vol. 485, no. 7400, pp. 619–22, 2012.

[177] Y. Zhang, W. Ong, I. Arakelyan, and J. E. Thomas, "Polaron-to-Polaron Transitions in the Radio-Frequency Spectrum of a Quasi-Two-Dimensional Fermi Gas," *Phys. Rev. Lett.*, vol. 108, no. 23, pp. 1–5, 2012.

[178] P. Dyke, E. Kuhnle, S. Whitlock, H. Hu, M. Mark, S. Hoinka, M. Lingham, P. Hannaford, and C. J. Vale, "Crossover from 2D to 3D in a Weakly Interacting Fermi Gas," *Phys. Rev. Lett.*, vol. 106, no. 105304, pp. 2–5, 2011.

[179] M. R. Andrews, D. M. Kurn, H. Miesner, D. S. Durfee, C. G. Townsend, S. Inouye, and W. Ketterle, "Propagation of Sound in a Bose-Einstein Condensate," *Phys. Rev. Lett.*, vol. 553, no. 1, pp. 553–556, 1997.

[180] R. Meppelink, S. B. Koller, and P. van der Straten, "Sound propagation in a Bose-Einstein condensate at finite temperatures," *Phys. Rev. A*, vol. 80, no. 043605, pp. 1–7, 2009.

[181] L. Salasnich, "Dynamical properties of the unitary Fermi gas: collective modes and shock waves," *ArXiv Prepr.*, 2012.

[182] E. Taylor, H. Hu, L. P. Pitaevskii, A. Griffin, and S. Stringari, "First and second sound in a strongly interacting Fermi gas 1 2," *Phys. Rev. A*, vol. 80, no. 053601, pp. 1–7, 2009.

[183] Y.-H. Hou, L. P. Pitaevskii, and S. Stringari, "First and second sound in a highly elongated Fermi gas at unitarity," *Phys. Rev. A*, vol. 88, no. 4, p. 043630, 2013.

[184] T. Ozawa and S. Stringari, "Discontinuities in the First and Second Sound Velocities at the Berezinskii-Kosterlitz-Thouless Transition," *Phys. Rev. Lett.*, vol. 112, no. 2, p. 025302, 2014.

[185] H. Hu, P. Dyke, C. J. Vale, and X.-J. Liu, "First and second sound of a unitary Fermi gas in highly oblate harmonic traps," *New J. Phys.*, vol. 16, no. 8, p. 083023, 2014.

[186] J. Tempere, S. N. Klimin, and J. T. Devreese, "Thermodynamic Functions for Superfluid Fermions in Two Dimensions," *J. Low Temp. Phys.*, vol. 171, no. 3-4, pp. 415–421, 2013.

[187] L. Tisza, "Sur la théorie des liquides quantiques. application a l'hélium liquide," *J. Phys. Radium*, vol. 350, pp. 164–172, 1940.

[188] L. D. Landau *J. Phys. USSR*, vol. 71, 1941.

[189] E. Taylor and A. Griffin, "Two-fluid hydrodynamic modes in a trapped superfluid gas," *Phys. Rev. A*, no. September, 2005.

[190] J. Kinast, S. L. Hemmer, M. E. Gehm, A. Turlapov, and J. E. Thomas, "Evidence for Superfluidity in a Resonantly Interacting Fermi Gas," *Phys. Rev. Lett.*, vol. 92, no. 15, p. 150402, 2004.

[191] M. Bartenstein, A. Altmeyer, S. Riedl, S. Jochim, C. Chin, J. Denschlag, and R. Grimm, "Collective Excitations of a Degenerate Gas at the BEC-BCS Crossover," *Phys. Rev. Lett.*, vol. 92, no. 20, p. 203201, 2004.

[192] G. Bruun and H. Smith, "Viscosity and thermal relaxation for a resonantly interacting Fermi gas," *Phys. Rev. A*, vol. 72, no. 4, p. 043605, 2005.

[193] R. J. Donnelly, "The two-fluid theory and second sound in liquid helium," *Phys. Today*, no. October, pp. 34–39, 2009.

[194] T.-L. Ho and Q. Zhou, "Obtaining the phase diagram and thermodynamic quantities of bulk systems from the densities of trapped gases," *Nature*, vol. 6, no. 2, pp. 131–134, 2009.

[195] M. Bartenstein, a. Altmeyer, S. Riedl, S. Jochim, C. Chin, J. Denschlag, and R. Grimm, "Crossover from a Molecular Bose-Einstein Condensate to a Degenerate Fermi Gas," *Phys. Rev. Lett.*, vol. 92, no. 12, p. 120401, 2004.

[196] P. A. Murthy, D. Kedar, T. Lompe, M. Neidig, M. G. Ries, A. N. Wenz, G. Zürn, and S. Jochim, "Matter wave Fourier optics with a strongly interacting two-dimensional Fermi gas," *arXiv*, pp. 1–7, 2014.

[197] M. G. Ries, A. N. Wenz, G. Zürn, L. Bayha, I. Boettcher, D. Kedar, P. A. Murthy, M. Neidig, T. Lompe, and S. Jochim, "Observation of pair condensation in a strongly interacting two-dimensional Fermi gas," *ArXiv Prepr.*, 2014.

[198] N. Luick, *Local probing of the Berezinskii-Kosterlitz-Thouless transition in a two-dimensional Bose gas*. Institute for Laser-Physics, University of Hamburg, 2014.

[199] T. Yefsah, A. Sommer, M. J. H. Ku, L. W. Cheuk, W. Ji, W. S. Bakr, and M. W. Zwierlein, "Heavy solitons in a fermionic superfluid," *Nature*, vol. 499, no. 7459, pp. 426–30, 2013.

[200] L. P. Pitaevskii and A. Rosch, "Breathing modes and hidden symmetry of trapped atoms in two dimensions," *Phys. Rev. A*, vol. 55, no. 2, pp. 853–856, 1997.

[201] M. Olshanii, H. Perrin, and V. Lorent, "Example of a Quantum Anomaly in the Physics of Ultracold Gases," *Phys. Rev. Lett.*, vol. 105, no. 9, p. 095302, 2010.

[202] S. K. Baur, E. Vogt, M. Köhl, and G. Bruun, "Collective modes of a two-dimensional spin-1/2 Fermi gas in a harmonic trap," *Phys. Rev. A*, vol. 87, no. 4, p. 043612, 2013.

[203] A. Bianchi, R. Movshovich, C. Capan, P. G. Pagliuso, and J. L. Sarrao, "Possible Fulde-Ferrell-Larkin-Ovchinnikov Superconducting State in CeCoIn_{5}," *Phys. Rev. Lett.*, vol. 91, no. 18, p. 187004, 2003.

[204] J. Hubbard, "Electron Correlations in Narrow Energy Bands," *Proc. R. Soc. A Math. Phys. Eng. Sci.*, vol. 276, no. 1365, pp. 238–257, 1963.

[205] J. G. Bednorz and K. A. Miiller, "Condensed Matt Possible High Tc Superconductivity in the Ba-La-Cu-O System," *Zeitschrift fur Phys.*, vol. 193, no. 64, pp. 189–193, 1986.

[206] Z. Hadzibabic, P. Krüger, M. Cheneau, B. Battelier, and J. Dalibard, "Berezinskii-Kosterlitz-Thouless crossover in a trapped atomic gas," *Nature*, vol. 441, no. 7097, pp. 1118–21, 2006.